Green's function retrieval from noise correlation in multiple scattering media

Aida Hejazi Nooghabi

Sorbonne Université

Faculté des Sciences et Ingénierie

ED 398 - Géosciences, Ressources Naturelles et Environnement

Institut des Sciences de la Terre de Paris (ISTeP)

Doctoral thesis

Green's function retrieval from noise correlation in multiple scattering media

Aida Hejazi Nooghabi

Supervisors:

Lapo Boschi (ISTeP, Paris), Julien de Rosny (Institut Langevin, Paris)

Co-supervisor: Philippe Roux (ISTerre, Grenoble)

Jury members:

Olivier Legrand - Professor - University of Côte d'Azur (Reviewer)

Florent Brenguier - Enseignant-chercheur - University of Grenoble Alpes (Reviewer)

Kees Wapenaar - Professor - Delft University of technology (Examiner)

Johan Robertsson - Professor - ETH (Examiner)

Loic Labrousse - Professor - Sorbonne University (Examiner)

Public defense on November 23, 2018

Summary

Ambient-noise interferometry is an approach to estimate the transient response between two receivers without an active source. Because it has the remarkable advantage of functioning even in the absence of controlled sources, this method has found applications in many fields, including ultrasonics, medical imaging, structural health monitoring, civil engineering, etc. More specifically, it has received a special attention in seismology. The method consists of cross-correlating recordings of ambient vibrations at a pair of passive instruments that act only as receivers. The resulting waveform resembles the one we would observe if there was a pulsed source at the location of one of the receivers. In seismology, ambient noise results mostly from the interactions between the solid Earth and ocean waves and most of its energy propagates in the form of seismic surface waves. Passive surface-wave estimation has been successfully used for tomographic and monitoring purposes. This method is based on the fundamental requirement that the wave-field be 'diffuse': i.e., it is the superposition of waves that travel in all directions with equal probability. The diffuse-field condition is only approximately met in real-world applications, and the limits of applicability of ambient-noise interferometry in this context have not been rigorously defined.

This dissertation contributes to evaluating the robustness and accuracy of Green's function reconstruction by cross-correlation of noise, disentangling the respective roles of ballistic and reverberated ('coda') signals. We focus our study on a strongly reverberating medium. We conduct a suite of experiments on a highly reverberating thin duralumin plate, where we generate an approximately diffuse flexural wave-field. We validate ambient-noise theory by comparing cross-correlation to the directly-measured Green's function for two different distribution of sources namely

as uniform (referred to the case where a set of point sources is homogeneously distributed all over the medium with regular spacing) and circular (referred to the case where point sources are distributed on a circle surrounding the receivers). We develop an analytical model, that predicts the dependence of the symmetry of the cross-correlations on the number of sources and the signal-to-noise ratio, which explains experimental results. We next study the effects of cross-correlating our data over time windows of variable length, possibly very short, and taken at different points in the coda of recordings. We find that, even so, a relatively dense/uniform source distribution could result in a good estimate of the Green's function; we demonstrated that the cross-correlation window does not have to include direct arrival part of the signals for the estimated Green's function to be a good approximation of the exact one. Afterwards, we explicitly study the role of non-deterministic noise on cross-correlations and establish a model which confirms that the relative effect of noise is stronger when the late coda is cross-correlated.

In the second part of the manuscript, we focus on a reverberating medium with a scatterer. Our objective is to passively estimate the scattering strength of the scatterer by implementing ambient-noise interferometry. We conduct experiments on a thin elastic plate and retrieve the Green's function through cross-correlation before and after the appearance of a scatterer. We also perform experiments for the case where the scatterer is always present in the medium but is displaced from one acquisition to the other. The variations in the coda of the Green's function are then tracked in time and quantified through similarity coefficient. Temporal variations of the similarity decay exponentially. We relate this decay to the appearance/removal or displacement of the scatterer within the medium of propagation and propose a formalism to find the scattering strength of the scatterer from this decay. Our approach which is based on the information carried by the coda of the passively recovered Green's function is then validated through a conventional method for the measurement of the scattering strength that is based on direct arrivals.

In the last part, we focus on a reverberating medium with locally resonant scatterers which acts as a metamaterial. Metamaterials are man-made materials and

have properties that cannot be found with natural materials. These materials are useful in manipulating the wave propagation for different purposes. For instance, these materials have the capability to prohibit the propagation of waves at certain frequency bands. This striking behavior has nothing to do with the order in the structure but with the presence of sub-wavelength resonators. These forbidden frequency bands that are generated as a result of the coupling between the resonators and the propagating incident wave are known as 'bandgap' while other permitted frequency ranges are considered as the 'propagation band'. These materials have recently started to gain interest among seismologists for their potential application in seismic hazard. We build an example of such materials in the laboratory by attaching an array of rods, arranged in a sub-wavelength order, to the surface of a thin elastic plate. Our objective is to assess the behavior of the cross-correlation in such a medium. We find different behaviors which are consistent with the regimes that correspond to propagation band, bandgap and edges of the bandgap. We explain the related regimes by introducing evanescent wave formalism. We also take advantage of the auto-correlation of the recordings to provide spatial maps of energy distribution on the plate. We find that the spatial maps provided based on auto-correlation and cross-correlation of recordings are helpful to locate the metamaterial region, i.e., the area covered by resonators. Locating the bandgap and the position of the locally resonant metamaterial embedded in a medium are necessary steps for further manipulations and hence applications of a metamaterial within a given structure. We next apply the cross-correlation technique to the real data obtained in METAFORET experiment. This experiment is a seismic survey that is conducted in a 120 m by 120 m flat area, partly occupied by a relatively regular grid of tall pine trees, and partly by a canola field. We study the scattering effects of trees on cross-correlations of ambient signal. Our findings are in consistent with the resonating behavior of trees at the corresponding frequency bands.

Résumé

L'interférométrie de bruit ambiant est une approche pour estimer la réponse impulsionnelle entre deux récepteurs sans source active. Cette technique, qui a l'avantage de fonctionner même en l'absence de sources contrôlées, a été appliquée avec succès dans différents domaines comme les ultrasons, l'imagerie médicale, le contrôle non destructif des structures ou l'ingénierie civile. Cependant, c'est en sismologie qu'elle a connue le plus grand essort. La méthode consiste à corréler les signaux vibratoires ambiants enregistrés à une paire de capteurs. Le front d'onde résultant ressemble à celui que l'on pourrait observer s'il y avait une source ponctuelle à la place d'un des récepteurs. En sismologie, le bruit ambiant est généré principalement par les interactions entre la Terre solide et la houle océanique. La plupart de l'énergie ainsi libérée se propage sous forme d'ondes sismiques de surface. La méthode d'estimation passive des ondes de surface a permis de réaliser des tomographies avec une résolution inégalée. La condition fondamentale pour que la méthode fonctionne bien est d'avoir un champ d'ondes 'diffus'; c'est-à-dire qu'il est statistiquement isotrope. Dans les applications réelles, la condition de champ d'ondes diffus n'est pas complétement satisfaite, ce qui induit une erreur sur l'estimation de la réponse. Cet effet a été quantifié en milieu libre, mais pas en milieu complexe.

Cette thèse contribue à l'évaluation de la robustesse et de la précision de la reconstruction de la fonction de Green par la corrélation du bruit ambiant dans les milieux réverbérants. Plus précisément, on distingue les rôles respectifs de la partie balistique et coda des signaux dans les corrélations. Nous présentons une série d'expériences réalisées sur une plaque mince de duralumin, où est généré un champ d'ondes de flexion diffus. Nous validons la théorie du bruit ambiant par comparaison de la corrélation obtenue pour deux distributions de sources différentes

(soit uniforme, soit circulaire) avec la fonction de Green directement mesurée. Nous développons également un modèle analytique, qui prévoit la dépendance de la symétrie de la corrélation en fonction du nombre de sources et du rapport de signal sur bruit. Ce modèle explique bien des résultats expérimentaux. Ensuite, nous avons corrélé des données sur des fenêtres de temps de différentes durées, et prises sur les différentes parties de la coda. Nous avons montré que la fenêtre choisie pour la corrélation ne doit pas nécessairement inclure la partie qui correspond aux ondes directes pour que la fonction de Green estimée soit une bonne approximation de la fonction de Green exacte. Nous trouvons même dans le cas d'une distribution de sources relativement uniforme la corrélation d'une petite partie de la coda entraîne une bonne estimation de la fonction de Green. Enfin, nous étudions explicitement le rôle du bruit non-déterministe sur les corrélations.

Dans la seconde partie de ce manuscrit, nous nous concentrons sur un milieu réverbérant incluant un diffuseur. Notre objectif est d'estimer de manière passive la force du diffuseur en utilisant l'interférométrie du bruit ambiant. Nous réalisons des expériences sur une plaque mince élastique et retrouvons la fonction de Green par corrélation avant et après l'apparition du diffuseur. Nous faisons aussi des expériences dans un cas où le diffuseur est toujours présent dans milieu, mais est déplacé d'une acquisition à l'autre. Les variations de la coda reconstruite augmentent avec le temps de propagation. La quantification de ces variations permet d'estimer la section efficace de diffusion du ou des diffuseurs. Notre approche est fondée sur l'information contenue dans la coda obtenue passivement. Cette approche est ensuite validée par une méthode classique fondée sur les ondes directes pour mesurer la puissance du diffuseur.

Dans la dernière partie de ce travail, nous nous concentrons sur un milieu réverbérant contenant les inclusions résonantes. Celui-ci se comporte comme un métamatériau qui possède des propriétés que l'on ne peut pas trouver dans les matériaux naturels. Certains de ces matériaux ont la capacité d'interdire la propagation des ondes dans certaines gammes de fréquence. Ce comportement impressionant n'a rien à voir avec l'ordre ou la périodicité de la structure. Il est lié à la

présence de résonateurs sub-longueur d'onde. Ces gammes interdites de propagation, intitulées 'bandgap' sont générées en raison du couplage entre l'onde incidente et les résonateurs. Les autres gammes de fréquence sont, par contre, considérées comme des 'bandes de propagation'. Comme ce type de matériaux a de potentielles d'applications dans le domaine des risques sismiques, il a récemment éveillé l'intérêt de la communauté des sismologues. Nous avons construit un de ces matériaux au laboratoire qui est constitué des tiges verticales à la surface d'une plaque mince élastique. L'espacement entre les tiges est inférieur à une longueur d'onde. Notre but est d'évaluer le comportement de la corrélation dans ce type de milieu. Nous trouvons que les différents comportements sont bien cohérents avec les régimes qui correspondent à la bande de propagation ou à la bande interdite. Nous expliquons ces régimes grâce au formalisme des ondes évanescentes. Nous faisons aussi une auto-corrélation et montrons comment l'énergie est distribuée dans la plaque. Nous trouvons que ces cartes spatiales obtenues par corrélation et auto-corrélation sont utiles pour localiser la surface couverte par des résonateurs. Déterminer la gamme de fréquence qui correspond au bandgap, ainsi que la localisation de la surface couverte dans le milieu par les résonateurs, sont des étapes nécessaires pour les futures expériences de propagation des ondes dans des structures sismiques. Enfin, nous appliquons la technique de corrélation aux données réelles récupérées lors de l'expérience METAFORET. Cette expérience a été réalisée sur une zone de 120 m par 120 m couverte de pins distribués sur une grille de manière relativement régulière et un champ de colza. Lors de cette étude sismique, les arbres jouent le rôle des résonateurs. Nous étudions l'influence du caractère diffusant des arbres sur la corrélation de bruit. Nos résultats sont en accord avec le comportement diffusant des arbres dans les gammes de fréquence correspondantes.

Acknowledgement

I would like to thank my supervisor Lapo Boschi whose enthusiasm, knowledge, patience and time were always present for me. Also, I am honored to be a part of WAVES project under your coordination. Thanks for giving me this amazing opportunity. *Grazie mille!*

I would like to express my gratitude to my supervisor Julien de Rosny for introducing me to the world of acoustic experiments and never leaving me alone in that wonderland. I was truly amazed by your persistence, modesty and perseverance. *Merci beaucoup!*

I want to thank my advisor Philippe Roux in Grenoble. I appreciate your wonderful way of encouraging and supporting me. *Merci beaucoup!*

My most special thanks goes to my dad, Khalilallah, and my mom, Mehri; the most precious people of my life. Those who always encouraged me to pursue my dreams. Thanks for your unconditional presence, being always close despite being far. I also want to thank the two strong mountains of my life who always kept my back safe since I remember, my brothers, Arash and Arvin. I also appreciate the support of my sister-in-law, Samira, who always sent me her positive energies.

Contents

Chapter 1

Fundamentals of Waves in Plates

1.1 Introduction

Lamb waves are guided elastic waves that propagate between the two boundaries in the plane of a plate. They are very useful while handling 2D propagation of guided waves. For instance, since many structures are flat and plate-like, Lamb waves propagate in them. Hence, these waves are used in SHM (Structural Health Monitoring) for inspection of structures like buildings, bridges and etc., because they can propagate over long distances [1]. Structural health monitoring is referred to all the methods that seek the safety and reliability of a structure and helps in finding the possible defects in the structure and hence is of use for maintenance goals. There have also been some fundamental studies on these waves in the laboratory scale.

The main purpose of this chapter is to give a brief introduction to the physics of propagation of waves in plates specifically Lamb waves. We present here the fundamental equations and concepts as well as assumptions and notations that will be used in the following chapters. Plate motion includes internal shear and bending resistance. We elaborate these concepts in the case of thin plates and introduce the two existing models for describing the motion of the plate each with different assumptions. For our study, we are particularly interested in the propagation of these waves in the low frequency regime. We then explain the modal decomposition approach and implement it for a finite reverberating plate and close the chapter with derivation of an expression for modal density is such a system.

1.2 Surface Elastic Waves in Plates

Suppose an isotropic homogeneous plate with a constant thickness of $e = 2h$ and infinite lateral dimension (Fig. 1.1). We consider the plate as a free plate. A free plate is defined as a plate whose outside medium is vacuum. For such a plate the two boundaries are stress-free.

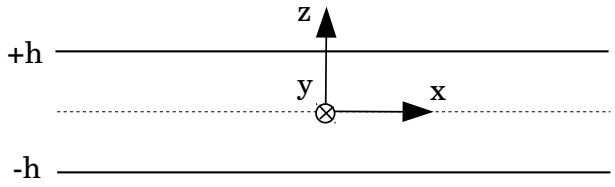

Figure 1.1: Homogeneous plate with infinite lateral dimensions and thickness of $2h$.

If this plate is excited with a bulk wave, the wave will be repeatedly reflected back from the boundary into the medium. As a result of these multiple reflections, the trapped waves start to interfere with themselves. At specific frequencies and angles, the resulting superposition of these waves will lead to the vibration of the whole sample at particular modes. The latter known as Lamb wave was introduced by the English mathematician Horace Lamb [2]. Symmetry of the structure defines two families of deformation for Lamb waves known as symmetric (S) and antisymmetric (A). It should be noted that the symmetric or antisymmetric modes are distinguished with respect to the mid plane of plate (dashed line in Fig. 1.1). As can be seen in Fig. 1.1, the coordinate system (x,y) corresponds to this mid plane. Assuming the x axis as the direction of propagation, two different categories of deformation are distinguished as the following:

I) Symmetric mode of propagation: For these modes, the longitudinal components of displacement (u_x) are equal on either side of the plate, while the transverse components (u_z) are opposite (see Fig. 1.2). As a result of the propagation of this mode, the plate stretches or compresses in the direction of wave propagation. That is why this mode is sometimes known as extensional mode.

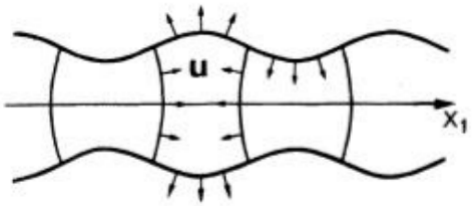

Figure 1.2: Fundamental symmetric mode of Lamb wave (Figure from [3]).

II) Antisymmetric mode of propagation: These modes have opposite longitudinal components on either side of the median plate while the transverse components are equal. The movement of the mid plane is flexion without compression and the plate bends as these modes propagate (see Fig. 1.3).

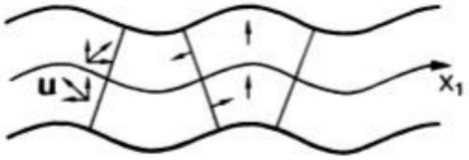

Figure 1.3: Fundamental antisymmetric Lamb wave (Figure from [3]).

Beside the symmetric and antisymmetric modes of Lamb wave, there exists another wave which is a horizontal transversal wave known as SH. These waves are polarized in the y direction and propagate at the speed given by $V_T = \sqrt{\frac{\mu}{\rho}}$ where μ is the shear modulus and ρ is the mass density of the plate.

The main characteristic of SH and Lamb waves is that they both have multimodal guided propagation, hence the modes are numbered. They are ordered according to their cut-off frequency. Higher modes have higher cut-off frequency. Cut-off frequency for the nth mode is defined as the lowest frequency at which this mode exists. Dispersion is another characteristic of these waves and is the focus of the following figure where the frequency-wavenumber representation for the first eight modes ($n = 0, ..., 3$) of Lamb waves (symmetric (S_n) and antisymmetric (A_n)) as well as phase and group velocity dispersion curves are shown (see Fig. 1.4).

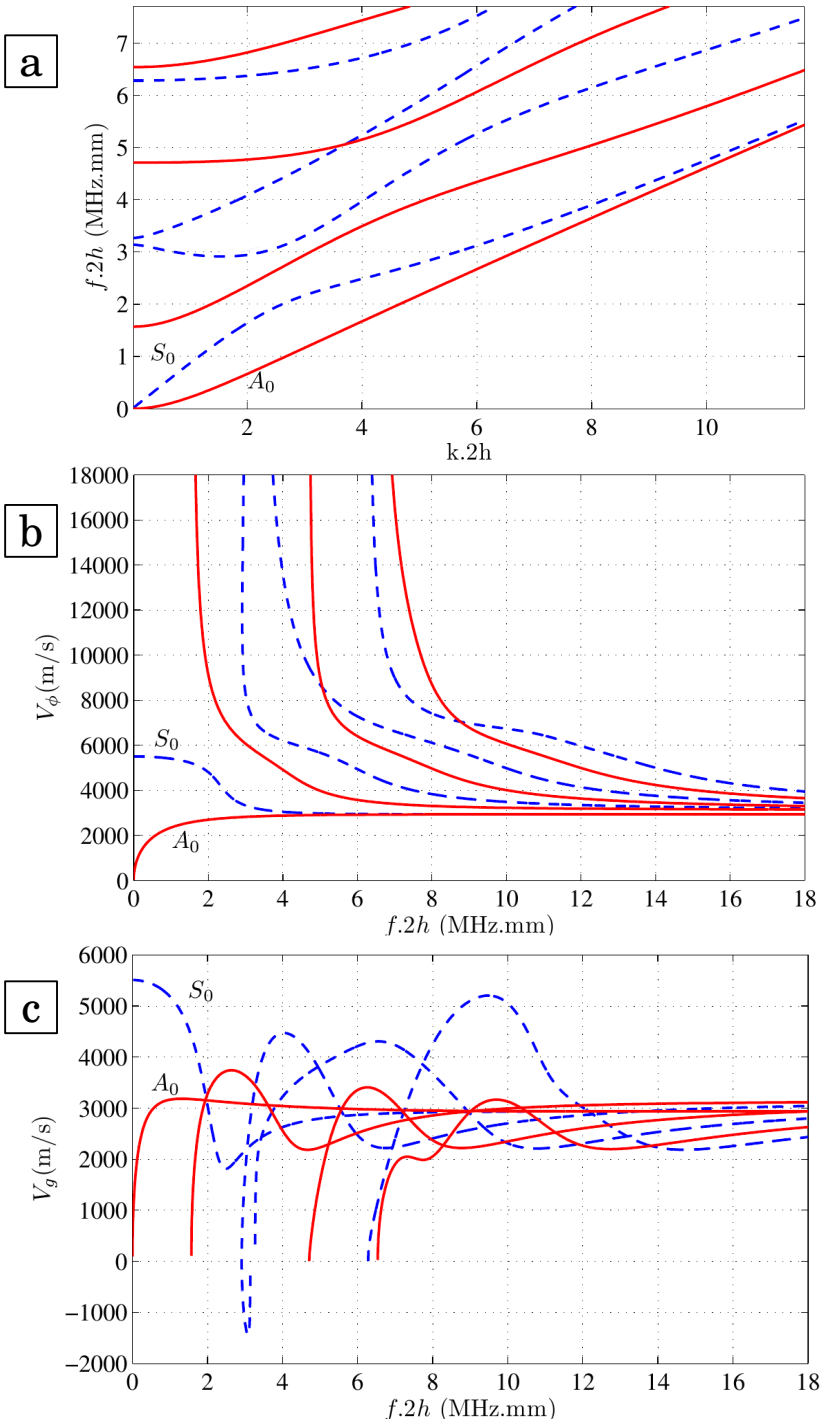

Figure 1.4: a) Frequency-wavenumber representation b) phase velocity dispersion curve c) group velocity dispersion curve for the first four modes of symmetric (dashed lines) and antisymmetric (solid lines) Lamb waves. The plate is infinite and made of aluminum. Poisson ratio and speed of transverse waves are 0.34 and 3140 m/s, respectively (Figures from [4]).

Dispersion means that waves with different frequencies travel with different phase speeds. The relation between ω and k is known as the dispersion relation and is given as the following for Lamb waves:

$$\frac{\omega^4}{{V_T}^4} = 4k^2q^2\left[1 - \frac{p}{q}\frac{\tan(ph+\alpha)}{\tan(qh+\alpha)}\right]. \tag{1.1}$$

α can be 0 or $\pi/2$ for symmetric and antisymmetric modes, respectively. p and q are defined as $p^2 = \frac{\omega^2}{{V_L}^2} - k^2$ and $q^2 = \frac{\omega^2}{{V_T}^2} - k^2$ where V_L and V_T are the phase velocity of the bulk longitudinal and transverse waves, respectively and h is half of the thickness of the plate. This dispersion relation between ω and k is known as Rayleigh-Lamb equation. Curves in Fig. 1.4a are obtained based on Eq. 1.1 for an infinite homogeneous isotropic aluminum plate of thickness $e = 2h$, Poisson ratio of $\nu = 0.34$, transverse wave speed of $V_T = 3140$ m/s and longitudinal wave speed of $V_L = 2512$ m/s. We observe that fundamental symmetric and antisymmetric Lamb waves (S_0 and A_0) do not have a cut-off frequency meaning that they exist at all frequencies. In general, these two modes are always generated regardless of the frequency bandwidth of the excitation source. Fig 1.4b and c are the phase and group velocity dispersion curves. Phase velocity is given by $V_\phi = \omega/k$ and group velocity by $V_g = \partial\omega/\partial k$. The strong dispersive behavior of these waves is clearly observed.

For SH waves, the dispersion relation is given by

$$f(k) = \frac{V_T}{2\pi}\left[k^2 + (\frac{n\pi}{2h})^2\right]^{1/2}. \tag{1.2}$$

The frequency-wavenumber representation for the first six modes of SH waves ($n = 0, ..., 5$) is shown in Fig. 1.5. As can be seen, SH_0 is the only mode that does not show a dispersive behavior. Besides, similar to S_0 and A_0 modes, this mode also exists at all frequencies. As we will see in the following chapters, throughout our study, we are working in a frequency band where the only propagating modes are fundamental modes of Lamb waves (i.e., S_0 and A_0) as well as SH_0. In our experiments, we mostly deal with A_0 mode which is known as flexural mode in vibroacoustics community.

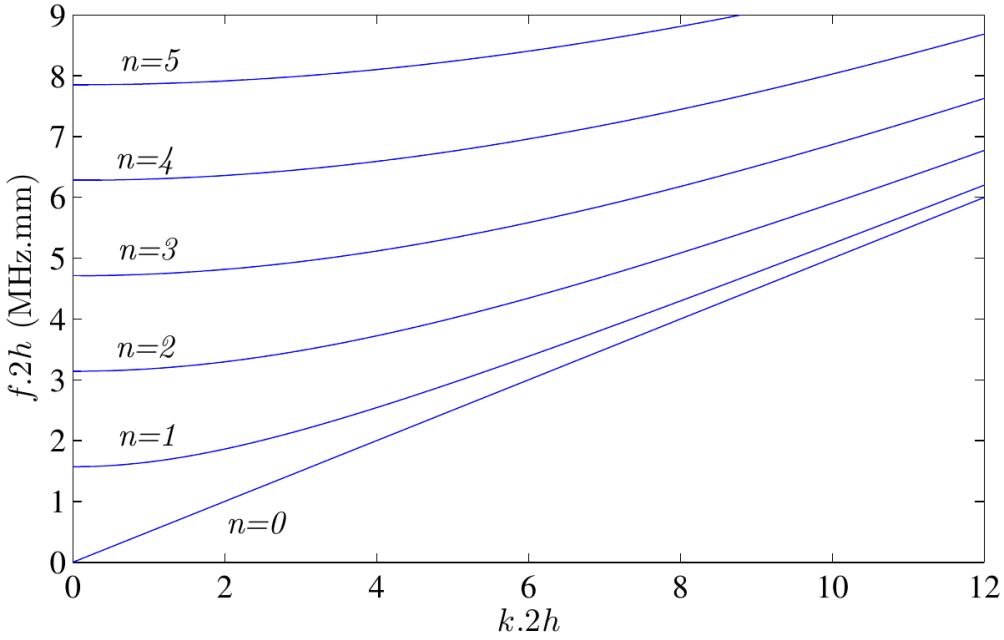

Figure 1.5: Frequency-wavenumber representation for SH waves based on Eq. 1.2. The plate is infinite and made of aluminum. Poisson coefficient and speed of transverse waves are 0.34 and 3140 m/s, respectively (Figure from [4]).

Next section describes the governing equations of the displacement of the plate for this specific mode as well as the dispersion relation.

1.3 Governing Equations for a Plate Under Flexural Vibration

Taking into account the experiments that we run on thin plates, we mostly deal with the fundamental mode of antisymmetric Lamb waves (A_0). For this reason, in the following we study the equation of motion and dispersion relation of this mode in the low frequency regime (in the order of tens of kHz). This range of frequency is our frequency band of interest in the experiments. Low frequency approximation corresponds to the case where the wavelength of the flexural modes is large compared to the thickness of the plate ($\lambda > e$). There are two different models with different assumptions that allow to describe flexion of the plates: model of Kirchhoff or classical theory of the plates ([5]) and Mindlin ([6], [7]).

1.3.1 Kirchhoff-Love Model

Theory of Kirchhoff is based on the following hypotheses ([5]):

- The material is elastic, homogeneous and isotropic.

- The plate is flat at $t = 0$.

- The plate is thin in the sense that the thickness of the plate is small compared to the other dimensions but is comparable or larger than the transverse displacement (w) of the mid plane.

- We neglect the transverse shear deformations. It means that the deformation is pure flexion and a segment of the plate that is initially perpendicular to the mid plane will stay the same in the deformation. This is known as the Kirchhoff-Love hypothesis.

- We neglect the rotation inertia and consider only $u_z = w(x, y, t)$.

In the frame of Kirchhoff-Love hypothesis, it can be shown that the normal component of the displacement $u_z = w(x, y, t)$ obeys the following equation of motion

$$D\Delta^2 w(x, y, t) + \rho e \left[\frac{\partial^2 w(x, y, t)}{\partial t^2}\right] = -q(x_s, y_s, t) \tag{1.3}$$

where Δ^2 is the biLaplacian operator defined as the squared Laplacian (i.e., $\Delta^2 u = \nabla^2(\nabla^2 u)$), ρ is the volume density, e is the thickness of the plate, $q(x_s, y_s, t)$ is the transverse component of the force per unit area and D is the flexural rigidity of the plate given by

$$D = \frac{Ee^3}{12(1 - \nu^2)} \tag{1.4}$$

where E and ν are the Young's modulus and Poisson ratio, respectively [8].

A possible solution for displacement $w(x, y, t)$ in the case of a harmonic flexural wave has the form

$$w(x, y, t) = w_0 e^{i[\omega t - (k_x x + k_y y)]} \tag{1.5}$$

where w_0 is the amplitude of the harmonic wave, ω is the angular frequency and k_x and k_y are the wavenumber in x and y directions and are related to the wavenumber k through $k^2 = k_x^2 + k_y^2 = \frac{\omega^2}{V_\phi^2(\omega)}$ where V_ϕ is the phase speed of the flexural waves. Substituting Eq. 1.5 in Eq. 1.3 without the source term, gives the following relation between k and ω known as dispersion relation for mode A_0 which is valid at low

frequencies:

$$k^4 = \frac{\rho e}{D}\omega^2. \tag{1.6}$$

From Eq. 1.6, we find phase velocity (V_ϕ) and group velocity (V_g) of the flexural waves as

$$V_\phi = \frac{\omega}{k} = \sqrt{\omega}(\frac{D}{\rho e})^{\frac{1}{4}}, \qquad v_g = \frac{\partial \omega}{\partial k} = 2\sqrt{\omega}(\frac{D}{\rho e})^{\frac{1}{4}}. \tag{1.7}$$

We infer from Eq. 1.7 that phase velocity depends on the frequency which implies the dispersive nature of flexural waves in isotropic thin plates. Fig. 1.6 shows the dispersion curves of the group and phase velocity for an aluminum plate of thickness of $e = 3$ mm versus frequency obtained by Eq. 1.7. The elastic parameters of the plate are: $\rho = 2690$ kg/m^3, $\nu = 0.346$ and $E = 69$ GPa, similar to plates used in our experimental study.

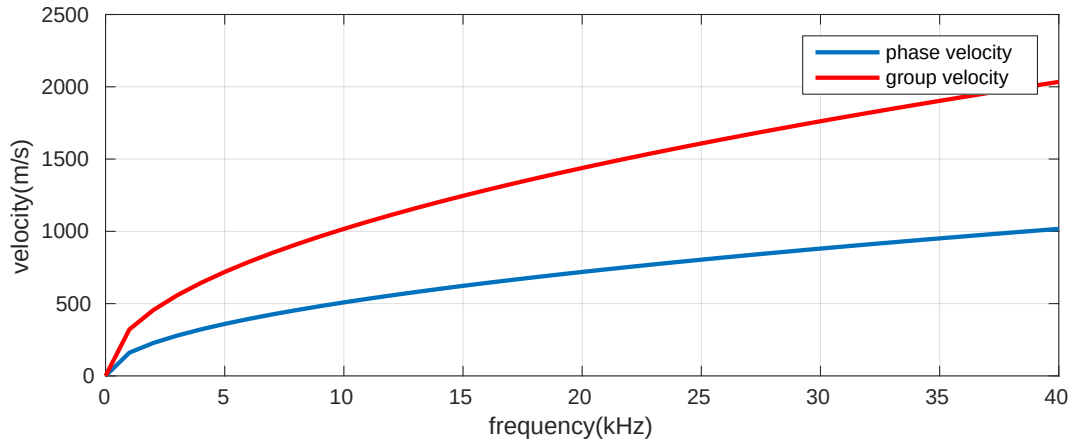

Figure 1.6: Dispersion curve for A_0 Lamb mode as a function of frequency. The thickness of the plate is 3 mm. The curves are obtained according to Eq. 1.7 for phase (blue curve) and group (red curve) velocity.

Taking into account the attenuation and absorption effects, it follows from Eq. 1.3 that

$$D\Delta^2 w(x,y,t) + \rho e\left[\frac{\partial^2 w(x,y,t)}{\partial t^2} + \frac{1}{\tau_a}\frac{\partial w(x,y,t)}{\partial t}\right] = -q(x_s, y_s, t) \tag{1.8}$$

where τ_a indicates the attenuation time.

1.3.2 Reissner-Mindlin Model

An enhanced version of Kirchhoff-Love model is the Reissner-Mindlin model where despite Kirchhoff-Love model the shear effects and rotational inertia are taken into account ([6], [7]). Kirchhoff-Love model does not work very well when the product (wavenumber × thickness) is high. In such a case, the assumptions behind Kirchhoff-Love model are not satisfied. In that model, we assumed that the segments of the plate that were initially perpendicular to the median plane of the plate stay the same when the deformation is occurring. Such an assumption does not hold here since the effects of rotation and transverse shear of the plate are not neglected. For such a case, the displacement field in cylindrical coordinates is given by [9]

$$u_r = -z\Pi_r(r,\theta) \tag{1.9}$$

$$u_\theta = -z\Pi_\theta(r,\theta) \tag{1.10}$$

$$u_z = w(r,\theta) \tag{1.11}$$

The transverse displacement w is decomposed into a propagative w_1 and evanescent w_2 part. The rotations Π_r and Π_θ are expressed by three potentials w_1, w_2 and V:

$$w(r,\theta) = w_1(r,\theta) + w_2(r,\theta) \tag{1.12}$$

$$\Pi_r = A_1\frac{\partial w_1}{\partial r} + A_2\frac{\partial w_2}{\partial r} + \frac{1}{r}\frac{\partial V}{\partial \theta} \tag{1.13}$$

$$\Pi_\theta = A_1\frac{1}{r}\frac{\partial w_1}{\partial \theta} + A_2\frac{1}{r}\frac{\partial w_2}{\partial \theta} + \frac{\partial V}{\partial r} \tag{1.14}$$

with $A_i = -1 + \frac{k_P^2}{k_i^2}$.

Each of these potentials obey one Helmholtz equation:

$$\Delta w_1 + k_1^2 w_1 = 0 \tag{1.15}$$

$$\Delta w_2 + k_2^2 w_2 = 0 \tag{1.16}$$

$$\Delta V + k_3^2 V = 0 \tag{1.17}$$

The wavenumbers are found by the following equations:

$$k_{1,2}^2 = \frac{1}{2}(k_P^2 + k_{T'}^2) \pm \sqrt{k_f^4 + \frac{1}{4}(k_P^2 - k_{T'}^2)^2} \qquad \text{and} \qquad k_3^2 = \kappa^2\frac{k_1^2 k_2^2}{k_P^2} \tag{1.18}$$

where k_f is the wavenumber that we obtain by Kirchhoff in Eq. 1.6, k_P is the wavenumber of longitudinal wave, $k_{T'}$ is the wavenumber of shear waves which includes a correction term $\kappa = \frac{\pi}{\sqrt{12}}$ such that $c_{T'} = \kappa c_T$ [10].

For frequencies smaller than the cut-off frequency of mode A_1, only the wavenumber k_1 is real which is associated to the propagation of the mode A_0. The wavenumbers k_2 and k_3 are imaginary and correspond to evanescent waves. So, Mindlin model explains the evanescent modes which are not explained by Kirchhoff model.

In our numerical simulations for modeling the flexural mode A_0, we use the ELMER software [1] which implements the Mindlin model for solving the propagation of Lamb waves in thin plates.

As an example, Fig. 1.7 summarizes the three different approaches for finding the dispersion relation. The material is a duralumin plate with the thickness of 3 μm. The elastic parameters of the plate are $E = 69$ GPa, $\nu = 0.346$ and $\rho = 2.69$ kg/m^3.

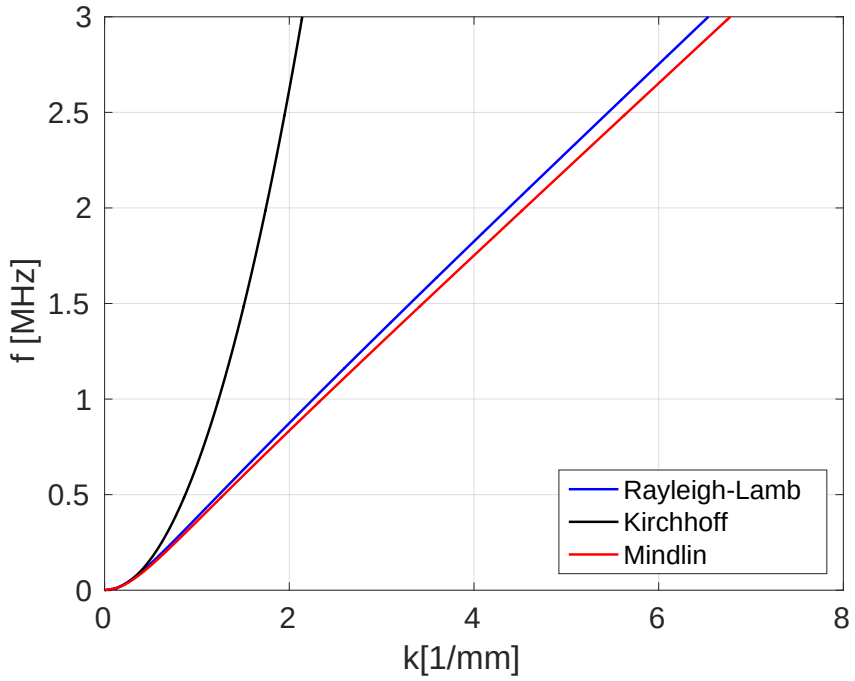

Figure 1.7: Frequency-wavenumber representation for A_0 mode obtained from three different approaches: exact theory of Rayleigh-Lamb (blue curve), theory of Kirchhoff (black curve) and theory of Mindlin (red curve) for a duralumin plate of thickness of 3 mm.

[1] https://www.csc.fi/web/elmer

We observe that at low frequencies the three models bring about very close results but as the frequency increases the distinction between the Kirchhoff model and the two other models becomes more and more significant indicating that the assumptions taken in Kirchhoff-Love model are not valid anymore at high frequencies. This verifies the fact that as long as we are in the low frequency regime, the implementation of Kirchhoff model is a reasonable choice. As we will see in the following chapters, our calculations are all based on the fact that the equation of motion based on Kirchhoff-Love model governs the regime under study. Considering the frequency regime we are dealing in our experiments ($f < 40$ kHz), this assumption seems to be acceptable.

1.4 Modal Representation of the Vibrations in the Plate

In a closed medium, the wave-field can be represented in terms of all the possible characteristic forms of vibration known as 'modes'. Modal decomposition of the wave-field is a common approach in physical problems dealing with closed media. In the case of a finite rectangular thin plate, these modes are the solutions of Eq. 1.3 and can be expressed as the product of a function of time and a function of space [11]. From a mathematical point of view, these functions are the eigen vectors for the Laplacian operator in case of a membrane and biLaplacian in case of a thin plate and they satisfy the boundary conditions.

For the case of a symmetric homogeneous isotropic thin plate with simply supported boundary conditions, vibrating under flexural modes the displacement $w(x, y, t)$ can be expressed as a linear combination of modes of the plate:

$$w(x, y, t) = \sum_{m=1}^{\infty} \sum_{n=1}^{\infty} e^{i\omega t} \phi_{mn}(x, y) \tag{1.19}$$

where $\phi_{mn}(x, y)$ is the modal displacement. m and n are positive integers and indicate the excited mode number. For the case of an irregular chaotic shaped plate these two indices cannot be separated. As Eq. 1.19 implies there exists a large number of modes in plates. Next section introduces a new quantity for dealing with modal nature of the vibrations in a plate known as 'modal density'.

1.4.1 Modal Density

As explained in the previous section, for a plate-like structure an infinite number of resonance frequencies exists. Each of these frequencies correspond to an eigenmode and the plate may vibrate at each of these frequencies. Similar physics governs the vibrations of beams and shells.

When we study the dynamic problems of such systems for the cases where the input force has a broad spectral content, many modes will contribute to the overall motion of the vibrating body. For statistical characterization of the reverberations, it is effective to introduce the concept of modal density.

For a given structure, modal density is defined as the asymptotic expression for the density of the frequency distribution obtainable from the frequency equation of the structure [12], [13]. In simple words, modal density is an estimation of the number of modes per unit frequency.

Modal density has the dimension of time and is sometimes known as Heisenberg time in literature. It characterizes the recording time needed for separating two modes after calculating the spectrum by Fourier transform. In other words, the inverse of modal density is an indication of the spacing of the resonant frequencies in the frequency domain [12]. For example, a low modal density is interpreted as low number of resonant frequencies in a short bandwidth, and the distance between the resonances in frequency domain is not small. In the following we derive the expression of the modal density for vibrations of a rectangular plate. We follow the approach adopted by [12].

For simplicity, we consider a rectangular plate with simply supported edges. Following Eq. 1.3, the source-free equation of motion for free vibration of a rectangular plate in 2D is given by

$$D\left[\frac{\partial^4 w}{\partial x^4} + 2\frac{\partial^4 w}{\partial x^2 \partial y^2} + \frac{\partial^4 w}{\partial y^4}\right] + \rho e \frac{\partial^2 w}{\partial t^2} = 0 \tag{1.20}$$

where D, ρ and e are flexural rigidity, density and thickness of the plate, respectively.

As a solution to this equation, we can assume that $w(x, y, t)$ has the form of

$$w(x, y, t) = W(x, y)e^{i\omega t} \tag{1.21}$$

where the spatial ($W(x, y)$) and temporal ($e^{i\omega t}$) terms are separated.

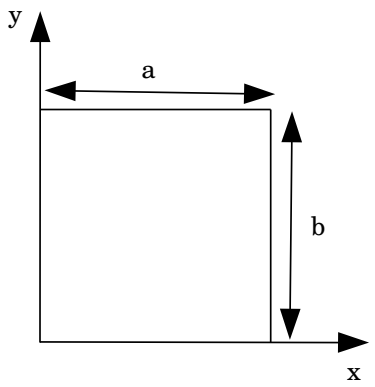

Figure 1.8: Supported rectangular plate with dimensions a and b along x and y directions.

By substituting Eq. 1.21 into Eq. 1.20, we find

$$D\Delta^2 w(x,y) - k^4 w(x,y) = 0 \tag{1.22}$$

where $k^4 = \frac{\rho e}{D}\omega^2$, which is known as dispersion relation.

The boundary conditions for a plate with dimensions a and b and simply supported edges (see Fig. 1.8) are

$$W(0,y) = W''(0,y) = W(a,y) = W''(a,y) = 0 \tag{1.23}$$

$$W(x,0) = W''(x,0) = W(x,b) = W''(x,b) = 0. \tag{1.24}$$

A plate with simply supported edges is a plate whose boundaries are prevented from deflection but they can rotate about a line along the boundary edge (such as a hinge). For a plate whose edges are simply supported, deflection and moment along the boundaries are zero. These conditions translate Eqs. 1.23 and 1.24.

It can be verified by direct substitution that the function

$$W(x,y) = \sin(\frac{m\pi x}{a})\sin(\frac{n\pi y}{b}) \tag{1.25}$$

where m and n are arbitrary integers, satisfies all boundary conditions (1.23) and (1.24). Substituting Eq. 1.25 into Eq. 4.10, we find a condition on ω for $W(x,y)$ to be solution, i.e., for each pair of values of m and n, only one value of k (or ω) is allowed,

$$k_{mn}^4 = (\frac{m\pi}{a})^4 + 2(\frac{m\pi}{a})^2(\frac{n\pi}{b})^2 + (\frac{n\pi}{b})^4 \tag{1.26}$$

which can be rewritten as

$$k_{mn}^4 = \left[(\frac{m\pi}{a})^2 + (\frac{n\pi}{b})^2\right]^2. \tag{1.27}$$

Eq. 4.18 can be expressed in terms of ω_{mn} as

$$\omega_{mn}^2 = (\frac{m^2\pi^2}{a^2} + \frac{n^2\pi^2}{b^2})V_\phi^2. \tag{1.28}$$

Next, we define

$$k_1 = \frac{m\pi}{a}, \quad k_2 = \frac{n\pi}{b} \tag{1.29}$$

and hence the difference between the two wavenumbers from one mode to the following one is

$$\Delta k_1 = \frac{\pi}{a}, \quad \Delta k_2 = \frac{\pi}{b}. \tag{1.30}$$

The wavenumber has two components corresponding to the propagation of waves along the length and width of the plate. In order to find the modal density, we should first find the number of modes in a given frequency band ($N(\omega)$) which is expressed as

$$N(\omega) = \frac{1}{\Delta k_1 \Delta k_2} \int\int_s dk_1 dk_2. \tag{1.31}$$

For the integration over the surface of k-space, we change to cylindrical coordinates:

$$k_1 = rcos\theta, \quad k_2 = rsin\theta. \tag{1.32}$$

So, Eq. 1.31 in the cylindrical coordinates becomes

$$N(\omega) = \frac{ab}{\pi^2} \int_0^{\pi/2} \left[\int_0^r r dr\right] d\theta. \tag{1.33}$$

Fig. 1.9 illustrates the rectangular plate in k-space and clarifies the limits of the integration both for r and θ. Taking the integrals, Eq. 1.33 equals to

$$N(\omega) = \frac{ab}{4\pi} r^2. \tag{1.34}$$

Keeping Fig. 1.9 in mind, r^2 is found by combining Eqs. 1.28 and 1.29:

$$r^2 = \frac{\omega^2}{V_\phi^2}. \tag{1.35}$$

We previously showed that in the regime that corresponds to our experimental set-up the phase velocity for A_0 Lamb waves is given by Eq. 1.7. Substituting the expression for V_ϕ

$$N(\omega) = \frac{ab}{4\pi}(\frac{\omega}{\sqrt{\frac{D}{\rho e}}}). \tag{1.36}$$

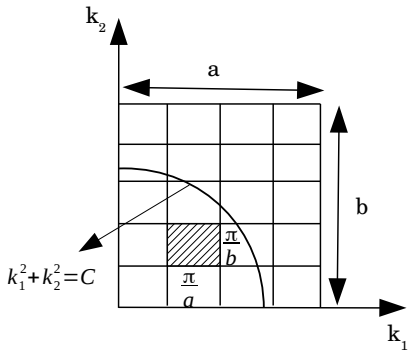

Figure 1.9: Supported rectangular plate with dimensions a and b in k-space.

Modal density (D_m) according to its definition is found by taking the derivative of $N(\omega)$ with respect to ω:

$$D_m = \frac{\partial N(\omega)}{\partial \omega} = \frac{ab}{4\pi}(\sqrt{\frac{\rho e}{D}}). \tag{1.37}$$

According to Eq. 1.37, the modal density of a plate is independent of the frequency and independent of the geometry of the plate. One may prefer to rewrite Eq. 1.37 in a more general form as

$$D_m = \frac{\partial N(\omega)}{\partial \omega} = \frac{S}{4\pi}(\sqrt{\frac{\rho e}{D}}) \tag{1.38}$$

where S is the surface of the plate with an arbitrary shape [14].

To summarize, we found the expression for the modal density of a rectangular plate. In general, the procedure for finding the modal density of a structure is: First, we find the frequency equation for the structure under study. We then determine an expression for the number of resonant frequencies up to an arbitrary frequency and finally differentiate this expression with respect to frequency. We followed this approach and found the modal density for a simply supported rectangular plate.

Chapter 2

Coda Reconstruction by Interferometry on Thin Elastic Plates

2.1 Introduction

Ambient-noise interferometry is a technique for passive estimation of the transient response of the medium between two receivers, also improperly called Green's function [1]. Here, we focus on the field of seismology where ambient noise interferometry has been shown to be a reliable method for retrieving the Green's function between two receivers without the need for an active source (such as man-made explosions, earthquake or volcanic eruptions). Back to 1957, Aki suggested using seismic noise for retrieving the dispersion properties of the subsoil [15]. This was the first step of using the information carried by ambient seismic noise. The interferometry method takes advantage of the seismic noise as well. This method is based on cross-correlation of the recordings of ambient vibrations at two receivers for recovering the coherent information i.e., waves propagating between the two receivers. In seismology, this technique has a few advantages over the conventional methods based on an active source (e.g., an earthquake): 1) Since this method is based on ambient noise which is always present, it can be applied to study the Earth structure in aseismic regions and also makes seismologists independent from waiting for an earthquake to occur in seismic regions. 2) By interferometry method, surface waves

[1] The reason why we consider the 'Green's function' as an improper name is that mathematically it is the response of the medium to a source of Dirac delta type, while in practice we never have such a source.

in the period of $\sim$ 5 s to $\sim$ 30 s can be recovered. Surface waves at this range of period are not easy to be recovered at the near field of an earthquake and they are almost completely attenuated in the far field. So, interferometry technique allows for studying the shallower structures of the Earth [16].

Green's functions obtained by cross-correlation have been used for tomographic and monitoring purposes in the past 20 years (e.g., [17], [18]).

After all, although the reliability of the interferometry technique has been proved through its application in seismic studies but there are some details and assumptions that must be fulfilled to ensure an acceptable retrieval of the Green's function. An imperfect Green's function will cause uncertainties in all further analyses based on the Green's functions. This imperfection can be due to different reasons such as an uneven distribution of sources. Therefore, we focus our study on finding out the role of source distribution in retrieval of the Green's function from correlation in a reverberating medium. We also study the contribution of different parts of the recordings in reconstruction of the Green's function for the case of impulsive sources. To do so, we implement physical acoustic experiments in the laboratory on thin plates and verify the theory by focusing on reverberating media.

In this chapter, we first explain in more detail the theory of ambient noise interferometry and then describe the experiments and set-ups and end with the obtained results and conclusion.

2.2 Basics of Ambient Noise Interferometry

Noise (seismic, acoustic, ...) had been always considered as some random undesired signal that superposes the desired signals. Several studies in 50s and 60s proposed a new interpretation to this noise and hence revealed application by using noise [15], [19]. Cross-correlation of recorded ambient waves to retrieve the Green's function is known as a passive method since there is no need for an active source. The pioneers in the experimental domain, were Weaver and Lobkis who showed the reliability of the method by considering the fluctuations in temperature as a source that excites the acoustic modes randomly in a block of aluminum and hence allows to recover the Green's function between two points on the surface of block by cross-correlating

the displacements measured at these two points [20]. From a theoretical point of view, they explain their observations by the principle of equipartition of energy over different modes. They do a similar study when the medium is reverberating and the source is an impulsive one. Thanks to the reverberation in the medium, there is an equipartition of the energy over different modes of vibration [21]. Before that in 1993, [22] measured the speed of waves from temporal cross-correlation of the intensity fluctuations on the surface of the sun. Later on, [23] and [24] used the stationary phase principle to generalize the theory to open spaces. This approach is explained later in the chapter. We start by a schematic illustration of the basics of interferometry in Fig. 2.1.

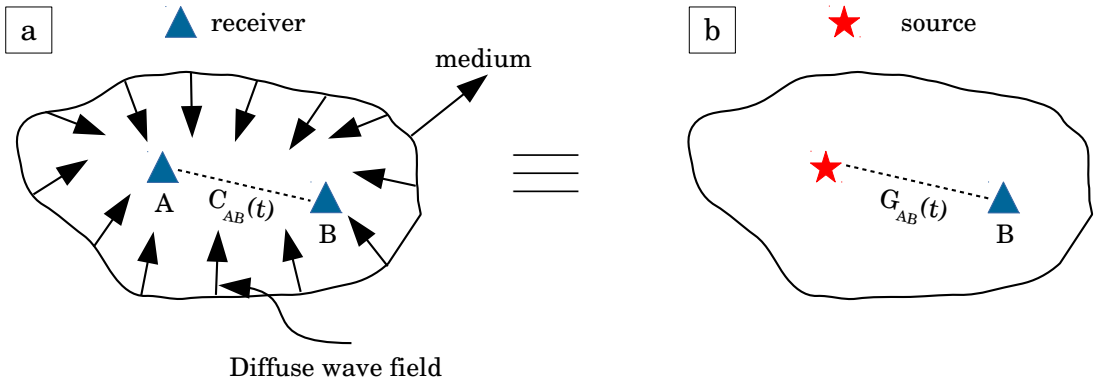

Figure 2.1: Schematic reconstruction of Green's function by cross-correlation of recordings of diffuse field.

If we have two receivers located at x_A and x_B in the medium that are illuminated by a wave-field from all directions (Fig. 2.1a), then the cross-correlation of the recordings at these two receivers ($C_{AB}(t)$) (or its time derivative) gives the Green's function between x_A and x_B ($G_{AB}(t)$) as if there was an active source at x_A (Fig. 2.1b).

In the following section, we derive the relation between the cross-correlation and the Green's function for acoustic waves.

2.2.1 Derivation of the Interferometry Relation for Acoustic Waves

In this section, we do the exercise for deriving the relation between the Green's function and cross-correlation for acoustic wave equation. The approach is the one explained in [25] and [26]. This approach is based on Green-Kirchhoff theorem sometimes called reciprocity theorem. A reciprocity theorem is a relation between two independent physical (in this case acoustic) states in a common domain (e.g., [27]). The governing equations for waves propagating in a lossless non-flowing acoustic media in time domain are the following equations

$$\rho \partial_t v_i + \partial_i p = f_i \tag{2.1}$$

known as linearized momentum equation and

$$\kappa \partial_t p + \partial_i v_i = q \tag{2.2}$$

where $\kappa = 1/\rho c^2$ is the compressibility. This is known as the stress-strain relation in an acoustic medium. In these equations, $\rho(\mathbf{x})$ is the mass density of the medium, $\kappa(\mathbf{x})$ is its compressibility, $f_i(\mathbf{x}, t)$ the external volume force density and $q(\mathbf{x}, t)$ is a source distribution in terms of volume injection rate density. $p(\mathbf{x}, t)$ and $v_i(\mathbf{x}, t)$ are the acoustic pressure and particle velocity in the medium where subscript i indicates the x_i direction. We adopt the following convention for Fourier transform of a quantity that is a function of time (t) and space ($\mathbf{x}$) like p as

$$\hat{p}(\mathbf{x}, \omega) = \int_{-\infty}^{+\infty} \exp(-j\omega t) p(\mathbf{x}, t) dt \tag{2.3}$$

where ω is the angular frequency. Eqs. 2.1 and 2.2 in frequency domain take the form

$$j\omega \rho \hat{v}_i + \partial_i \hat{p} = \hat{f}_i \tag{2.4}$$

and

$$j\omega \kappa \hat{p} + \partial_i \hat{v}_i = \hat{q}. \tag{2.5}$$

The hat denotes the Fourier transform and Einstein's summation convention [2] applies for repeated subscripts. We consider the 'interaction quantity' ([27]) as

$$\partial_i \left\{ \hat{p}_A \hat{v}_{i,B} - \hat{v}_{i,A} \hat{p}_B \right\}. \tag{2.6}$$

A and B indicate two independent acoustic states. In other words, p and v in either of the states A and B are the solutions to the same set of equations (Eqs. 2.4, 2.5). We assume here that the medium parameters do not vary from state A to B. [28] explain the concepts of reciprocity theorem and interaction quantity from the point of view of conservation law. They define a 'conserved current'. According to conservation law, the sum of partial derivatives of the conserved current called 'interaction quantity' is equal to the source of the current. The 'conserved current' does not necessarily have an obvious physical existence. In the case of linear wave-fields, the conserved current is always a bilinear form in the field variable and its first-order derivative.

We integrate the interaction quantity over an arbitrary domain V whose boundary is S and use Eqs. 2.4 and 2.5 to substitute for the parameters in states A and B. Applying the divergence theorem to the resulting integral gives

$$\int_V \left\{ \hat{p}_A \hat{q}_B - \hat{v}_{i,A} \hat{f}_{i,B} - \hat{q}_A \hat{p}_B + \hat{f}_{i,A} \hat{v}_{i,B} \right\} d^3\mathbf{x} = \oint_S \left\{ \hat{p}_A \hat{v}_{i,B} - \hat{v}_{i,A} \hat{p}_B \right\} n_i d^2\mathbf{x} \tag{2.7}$$

where n_i are the components of normal vector $\mathbf{n}$ pointing outward the boundary S. As products in the frequency domain correspond to convolution in the time domain, we call this a Green-Kirchhoff theorem of convolution type.

Here, we assume that the medium is lossless and hence take advantage of the time-reversal invariance of the acoustic wave equation [29]. Time reversal in the time domain translates to complex conjugate in the frequency domain as FT $[u(x,-t)] = \hat{u}^*(x,\omega)$. In time-reversed domain, $\hat{p}^*$ and $-\hat{v}_i^*$ satisfy Eqs. 2.4 and 2.5 with source terms $\hat{f}_i^*$ and $-\hat{q}_i^*$. Substituting these parameters in Eq. 2.6 for state A gives

$$\int_V \left\{ \hat{p}_A^* \hat{q}_B + \hat{v}_{i,A}^* \hat{f}_{i,B} + \hat{q}_A^* \hat{p}_B + \hat{f}_{i,A}^* \hat{v}_{i,B} \right\} d^3\mathbf{x} = \oint_S \left\{ \hat{p}_A^* \hat{v}_{i,B} + \hat{v}_{i,A}^* \hat{p}_B \right\} n_i d^2\mathbf{x}. \tag{2.8}$$

In the frequency domain, the products like $\hat{p}_A^* \hat{q}_B$ correspond to correlation in time domain and so this relation is known as the Green-Kirchhoff theorem of the correlation type. We now introduce the Green's functions and substitute them in both

[2] $\partial_i v_i = \sum_{i=1}^{3} \partial_i v_i$

reciprocity theorems. The Green's function is obtained when the source term is an impulsive one. Mathematically speaking, Green's function in the time domain is the response to a Dirac delta function in time and space. This function in the frequency domain for both states is given as

$$\hat{q}_A(\mathbf{x},\omega) = \delta(\mathbf{x}-\mathbf{x}_A) \tag{2.9}$$

$$\hat{q}_B(\mathbf{x},\omega) = \delta(\mathbf{x}-\mathbf{x}_B) \tag{2.10}$$

$\mathbf{x}_A$ and $\mathbf{x}_B$ are inside the domain V. We set the external forces to zero and volume injection rate densities as Eqs. 2.9 and 2.10. Then the wave-fields can be expressed in terms of acoustic Green's functions as

$$\hat{p}_A(x,\omega) \triangleq \hat{G}(\mathbf{x},\mathbf{x}_A,\omega), \tag{2.11}$$

$$\hat{v}_{i,A}(\mathbf{x},\omega) = -(j\omega\rho(\mathbf{x}))^{-1}\partial_i\hat{G}(\mathbf{x},\mathbf{x}_A,\omega) \tag{2.12}$$

$$\hat{p}_B(x,\omega) \triangleq \hat{G}(\mathbf{x},\mathbf{x}_B,\omega), \tag{2.13}$$

$$\hat{v}_{i,B}(\mathbf{x},\omega) = -(j\omega\rho(\mathbf{x}))^{-1}\partial_i\hat{G}(\mathbf{x},\mathbf{x}_B,\omega). \tag{2.14}$$

$\hat{G}(\mathbf{x},\mathbf{x}_A,\omega)$ is the Fourier transform of the causal Green's function between a source at $\mathbf{x}_A$ and a receiver at $\mathbf{x}$ known as $G(\mathbf{x},\mathbf{x}_A,t)$. We substitute Eqs. 2.9, 2.11 and 2.12 in the Eq. 2.5 and find out that $\hat{G}(\mathbf{x},\mathbf{x}_A,\omega)$ satisfies the wave equation

$$\partial_i(\rho^{-1}\partial_i\hat{G}) + (\omega^2/\rho c^2)\hat{G} = -j\omega\delta(\mathbf{x}-\mathbf{x}_A) \tag{2.15}$$

The propagation velocity is $c(\mathbf{x}) = \{\kappa(\mathbf{x})\rho(\mathbf{x})\}^{-1/2}$. $\hat{G}(\mathbf{x},\mathbf{x}_B,\omega)$ follows a similar equation.

Substituting Eqs. 2.9-2.14 into Eq. 2.7, we find

$$\hat{G}(\mathbf{x}_B,\mathbf{x}_A,\omega) - \hat{G}(\mathbf{x}_A,\mathbf{x}_B,\omega) = \oint_S \frac{-1}{j\omega\rho(\mathbf{x})}(\hat{G}(\mathbf{x},\mathbf{x}_A,\omega)\partial_i\hat{G}(\mathbf{x},\mathbf{x}_B,\omega) - \partial_i\hat{G}(\mathbf{x},\mathbf{x}_A,\omega)\hat{G}(\mathbf{x},\mathbf{x}_B,\omega))n_i d^2\mathbf{x}. \tag{2.16}$$

We choose S as a spherical surface with infinite radius and assume that there is no sources at infinity. As $\hat{G}(\mathbf{x},\mathbf{x}_A,\omega)$ and $\hat{G}(\mathbf{x},\mathbf{x}_B,\omega)$ in the integrand are the Fourier transform of the causal part of the Green's functions in time domain, the integral on the right hand side of Eq. 2.16 vanishes due to radiation conditions. We take advantage of the fact that the right hand side of this equation is independent of how

boundary S is chosen, so it vanishes for any S. The boundary S should only enclose $\mathbf{x}_A$ and $\mathbf{x}_B$. Consequently,

$$\hat{G}(\mathbf{x}_B, \mathbf{x}_A, \omega) = \hat{G}(\mathbf{x}_A, \mathbf{x}_B, \omega). \tag{2.17}$$

This is source-receiver reciprocity relation for the acoustic Green's function. We will use this relation later in our study.

We follow the same procedure for the reciprocity of correlation type. By substituting Eqs. 2.9-2.14 into Eq. 2.8, we find

$$\hat{G}^*(\mathbf{x}_B, \mathbf{x}_A, \omega) + \hat{G}(\mathbf{x}_A, \mathbf{x}_B, \omega) = \oint_S \frac{-1}{j\omega\rho(\mathbf{x})}(\hat{G}^*(\mathbf{x}, \mathbf{x}_A, \omega)\partial_i\hat{G}(\mathbf{x}, \mathbf{x}_B, \omega) - \partial_i\hat{G}(\mathbf{x}, \mathbf{x}_A, \omega)\hat{G}(\mathbf{x}, \mathbf{x}_B, \omega))n_i d^2\mathbf{x}. \tag{2.18}$$

We have the same condition as the previous case for S as it should enclose $\mathbf{x}_A$ and $\mathbf{x}_B$. In contrast to the previous case, the right hand side does not vanish. The reason is that $\hat{G}^*(\mathbf{x}, \mathbf{x}_A, \omega)$ is the Fourier transform of the anticausal Green's function in the time domain $G(\mathbf{x}, \mathbf{x}_A, -t)$ and thus the radiation conditions are not fulfilled. Using Eq. 2.17, Eq. 2.18 takes the form

$$2\Re\left\{\hat{G}(\mathbf{x}_A, \mathbf{x}_B, \omega)\right\} = \oint_S \frac{-1}{j\omega\rho(\mathbf{x})}(\hat{G}^*(\mathbf{x}_A, \mathbf{x}, \omega)\partial_i\hat{G}(\mathbf{x}_B, \mathbf{x}, \omega) - \partial_i\hat{G}^*(\mathbf{x}_A, \mathbf{x}, \omega)\hat{G}(\mathbf{x}_B, \mathbf{x}, \omega))n_i d^2\mathbf{x}. \tag{2.19}$$

$\Re$ denotes the real part. $\hat{G}$ and $\partial_i\hat{G}n_i$ in the right hand side are responses to monopole and dipole sources. The products like $\hat{G}^*\partial_i\hat{G}n_i$ translate to cross-correlation in time domain. So, right hand side is the integral of the Fourier transform of the cross-correlations of recordings at $\mathbf{x}_A$ and $\mathbf{x}_B$ due to an impulsive source at $\mathbf{x}$. Left hand side is the Fourier transform of $G(\mathbf{x}_A, \mathbf{x}_B, t) + G(\mathbf{x}_A, \mathbf{x}_B, -t)$ which is the superposition of the response at $\mathbf{x}_A$ due to a source at $\mathbf{x}_B$ and its time-reversed version.

Eq. 2.18 applies to any lossless arbitrary inhomogeneous fluid medium. Moreover, integration boundary S is an arbitrary boundary enclosing $\mathbf{x}_A$ and $\mathbf{x}_B$. Inside and outside this boundary, the medium can be inhomogeneous. In the literature on Green's function retrieval by interferometry, we may see a similar equation to Eq. 2.19 but instead of the real part on the left hand side, there is the imaginary part of the Green's function. The difference lies in the definition of the source. Let us define the source term in terms of volume injection instead of volume injection

rate. In this case, the source term in Eq. 2.9 is defined $-\delta(\mathbf{x}-\mathbf{x}_A)$ and the Green's function in the frequency domain is denoted by $\hat{g}(\mathbf{x},\mathbf{x}_A,\omega)$. This Green's function obeys a wave equation similar to Eq. 2.15, but the source on the right hand side is replaced by $-\delta(\mathbf{x}-\mathbf{x}_A)$ as following:

$$\partial_i(\rho^{-1}\partial_i\hat{g}) + (\omega^2/\rho c^2)\hat{g} = -\delta(\mathbf{x}-\mathbf{x}_A). \tag{2.20}$$

$\hat{g}(\mathbf{x},\mathbf{x}_B,\omega)$ satisfies a similar wave equation. $\hat{g}$ and $\hat{G}$ are related via $\hat{g} = (1/j\hat{\omega})\hat{G}$. Following a similar approach for deriving Eq. 2.19, we obtain

$$2j\Im\left\{\hat{g}(\mathbf{x}_A,\mathbf{x}_B,\omega)\right\} = \oint_S \frac{-1}{\rho(\mathbf{x})}(\hat{g}^*(\mathbf{x}_A,\mathbf{x},\omega)\partial_i\hat{g}(\mathbf{x}_B,\mathbf{x},\omega) - \partial_i\hat{g}^*(\mathbf{x}_A,\mathbf{x},\omega)\hat{g}(\mathbf{x}_B,\mathbf{x},\omega))n_i d^2\mathbf{x}. \tag{2.21}$$

$\Im$ denotes the imaginary part. The left hand side of this equation is the Fourier transform of $g(\mathbf{x}_A,\mathbf{x}_B,t) - g(\mathbf{x}_A,\mathbf{x}_B,-t)$. $g(\mathbf{x}_A,\mathbf{x}_B,t)$ is causal and can be obtained by taking the causal part of the difference. Since $2j\Im\left\{\hat{g}\right\} = \frac{1}{j\omega}2\Re\left\{\hat{G}\right\}$, Eq. 2.21 does not provide new information compared to Eq. 2.19.

The reconstructed Green's function by interferometry includes direct wave traveling between $\mathbf{x}_A$ and $\mathbf{x}_B$ as well as all the scattering contributions from heterogeneities inside and outside boundary S.

Eq. 2.19 is the basic equation for acoustic seismic interferometry but it is not very suitable from an application point of view since it needs the evaluation of two correlation products separately. To simplify this equation, we assume that the most contribution comes from stationary points on S. These regions are those where the changes in the phase are zero (This concept is explained in the following section). This assumption simplifies Eq. 2.19 into

$$2\Re\left\{\hat{G}(\mathbf{x}_A,\mathbf{x}_B,\omega)\right\} \simeq \oint_S \frac{2}{j\omega\rho(\mathbf{x})}\partial_i\hat{G}^*(\mathbf{x}_A,\mathbf{x},\omega)\hat{G}(\mathbf{x}_B,\mathbf{x},\omega)n_i d^2x \tag{2.22}$$

where the approximation is to include all the spurious events that deteriorate the reconstructed Green's function $\hat{G}(\mathbf{x}_A,\mathbf{x}_B,\omega)$. We see that now the right hand side includes a single cross-correlation instead of two [16], [25].

In the following, we address the interferometry technique in the domain of seismology and introduce the stationary phase regions.

2.2.2 Direct-Wave Interferometry: An Introduction to Stationary Phase Regions

In the domain of seismology, Eq. 2.22 translates to as

$$\frac{dC_{AB}(t)}{dt} \approx G(\mathbf{r}_A, \mathbf{r}_B, t) - G(\mathbf{r}_A, \mathbf{r}_B, -t) \tag{2.23}$$

where $(C_{AB}(t))$ is the cross-correlation of the recordings of ambient seismic noise at two seismic stations A and B averaged over long times and $G(\mathbf{r}_A, \mathbf{r}_B, t)$ is the causal Green's function of the medium between these two receivers. As you see, there is a time derivation of the cross-correlation involved, here. Depending on how mathematically we define the source term, the cross-correlation itself or its time derivative gives the Green's function.

Since generation of ambient seismic noise at some periods (around 7 s) is as a result of the interaction of ocean waves, it is therefore dependent on the storm activity in the oceans. Storm activity occurs typically in winter season in either of the hemispheres. In other words, in the Earth, the noise is generated in preferential positions. If the Green's function of the medium is to be reconstructed using interferometry method, then the ambient wave-field should be diffuse. Here, we assume the definition of diffuse given by [30]: A wave-field is diffuse if all of the propagation directions have equal probability. As we saw in the derivation of the interferometry, by cross-correlation one retrieves both the causal and anticausal part of the Green's function, thus in a perfect case, we expect to retrieve a symmetric cross-correlation. Fig. 2.2 shows schematically how the retrieved cross-correlation is influenced by the source distribution. A symmetric cross-correlation in time and amplitude is obtained when the noise sources are distributed randomly and isotropically (Fig. 2.2a). The cross-correlation loses its symmetry in amplitude as the distribution of sources becomes non isotropic and waves arrive from a dominant direction (Fig. 2.2b). So, we find that the source distribution plays a crucial role in retrieving a symmetric cross-correlation. Moreover, it has been shown in direct wave interferometry that not all the sources contribute to the retrieval of the Green's function. Direct wave interferometry is a term corresponding to the case where only the direct waves propagating between two stations (receivers) are of interest to be retrieved

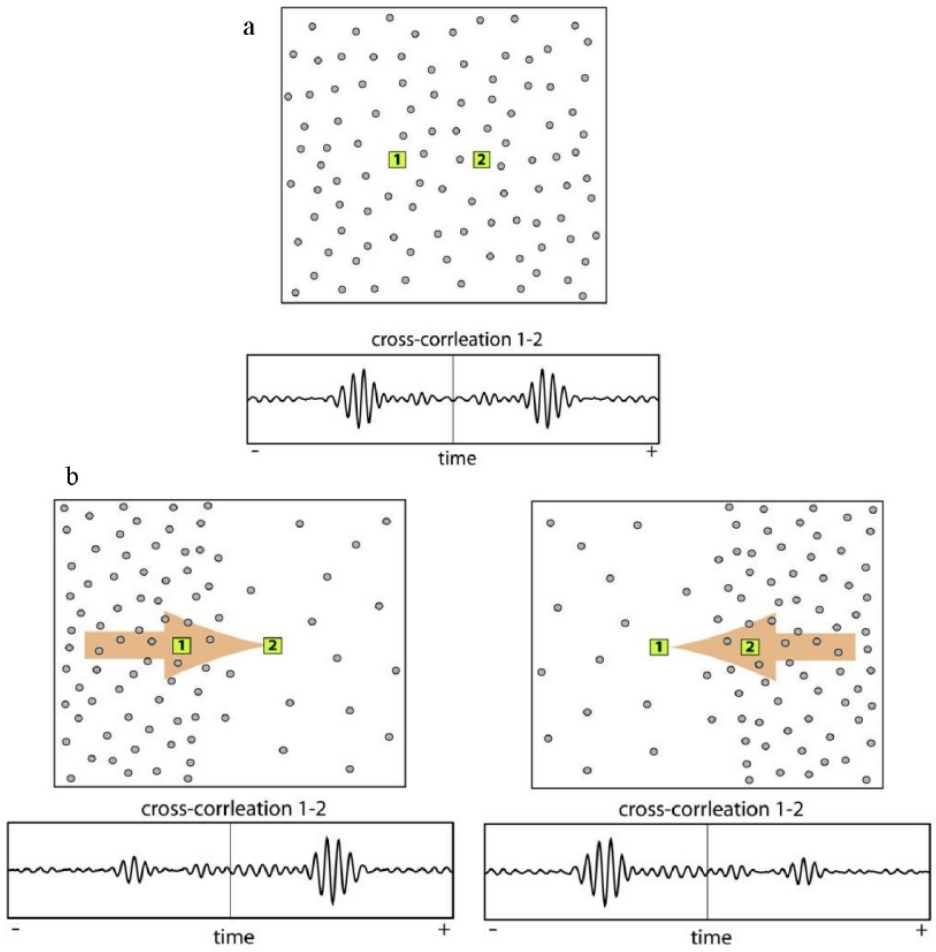

Figure 2.2: Schematic representation of the influence of distribution of noise sources on symmetry of the cross-correlation. a) Symmetric cross-correlation for the homogeneous distribution of sources. b) Asymmetric cross-correlations for the inhomogeneous and non isotropic distribution of sources. The asymmetry is in the amplitude while there is symmetry in time (Figure from [31]).

by interferometry and not the later (coda) arrivals. To illustrate the contribution of different sources, we consider a 2D case where the receivers A and B located at x_A and x_B are surrounded by point sources distributed on a circle enclosing the two receivers (black dots in Fig. 2.3a). We assume a lossless medium where the propagation velocity is 2000 m/s and the distance between the receivers is 1200 m. The position of sources is given in polar coordinates as (r_s, ϕ_s). Each source emits an impulse that travels in the medium and is received at the two receivers. The responses at each receiver are plotted in Fig. 2.3b,c as a function of the source

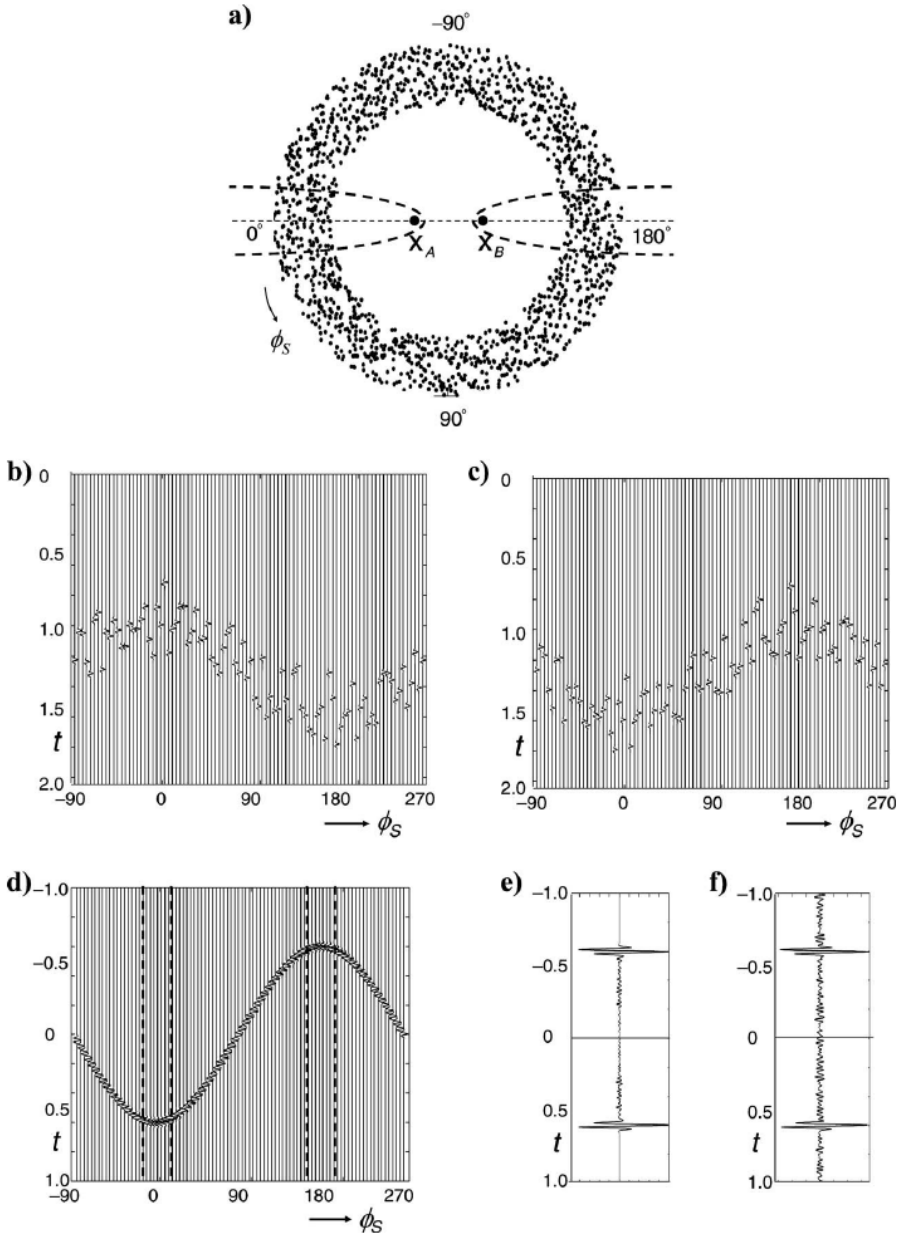

Figure 2.3: Demonstration of 2D direct-wave interferometry. a) Configuration of two stations at x_A and x_B enclosed by sources distributed on a circle. Dashed lines marks the Fresnel zones. b) Recorded signals at x_A as a function of azimuth ϕ_s. c) Recorded signals at x_B as a function of azimuth ϕ_s. d) Cross-correlation of recordings at x_A and x_B. Dashed lines mark Fresnel zones. e) Sum of cross-correlations in (d) f) Single cross-correlation of the recordings of simultaneously acting uncorrelated noise sources at x_A and x_B (Figure from [32]).

coordinate (ϕ_s). These two sets of signals are then cross-correlated and the result is shown in Fig. 2.3d as a function of ϕ_s. Next, the cross-correlations are summed over all possible azimuths and the outcome is shown in Fig. 2.3e. We clearly observe the emergence of coherence arrivals at $\pm$ 0.6 s. These wavefronts are associated with the Green's function of the medium between x_A and x_B and indicate the waves that travel in the opposite directions between the two stations. The arrival time is well in accordance with the expected arrivals considering the distance between the receivers and the wave speed. Note that since the source wavelet is not a Dirac delta function the cross correlation of recordings is in fact the Green's function convolved with the autocorrelation of the source signal according to

$$\{G(x_B, x_A, t) + G(x_B, x_A, -t)\} * S_s(t) = \Sigma_{i=1}^{N} u(x_B, x_S^{(i)}, t) * u(x_A, x_S^{(i)}, -t) \quad (2.24)$$

where $S_s(t)$ is the autocorrelation of the source function, i is the index of each point source located at x_S, u is the recordings and $*$ denotes the convolution operator. Fig. 2.3f is a single cross-correlation for the case where the sources are noise sources acting simultaneously. Another important observation in Figs. 2.3e and 2.3f is that when we sum the cross-correlations from sources in different azimuths, the contribution of sources that are not aligned with the station pair cancels out and only the point sources that are inside the zones marked by dashed line have a contribution in building the cross-correlation. These areas where the noise sources contribute constructively to the Green's function reconstruction are known as 'Fresnel zones' or 'stationary phase regions' ([23] and [32]). Sources that act outside these zones result in a destructive interference and hence no coherent contribution comes from these points. Size of these Fresnel zones that have a hyperbola shape depends on the period of the source signal and thus increases with increasing period. The direct-wave interferometry in the context of seismology refers to reconstruction of the seismic surface waves for further tomographic or monitoring purposes.

So far, we explained the basics of the interferometry method and the necessary assumption for the theory to work well. As we saw, source distribution plays an important role in passive reconstruction of the Green's function. Different studies in literature prove the reliability of the method in various domains by applying it to different datasets. But in terms of the theory there are still open questions that need to be addressed. We saw that the stationary phase regions have been

recovered for the case of open media in order to retrieve the direct waves propagating between two points. We are interested to recover these regions for the case of a close reverberating medium. In our study, we focus on the role of source distribution and also the contribution of different parts of the correlated signals in passive retrieval of the Green's function where not only the direct arrivals but also the coda arrivals are to be recovered. We focus our study on reverberating media and start by an experimental study and then we develop theories to explain our experimental results. The rest of this chapter is dedicated to our work and most of it is published in [33].

2.3 Interferometry with Lamb Waves

In practical applications, the necessary conditions for interferometry method (mentioned earlier) are only partially fulfilled. The mismatch between the cross-correlation and the Green's function for a real noise source distribution is a measure of the accuracy of the method. The mismatch in homogeneous open media can be straightforwardly deduced from geometrical considerations of the source distribution [24]. In complex random media, only statistical quantities can be inferred, and a mismatch appears as a fluctuation of the cross-correlation. In the case of multiple scattering media, these fluctuations can be relatively well predicted from a shot-noise model [34]. However, only the use of multiple scattering wave theory leads to fully consistent results [35], [36].

Only a few studies have been devoted to the interferometric reconstruction of Green's functions in bounded media. The related theory is, however, relevant to room acoustics [37] and passive structural health monitoring [38], [39]. In thin plates, the dispersion relation for noise generated by an air jet has been recovered [40]. More recently, an experimental and numerical study was also conducted to determine the role of the ballistic and coda part on the cross-correlation when the source distribution was circular and uniform [41]. Our study here follows Duroux et al. [42], who investigated the convergence of the cross-correlation of vibrational waves in a thin aluminum plate. A heuristic shot-noise model introduced by Larose et al. was used to interpret the results.

Here, similar to [42], the use of a Doppler vibrometer and the source-receiver reci-

procity theorem allows a very flexible study of the effects of the source distribution on the cross-correlation. The set-up allows the comparison of the cross-correlation result with the transient response that is estimated with an active source. We also study the symmetry of the correlation, because this is often an experimental proxy for the convergence toward the Green's function.

In the second part of our study, we cross-correlate a part of the multiply reflected wave ('coda') instead of the entire reverberating time. Then the results are analyzed through modal decomposition of the cross-correlation over the eigen vibrational modes of the plate.

We run our experiments on thin plates and hence record the guided plate waves, which are known as Lamb waves. The physics of propagation of these waves is explained in chapter 1. At low frequency, the fundamental antisymmetric and dispersive Lamb mode (A_0) dominates the vertical plate displacements. According to the Kirchhoff-Love hypothesis the Green's function (G) of the A_0 or flexural mode is the solution to the equation of motion associated with an impulsive point source,

$$D\Delta^2 G(\mathbf{r}-\mathbf{r}_0,t)+\rho_s(\frac{\partial^2 G(\mathbf{r}-\mathbf{r}_0,t)}{\partial t^2}+\frac{1}{\tau_a}\frac{\partial G(\mathbf{r}-\mathbf{r}_0,t)}{\partial t})=-\delta(\mathbf{r}-\mathbf{r}_0)\delta(t), \quad (2.25)$$

where Δ^2 is the biLaplacian operator that is defined as the squared Laplacian, ρ_s is the surface density of the plate, τ_a is the attenuation time, $\mathbf{r}$ is the position vector, t is the time, and $D = e^3E/12(1-\nu^2)$ is the bending stiffness, where E and ν are the Young's modulus and Poisson's ratio, respectively, and e is the thickness of the plate [43]. If the signal is generated by N point sources of identical power spectral density $S(\omega)$, the Fourier transform of the cross-correlation estimated from a record of duration ΔT is given by

$$C(\mathbf{r}_l^R,\mathbf{r}_{l'}^R,\omega)=\Delta T\sum_{k=1}^{N}G(\mathbf{r}_l^R,\mathbf{r}_k^S,\omega)G^*(\mathbf{r}_{l'}^R,\mathbf{r}_k^S,\omega)S(\omega), \quad (2.26)$$

where G^* is the complex conjugate of G, $\mathbf{r}_l^R$ and $\mathbf{r}_k^S$ are the l-th receiver position and the k-th source position, respectively. According to [1], the cross-correlation is related to the imaginary part of the Green's function by

$$C(\mathbf{r}_l^R,\mathbf{r}_{l'}^R,\omega)=\frac{\Delta T S(\omega)N\tau_a}{\rho_s\omega A}ImG(\mathbf{r}_l^R,\mathbf{r}_{l'}^R,\omega)+Q(\omega) \quad (2.27)$$

where A is the plate area, and the deviation $Q(\omega)$ can be caused, in particular, by non-uniformities in the source distribution, as well as by instrumental error. Eq. 2.27 shows that the Green's function associated with two locations $\mathbf{r}_l^R$ and $\mathbf{r}_{l'}^R$ where sensors are deployed can be reconstructed by cross-correlation of the ambient recordings made by the two sensors, provided that the ambient noise is diffuse [1].

2.4 Plate Experiments Set-up

The experimental set-up consists of a homogeneous duralumin plate of 50 × 60 × 0.3 cm, with five piezoelectric transducers attached to the plate using instant glue (Fig. 2.4). There are neither significant material heterogeneities within the plate, nor scattering obstacles attached to it. The temperature of the room is controlled by an air conditioning system. We measured the room temperature continuously during the experiment and no significant variation was observed.

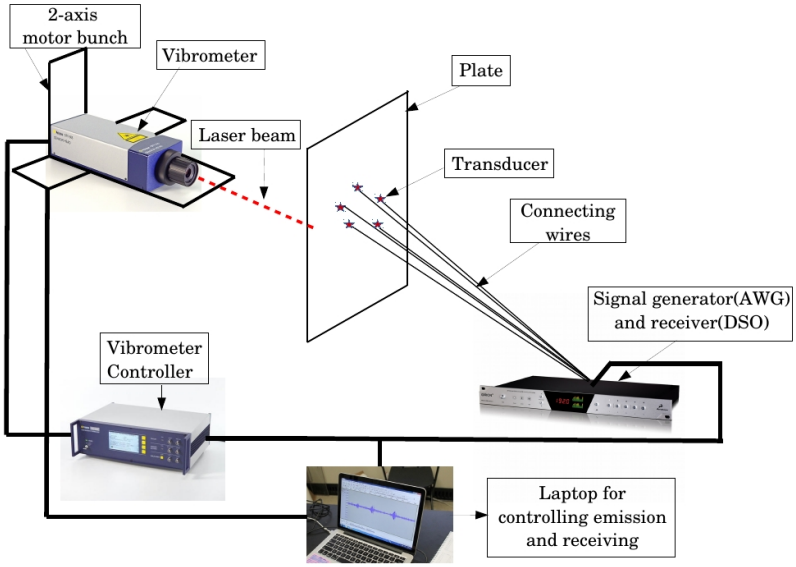

Figure 2.4: Experimental set-up, consisting of a duralumin plate and five piezoelectric transducers. The normal displacement of the plate is measured using a laser vibrometer placed on a two-dimensional motor.

All of the transducers are located at a minimum distance of 10 cm from the sides of the plate. Instead of a short pulse, a linear 'chirp' in the frequency band of 100 Hz to 40,000 Hz with the rate of frequency change of 39900 Hz/s is sent via these

transducers. The transducers are made of a 200μm-thick ceramic piezoelectric disk adhered to a thin 20mm-diameter and 200μm-thick metallic disk. Effect of such a transducer on the propagation is limited because total thickness of the transducer is only 13% of the plate thickness (the mass of the transducer equals 0.5 g). On the other side of the plate, the vertical displacement induced by the vibration (i.e., Lamb waves) is scanned with a laser vibrometer. Since the higher Lamb modes (A_1, S_1, A_2, S_2, ...) have a minimum cut-off frequency of 500 kHz, within our frequency band of interest, we can only generate the fundamental modes A_0, S_0 and SH Lamb modes. Moreover, because we are working at less than a tenth of the cut-off frequency, the displacements recorded by the vibrometer are dominated by the A_0 mode. The latter, dubbed 'flexural-plate mode' in the field of structural acoustics is very dispersive. Indeed, between 100 Hz to 40000 Hz, the phase velocity ranges between 17 m/s to 1000 m/s (i.e., wavelength between 170 to 25 mm). The group velocity has almost twice the value of the phase velocity. At such low frequency range, propagation of the A_0 mode is well described by Eq. 2.25. Note that in this frequency range, Kirchhoff-Love model holds. With this set-up, we scan the surface of the plate over two different distributions of laser points. Doing so allows us to study the role of source distribution. The procedure for doing so and the results are described in the following section.

2.5 Role of Source Distribution in Convergence of Cross-Correlation towards the Green's Function

Laser vibrometer scans are performed on two different geometries as shown in Fig. 2.5. In this analysis, we use the well-known source-receiver reciprocity theorem given by Eq. 2.17 [25]. This equation in the time domain translates to

$$G(\mathbf{x}_B, \mathbf{x}_A, t) = G(\mathbf{x}_A, \mathbf{x}_B, t). \tag{2.28}$$

In other words source and receiver can be interchanged with no difference in the recorded wave-field.

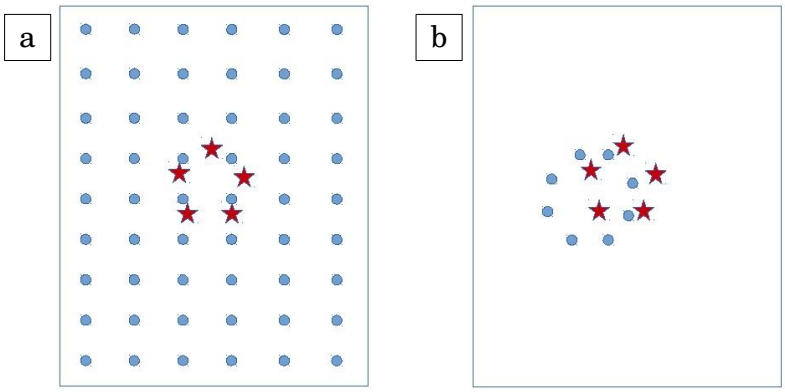

Figure 2.5: Two different distributions for the scanning points on the plate: (a) uniform (b) circular. The red stars denote the location of transducers and blue circles show schematically the position of points scanned by vibrometer.

We use this theorem to define two different virtual source distributions (uniform and circular) according to the geometry of the scanned points.

2.5.1 Uniform Source Distribution

First, we focus on the uniform source distribution. We do the scan on a grid of 2773 regularly spaced locations with a uniform distance of 1 cm between two points along the x and y plate directions (Fig. 2.5a). In this experiment, the transducers are acting as sources and the scanned points are the receivers but from now on we think of our readings as virtually emitted at the locations scanned by the vibrometer, and virtually recorded at transducer locations. This justifies why we refer to this distribution as a uniform source distribution. An example of the recorded signals after chirp pulse compression is shown in Fig. 2.6.

The envelope of the multi-reverberated impulse response shows exponential decay. By fitting an exponential function to the squared signal (intensity), an attenuation time (time that it takes for the amplitude to decrease by 1/e of the maximum amplitude) of 9 ms is found. At 10 kHz, this time corresponds to about 18 reflections off the boundaries. For a single pair of receivers separated by 12 cm and placed at minimum distance of about 19 cm from the borders of the plate, we cross-correlate the recordings from all virtual noise sources. The cross-correlation results are plotted as a shot gather in Fig. 2.7 top panel for all 2773 virtual point sources. Then

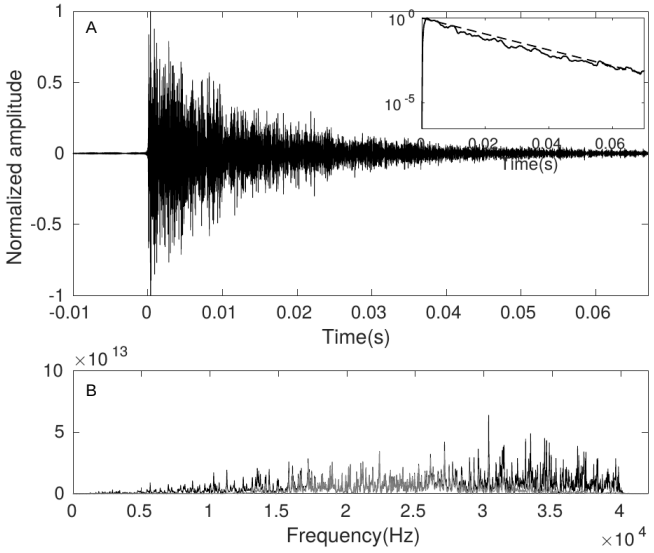

Figure 2.6: (A) Example of the Lamb waves recorded by a transducer after pulse compression of the emitted chirp signal. The source-receiver distance is about 21 cm. The inset illustrates the envelope of the intensity of the signal (solid line) and the exponential fit according to $\exp(-t/\tau_a)$ (dashed line), as a semilog scale. The attenuation time (τ_a) is 9 ms. Data at negative time gives a sense of the noise level. (B) Power spectrum of the raw signal (black) and bandpass filtered one (gray). The data is filtered between 15 kHz and 30 kHz using a Butterworth filter of 4th order.

we take the average of all these cross-correlations and normalize it by the maximum energy according to

$$l_{12}(t) = \frac{C_{12}(t)}{\sqrt{C_{11}(0)C_{22}(0)}} \tag{2.29}$$

where $C_{12}(t)$ is the cross-correlation of the signals between receivers 1 and 2 and C_{11} and C_{22} denote the auto-correlation signals [44]. The normalized average cross-correlation is shown in Fig. 2.7 bottom panel. We infer from both panels that the resulting cross-correlations are remarkably symmetric with respect to time $t = 0$, including several reverberated arrivals after the direct wave. The arrival time of vertical stripes appearing in the shot gather coincide with the arrivals in the averaged signals. This averaged signal is representative of the Green's function between the two transducers.

As transducers are reciprocal devices, they can also be efficiently used as emitters. What we measure is the convolution of the electro-elastic response of the transducer that acts as the source, the Green's function, the electro-elastic response of the

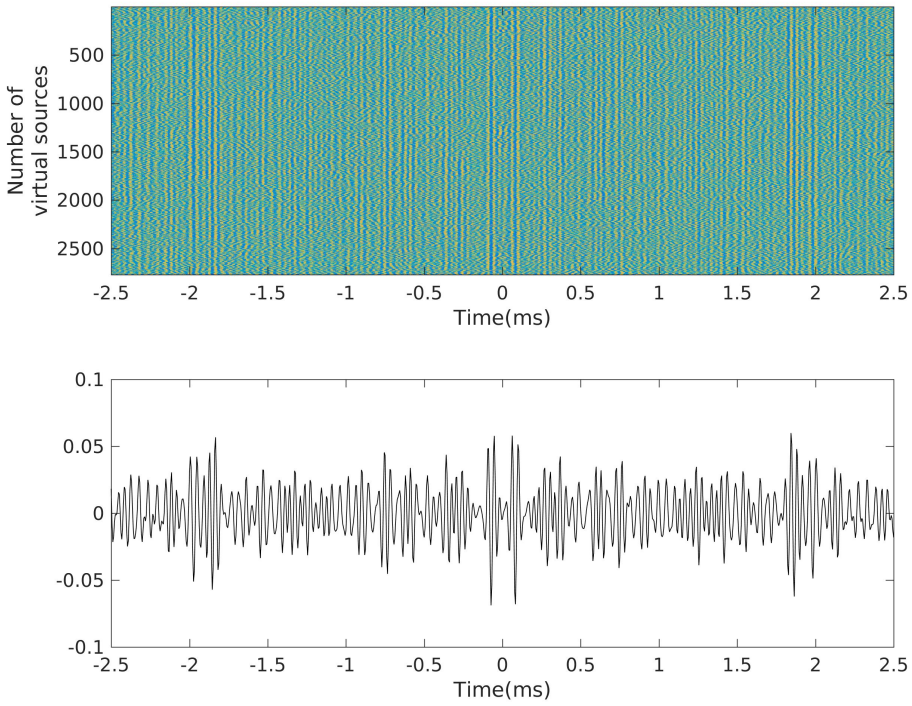

Figure 2.7: Top: Cross-correlation gather for all of the available virtual point sources (2,773 points) distributed uniformly on the plate. Bottom: Normalized cross-correlation averaged over all of the source positions. All of the cross-correlations in this plot are bandpass filtered by a Butterworth filter of 4th order between 15 kHz and 30 kHz, and normalization is performed with respect to the maximum energy of the correlated signals.

transducer that acts as the receiver, and the emitted signal. Note that this $G(t)$ is the vertical-vertical component of the Green's function. We assume that within the frequency band of interest, the frequency responses of the transducers are flat, and hence the impulse response is obtained by applying pulse compression of the emitted signals on the recordings. Hence, the impulse response can be measured directly between the pair of transducers. The time-integration result of this directly measured response after pulse compression ($G(t)$) of the emitted signal is compared with the cross-correlation, to validate the theoretical result (Eq. 2.27), as discussed in section 2.3. There is excellent agreement between the two, even for multiply reflected contributions, as shown in Fig. 2.8 (similar to the results of [45]). This impulse response corresponds to the vertical component of the Green's function.

We conclude here that the cross-correlation of full-time recorded signals in case

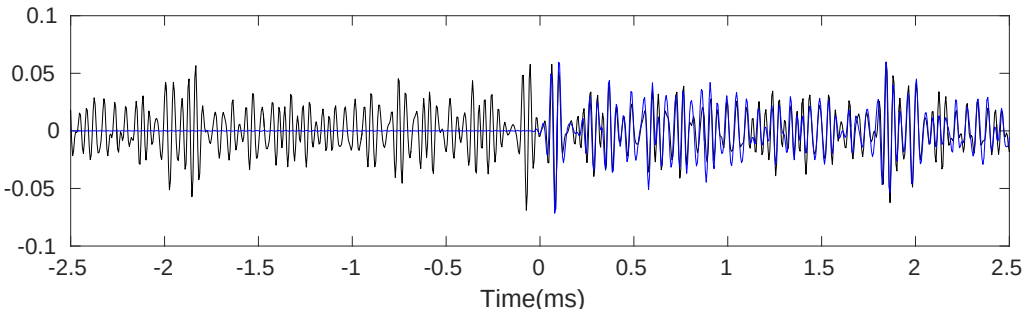

Figure 2.8: Comparison of the normalized cross-correlation averaged over all of the source positions when the sources are distributed uniformly all over the plate (black), and direct measurement of the source-to-receiver 'time-integrated' impulse response (blue) in the frequency band of 15 kHz to 30 kHz.

of a uniform source distribution converges to the Green's function of the medium.

2.5.2 Circular Source Distribution

To study the cross-correlation results for a circular source distribution, we scan the field according to Fig. 2.5b. The scan is performed on a circle of radius of 12 cm and the points are separated by 2.27 degrees. The recordings at a given pair of transducers are then cross-correlated and the shot gather for the 158 points and the averaged cross-correlation over all possible virtual source positions are shown in Fig. 2.9. The averaged cross-correlation is normalized by the maximum energy of individual signals. The results are for the frequency band of 15 to 30 kHz.

The number of point sources here are much smaller compared to the uniform case and this is why in Fig. 2.9 top, looks less clear than Fig. 2.7 top.

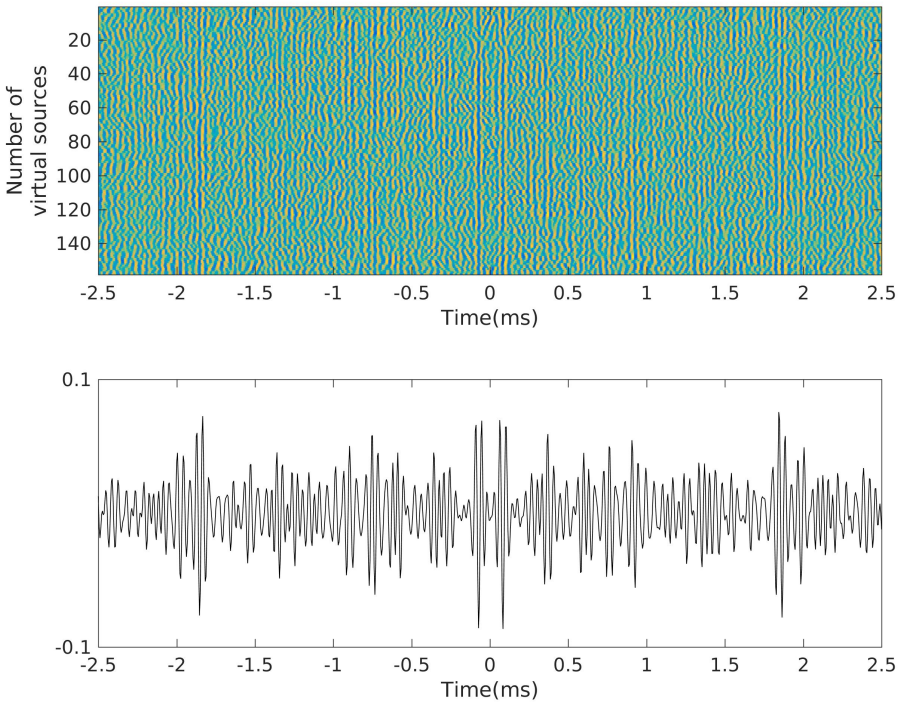

Figure 2.9: Top: Cross-correlation gather for all of the available virtual point sources (158 points) distributed in a circular form on the plate. Bottom: Normalized cross-correlation averaged over all of the source positions. All of the cross-correlations in this plot are bandpass filtered by a Butterworth filter of 4th order between 15 kHz and 30 kHz, and normalization is performed with respect to the maximum energy of the correlated signals.

Similar to the previous case, we compare the averaged cross-correlation with the time-integration of what we measure directly by using one transducer as a source and the other one as a receiver. The result is plotted in Fig. 2.10. We observe that the match between the two is quite close although the number of sources is smaller compared to the uniform case. This close match between the time-integration of directly measured Green's function and the cross-correlation for both uniform and circular source distributions highlights the importance of reverberation. We conclude here that in a reverberating medium, cross-correlation of recordings from sources that are distributed uniformly or on a circle, converges very well towards the Green's function.

Furthermore, with the data that we obtain in the case of circular source distribution, we can reconstruct the stationary phase regions. For a given pair of transducers,

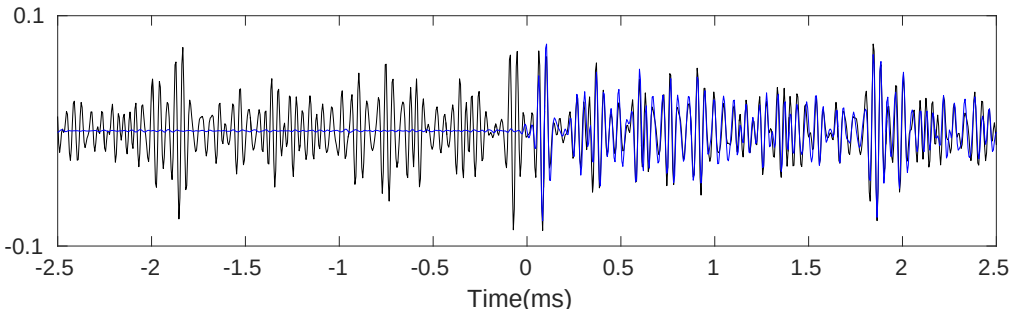

Figure 2.10: Comparison of the normalized cross-correlation averaged over all of the source positions when the sources are distributed on a circle (black), and direct measurement of the source-to-receiver 'time-integrated' impulse response (blue) in the frequency band of 15 kHz to 30 kHz.

we cross-correlate only the part of the recordings that correspond to direct arrivals. We plot each cross-correlation in time and for each angle (Fig. 2.11). We observe the emergence of the S-shaped shot gather (similar to Fig. 2.3d). Bottom panel in Fig. 2.11 is the average of all the cross-correlations plotted in the top panel. We see that retrieval of direct part of the Green's function is achieved and these arrivals are mostly constructed by the cross-correlation of the signals that are coming from the sources located at angles of $\pi/2$ and $3\pi/2$. These angles correspond to points that are approximately aligned with the line that connects the two transducers. On the other hand, arrivals coming from sources located at π and 2π radians do not contribute to the retrieval of the Green's function. This experimental observation is well in consistence with the theoretical demonstration explained in section 2.2.2.

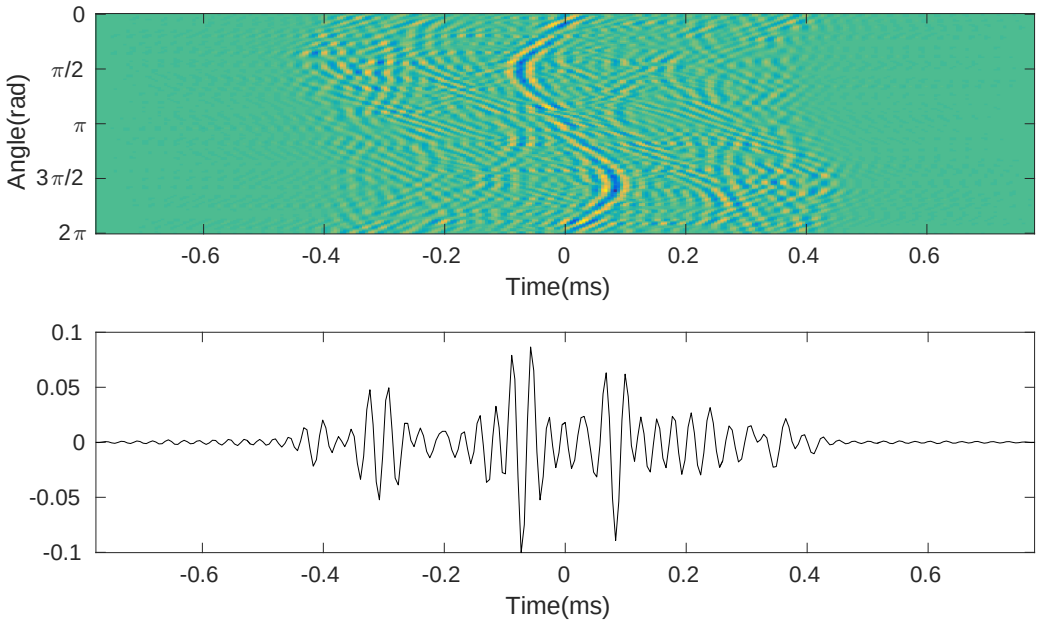

Figure 2.11: Stationary phase regions retrieval by experimental data. Top: Gather of cross-correlation of the direct arrivals for circular distribution of sources. Bottom: average of the cross-correlations shown in top panel.

2.6 Symmetry of the Cross-correlation of the Observed Data

Symmetry of the averaged cross-correlation in time is often used as a signature of its convergence toward the Green's function (e.g., [24]). Symmetric behavior of the resulting cross-correlation is observed in Fig. 2.7 bottom panel. Fig. 2.12 demonstrates the anticausal part of this averaged cross-correlation that is flipped in time and superimposed on the causal part. We infer that to a good approximation, the cross-correlation is symmetric with respect to time when averaged over all of the available sources in the two-dimensional plate.

In this section, we quantitatively study the dependence of the time symmetry of the cross-correlation on the number of sources. As for the experimental data, we work with the data that we obtained in the case of uniform source distribution.

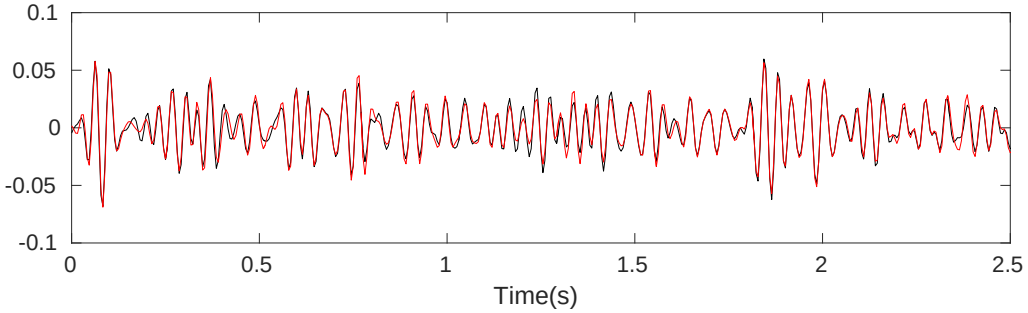

Figure 2.12: Causal (black) and anticausal (red) parts of the averaged cross-correlation over 2773 point sources when they are distributed uniformly. Note that the anticausal part is flipped in time.

To this end, $C_N(t)$ (i.e., the cross-correlation averaged over N sources) can be written as the sum of two terms:

$$C_N(t) = C_N^+(t) + C_N^-(t), \tag{2.30}$$

where

$$C_N^+(t) = \frac{C_N(t) + C_N(-t)}{2} \text{ and } C_N^-(t) = \frac{C_N(t) - C_N(-t)}{2}, \tag{2.31}$$

where for the sake of simplicity, $\mathbf{r}_l^R$ and $\mathbf{r}_{l'}^R$ have been dropped from the argument of C_N.

By definition, $C_N^+(t)$ (resp. $C_N^-(t)$) is symmetric (resp. antisymmetric) with respect to time.

We then compute the ratio of the integrated squared $C_N^+(t)$ and $C_N^-(t)$; i.e.,

$$r_N \triangleq \frac{\int_{-\infty}^{+\infty} C_N^+(t)^2 dt}{\int_{-\infty}^{+\infty} C_N^-(t)^2 dt}. \tag{2.32}$$

In Fig. 2.13, the experimental estimation of this symmetry ratio is plotted with respect to the number of sources used in the averaging process. This curve is determined by repeatedly implementing Eq. 2.32, based on a growing number of randomly

distributed sources, until all of the available sources are taken into account.

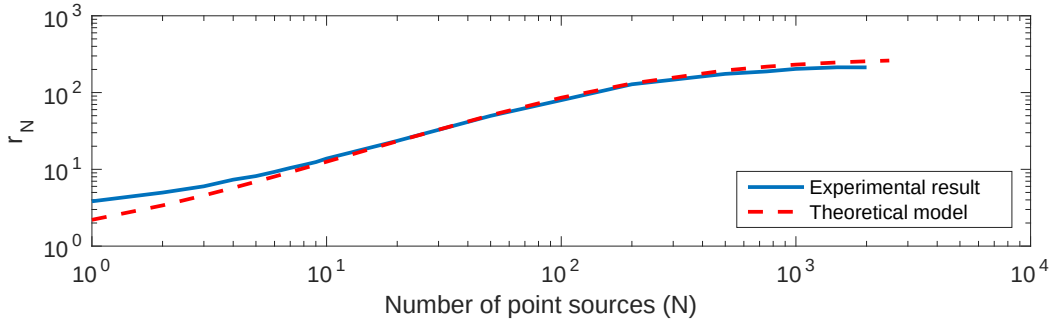

Figure 2.13: r_N as a function of the number of sources N picked randomly, derived from the experimental data (blue line) using Eq. (2.32), and modeled (dashed red line) based on the theory developed and summarized by Eq. (2.40). A 4th order Butterworth filter between 5000 Hz and 15000 Hz is applied to experimental data.

From Fig. 2.13, it appears that the cross-correlation is far from symmetric if only a limited number of sources are used in the averaging process. In this case, the assumptions that allowed the derivation of Eq. 2.27 do not hold. Nevertheless, as the number of sources grows, the averaged cross-correlation becomes more and more symmetric in time. This behavior is directly related to the convergence of the Green's function reconstruction. Let us first write the cross-correlation obtained for a subset N of all of the point sources as

$$C_N(t) = C_\infty(t) + \delta C_N(t), \tag{2.33}$$

where $C_\infty(t)$ is the cross-correlation obtained when all of the recordings from all of the available sources in this experimental set-up are taken into account.

While $C_\infty(t)$ is the best possible approximation of the Green's function, given the experimental set-up, there is no such thing as a perfectly uniform source distribution and infinite source density in practical applications. It follows that $C_\infty(t)$ does not exactly coincide with ImG (see Eq. 2.27), and should in principle be slightly asymmetric with respect to time. After defining the symmetric and antisymmetric components of $C_\infty(t)$, similar to Eq. 2.31, and substituting Eq. 2.33 into Eq. 2.31 and Eq. 2.32, we find that

$$r_N = \frac{4\int_{-\infty}^{+\infty} C_\infty^2(t)dt + 2\int_{-\infty}^{+\infty} \delta C_N^2(t)dt}{4\int_{-\infty}^{+\infty} (C_\infty^-(t))^2 dt + 2\int_{-\infty}^{+\infty} \delta C_N^2(t)dt}, \tag{2.34}$$

where $C_\infty^-(t)$ is the antisymmetric component of $C_\infty(t)$. Eq. 2.34 is directly related to the ratio of the noise level (L), which is a measure of the quality of the reconstructed Green's function from a finite number N of sources compared to the one obtained over an infinite number of sources introduced in [46]. This can be expressed in terms of $C_\infty(t)$ and $\delta C_N(t)$

$$L = \frac{\int_{-\infty}^{+\infty} \delta C_N^2(t)dt}{\int_{-\infty}^{+\infty} C_\infty^2(t)dt}. \tag{2.35}$$

Thus, Eq. 2.34 can now be rewritten as

$$r_N = \frac{2+L}{2\zeta+L} \tag{2.36}$$

where $\zeta = \int (C_\infty^-(t))^2 dt / \int C_\infty^2(t)dt$ is the relative degree of asymmetry of the cross-correlation function when $N \to \infty$. For a rectangular plate, L is given by ([47], pages 35-39)

$$L \approx \frac{\pi n_0}{N\tau_a}, \tag{2.37}$$

where τ_a is the attenuation time and n_0 is the plate modal density (modes per unit of frequency ω), which in turn depends on the area of the plate surface A, the surface density ρ_s, and the bending stiffness D, through the relationship [43]

$$n_0 = \frac{A}{4\pi}\sqrt{\frac{\rho_s}{D}}. \tag{2.38}$$

Then, defining k as the ratio of the attenuation time to the modal density,

$$k = \frac{\tau_a}{n_0}, \tag{2.39}$$

Eq. 2.36 finally becomes

$$r_N = \frac{1+2Nk/\pi}{1+2\zeta Nk/\pi}. \tag{2.40}$$

By finding adequate values of k and ζ, the best-fit is obtained at 1.9 and 0.0035, respectively, which results in the dashed red curve in Fig. 2.13. On the other hand, the experimental values for τ_a and n_0 are 0.009 s and 0.005 s/rad, respectively, which leads to $k = 1.8$, according to Eq. 2.39. This experimental value for k and that obtained from the fitting are consistent. The relative degree of asymmetry ζ can be

explained as a consequence of the fact that the laser vibrometer is only sensitive to vertical displacement (mainly A_0 mode). However, to some extent, the transducer also excites in-plane components (mainly S_0 and SH mode). As a result, the in-plane components modes do not contribute to the reconstruction of the Green's function.

2.7 Similarity between Impulse Response and Cross-correlation

The Pearson similarity coefficient between the two signals $G(t)$ and $C_N(t)$ is defined as (e.g., [48]),

$$S(G, C_N) = \frac{\left\langle \left| \int_{\Delta\theta} G(t) C_N(t) dt \right| \right\rangle}{\sqrt{\left\langle \int_{\Delta\theta} G(t)^2 dt \right\rangle \left\langle \int_{\Delta\theta} C_N(t)^2 dt \right\rangle}}, \tag{2.41}$$

where $\Delta\theta$ is the time-integration window to compute the similarity coefficient, and $\langle \ldots \rangle$ is the averaging over the different sets of point sources that are picked randomly. The latter is required for $S(G, C_N)$ to be independent of the measurement positions. While the word 'similarity' is preferred here for clarity, S is more often referred to in the literature as the 'correlation' coefficient [48]. Fig. 2.14 shows $S(G, C_N)$; i.e., the similarity coefficient between the time-integrated impulse response and the cross-correlation of signals recorded at transducers #3 and #4 for increasing number of sources (The coordinates of the transducers on the plate are given in the Supplemental Material part IV). The similarity coefficient $S(G, C_N)$ is computed over a time window with a length ($\Delta\theta$) equal to the decay time τ_a (see Fig. 2.14).

To discriminate the contribution of the direct arrival, we have also plotted $S(G, C_N)$ where only direct arrivals are cross-correlated to get C_N. We clearly observe a lower similarity unless there exists a very large number of sources. However, this contribution is negligible because when we cross-correlate the coda i.e., all the reverberated signal without direct arrival, the same value of the similarity coefficient is obtained as when all the signal is cross-correlated.

First, for a large number of sources ($N > 100$), $S(G, C_N)$ reaches a plateau ($S \approx 0.82$) that is less than 1.0. From the analysis of the symmetry of the correlation,

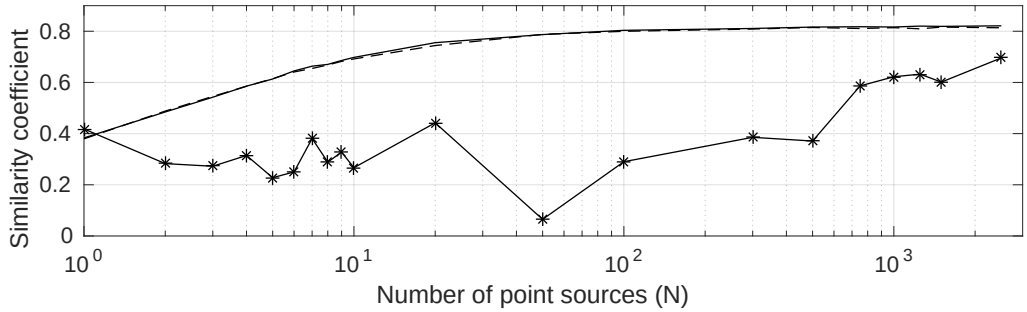

Figure 2.14: Similarity coefficient $S(G, C_N)$ between the $C_N(t)$ and $G(t)$ versus the number of point sources (picked randomly) when the whole time signal is cross-correlated (solid line), and when only a part of the coda signal ($dT = 0.2$ s; see Eq. 2.42) is cross-correlated (dashed line). A 4th order Butterworth filter between 15 kHz and 30 kHz is applied on $C_N(t)$ and $G(t)$. $\Delta\theta$ is equal to the attenuation time. Curve with the star symbols is $S(G, C_N)$ where $C_N(t)$ is the result of the averaged cross-correlation of only direct-arrival window. In this case, $\Delta\theta$ is 0.7 ms.

we measured that the latter is asymmetric with $\zeta = 0.0035$. Assuming that the deviation to the perfectly reconstructed Green's function is as much symmetric as anti-symmetric, the total deviation reaches 0.0070. Consequently, the difference with the 18% mismatch observed in Fig. 2.14 cannot be explained by the missing of in-plane components to the reconstructed Green's functions. We interpret this increase of discrepancy by the fact that when considering the directly-measured Green's function, the effect of the transducer response appears as the convolution of the two transducer responses, while when the recordings are cross-correlated, we deal with the cross-correlation of the transducer responses. A probably weaker effect comes from the absorption by the transducers that induces a deviation from the Green's function estimation as shown in [49].

Second, somewhat surprisingly, even with only one or very few sources the cross-correlation matches the time-integrated Green's function relatively well ($S \approx 0.4$), even when only a part of the coda is correlated.

In the next two sections, we propose models to explain these behaviors. This begins with a study of the impact of the number of noise sources and the length of the correlated coda on the emergence of the Green's function. Then, the effects of

uncorrelated noise are taken into account.

2.8 Correlation of Windowed Coda

We next study the contribution of different parts of the coda signal to the reconstruction of the Green's function. In practice, rather than cross-correlating the entire signal, as above, the cross-correlation is now limited to a time interval of variable length, where the variable start-point and end-point are denoted as T_0 and $T_0 + dT$, respectively. This is expressed by

$$C_N^{dT}(\mathbf{r}_l^R, \mathbf{r}_{l'}^R, t) = \sum_{k=1}^{N} \int_{T_0}^{T_0+dT} G(\mathbf{r}_l^R, \mathbf{r}_k^S, \tau) G(\mathbf{r}_{l'}^R, \mathbf{r}_k^S, \tau - t) d\tau. \tag{2.42}$$

Note that there is a distinction between the two time windows dT and $\Delta\theta$ defined in Eq. 2.41; the former is the cross-correlation window, while the latter is the time window over which the similarity coefficient is computed. In Fig. 2.15, cross-correlations are compared when the time window includes: only the ballistic wavefront, only the multi-reverberated waves, and the whole wave-field.

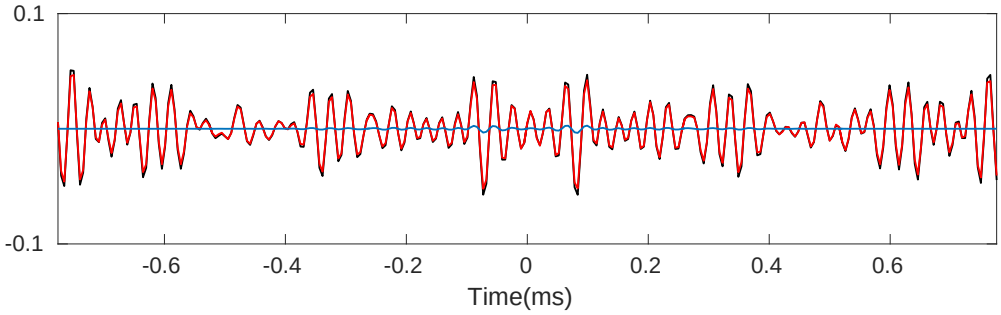

Figure 2.15: Comparison of the cross-correlation results for three different time windows when the sources are distributed over all of the plate, considering the whole length of the signal (black line), only the ballistic part of the signal [$dT = 0.7$ ms] (blue line), and only a part of the coda arrivals [$T_0 = 0.4$ ms, $dT = 0.02$ s] (red line). All the cross-correlations are bandpass filtered between 15 kHz and 30 kHz by a 4th order Butterworth filter.

We observe that cross-correlation of only the ballistic part of the signals builds only the ballistic part of the Green's function, while cross-correlation of the coda part

reconstructs both the ballistic and coda parts of the Green's function. Moreover, the contribution due to the ballistic path is negligible, and the recovery of the Green's function is dominated by the coda part.

To study the convergence process, the similarity coefficient is computed between a reference cross-correlation $C_{ref}(\mathbf{r}_l^R, \mathbf{r}_{l'}^R, t)$ and the cross-correlation function obtained for different time windows, averaged over randomly-picked sources $C_N^{dT}(\mathbf{r}_l^R, \mathbf{r}_{l'}^R, t)$. We recall that $C_{ref}(\mathbf{r}_l^R, \mathbf{r}_{l'}^R, t)$ is obtained when all of the sources are emitting and all of the signals are cross-correlated (in the case of uniform source distribution). In this section and the next one, the reference to obtain the similarity coefficient is not the empirical Green's function ($G(t)$), but $C_{ref}(\mathbf{r}_l^R, \mathbf{r}_{l'}^R, t)$. The reason for this is that according to Fig. 2.14, $G(t)$ never perfectly converges to $C_{ref}(\mathbf{r}_l^R, \mathbf{r}_{l'}^R, t)$, and they are not perfectly similar, which avoids reaching 1.0 for the similarity coefficient even when all of the sources are considered and the cross-correlation is over the whole signal. Also, as explained before, this new choice for reference circumvents any influence on the results by the difference in the frequency response of the transducers and the vibrometer.

The similarity coefficient $S(C_{ref}, C_N^{dT})$ is computed in a window that contains the direct arrivals and that lasts as long as the attenuation time, following Eq. 2.41. Fig. 2.16 shows the values of $S(C_{ref}, C_N^{dT})$ versus the number of point sources (N) for the three different correlation window lengths (dT). It can be seen that all of the curves have a similar trend. The values of the similarity coefficient ($S(C_{ref}, C_N^{dT})$) increase with the number of sources (N), and the resulting cross-correlation converges toward the reference one after a certain number of sources, which indicates that the cross-correlation of a short time window (compared to the decay time $\tau_a = 9$ ms) leads to a reasonable impulse response.

See Supplemental Material (part I) for our proposed model based on the modal decomposition of the plate Green's function solution of Eq. 2.25 to derive $S(C_{ref}, C_N^{dT})$. Note that in the theoretical approach, we refer to the reference cross-correlation or the 'perfect' cross-correlation by C_∞. This difference in the notation between the theoretical (C_∞) and experimental (C_{ref}) approach is a reminder for the fact that in the experimental case we cannot have an infinite number of sources and hence a

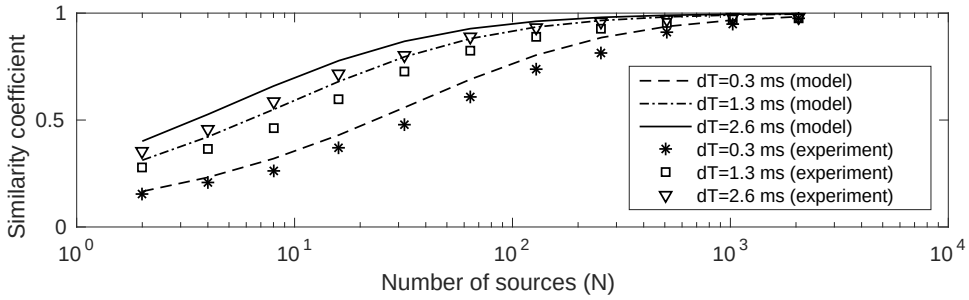

Figure 2.16: Similarity coefficient $S(C_\infty, C_N^{dT})$ between C_∞ and C_N^{dT} (cross-correlation obtained by windowing one signal before the cross-correlation, and then averaged over a subset of available sources picked at random). Symbols and lines show the experimental results and theoretical model, respectively, for the various window lengths (dT). The starting time (T_0) in all three cases is 2.3 ms, i.e., no ballistic signal is cross-correlated.

perfect cross-correlation. $S(C_\infty, C_N^{dT})$ is finally given by

$$S(C_\infty, C_N^{dT}) = \left[1 + \frac{2}{N}(1+Z)\right]^{-0.5}, \tag{2.43}$$

with

$$Z = \frac{\int \kappa(\delta\omega, \omega)\left|\widetilde{M}(\delta\omega)\right|^2 d\delta\omega}{\left|\widetilde{M}(0)\right|^2 (1 + F(\delta r))}, \tag{2.44}$$

where $F(\delta r)$ accounts for the spatial correlation of the squared eigen-modes, N is the number of point sources, $\kappa(\delta\omega, \omega)$ is the two-level correlation and $\tilde{M}$ is the Fourier transform of the time windowed (the window duration being dT) squared mean intensity (see Supplemental Material for more details).

The two-level correlation function, that has been formally introduced in quantum chaos theory, is defined in terms of the modal density ($n_0(\omega)$) as

$$\kappa(\delta\omega, \omega) = \frac{\langle n_0(\omega) n_0(\omega + \delta\omega)\rangle}{\langle n_0(\omega)\rangle}. \tag{2.45}$$

Lyon [50] also introduced it when analyzing the statistical properties of sound power in structures.

In a chaotic-shaped plate, due to repulsion between the modes, κ is null when $\delta\omega = 0$ and is close to n_0 when $\delta\omega$ is larger than the modal density. The expression of κ can be found in [51, 52]. But here, as the plate geometry is regular, the eigenfrequency statistics follow a Poisson's distribution [50, 53]. As a consequence, there are no correlations between the eigenfrequencies, $\kappa(\delta\omega, \omega)$ is equal to the modal density and Z can be simplified into

$$Z = \frac{\pi n_0}{\tau_a \left(1 + F(\delta r)\right)} \coth\left(\frac{dT}{\tau_a}\right). \tag{2.46}$$

The coefficient Z can be interpreted as the average number of overlapping modes of the plate within the windowed cross-correlation at angular frequency ω.

See Supplemental Material (part III) on derivation of the expressions for the spatial correlation of the squared eigenmodes and F for chaotic and rectangular cavities. In the case of a chaotic cavity, based on the Berry conjecture [54], $F(\delta r)$ is given by $2J_0(k\delta r)^2$, where J_0 is the zero-th order Bessel function of the first kind. In the case of a rectangular cavity, using the same methodology as the one that led to the spatial correlation of the eigenmodes in a rectangular plate [55], we find

$$F(\delta r) = \frac{J_0(2k\,|\delta x|) + J_0(2k\,|\delta y|)}{2} + \frac{J_0(2k\delta r)}{4}. \tag{2.47}$$

Note that now the correlation of squared eigenmodes is anisotropic because it not only depends on modulus of $\delta\mathbf{r}$, but also on the projection dx (respect. dy) of $\delta\mathbf{r}$ along the x-axis (respect. y-axis).

The continuous curves in Fig. 2.16 result from the model described by Eq. 2.43, where $F(\delta r) \sim 1/2$ for $\delta r \gg \lambda$ and $1 + F(\delta r)$ is set to 1.5. We believe that this long-range correlation is due to strong periodic orbits that are not taken into account by our correlation models.

The convergence toward the Green's function is driven by three characteristic times: the modal density (n_0), the attenuation time of the plate (τ_a); and the time window selected for the cross-correlation (dT). Schematically, three asymptotic cases can be identified:

1. When $\tau_a \gg n_0$ and $dT \gg n_0$, the modes of the plate are resolved because

the attenuation is low (see Fig. 2.17a). Moreover, the integration time dT is sufficiently large to include a sufficient amount of coda to not induce modal overlapping by a windowing effect. In such a case, the similarity coefficient $S(C_\infty, C_N^{dT})$ is high, and therefore the 'best' correlation is obtained. In the case of a single source $S(C_\infty, C_N^{dT})$ is $1/\sqrt{3}$.

2. When $\tau_a \lesssim n_0$ and $dT \gg \tau_a$, $Z \approx \pi n_0/\tau_a$, the overlapping due to the attenuation is not negligible anymore (see Fig. 2.17b). The convergence of the cross-correlation toward the Green's function is slower. Hence, at least Z sources are required to obtain a good estimation of the Green's function from the cross-correlation.

3. Finally when, $dT \ll \tau_a$ and $dT \lesssim n_0$, the mode overlapping is dominated by the effects of the coda truncation, and is given by $Z \approx \pi n_0/dT$ (see Fig. 2.17c). Again, to get a good estimation of the Green's function, at least Z sources have to be used.

Hence, when N is large compared to $1 + Z$, $S(C_\infty, C_N^{dT})$ converges toward 1.0, independent of the window length dT. In other words, even with a very short integration time in Eq. 2.42, the Green's function can be completely recovered.

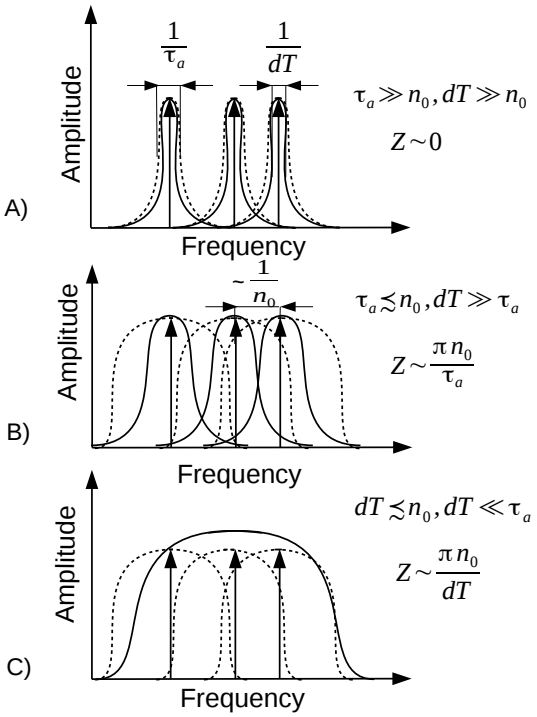

Figure 2.17: Three schematic representations of a small part of the Fourier transform of the window cross-correlations for different values of the characteristic times of the system, namely as: modal density (n_0), attenuation time (τ_a), and selected time window for cross-correlation (dT). The vertical arrows mark the eigen-modes that are separated on average by $\frac{1}{n_0}$. The dashed curves represent Lorentzian spectra of the width $1/\tau_a$, which is the inverse Fourier transform of the exponential attenuation. Finally, the solid continuous curves show the sinc functions of the width 1/dT, which is the Fourier transform of the window. The regimes and the corresponding approximate values of Z are denoted at the top right-hand corner of each plot.

Fig. 2.16 shows that the experimental results approximately confirm this model; the similarity coefficient $S(C_\infty, C_N^{dT})$ does not converge to 1.0 exactly, which we ascribe to the presence of a small amount of random noise in the measurements.

2.9 Effects of Random Noise

A comparison between the model and the experimental results (Fig. 2.16) suggests that uncorrelated noise (e.g., electronic noise) degrades the Green's function. We next analyze this effect by performing the cross-correlation over time windows that start between $T_0 = 0$ and $T_0 = 57$ ms after the beginning of the transient response, and end at time $T_0 + dT = 250$ ms (see inset in Fig. 2.18). Time $T_0 + dT$ is chosen to be a lot larger than τ_a, to increase the relative contribution of noise in the correlation process. The similarity coefficient $S(C_{ref}, C_{ref}^{dT})$ is then retrieved according to Eq. 2.41 and from the direct path and primary coda signal ($\Delta\theta = 2$ ms). As for the previous section, the reference of the similarity coefficient is the one obtained when the number of sources is large and the effects of noise are negligible. Note that, in this case, all of the sources N are considered in the computation of $S(C_{ref}, C_{ref}^{dT})$, and the similarity coefficient is plotted in Fig. 2.18 as a function of T_0.

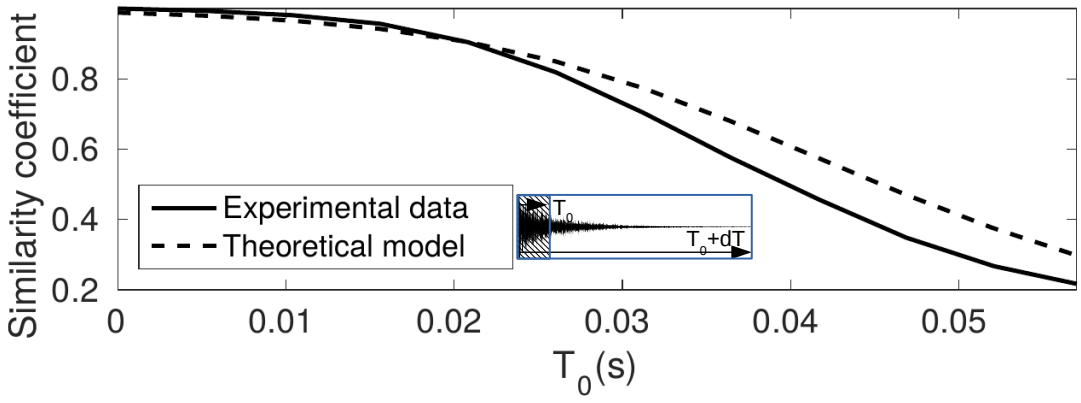

Figure 2.18: $S(C_\infty, C_\infty^{dT})$ between $C_\infty(\mathbf{r}_l^R, \mathbf{r}_{l'}^R, t)$ and $C_\infty^{dT}(\mathbf{r}_l^R, \mathbf{r}_{l'}^R, t)$. The end of the time windows ($T_0 + dT$) is fixed at 250 ms. $S(C_\infty, C_\infty^{dT})$ is then evaluated in a window that includes direct path and primary coda ($\Delta\theta = 2$ ms).

We observe that the effects of noise becomes significant only when T_0 is >15 ms. The decay of the $S(C_{ref}, C_{ref}^{dT})$ can be explained by assuming that the field measurement is perturbed by a constant amount of uncorrelated noise at each transducer, according to Eq. 2.48. See Supplemental Material (part II) for the complete derivation of $S(C_\infty, C_\infty^{dT})$. Similar to the previous section, we discriminate the experimental case from the theoretical one by changing C_{ref} to C_∞. After some algebra, we

find

$$S(C_\infty, C_\infty^{dT}) \approx \left(1 + \frac{\beta B(dT)}{N[e^{-T_0/\tau_a}(1 - e^{-dT/\tau_a})]}\right)^{-0.5}, \tag{2.48}$$

where B is the bandwidth of the system, and the dimensionless value β is an indication of the noise-to-signal ratio.

The experimental data were fitted to Eq. 2.48. We observe that the model explains the decay in $S(C_{ref}, C_{ref}^{dT})$ and as we go further in time, it is the noise content that dominates, which consequently causes degradation of the reconstructed Green's function. Note that unlike the experimental curve, the theoretical one does not start from the value of 1.0. This is due to a different reference in the similarity coefficient in these two cases. On the one hand, for $T_0 = 0$, the correlation and the reference correlation are identical because we chose the best correlation possible for the reference cross-correlation (i.e., at $T_0 = 0$). Consequently, $S(C_{ref}, C_{ref}^{dT})$ is exactly 1.0. On the other hand, from a theoretical point of view $S(C_\infty, C_\infty^{dT})$ is smaller than 1.0 because the reference correlation is the ideal one, i.e., the difference between the advanced and delayed Green's function, while the noise slightly contaminates the cross-correlation.

2.10 Discussion

As explained by [56], the process of reconstructing a Green's function by diffuse-field cross-correlation is closely related to that of acoustic time reversal [57]. Accordingly, this study has some implications in the context of time reversal. To illustrate this point, let us assume that a pulse is sent at position $\mathbf{r}_A$ and the N transient responses are recorded by N receivers at positions $\mathbf{r}_i$. Each response is then flipped in time and sent back into the medium by the N emitters located at the same positions as the N receivers. In a reciprocal medium, it can be formally shown that the time-dependent amplitude of the time-reversed field at position $\mathbf{r}_B$ is proportional to the correlation $C_N(t)$ between positions $\mathbf{r}_A$ and $\mathbf{r}_B$. When only a part of the transient responses between times T_0 and $T_0 + dT$ are flipped and sent back, the time-reversed field is then given by $C_N^{dT}(t)$. This formal equivalence between the cross-correlation and

the time reversal provides new insights [57]. First, when there is only one source, the cross-correlation behaves approximately as the one-channel time-reversal signal of flexural waves obtained by Draeger and Fink [58]. In particular, it has been shown that in a lossless cavity, the time reversed field at position $\mathbf{r}_1$ is equal to $G(\mathbf{r}_1, \mathbf{r}_1, t) \otimes G(\mathbf{r}_A, \mathbf{r}_B, -t)$ [59]. For this set-up, we infer from Eqs. 2.43 and 2.46 that when $dT \gg \tau_a \gg n_0$, the similarity coefficient $S(C_\infty, C_1^{dT})$ for one single source is equal to $1/\sqrt{3}$. Hence, the mismatch is due to $G(\mathbf{r}_1, \mathbf{r}_1, t)$, i.e., fluctuations induced by alternation of nodes and antinodes at $\mathbf{r}_1$. Secondly, the case where the sources are uniformly distributed over the surface corresponds to the instantaneous time reversal [60], which is also called the Loschmidt echo [61]. In this case, a field can be perfectly time reversed at time t_0 by imposing the initial condition $\psi(\mathbf{r}, t_0)$ and its negative time derivative $-\partial\psi(\mathbf{r}, t_0)/\partial t$. Consequently, by time reversing a very small window around time t_0 of the transient responses by many sources over all of the surface, the time-reversed field is perfectly recovered for $t < t_0$. This result is in agreement with our finding that $S(C_\infty, C_{N>>1}^{dT})$ converges to 1.0 as N grows.

A popular technique used in order to improve the estimation of the Green's function consists of correcting the exponential attenuation decay to artificially increase the attenuation time. In such a case, because τ_a is larger (see Eq. 2.40), the symmetry ratio r_N increases faster with the number of sources. The similarity coefficient is also improved because τ_a can be larger than the modal density (also called Heisenberg time and explained in details in Chapter one, section 1.4.1) and the system behaves as if the plate modes are resolved (see Eq. 2.43). However, this correction also increases exponentially noise-to-signal (β) and therefore limits the efficiency of the method (see Eq. 2.48).

In the case of continuous incoherent noise sources, the cross-correlation converges toward the windowed cross-correlation, but with a window that includes all of the transient signal. The present study provides new insights into the understanding of the relative contributions of the different parts of the transient response (e.g., ballistic and early coda, late coda) for building the cross-correlation. Considering the transient recorded signals that consist of direct and later arrivals, and cross-correlating these parts of the signals separately, we show that exclusion of the direct arrivals and cross-correlation of only the coda arrivals is very close to the case where

we cross-correlate the full-time signals.

2.11 Conclusion

Given any receiver pair, the signal that would be obtained at either one from a source at the other can be reconstructed experimentally by cross-correlation of the recordings provided that the field is diffuse. The field can be diffuse as a result of a dense, homogeneous source distribution throughout the medium, and/or of scattering or reverberation: this study was aimed at the disentangling of these two effects. We conducted experiments with a thin plate where the surface was densely scanned by a laser vibrometer, and where an array of transducers was deployed. This set-up provides almost perfect control of the spatial distribution of the transient sources. We first validated the theory through comparison of the averaged cross-correlations and the directly observed Green's function for two different distribution of sources. We also experimentally studied the symmetry (with respect to time) of the cross-correlations, as well as their similarity to the Green's function, as a function of the number of uniformly distributed point sources. To explain these observations quantitatively, an analytical model was developed that predicts the observed asymmetry of the averaged cross-correlation. We next studied the convergence of the averaged cross-correlation for time windows of variable lengths, which might be very short, and taken at different points in the coda of the recordings. Here, a relatively dense/ uniform source distribution can result in good estimation of the Green's function. We demonstrated that this time window does not have to include the direct-arrival part of the signals for the estimated Green's function to be a good approximation of the exact one. Through statistical modal analysis, the respective contributions of attenuation time, modal density, and number of sources to the convergence of the cross-correlation toward the Green's function were identified. Finally, we demonstrated both theoretically and experimentally that this convergence strongly depends on the position of the correlation time window only when additive random noise is taken into account. The relative effects of the noise are stronger when the late coda is cross-correlated.

Chapter 3

Retrieving the Scattering Cross-Section using Noise Correlation in a Reverberant Medium: A Theoretical and Experimental Approach

3.1 Introduction

The phenomenon of scattering is defined as redirection of the incident wave due to a local inhomogeneity in the medium. In complex media, waves are scattered or reflected many times before their extinction, producing random-like and time-dispersed wave-fields. However, the late parts of the echo arrivals remain strongly imprinted upon by the propagation medium. Long/infinite-range correlations [62] and back-scattering enhancement are several of the expressions of this property. With a complex medium that changes with time, the dynamics of the fluctuation of the scattered field is directly related to the medium dynamics. For instance, coda wave interferometry (CWI) [63] focuses on the coda evolution when a global modification of a complex medium occurs, such as changes in velocity associated with changes in temperature. The coda is the part of the transient response (i.e., Green's function) that results from multiple scattering interferences. Temporal variations in the elastic behavior of the Earth's crust are an indicator of the changes in the stress transfer with time. Changes in the stress, modify the elastic behavior of the Earth's crust. Therefore, by analysing the Earth's seismic response and its temporal evolution, these variations can be recovered. This is particularly true

when earthquake codas, microtremors or microseismic noise are considered, as these are very sensitive to the effects of the often small perturbations in the Earth's elastic properties as they sample it both randomly and repeatedly ([64]). For understanding the dynamic behavior of the crust, tectonically and volcanically active regions are of particular interest since in these regions stress changes are frequent and may precede earthquakes and volcanic eruptions. Deformations at the Earth's surface associated with plate movements, earthquakes and volcanoes can be observed with GPS and InSAR techniques. To measure the dynamic evolution inside the Earth and in time, we need to have repeated measurements in which we use the same seismic source and receiver position several times to have identical seismic ray path. Poupinet et al., [65] pointed out that a few number of similar earthquakes which are called 'microearthquake doublet' or 'multiplet' are a very convenient source for seismic velocity monitoring that allows very accurate timing measurements. Despite the numerous advantages of using multiplets instead of explosives as sources, this method still has the disadvantage of being dependent on earthquake occurrence. To find the temporal variations in the shear waves speed due to local variations in the Earth's crust, the decorrelation between the coda of these multiplets is measured. This decorrelation is highlighted as a time shift in the part corresponding to coda arrivals and from that, the relative velocity changes are found. In parallel to the application of CWI for real data, there have been some studies in the laboratory as well and the reliability of the method has been confirmed. One of the studies is the one of [66] where the thermally-induced velocity changes in a granite sample are measured. With this experimental data, we can clearly observe (as shown in Fig. 3.1) that the variations in the temperature appear as a time shift in the coda of the recordings at two different temperatures (bottom inset) while the direct arrivals stay unchanged (top inset).

To locate a weak and local modification in a multiple-scattering medium, the LOCADIFF algorithm was proposed by [67], which is based on diffusion theory [68]. LOCADIFF involves an inversion procedure that consists of the spatial sensitivity map of the wave-field with respect to local changes in the medium. Diffusive-wave spectroscopy [69] is another method based on analysis of light intensity fluctuations when all of the scatterers are moving randomly. This idea was originally developed

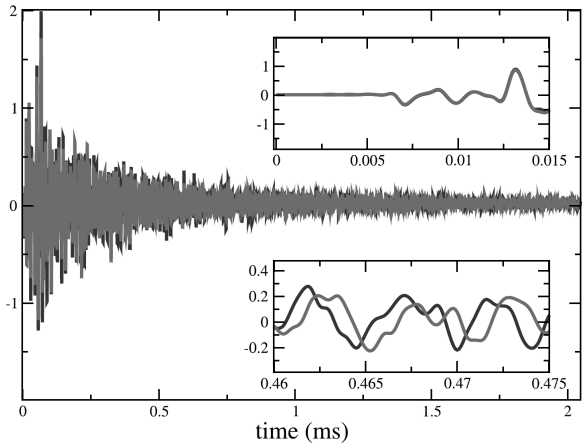

Figure 3.1: Recorded waveforms in a sample of granite for two different temperatures, 45°C (gray) and 50°C (black). The top inset shows the waveforms at these two temperatures around the direct arrivals and the bottom one shows the one for the part of coda arrivals (Figure from [66]).

in the context of optics, but has since been applied to acoustics [70], [71]. Contrary to diffusive-wave spectroscopy, which works in the frequency domain, diffusive acoustic-wave spectroscopy is based on temporal analysis of the late time fluctuations of the coda. More recently, the coda generated in a reverberant cavity when one or several scatterers are moving was analyzed [72], [73]. This method, known as diffuse reverberant acoustic-wave spectroscopy (DRAWS), has been shown to be promising for finding scattering cross-sections [72] and the displacement magnitudes [74] of a discrete set of moving scatterers. The scattering cross-section is a property of a scatterer that quantifies its strength averaged over all of the incident angles. All of these techniques, from coda wave interferometry to DRAWS, are based on the measurement of the two-point Green's functions between a set of sources and receivers, either in the frequency domain or in the time domain. However, when dealing with time-domain techniques, it might not be possible to have access to point-like and transient sources to directly measure the Green's function. Through the advent of noise interferometry, the Green's function between two points in a medium can be retrieved by cross-correlation of the noise recorded at these locations; i.e., without the need for an active source. The first, pioneering, validation of this theoretical result in the experimental domain was carried out by [20], who prop-

agated elastic waves through a block of aluminum, and explained their observations by the principle of equipartition of energy over different modes. Later, this method found applications in different domains, such as ocean acoustics (e.g., [75]), seismology (e.g., [76], [16]), and medical imaging (e.g., [77]). A number of studies have shown that this method can be used to estimate the coda in a multiple-scattering medium or in a reverberant cavity ([34], [78], [33]). Following these studies, passive coda wave interferometry was successfully applied in seismology, based on the analysis of coda estimated from noise correlations (e.g., [18], [79]). In reverberating media, several studies have shown that it is possible to passively localize a scatterer on a thin elastic plate from the analysis of the direct path recovered by noise correlation (e.g., [1]). However, the sensitivity of the method is poor, and does not yet provide the cross-section of the scatterer.

The present study is based on the DRAWS approach, and we show that the scattering cross-section can be estimated in reverberant media without controlled sources. This study demonstrates the reliability of DRAWS based on passive retrieval of the Green's function for monitoring of the variations in the medium, with possible applications to acoustic or seismic waves. We carry out experiments on a thin duralumin plate and recover the Green's function through cross-correlation. In the first test, we repeat our experiment with and without a single scatterer. In the second test, we repeat the experiment before and after changing the position of the scatterer. In both cases, the decorrelation in the coda of these passively recovered Green's functions is tracked by computing the similarity coefficient between the Green's functions. We next develop a formalism that is similar to that proposed by [73], and the scattering cross-section is estimated. The possibility to track the temporal fluctuations in a coda caused by the appearance of a scatterer, and not only by a change in its position, is an extension, first attempted here, of classical DRAWS. Moreover, DRAWS is applied to highly dispersive plate waves for the first time here.

The passive estimation of the scattering cross-section is also double checked: first by the use of active DRAWS, and then by classical estimation of the cross-section based on the measurement of the scattering phase function from direct plane-wave illumination. There is a close match between the passive measurements and the two

active measurements.

This chapter first introduces a numerical test for finding the scattering cross-section of a defect. In the second part, our theoretical model is elaborated. Next, the experimental set-up that used for the passive/ active scattering cross-section estimations is presented and then the experimental results are presented and discussed, before the final conclusion.

3.2 Evaluating the Scattering Cross-Section in the Far Field

3.2.1 General Overview

A scatterer in the medium is usually characterized by the local changes of elastic parameters. In other words, when the incident wave faces a region in the medium of propagation where the elastic parameters are different from the ones in the background medium, it becomes scattered and continues propagating in random directions. The elastic parameters can be the density, Young's modulus, poisson ratio, etc. One parameter to characterize the strength of the scatterer (defect) is the scattering cross-section. The scattering cross-section represents the capability of the scatterer to intercept the incident wave and scatter it. In 2D, it has the dimension of the length. A schematic demonstration of the history of a plane incident wave in the presence of a local heterogeneity is shown in Fig. 3.2.

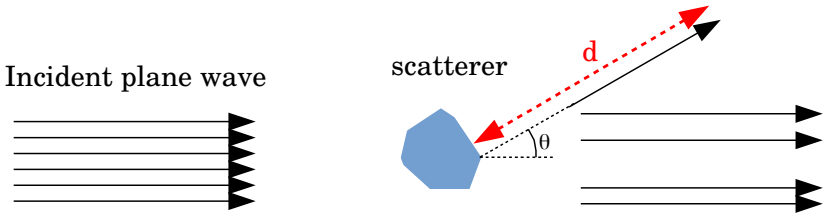

Figure 3.2: Scattering of a plane wavefront by a rigid heterogeneity.

To calculate the scattering cross-section we need a measure of the scattered wave-field. In the frequency domain, the scattered wave-field in 2D, in the far field, and for all the directions in space is given by

$$W_{diff}(\theta,\omega) = f(\theta,\omega)\frac{W_{inc}(\omega)e^{-jk(\omega)d}}{\sqrt{d}} \tag{3.1}$$

where k is the wavenumber, $W_{inc}(\omega)$ is the incident wavefront, d is the distance between the measurement point and the scatterer and ω is the angular frequency [68]. $f(\theta,\omega)$ is a measure of the scattered wave as a function of frequency and for different angles and is known as 'scattering phase function' or 'far-field radiation pattern'. In other words, f is a record of relative amplitude and phase of the scattered components along the direction of θ relative to the direction of the incident wave. The total scattering cross-section is then found through

$$\sigma(\omega) = \int_0^{2\pi} |f(\theta,\omega)|^2 d\theta. \tag{3.2}$$

In the following, we implement this formalism on a numerical experiment to find the scattering cross-section.

3.2.2 Special Case of a 2D Inclusion in the Plate: Analytical and Numerical Solution

We start this study by a numerical test. We are interested in finding the scattering cross-section of a rigid inclusion in a plate. To solve this problem numerically, we use a free software of finite element method called ELMER [1] and build a numerical set-up as close to the theoretical case as possible. As explained in the previous section, the scattering cross-section is calculated in the far field with a plane incident beam which requires an infinite background medium (in our case, plate). In order to approach these requirements, we run our numerical experiment on a large rectangular plate whose dimensions are 1 m by 1 m and the thickness is 3 mm. We place the receivers on a circle of radius of 5 cm whose center is the center of the plate. The emitted source signal is one period of a sine with the central frequency of 40 kHz. The displacement wave-field is measured on a circle of radius of 5 cm when there is no inhomogeneity on the plate and then a cylindrical inclusion is added right at the center of the circle and the displacement measurements are repeated. The inclusion is defined as the local variation in the elastic parameters of the plate. We keep the

[1] https://www.csc.fi/web/elmer

thickness unchanged and define the inclusion as a rigid one whose Young's modulus and poisson ratio are 10 times larger than the one of the surrounding aluminium plate and the diameter is 1 cm. The sampling frequency in both cases is 500 kHz with a temporal step of 2 μs. The numerical set-up in these two cases is shown in Fig. 3.3. Having measured the displacement field on a circle for the homogeneous

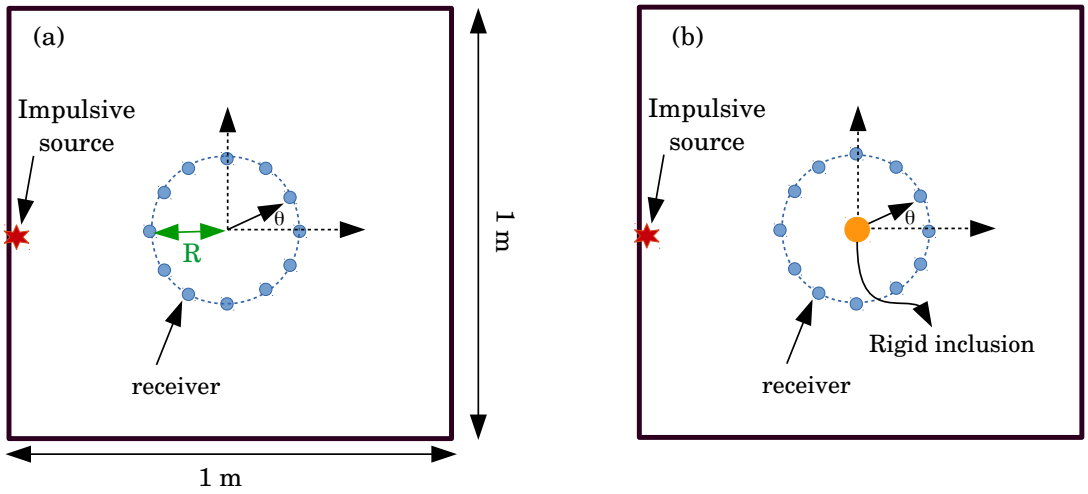

Figure 3.3: Numerical set-up for calculating the total scattering cross-section of a defect of diameter of 1 cm. a) plate without the inclusion, b) plate with the inclusion at its center.

plate ($W_{w/o}$) and for the case where the inclusion is added ($W_{w/}$), we subtract these two wave-fields and find the scattered wave-field ($W_{w/} - W_{w/o}$).

It should be noted that the measurements on the circle are done for 120 points separated every $\pi/60$ radians. The subtraction is applied only on the direct wave packets. The incident wave-field (W_{inc}) is the average of the recordings on points corresponding to zero and π degree on the circle when there is no inclusion in the plate. Next, by having all of this, we find the far-field radiation pattern given by [68]

$$|f(\theta,\omega)| = \frac{W_{w/}(\theta,\omega) - W_{w/o}(\theta,\omega)}{|W_{inc}(\omega)|}\sqrt{R} \tag{3.3}$$

where R is the radius of the circle of the scan. The amplitude of the phase function for three different frequencies is shown in Fig. 3.4 in polar coordinates. As we can see, at frequency $f = 250$ Hz, the amplitude of scattered wave-field is almost

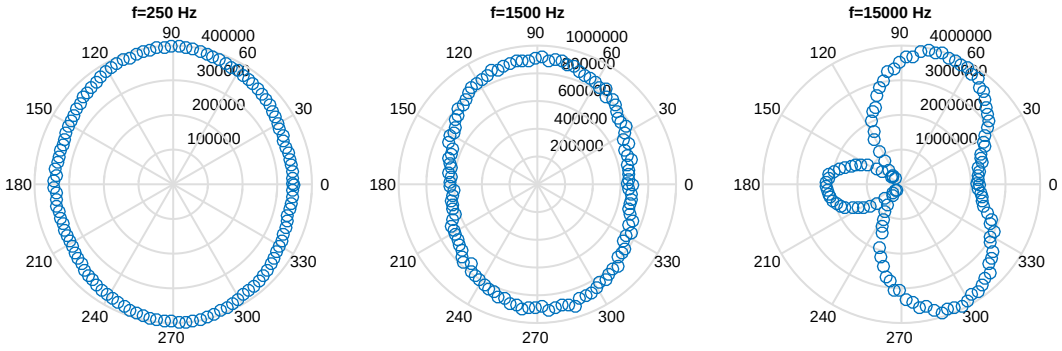

Figure 3.4: Amplitude of the phase function for a defect of diameter of 1 cm at three different frequencies. The incident wave-field illuminates the medium from the angle of 180°.

the same in all directions. In other words, the radiation pattern of the defect is isotropic. This can be explained by the fact that at this frequency the wavelength is about 35 cm which is large compared to the size (diameter) of the inclusion and so the scatterer behaves as a point-like one. On the other hand, at slightly higher frequencies (e.g., f= 1500 Hz), the wavelength decreases and an anisotropic radiation pattern shows up. At higher frequencies, we observe the appearance of a lobe toward the direction of the incident wave which corresponds to backscattered waves.

By having the phase function, we can calculate the total scattering cross-section (σ) versus frequency according to Eq. 3.2. We compare the σ obtained by the numerical simulation with the σ obtained from the analytical study of Norris and Vemula ([80]). The comparison of the two is shown in Fig. 3.5.

As we observe, the numerical and analytical solution for the scattering cross-section of a rigid cylindrical inclusion are in agreement with one another. We note that this close match is obtained although in the case of numerical simulations, there a few assumptions that are not completely satisfied. For example, the analytical solution of Norris and Vemula is obtained for an infinite plate and a plane incident wave which are not satisfied in our numerical set-up. In our numerical experiment, the medium is finite. Moreover, ELMER is based on the Mindlin-Reissener model (see chapter one, section 1.3.2) for the Lamb waves while Norris and Vemula calculations are based on Kirchhoff-Love model (see chapter one, section 1.3.1). But

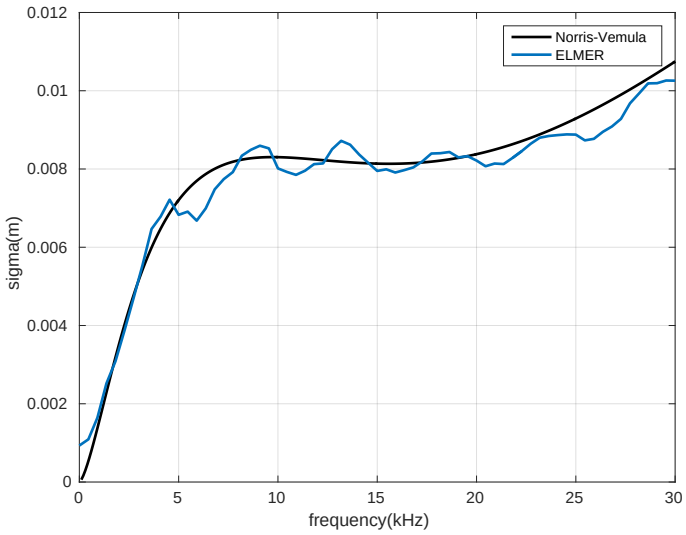

Figure 3.5: Comparison of the values of total scattering cross-section obtained with the numerical modeling using ELMER code (blue curve) and the one obtained through the analytical study of Norris and Vemula (black curve). The defect is a rigid cylindrical inclusion with the diameter of 1 cm.

despite all these differences, we still can have very similar results for the scattering cross-section. We propose and derive a formalism in the following section based on the coda of the arrivals and then validate it experimentally.

3.3 Theoretical Analysis for Estimation of the Scattering Cross-Section of a 3D Inclusion on a Plate

In contrast to coda wave interferometry, where nonlocal distributed variations in wave speed are of interest, in the present study, we focus on the effects of very sharp and localized heterogeneities, which we refer to as scatterers.

In this section, we discuss two slightly different cases for estimation of the scattering cross-section of a scatterer based on the coda of the source-to-receiver Green's function. As demonstrated by [73], the basic assumption in this formalism is that the scattering mean free path (l_s) is much larger compared to the dimension of the cavity. First, we study the case where the Green's function of the medium in the

presence of the scatterer is compared to that obtained in its absence. This will be referred to as case I in the following.

In a strongly reverberating medium, the time-domain Green's function (i.e., impulse response) between a source at x_1 and a receiver at x_2 ($G(x_1, x_2, t)$) can be described as:

$$G_{w/,i}(x_1, x_2, t) = G_{0i}(x_1, x_2, t) \exp(-t/2\tau) + s_i(t), \tag{3.4}$$

where i is an integer index that indicates a certain source-receiver within a database. The subscript $w/$ serves to remind us that one scatterer is present somewhere in the medium. $G_{0i}(x_1, x_2, t)$ is the impulse response in the absence of the scatterer, which is known to introduce an exponential decay with a decay time of τ [73]. $s_i(t)$ is a term due to the presence of the scatterer [73].

In the second set of experiments, the scatterer is removed. For such a situation, the exponential decay due to the presence of the scatterer will disappear, and hence $G_{w/o,i}(x_1, x_2, t)$ can be written as:

$$G_{w/o,i}(x_1, x_2, t) = G_{0i}(x_1, x_2, t), \tag{3.5}$$

where the subscript w/o indicates 'without scatterer'. We are interested in measuring the similarity between the Green's functions given by Eqs. (3.4) and (3.5). We repeat the measurements of $G_{w/}$ and $G_{w/o}$, and take their mean (<>) over all of the available source-receiver pairs, to find the time-dependent Pearson correlation coefficient (hereafter referred to as 'similarity'),

$$S(t) = \frac{< G_{w/,i}(x_1, x_2, t) G_{w/o,i}(x_1, x_2, t) >}{\sqrt{< (G_{w/,i}(x_1, x_2, t))^2 >} \sqrt{< (G_{w/o,i}(x_1, x_2, t))^2 >}}. \tag{3.6}$$

Substituting Eqs. (3.4) and (3.5) into Eq. (3.6) and defining the residual terms as uncorrelated, it turns out that

$$S(t) = \exp\left(-t/2\tau\right). \tag{3.7}$$

In a diluted scattering medium where the density of scatterers is not high, the scattering mean free path (l_s) that is defined as the mean distance between two scatterers can be expressed as [68]:

$$l_s = \frac{1}{n\sigma} \tag{3.8}$$

where n is the density of scatterers and σ is the scattering cross-section of the scatterer. The scattering mean free path is one of the parameters that describes the propagation of waves in a multiple scattering medium (e.g., [81]). In the present case, we deal with an unusual scattering regime, because as in the DRAWS technique, an important number of reverberations occur between two scattering events. Following that, the decay time is found by dividing Eq. 3.8 by group velocity $V_g(\omega)$,

$$\tau = \frac{1}{V_g(\omega) n \sigma}. \tag{3.9}$$

Eq. (3.7) can be rewritten as:

$$S(t) = \exp\left(-t V_g(\omega) n \sigma / 2\right). \tag{3.10}$$

The reason why we consider the group velocity of the waves is that we perform our experiments on a duralumin plate. In such a medium, the energy propagates in the form of Lamb waves, which are highly dispersive; i.e., the wave speed changes with the frequency. In the low-frequency regime, the phase speed (V_ϕ) of the fundamental mode of antisymmetric Lamb waves at a given angular frequency (ω) and for a plate of thickness e, density ρ, and flexural rigidity D is given by [3]

$$V_\phi(\omega) = \sqrt{\omega} \left(\frac{D}{\rho e}\right)^{\frac{1}{4}}. \tag{3.11}$$

In the measurements here, we are interested in the velocity of the propagation of wave packets and not of a single phase. So, we apply the group velocity ($V_g(\omega)$) in our formalism, which in the low-frequency regime is twice the phase speed given by Eq. (3.11). Substituting for $V_g(\omega)$ leads to

$$S(t) = \exp\left(-\left(\frac{D}{\rho e}\right)^{\frac{1}{4}} t \sqrt{\omega_0} n \sigma\right) \tag{3.12}$$

where ω_0 is the mean angular frequency in the bandwidth of interest.

For case II, the Green's functions are compared when the position of the scatterer has changed between successive acquisitions. To avoid repetition, we only describe here the differences with respect to case I. Here, as the scatterer is always present in the medium, the Green's function between the same source and receiver in the second experiment is

$$G_{w/,i'}(x_1, x_2, t) = G_{0i'}(x_1, x_2, t) \exp(-t/2\tau) + s_{i'}(t). \tag{3.13}$$

Similar to case I, i indicates the source-receiver pair and the change in the position of the scatterer is indicated by the prime sign.

Replacing $G_{w/o,i}(x_1, x_2, t)$ with $G_{w/,i'}(x_1, x_2, t)$ in Eq. (3.6), and following the same procedure as above, the similarity coefficient is written as:

$$S(t) = \exp\left(-2\left(\frac{D}{\rho e}\right)^{\frac{1}{4}} t\sqrt{\omega_0} n\sigma\right). \tag{3.14}$$

Eqs. (3.12) and (3.14) suggest that the scattering cross-section can be determined based on experimental or field observations of S. In other words, if a single or a set of unknown scatterers are added to the plate, the measures of the Green's function carried out before and after the introduction of the scatterers can recover the strength of the scatterers. This is also true where the Green's functions are measured following the displacement of the scatterer. In the following, we experimentally verify this theoretical analysis, and we confirm its validity through comparison with a conventional method.

3.4 Experimental Validation

To validate the proposed formulae for cases I and II, acoustic experiments are carried out on plates. The experimental set-up is as shown in Fig. 3.6, and consists of a quarter Sinai billiard [82] shaped duralumin plate of 75 × 75 × 0.3 cm. The plate is suspended using two thin vertical supports to provide free boundary conditions. There are five piezoelectric transducers attached to the plate surface. A pair of cylindrical magnets of 12 mm diameter and 5 mm height are attached to the plate at the exact same location on both sides of the plate. This pair of magnets acts as a single scatterer that is symmetrical with respect to the mid-plane of the plate, and redirects the propagating Lamb waves without mode conversion. To retrieve the Green's function between each pair of transducers, ambient-noise interferometry is used, which is valid provided that the propagating waves travel along all directions with equal probability. This condition is what is referred to as a 'diffuse wavefield' (see [30], section 12.1; see also [16], [76] for reviews of seismic applications of noise interferometry). In a reverberating or strongly scattering medium, whatever the source, the coda tends to be at least approximately diffuse after a sufficient

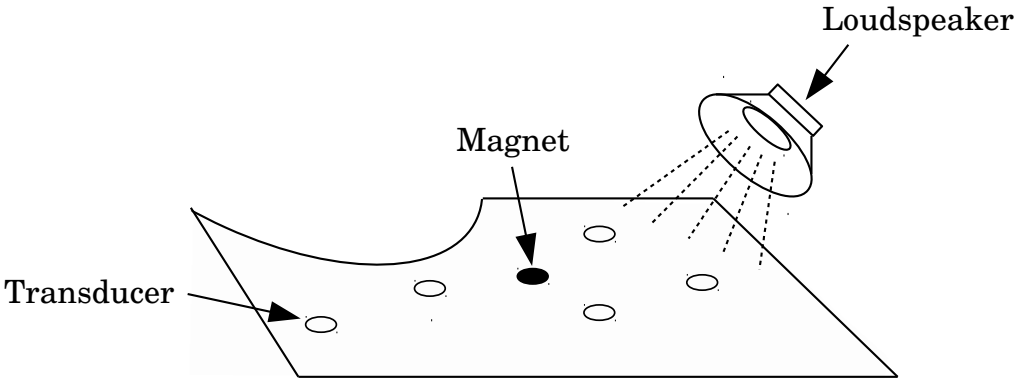

Figure 3.6: Sinai billiard-shaped plate used in the experimental set-up to find the scattering cross-section by interferometry. The plate is suspended horizontally and transducers are connected to an audio card.

number of reverberations and/or scattering events have occurred. In this set-up, the geometry of the plate is selected so as to eliminate any preferential direction of the propagation. This has been shown to result in the condition of diffusivity being more easily met [83]. We showed in chapter 2 of this manuscript the reliability of ambient-noise interferometry technique in retrieval of the Green's function in duralumin plates using point sources [33]. Here, we implement a continuous noise source. Pseudo-random noise is emitted by a loudspeaker (Ryght). The loudspeaker is moved erratically at 10 cm above the surface during the acquisition. At the same time, the propagating waves are recorded at all of the deployed transducers. The Green's function between each pair of transducers is determined by cross-correlation of the corresponding pair of long-duration recordings. The retrieved Green's function includes the direct and coda waves that propagate between the transducers, which coincides with the signal that one transducer would record if the other were an impulsive source. The Green's function obtained by this method will be referred to here as the 'passive' Green's function, as there is no active source involved. The advantage of using transducers attached to the plate is that they can be used both as sources and receivers. This allows the direct measurement of the Green's function between each pair of transducers. The Green's functions so obtained will be referred to here as 'direct' or 'active', because in this case each transducer has the role of

an active source. We use the active Green's functions as reference to determine the reliability of the Green's functions obtained by cross-correlation. The source signal is a linearly varying frequency chirp between 1500 Hz and 90000 Hz. We record the response of the medium to this source while Green's function is defined as the response of the medium to a source of Dirac-delta type. In order to find the response to a source as close as possible to a Dirac delta distribution, we apply a technique to our recordings known as 'pulse compression' in signal processing. When we emit a chirp as the source, the response we record is the convolution of the Green's function with source function (which is a chirp). Pulse compression consists of cross-correlating this recording with the source function which mimics the response of the medium to a source that is pulse-like. Pulse compression technique improves the signal-to-noise ratio as well.

An example of the comparison between active and passive Green's functions is shown in Fig. 3.7 in the frequency band of 5 kHz to 10 kHz.

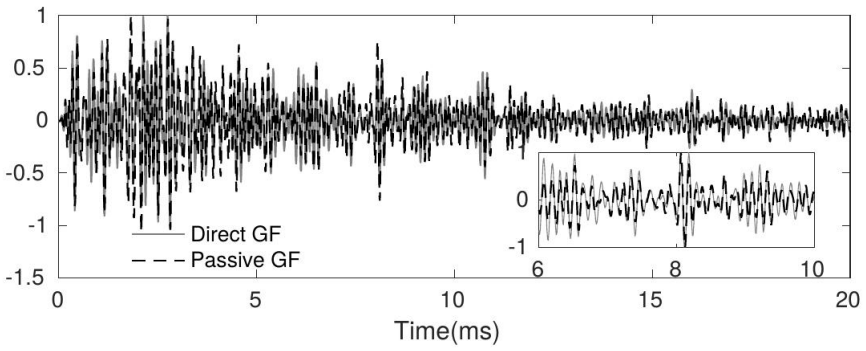

Figure 3.7: Comparison between actively (gray solid line) and passively (black dashed line) retrieved Green's functions bandpass filtered from 5 kHz to 10 kHz and normalized by maximum amplitude. The inset shows the zoom from 6 ms to 10 ms that corresponds to ∼4 m of propagation in the reverberating plate.

Fig. 3.7 shows a close match between these two Green's functions. Once the high-quality Green's functions are retrieved passively, we apply them to Eq. 3.6 to find the similarity $S(t)$, and then Eqs. 3.12 or 3.14 are implemented to determine the scattering cross-section. The corresponding procedure to find the scattering cross-section after the retrieval of the Green's function is explained in the following.

3.4.1 Reconstruction of Scattering Cross-Section by Interferometry When a Scatterer Appears in the Propagation Medium (Case I)

Given a discrete set of five transducers, we deal with Green's function between 10 combinations of two receivers. Following the passive estimation of the Green's functions in the presence of the magnets, we next remove the magnets and repeat the same measurement. For each of 10 pairs of transducers, we calculate the similarity coefficient between the Green's function in the presence versus absence of the scatterer. We then take the mean of the similarity coefficients over all of the 10 possibilities according to Eq. 3.6. These measurements are repeated for different magnet positions, and show that the similarity coefficients in the presence versus absence of the scatterer are independent of the position of the magnet. To take into account the dispersion effect with the plate waves, the similarity coefficient is calculated for Green's functions that are filtered over a limited frequency band of 5 kHz, with the central frequency varying from 5 kHz to 17.5 kHz. The group velocity for the central frequency in each bandwidth is substituted in the calculation, and $\sigma(\omega)$ is determined by fitting the exponential decay according to Eq. 3.12. Approximating the velocity by the group velocity of the central frequency in the bandwidth, imposes a condition on the maximum time considered in the fitting to the similarity coefficient curve. This time depends on the central frequency, bandwidth, group velocity of the central frequency and scattering mean free path (See Supplemental Material part V for the detailed derivation of the condition on the maximum time of the similarity coefficient curve considered in fitting). Substituting the values considering the set-up and the frequency band of interest, this time should be smaller than ~ 0.027 s. We set this maximum time to 0.01 s in all fittings. An example of the decay of the similarity coefficient with time for one pair of transducers at 10 kHz is shown in Fig. 3.8, along with the fit according to Eq. 3.12. All of the experiments that are performed for the interferometry method are then repeated with active signals, to determine the scattering cross-section based on these actively recovered Green's functions. A comparison of the values of the scattering cross-sections based on the active and passive Green's functions in case I is shown in Fig. 3.9.

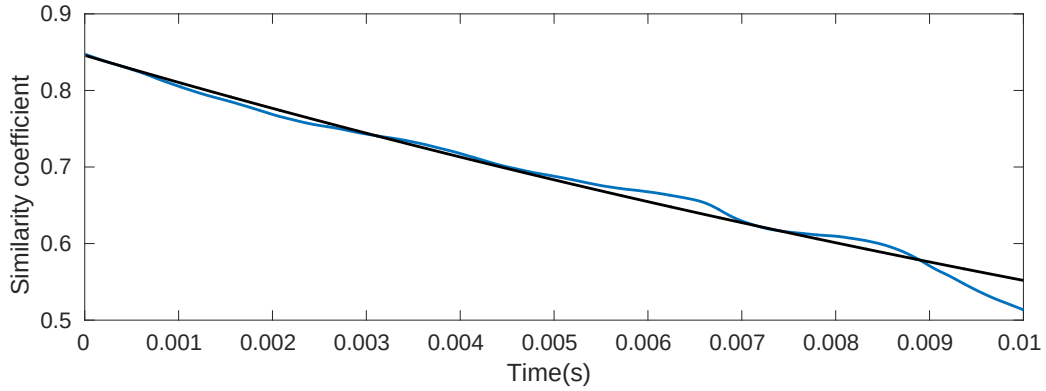

Figure 3.8: Similarity coefficient between the 'passive' Green's functions 'with' and 'without' the magnets, filtered between 7.5 kHz and 12.5 kHz (blue), and the fitting based on Eq. 3.12 (black).

3.4.2 Reconstruction of the Scattering Cross-Section by Interferometry for Displacement of a Scatterer (Case II)

As opposed to case I, where the variations in the Green's function were tracked in the presence and absence of the magnets, here the scatterer is always present in the medium and the similarity coefficient is calculated when the position of the scatterer (magnets) has changed from one acquisition to the other. We follow an experimental measurement approach similar to that described in the previous section for case I. The mean of the similarity coefficient over different pairs of transducers is calculated in the same way, over the different frequency bands. The exponential decay according to Eq. 3.14 is then fitted, and finally, the scattering cross-section is obtained as a function of the frequency. The $\sigma(\omega)$ for the actively measured Green's functions are also measured (see Fig. 3.9). In the following subsection, the scattering cross-section of the magnet is measured with an entirely different approach that is based on the direct arrivals.

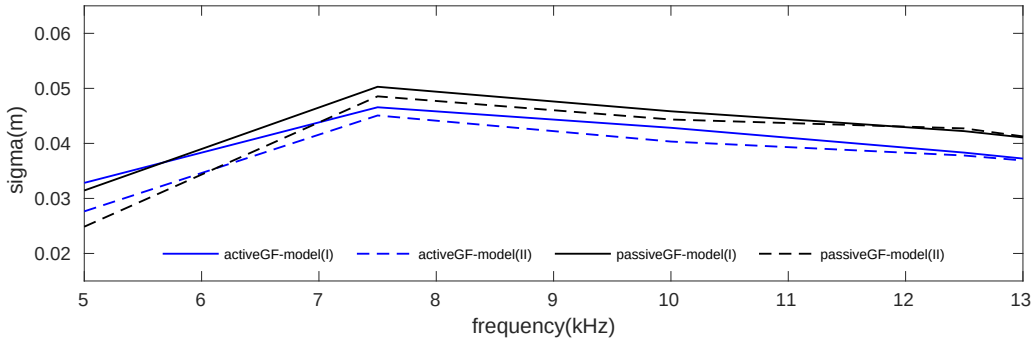

Figure 3.9: Values of σ obtained by fitting according to model I and model II to the actively- and passively- reterieved Green's functions vs frequency.

3.4.3 Reference Measurement of the Scattering Cross-Section According to a Conventional Method Based on Direct Arrivals

In order to evaluate the values for scattering cross-section that are obtained by taking into account the information that is carried by the coda part of the wave-field, we now use another approach to measure the scattering cross-section of a cylindrical steel magnet by focusing on the wave-field corresponding to direct waves. The set-up for this experiment is very similar to the one we tested in our numerical study at the beginning of this chapter. We remind that in this section we intend to measure the scattered wave-field from direct waves in the far field. The difference with the numerical study is that here we have a 3D inhomogeneity. In other words, at the location of the defect not only the elastic parameters are different from the ones of the background medium but also the thickness is different. To approach the assumption of plane incident wave and far field approximation, we run the experiment on a large duralumin plate whose dimensions are 1.5 m by 1 m by 0.003 m (see Fig. 3.10).

The defect here is the same couple of magnets used in the previous experiment. The source is a piezoelectric transducer placed at the edge of the plate along with the center of the circle. The source signal is a linear chirp with frequency varying from 1500 Hz to 90 kHz and duration of 2 s. We then use the same approach as the numerical test. In the first step, we scan the velocity field on a circle of radius

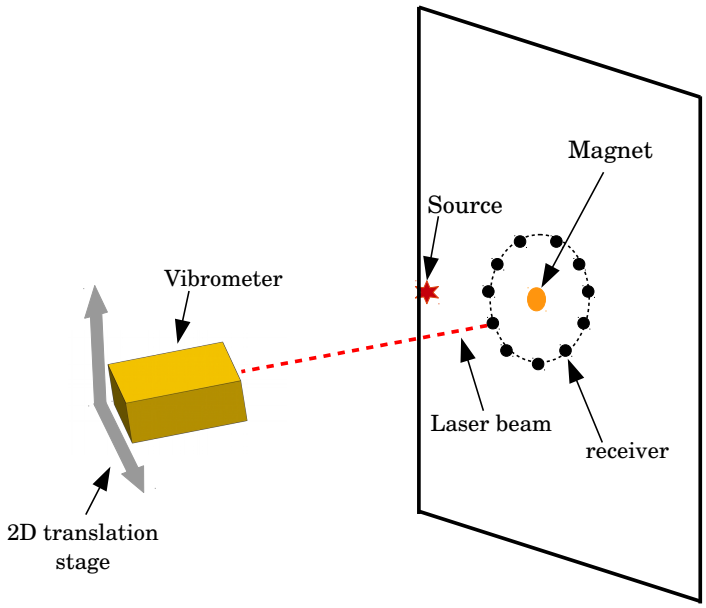

Figure 3.10: Experimental set-up for estimating the scattering cross-section from analysis of the direct arrivals.

of 15.3 cm whose center is the center of the plate. The measurement points on the circle are separated by an angular distance of $\pi/60$ radians which gives rise to 120 measurement points. We use a Laser Doppler Vibrometer (LDV) to scan the field. Next, we add the magnets to each side of the plate, on the center of the scanning circle and repeat the measurements. The pulse-compressed recorded wave-fields for all measurement points in the absence and presence of the magnet are shown in Fig. 3.11.

By comparing the two panels, we observe the scattered wave-field in the right panel corresponding to the presence of the magnet. By subtracting the wave-field in the presence and absence of the defect, we can find the scattered wave-field. But before doing the subtraction, there is an issue that should be corrected. In the following we address this issue.

As we run our experiments on a thin plate, we are dealing with dispersive waves. Dispersion and reflections from the boundaries as well as finite size of the plate complicate the recorded wave-field in a way that separating the direct waves (which are of interest here) from later (coda) arrivals becomes less obvious.

The dispersion effect is observed in Fig. 3.11 as higher frequencies arrive earlier in time than the lower frequencies indicating that different frequencies travel with

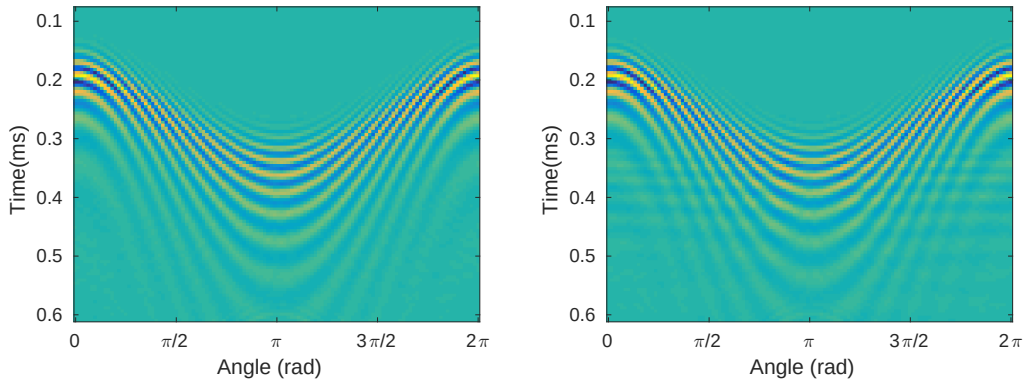

Figure 3.11: Recorded wave-field after pulse compression in the absence (left panel) and presence (right panel) of magnets. Note that the vertical time axis is oriented downward.

different speeds. Fig. 3.12 left is the pulse-compressed recorded waves in the absence of magnet in a time interval longer than the one shown in Fig. 3.11. We observe the mixing between the direct arrivals and reflections that arrive later. In order to handle this issue, we design a filter that compensates for the dispersion effect. Dispersion marks itself as a phase term, $S(x, \omega)$ of the form

$$S(x, \omega) = e^{-ik(\omega)x} \tag{3.15}$$

where x is the distance between the source and receiver and k is the wavenumber that depends on the frequency. We calculate the corresponding k of each frequency through Rayleigh-Lamb dispersion relation given by

$$\frac{\omega^4}{{V_T}^4} = 4k^2q^2\left[1 - \frac{p}{q}\frac{\tan(ph+\alpha)}{\tan(qh+\alpha)}\right] \tag{3.16}$$

where α is 0 or $\pi/2$ for symmetric and antisymmetric modes, respectively. p and q are defined as $p^2 = \frac{\omega^2}{{V_L}^2} - k^2$ and $q^2 = \frac{\omega^2}{{V_T}^2} - k^2$ where V_L and V_T are the phase velocity of the bulk longitudinal and transverse waves, respectively. h is half of the thickness of the plate.

We convolve our recordings with the inverse of this filter ($e^{ik(\omega)x}$) where we replace x with the distance of the farthest point from the source ($x = 0.5 + 0.153$ m). The resulting wave is the response we get from a source whose dispersion effects

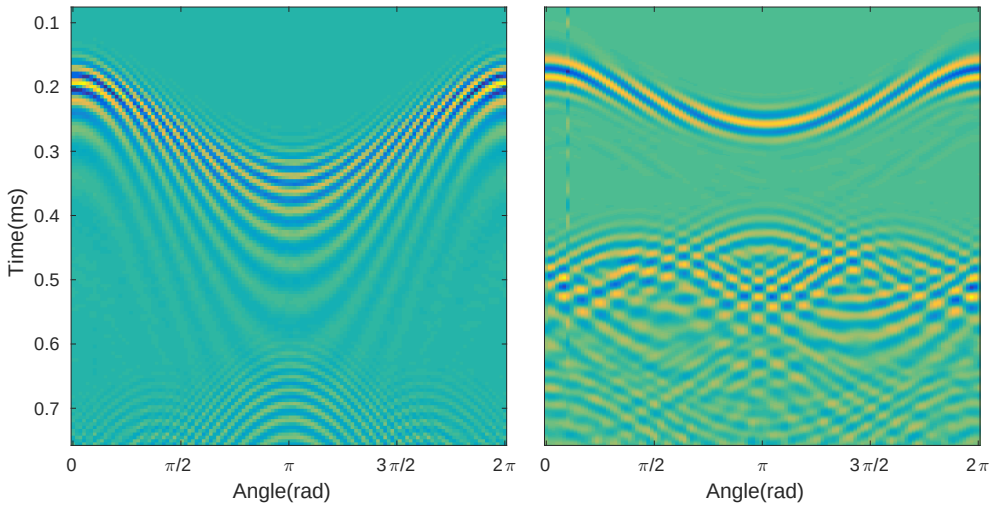

Figure 3.12: Raw recorded wave-field after pulse compression in the absence of magnet (left panel). Same data of left panel after compensation for the dispersion of Lamb waves (right panel).

are compensated. The outcome is plotted on Fig. 3.12, right panel. We observe the effect of filter as it mitigates the dispersion effect and hence we can separate the direct wave packet from later arrivals. We apply the same correcting filter to the recordings where the magnets are present in the medium. Doing so, we next take the difference of the direct arrivals in the case of presence and absence of the magnets. From this data and using Eqs. 3.1 and 3.2, we compute the scattering cross-section for this pair of magnets. We consider the values of σ obtained by this conventional method as a reference for evaluating the values of σ that we obtained in the previous section based on coda of the arrivals. Fig. 3.13 shows the values of scattering cross-section obtained by different methods and set-ups.

We plot the results as a function of ka where k and a are the wavenumber and the radius of the defect, respectively. This normalized axis helps in defining the scattering regime we are dealing. Scattering regimes are classified according to the product of the characteristic dimension of the scatterer (i.e., radius in case of a circular scatterer (a)) and the wavenumber. According to this classification, the following regimes can be defined: 1) $ka << 1$ known as Rayleigh regime and occurs when the characteristic size of the scatterer is much smaller than the propagating wavelength. 2) $ka \sim 1$ known as Mie scattering and 3) $ka >> 1$ know as geometric

scattering. Fig. 3.13 indicates that we are in the Rayleigh regime.

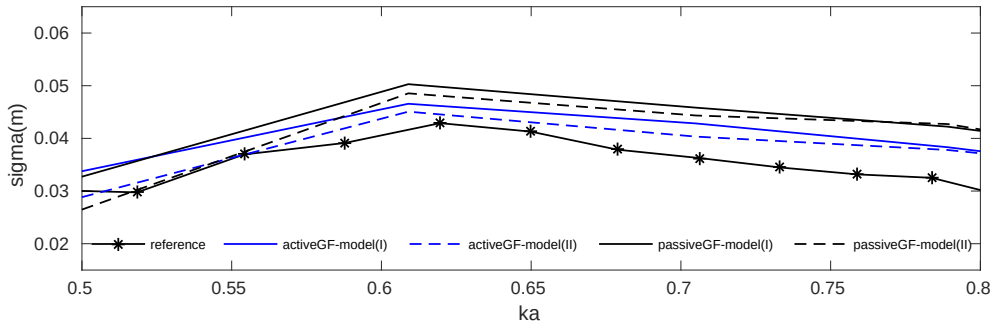

Figure 3.13: Total scattering cross-sections obtained for the cylindrical magnet of 12 mm diameter and 5 mm height for the different methods and different data. Solid line with stars, reference curve obtained by the conventional method based on direct arrivals; solid blue line, case I for the active Green's function; dashed blue line, case II for the active Green's function; solid black line, case I for the passive Green's function; dashed black line, case II for the passive Green's function.

In general, the proposed formulae for cases I and II give slightly higher values for $\sigma(\omega)$. We explain this on the basis that these formulae result from an ensemble average, and that these experiments are limited to a relatively small number of receiver-receiver pairs (i.e., five receivers, providing 10 pairs). Also, the strong dispersion in the plate and the finite size of the plate result in the mixing of the direct and reverberated wavefronts. This complicates the separation of the direct waves in the reference measurement of the scattering cross-section. The dispersion is compensated for by applying a filter based on the source-receiver distance. However, this compensation does not work correctly for all frequency bands. Moreover, in the measurements based on the coda of the Green's functions, as for the group velocity, we substitute the group velocity of the central frequency in a bandwidth. These approximations give rise to a small bias between the different methods of measuring the scattering cross-section. Another observation is that the passive and active Green's functions do not provide similar values, with a small average bias of about 0.3 percent. We speculate that this is mostly because the cross-correlation of the diffuse wave-field has still not fully converged to the Green's function. Moreover, the

ratio of the antisymmetric to symmetric excited modes decreases with the frequency, which leads to larger bias between the results obtained from the reference and the model at higher frequencies. Limitations such as using a loudspeaker as a noise source prevent the extension of these investigations to higher frequencies, at this stage.

We do not compare our results with the analytical solution of Norris and Vemula since they solve the problem of the rigid inclusion in 2D. Also the type of the inclusion in their study is not exactly the one we use in our experiments. We attach the magnets to either sides of the plate, so in the location of magnets we have two different materials (magnet, plate, magnet) which is not the case for the study of Norris and Vemula.

3.5 Conclusion

The study in this chapter was oriented toward a reverberating medium with the main objective to find the scattering cross-section of a scatterer in a reverberating medium from coda part of the Green's function. We started by a numerical test to study the possible effects that a non-perfect plane incident wave and finite medium can impose on the values of the scattering cross-section we obtain based on direct arrivals. We found a close match between the numerical results and theoretical ones confirming that a semi-plane incident wave is sufficient for this type of measurement. Next, we provided two theoretical models based on the temporal variations of the Green's function due to the appearance or movement of a scatterer. In these models, we take advantage of the coda of the Green's functions which are sensitive to the variations of the elastic parameters in the medium. We next validate the models by performing experiments on a thin irregular-shaped duralumin plate. We use noise interferometry technique to find the Green's function of the medium without an active source and then track the temporal changes in the Green's function. We find the scattering cross-section values based on this data and our models. We next apply the same models to the Green's function that we measure directly using an active source.

In the final part, we find the scattering cross-section of the scatterers (cylindri-

cal magnets) through a conventional method based on direct part of the arrivals. We verify the values of the scattering cross-section obtained from our models by this conventional one which is based on the direct arrivals. Validation of our models confirms that the coda of Green's function contain useful information on the scatterer in the medium and by temporally tracking the Green's function in the absence and presence of the scatterer, one can find the property of the scatterer. More importantly, we validate the reliability of this method in a more complex medium (i.e., thin plates) where we deal with strongly dispersive waves.

Chapter 4

Noise Correlation in a Metamaterial: from Laboratory to Field Data

4.1 Introduction

In chapter 2, we focused on cross-correlation of the recordings of impulsive-like sources on a homogeneous plate, as there was no scatterer or inhomogeneity in the medium. In this chapter, by implementing source-receiver reciprocity, we study the cross-correlation of the wave-field propagating in a medium of locally resonant elements. For this purpose, we use both laboratory and field data. For the laboratory part, we conduct an experiment on a thin elastic plate, to which are attached an array of vertical rods with sub-wavelength distance that have the role of the locally resonant elements. As well as cross-correlation, we also auto-correlate recordings that correspond to each virtual source-receiver pair, and visualize the auto-correlation maximum as a function of the virtual-source location: this provides a map of the energy contribution of each virtual source, inside and outside the region of resonators.

As for the field data, we process the recordings obtained in the experiment conducted at the seismic scale that is known as 'METAFORET'. In this experiment, the medium consists of a field and a forest of tall pine trees, where the trees act as resonators. A series of point-like sources were activated within this medium, and the responses to each source were collected using geophones. We use these data to perform the cross-correlations between virtual receivers for different frequency bands. In the experimental case, we deal with Lamb waves, while in the field data,

the surface Rayleigh waves are of interest. Both of these waves are two-dimensional (2D) dispersive waves, and they can couple with resonators in the medium.

We start this chapter by an introduction to the concept and nature of metamaterials. We next elaborate on the concept of bandgap, which is a remarkable characteristic that is related to the propagation of waves in materials with order in the structure, or materials that consist of resonant scatterers arranged at sub-wavelength scales. Afterwards, we recap on the state of the art of metamaterials in seismology, and review some related experiments that have been conducted at different scales. Finally, we focus on the experiments that we used for this study (i.e., plate and METAFORET), and elaborate the results we obtain based on the cross-correlation and auto-correlation of the wave-field at different frequency bands.

4.2 Metamaterials: Definition, History and Application

Metamaterials are a kind of unconventional materials with unusual properties that are not found in natural materials. For instance, in electromagnetism, this unusual property is negative electrical permittivity, magnetic permeability, or refraction index.

The theoretical demonstration of the properties of a material with simultaneous negative values for electric permittivity and magnetic permeability was first provided by the Russian physicist, Victor Veselago in 1968 [84]. However, this did not receive much attention until the late 1990s, when Pendry showed experimental verification of such a material [85]. As one of the first applications of metamaterial in the domain of optics, there was the 'super lens' [86]. In a conventional lens, due to the diffraction limit, we are always limited by the wavelength of the light used for focusing. Taking advantage of a lens made of a metamaterial with negative refractive index, a super lens that can focus on features smaller than the wavelength of light might be possible. Apart from optical purposes, these materials have found applications in various wave-related domains, such as building antennas, as well as strong absorbers [87], in acoustics and seismology.

4.3 Physics of Bandgaps

Apart from negative effective parameters, metamaterials show a characteristic feature that is known as the 'bandgap'. A bandgap is defined as a frequency band where the propagation of wave is forbidden. These forbidden bands for the propagation of wave have the potential to be implemented for controlling and filtering the vibrations. In talking about bandgaps, the first mechanism for generating them that might come to mind is Bragg diffraction. This is based on the periodicity in the lattice or distribution of the scatterers, but as we will see, this is not the only possible mechanism for generating bandgaps. Indeed, bandgaps have been observed in media with locally resonant scatterers as well, regardless of the periodicity in the system. In the following, we elaborate in more detail on the bandgap phenomenon for these two cases.

4.3.1 Origin of Bandgap of Bragg Diffraction

Assume a one-dimensional atomic chain where the interatomic distance is a. The atoms and the elastic forces between them can be considered as a mass-spring system. We assume a longitudinal plane wave that is incident to this layer of atoms. If one of the atoms is displaced, then propagation occurs. If we assume that displacements from the equilibrium are small and the interactions mostly occur between neighboring points, the equation of motion for the system described in Fig. 4.1 for the nth atom with mass M can be written as:

$$M\frac{\partial^2 u_n}{\partial t^2} = K(u_{n+1} + u_{n-1} - 2u_n) \tag{4.1}$$

where K is the spring constant, and u_n is the displacement of the nth atom from its equilibrium position at x_n.

Assuming that each atom undergoes sinusoidal motion and that there is no attenuation, it turns out that for such a system the dispersion relation obeys the following:

$$\omega = 2\sqrt{\frac{K}{M}}\left|\sin\frac{ka}{2}\right| \tag{4.2}$$

where k the wavenumber. This periodic dispersion relation is plotted in Fig. 4.2. The interval $-\pi/a < k < \pi/a$ that is shown in Fig. 4.2 is known as the first

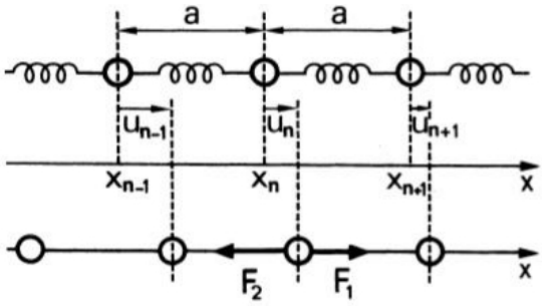

Figure 4.1: Demonstration of a set of atoms in one dimension. The propagation of the disturbance is represented by mass and spring (Figure from [3]).

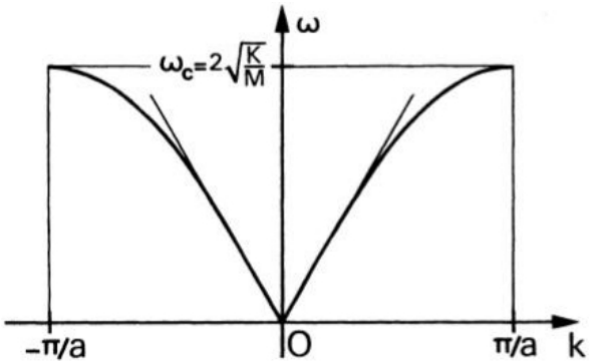

Figure 4.2: Dispersion curve for the waves that propagate in a one-dimensional array of atoms (as shown in Fig. 4.1). ω_c is the cut-off frequency, below which two modes can propagate in opposite directions (Figure from [3]).

Brillouin zone. It is at the boundary of this zone that the incident wave gets Bragg-diffracted. Next Brillouin zones occur at integer multiples of π/a. We observe that for the wavelengths that are large compared to the periodic distances between atoms (i.e., $ka << 1$), the frequency-wavenumber relation is a straight line which is that of a homogeneous medium. As the wavelength becomes comparable with respect to a so that ka is close to π, the dispersion shows up. This is the regime where the waves can propagate in a crystal only when the frequency is smaller than $f_c = \frac{1}{\pi}\sqrt{\frac{K}{M}}$, which is known as the cut-off frequency. We observe that at the cut-off frequency, group velocity defined as $V_g = d\omega/dk$ is zero, because the slope of the frequency-wavenumber representation is zero. The cut-off frequency where the zero

group velocity occurs is an indication of a bandgap where there is no transmission of energy [88].

This effect can be explained by considering the ratio of the displacement at two neighboring atoms. Assuming the displacements as $u_n = e^{i\omega t}$ and $u_{n+1} = e^{i\omega t - ika}$, the ratio of the two is given by e^{-ika}. At $k = \pi/a$, this ratio takes the value of -1, which is why the displacements of consecutive atoms are opposite in phase, and hence the appearance of the bandgap is a result of destructive interference, as the two neighboring atoms vibrate with opposite phase. This type of bandgap is called Bragg bandgap. We emphasize here that the appearance of this type of bandgap depends only on the periodicity of the structure and once the periodic structure is broken, we will no more observe this bandgap. For electromagnetic or acoustic waves, the materials that have bandgaps due to the periodicity in the system are known as photonic (e.g., [89]) or phononic (e.g., [90]) crystals, respectively.

In the following, we explain another possible structure that shows bandgaps without the need for periodicity in the system.

4.3.2 Origin of Bandgap in the Presence of Resonant Scatterers

Several studies have shown that the existence of frequency bands where wave propagation is forbidden is not only a result of the periodicity in the structure, known as Bragg diffraction, but it can also be due to the resonance of the elementary cells [91]. These bandgaps are called 'hybridization bandgaps'. The choice of this name is to emphasize that these bandgaps appear as a result of a phenomenon called hybridization and not the periodicity in the system.

Hybridization was initially introduced in quantum chemistry to explain the formation of chemical bonds. When two atoms approach each other, the coupling between the atomic orbitals of these atoms occurs. This coupling leads to a repulsion of the energy levels of the initial orbitals which, results in hybrid orbitals. So, from atomic orbitals a single molecular support is formed which is displaced and has lower global energy.

The phenomenon of hybridization is not only restricted to atomic orbitals. Indeed, all coupling phenomena can be interpreted as hybridization. In the community

of wave physics, hybridization is used for explaining the coupling between the resonators or nano-particles [92], [93]. In the framework of our study, this phenomenon explains the emergence of what is known as hybridization bandgap [94], [95], [96] .

Hybridization usually leads to exotic dispersion behavior, as shown schematically in Fig. 4.3. At a certain frequency (around the resonance frequency of the scatterer), the interaction between the propagation in the medium and the resonant scatterer causes a repulsion in the energy. This is known as 'anti-crossing'. This repulsion results in the bending of the curves before and after the anti-crossing point, and hence a discontinuity in the dispersion relation. Consequently, an 'S' shape comes out in the frequency-wavenumber representation. At frequencies far from the resonance frequency (ω_0), the frequency-wavenumber relation, which is also known as the dispersion relation, is the one of free space.

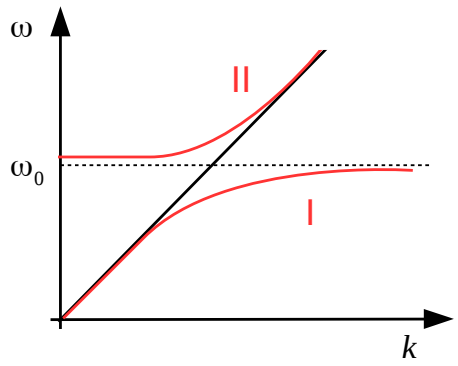

Figure 4.3: Schematic frequency-wavenumber representation showing anti-crossing. Solid/dashed black lines depict the dispersion relation in free space and for the resonator, respectively. Red curves are the dispersion curves after anti-crossing, which show an 'S' shape.

The dispersion relation in free space represents a single possible type of propagation. This behavior changes to a dispersion relation that shows two types of propagation, which cannot coexist. We observe that in the anti-crossing region, a dispersive behavior shows up which imposes two regimes. One of these is the propagation mode that becomes more and more *sub*-wavelength as we approach the resonance frequency from low frequencies (this is observed in the branch of the curve in Fig. 4.3 that is marked as I). Furthermore, we have a propagation mode that gets more and more *supra*-wavelength as we approach the resonance frequency from high

frequencies (see branch II in Fig. 4.3). In the vicinity of the resonance frequency, for branches I and II, we find that the wave speed is smaller or larger than the one in the free space, respectively. A similar curve was extracted experimentally by [97] for the interactions of light and phonons; the process that produces the quasi-particle called 'polariton'.

The case discussed here included a single scatterer in the medium. In the following section, we study a system consisting of a set of scatterers, and we extract the dispersion relation that explains the collective behavior of such a system in the presence of resonant elementary units.

4.4 Dispersion Relation for a System Consisting of a Set of Resonators

Let us assume a system that is made of an array of equally spaced resonators. Our demonstration is developed in terms of impedance in electrical engineering. The impedance associated to each resonator consists of two terms: (1) the impedance that corresponds to the resonance of each single resonator (Z_c); and (2) the impedance due to interactions between the resonator and its neighbors through propagation (Z_{lm}). Based on impedance theory, we can describe the system as:

$$\sum_m \left(Z_c \delta_{lm} + Z_{lm}\right) I_m = 0 \tag{4.3}$$

where I_m is the current passing through each resonator m, and δ_{lm} is the Kronecker Delta that is defined as:

$$\delta_{lm} = \begin{cases} 0, & \text{for} \quad l \neq m \\ 1, & \text{for} \quad l = m \end{cases} . \tag{4.4}$$

For a resonator, Z_c is given by

$$Z_c = i\omega L - \frac{i}{\omega C} \tag{4.5}$$

where L is the inductance and C is the capacitance.

It has been shown that $Z_{lm} \propto -iG(x_l, x_m)$ where G is the Green's function between the resonators l and m [98]. According to Eq. 4.5, Z_c can be considered as

$Z_c = -iA$, where $A = -\omega L + \frac{1}{\omega C}$. Consequently, Eq. 4.3 is rewritten as

$$\sum_m \left(A\delta_{lm} + G(x_l - x_m)\right) I_m = 0. \tag{4.6}$$

The reason why the right hand side of the equation is set to zero is that we are looking for a condition where the propagation can continue without the presence of a source. We look for the solutions as discrete plane waves due to the periodicity of the system, as:

$$I_m = I(k) \exp\left(ikx_m\right) \tag{4.7}$$

where k is a complex wavenumber. The real part of k is related to propagating waves, and its imaginary part is associated with evanescent waves or attenuation. Substituting Eq. 4.7 in Eq. 4.6, we get:

$$I(k) \sum_m \left(A\delta_{lm} + G(x_l - x_m)\right) \exp(ikx_m) = 0. \tag{4.8}$$

Multiplying both sides of Eq. 4.8 by $\sum_l \exp(-ikx_l)$ gives:

$$I(k) \sum_l \sum_m A\delta_{lm} \exp(ikx_m) \exp(-ikx_l) + I(k) \sum_l \sum_m G(x_l - x_m) \exp(ikx_m) \exp(-ikx_l) = 0. \tag{4.9}$$

Using Eq. 4.4, Eq. 4.9 simplifies to

$$I(k)A + I(k) \sum_{l,m} G(x_m - x_l) \exp(ik(x_m - x_l)) = 0. \tag{4.10}$$

Now, let us focus on the second term on the left hand side of Eq. 4.10. Defining $x_r = x_m - x_l$, this can be rewritten as $I(k) \sum_{l,m} G(x_m - x_l) \exp(ik(x_m - x_l)) = I(k) \sum_r G(x_r) \exp(ik(x_r))$. We see the emergence of the Fourier series of G, which can be described in terms of Fourier transform as:

$$\sum_r G(x_r) \exp(ik(x_r)) = \mathscr{C}_{1/d}(k) * \tilde{G}(k) \tag{4.11}$$

where $\mathscr{C}$ is the Dirac Comb distribution and assuming that d is the periodicity of the system and $\tilde{G}(k)$ is the spatial Fourier transform of G. $*$ indicates the convolution operator. We remind that Dirac Comb consists of an infinite sum of Dirac deltas with a given period. It is particularly helpful in replicating a function to get its periodic version. A Dirac Comb with spatial periodicity of d translates to a Dirac

Comb with the periodicity of $1/d$ in spatial frequency domain. So, Eq. 4.10 simplifies to

$$A + \mathscr{C}_{1/d}(k) * \tilde{G}(k) = 0. \tag{4.12}$$

Assuming that the resonators are very close, $1/d$ is very large and hence Eq. 4.12 simplifies to

$$A + \tilde{G}(k) = 0. \tag{4.13}$$

We note that the spatial-dependent solution of the Green's function was obtained from the Helmholtz equation, with a source type of dirac Delta as:

$$\nabla^2 G(x) + k_0^2 G(x) = \delta(x) \tag{4.14}$$

where $k_0 = \omega^2/c^2$, with c as the propagation speed. So, $\tilde{G}(k)$ is found by applying the spatial Fourier transform to this equation, to give:

$$-k^2\tilde{G}(k) + k_0^2\tilde{G}(k) = 1 \tag{4.15}$$

and hence:

$$\tilde{G}(k) = \frac{1}{k_0^2 - k^2}. \tag{4.16}$$

Now, let us focus on A. Considering Eq. 4.5 and going back to the definition of A, this can be written in terms of a resonance angular frequency (ω_0) as:

$$A = B\left(\frac{\omega_0}{\omega} - \frac{\omega}{\omega_0}\right) \tag{4.17}$$

where $B\omega_0 = 1/C$ and $B/\omega_0 = L$. B is a real and positive number that is representative of the strength of the resonance. We now substitute for A and $\tilde{G}(k)$ according to Eq. 4.17 and Eq. 4.16, into Eq. 4.13. Rearranging the resulting equation gives:

$$k^2 - {k_0}^2 = \frac{1}{B\left(\frac{\omega_0}{\omega} - \frac{\omega}{\omega_0}\right)} \tag{4.18}$$

and eventually the wavenumber (k) is found in terms of the angular frequency, as:

$$k = \sqrt{k_0^2 + \frac{1}{B\left(\frac{\omega_0}{\omega} - \frac{\omega}{\omega_0}\right)}}. \tag{4.19}$$

To have an idea of the frequency-wavenumber representation of such a system, we

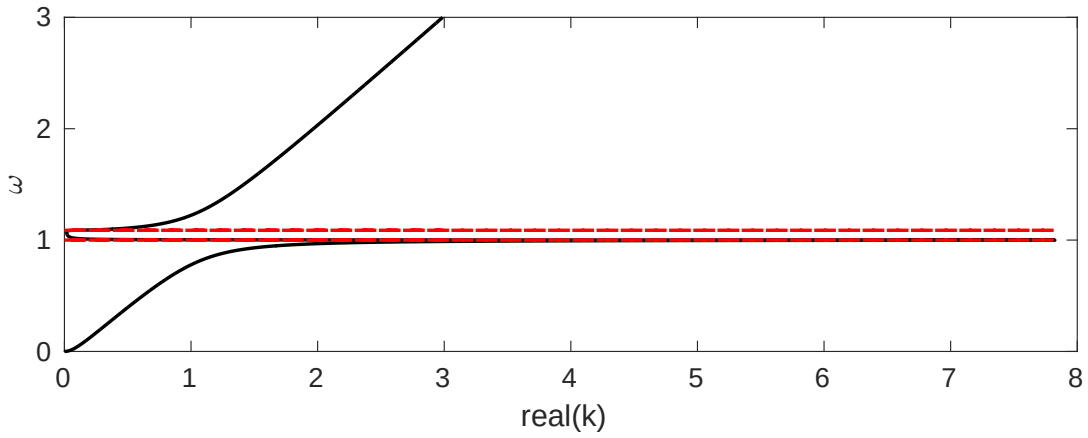

(a)

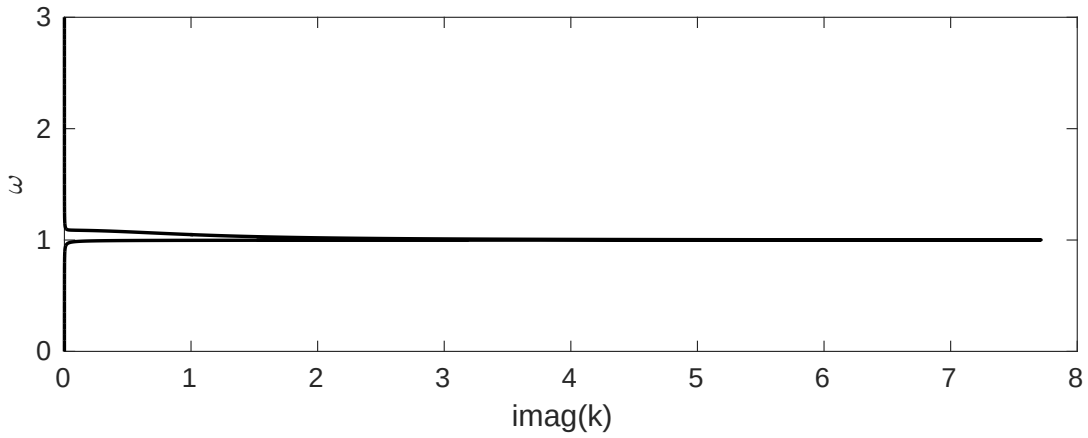

(b)

Figure 4.4: Frequency-wavenumber representation of the real (a) and imaginary (b) parts of the wavenumber for a system consisting of a set of resonators. The resonance frequency of each single element is 1 rad/s and the wave propagation speed is 1 m/s. Horizontal red lines mark the frequencies of start and end of the bandgap.

plot the imaginary and real parts of the wavenumber according to Eq. 4.19, assuming ω_0 (resonance frequency) as 1 rad/s, $c = 1$ m/s, and $B = 5$ (see Fig. 4.4).

This classical representation is consistent with the fundamentals of the hybridization phenomenon explained previously. As we expect, the hybridization effect occurs at the angular frequency that coincides with the resonant frequency of each single element. The imaginary part of the wavenumber has a non-zero value starting at the resonance frequency. An imaginary wavenumber is associated with purely evanescent waves. In Fig. 4.4, a small attenuation factor is added to A. Along with the

attenuation, B defines the width of the bandgap.

Now let us find the corresponding two ωs where the hybridization occurs. As at this interval the waves are purely evanescent, we look for the values of ω where k is purely imaginary. This condition translates to:

$$k_0{}^2 + \frac{1}{B\left(\frac{\omega_0}{\omega} - \frac{\omega}{\omega_0}\right)} < 0. \tag{4.20}$$

The hybridization starts at resonance frequency $\omega = \omega_0$, as observed in Fig. 4.4. The other real root occurs at:

$$\omega = \left(\frac{\sqrt{27\left(\frac{\omega_0 c^2}{B}\right)^2 - 4\omega_0^6}}{2(3)^{\frac{3}{2}}} + \frac{\omega_0 c^2}{2B}\right)^{\frac{1}{3}} + \frac{\omega_0^2}{3\left(\frac{\sqrt{27\left(\frac{\omega_0 c^2}{B}\right)^2 - 4\omega_0^6}}{2(3)^{\frac{3}{2}}} + \frac{\omega_0 c^2}{2B}\right)^{\frac{1}{3}}}. \tag{4.21}$$

Substituting for ω_0, c and B, ω is found to be 1.0880 rad/s. The values of ω where the hybridization occurs are superimposed as horizontal red dashed lines in Fig. 4.4a.

In summary, to have bandgaps of hybridization type, the medium should consist of locally resonant scatterers that are arranged at the sub-wavelength scale; i.e., there are many of these resonators within a wavelength. This spatial organization implies that the response of such a system cannot be explained by Bragg scattering. Moreover, the small distance between the resonators allows coupling and interactions between the single resonators. The idea of generating bandgaps through hybridization processes has been studied for cases of acoustic, electromagnetic, elastic, and seismic waves. For instance, [99] used a series of narrow and long pipes to build a super lens. The idea of the super lens was first proposed by [86], where he proposed using a slab of glass with negative refractive index to focus both propagating and evanescent waves, and hence to break the limit of the focus imposed by the diffraction limit. In the present study, we are mainly interested in studies that focused on elastic and seismic waves.

4.5 Examples of Previous Studies on Acoustic and Seismic Metamaterials

The idea of locally resonant metamaterials has found particular interest in the domain of seismology. In that context, several laboratory experiments as well as one large-scale field experiment have been conducted. Some numerical studies have also been performed to support these experiments. The main objective of all these efforts is to better understand the coupling between the propagating waves and the resonators. This can be used to manipulate the propagation of seismic surface waves, and to specifically forbid their propagation in the frequency bands where they are the most hazardous and destructive. In this section, we will review the experiments that are relevant to the present study.

4.5.1 Laboratory Experiment

In this section, we focus on a study carried out by [100], involving the construction and deployment of an uniaxial metamaterial on a thin elastic plate. In 2D, the resonators have small dimensions compared to the wavelength, but there is no limit on the third dimension. The idea of uniaxial metamaterials has already been implemented in electromagnetism in the wire medium (e.g., [101]), as well as in acoustics with a series of narrow long pipes (e.g., [99]). [100] specifically study the propagation of Lamb waves. The experimental set-up consists of a Bunimovich-shaped aluminum plate. A total of 100 cylindrical aluminum rods (length, 61 cm; diameter 6.35 mm) are attached to the surface of the plate in two different configurations (random *versus* periodic). For both cases, the region of the plate where rods are attached is a rectangle with an area of 400 cm^2. The average distance between the rods is around 2 cm for the periodic configuration, and 5 mm for the random one. The 2-cm inter-rod distance implies a sub-wavelength arrangement of the resonators (2 cm distance is equivalent to $\lambda/9$ and $\lambda/4$ at 2 kHz and 10 kHz for A_0 mode of Lamb waves). Wave motion is generated in the plate via a shaker. The full set-up is shown in Fig. 4.5. The vertical displacement of the plate is measured using a laser vibrometer: an example of the resulting data is shown, after transformation to the Fourier domain, in Fig. 4.6a. The Fourier transform is spatially averaged.

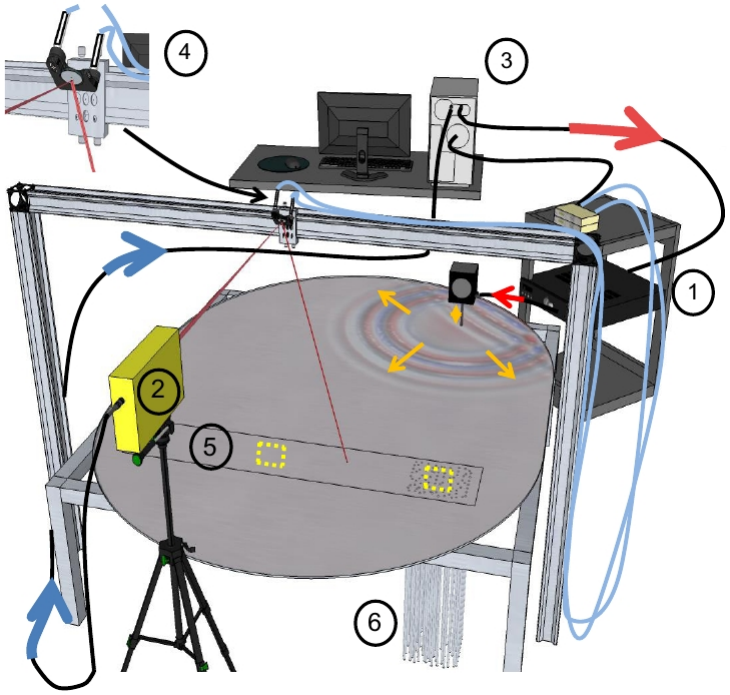

Figure 4.5: Experimental set-up in the study of [100], consisting of: (1) a shaker to excite the A_0 mode of the Lamb waves in the aluminum plate; (2) a laser Doppler velocimeter to measure the wave-field on the plate; (3) a computer to control the set-up; and (4) a motorized mirror. The scan of the surface of the plate is performed over rectangle 5, and the metamaterial region is constructed by attaching the vertical aluminum rods, marked as 6 (Figure from [100]).

According to Fig. 4.6a, once we are outside the metamaterial region, the average amplitude spectrum decreases continuously (albeit slightly) as frequency grows up to 2 kHz, and then it is flat up to 11 kHz. This drop is explained by the speed of the antisymmetric mode of Lamb waves (A_0) at 2 kHz ($\sim$ 340 m/s), which is close to the speed of sound in the air, and hence there is some energy that is radiated from the plate to the air. However, our interest is the two other curves, which show three bandgaps that start at frequencies of 2, 6, and 10 kHz. Fig. 4.6b shows the measured signals inside and outside the metamaterial region, filtered in the frequency band that corresponds to the first bandgap. This panel provides a direct illustration of the effects of the bandgap on propagation. A wave packet where the frequency content fits the bandgap is emitted on the plate. We observe that the amplitude

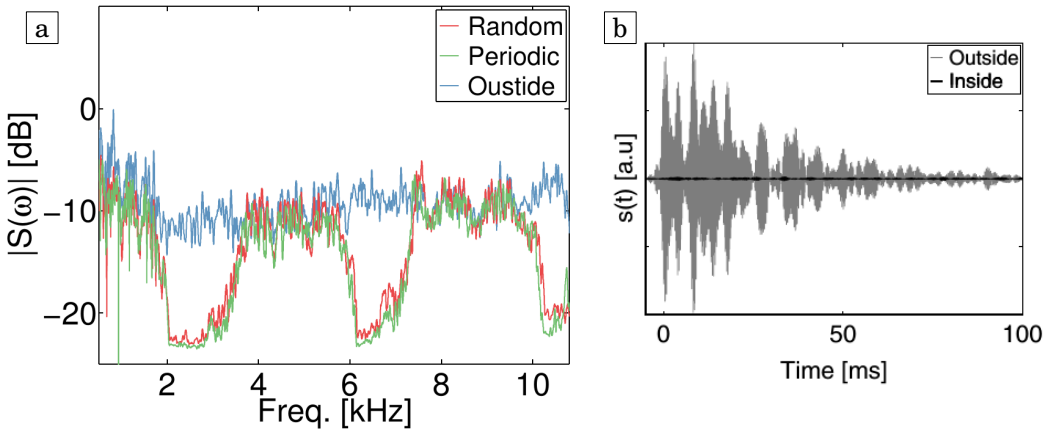

Figure 4.6: (a) Average amplitude spectrum of the signals measured outside the metamaterial region (blue curve) and inside the region for periodic (green curve) and random (red curve) distributions of the rods (resonators). The averaging areas are marked by the yellow dashed rectangles in Fig. 4.5. (b) Measured signals inside (black solid line) and outside (dashed gray line) the metamaterial filtered in the first bandgap. Outside the metamaterial, multiplied reverberated signals are obtained, while inside metamaterial, there is no energy propagation (Figure from [100]).

of the displacements is much smaller inside the rod forest than outside of it. We also observe that the effects of bandgap are not restricted to direct waves, but are also seen for the late reverberated waves. Also, due to the shape of the plate, which randomizes wave propagation in all directions, we can conclude that the bandgaps appear for all angles of incidence. The specific geometry of the plate guarantees that after a few reverberations, the propagating waves cover all of the angles, or in other words, the wave-field is diffuse.

This can be confirmed from another point of view; e.g., by following the spatiotemporal map of the field in the frequency band that corresponds to the bandgap at different times (see Fig. 4.7 for the data filtered within the first bandgap). Different snapshots show maps of the wave-field at different times, starting from the time corresponding to the first arrivals, and continuing until multiply reverberated waves. These maps demonstrate the efficiency of the bandgap over all of the incident angles, which continue until late times.

It is also useful to recover the bandgaps by focusing on the dispersion curves

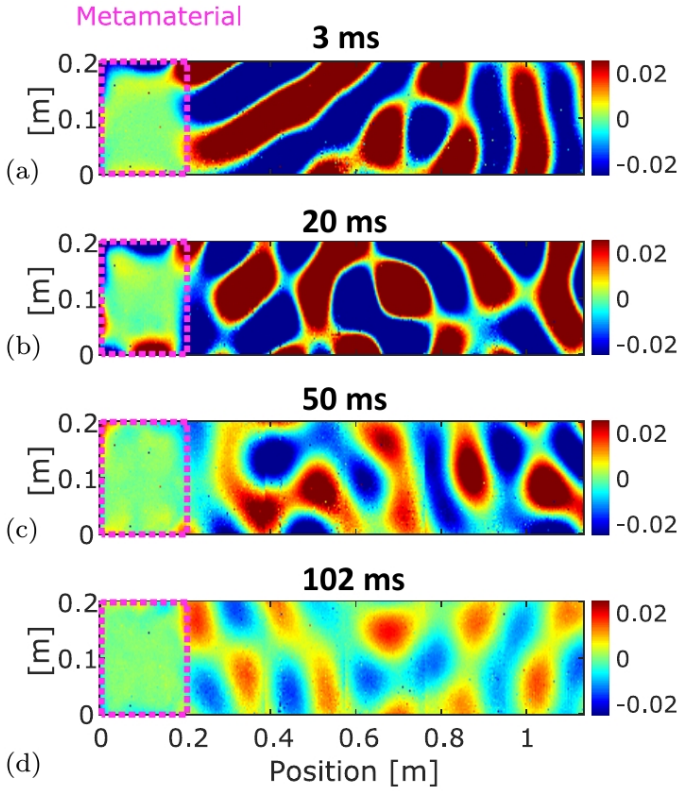

Figure 4.7: Field maps inside and outside the metamaterial region (rectangle marked by dashed line) at different times. The signals are all filtered in the frequency band of 2100 Hz to 2800 Hz (i.e., inside the first bandgap). After 100 ms, we can assume an omni-directional incident field to the metamaterial, since this time corresponds to 40 m of propagation inside the plate (Figure from chapter 6 of [102]).

inside the metamaterial region. This is achieved by applying a 2D spatial Fourier transform to the measured signals. The frequency-wavenumber representation for the waves inside the metamaterial is shown in Fig. 4.8a. In this panel, the dispersion relation for the modes of A_0 and S_0 for the free plate (i.e., plate without any rods) are also plotted. We observe three frequency bandgaps for a plate with metamaterial. To check the relationship between the frequencies where the bandgaps start and the resonance frequency of the scattering elements, they measured the response of individual rods.

Fig. 4.8c shows the frequencies where the compressional and flexural resonances of the rods occurred. There is a close match between the frequencies where the compressional resonances of the rods occur and the start of the bandgap. This ob-

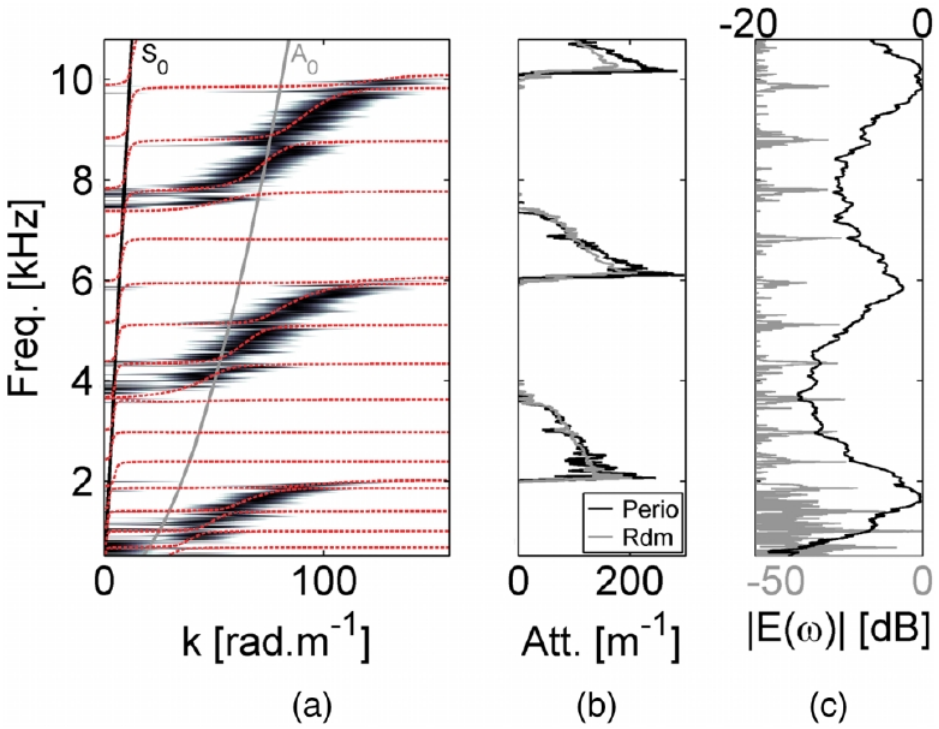

Figure 4.8: (a) Frequency-wavenumber representation of the wave-field inside the metamaterial when the resonators are distributed randomly, as well as the theoretical dispersion curves for a free plate (i.e., plate without any rods). The black curve is for S_0 mode, and the gray curve is for A_0. Red dashed curves are the results of a numerical simulation for a periodic metamaterial based on the Bloch theorem. (b) Imaginary part of the wave vector for random and periodic arrangements in gray and black, respectively, and measured inside the metamaterial. (c) Frequency spectrum of the vertical (black) and horizontal (gray) displacements measured for an individual rod, to define the compressional and flexural resonance frequencies (Figure from [100]).

servation confirms the hybridization effect between the compressional resonances of the rods and A_0 mode. The wide compressional resonance and the dense distribution of the resonators finally lead to wide bandgaps. Fig. 4.8b shows the attenuation in the bandgap based on the imaginary part of the wavenumber. The attenuation pattern is very similar for periodically and randomly arranged resonators.

Another interesting feature, also related to the presence of resonators, is apparent from Fig. 4.8a. As well as the hybridization effect, comparison of the dispersion curves inside the metamaterial with those obtained for a plate without rods, we see

that the metamaterial allows the propagation of some sub-wavelength and supra-wavelength modes that are not possible for a free plate. This significant effect can be used, for instance, to modify the wave velocity, and thus mold the propagation of Lamb waves. The sub-wavelength modes can be used in focusing applications, to overcome the diffraction limit. These sub-wavelength and supra-wavelength modes can also be observed through the spatiotemporal wave-field. If we pick the frequencies of 5805 Hz and 7512 Hz, we see from the dispersion curve that the first one is located in the sub-wavelength region, while the second one is in the supra-wavelength region. Fig. 4.9, top and bottom panels, show these sub-wavelength and supra-wavelength modes, respectively, inside the metamaterial region. In the next

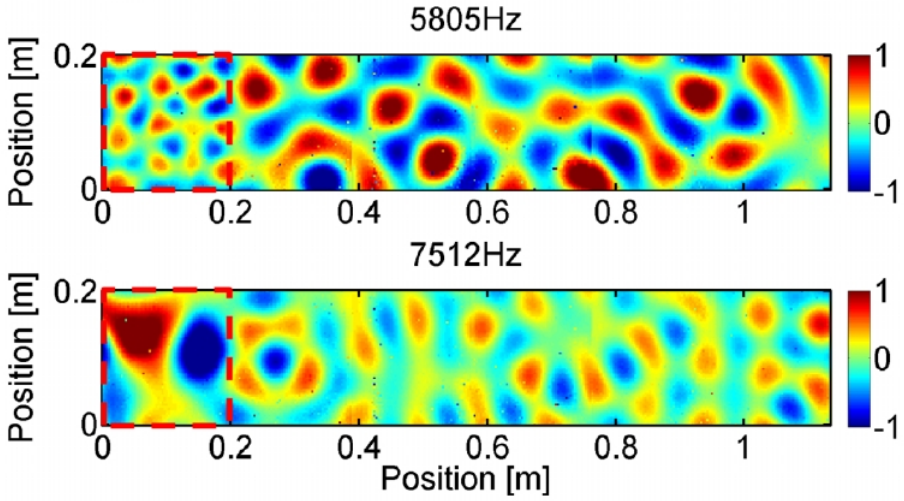

Figure 4.9: Demonstration of the wave-field inside and outside the metamaterial region in the frequency domain at frequencies that are located before and after the bandgap. The rectangle with red dashed lines marks the metamaterial region on the plate. Sub-wavelength and supra-wavelength modes inside the metamaterial are observed in the top and bottom panels, respectively (Figure from [100]).

sections, we will come back to this experiment.

These experiments were complemented by numerical simulations; the unit cell in the numerical set-up consisted of one rod attached to the center of an elastic plate with dimensions of 2 cm by 2 cm. Numerical results are shown as the red dashed curves in Fig. 4.8a. The interesting features of these curves are the following: First, they confirm the experimental results, as the frequency interval corresponding

to the bandgap and propagation band predicted numerically match those found experimentally. Second, they mark a behavior that is not seen in the experimental case. The numerical dispersion curves for A_0 show two bends: one matching the frequency where the hybridization, and hence bandgap, takes place, and the other occurring at a lower wavenumber. This implies that the A_0 mode not only couples with the compressional resonances, but also with the flexural ones. The asymmetry of the plate + rods system allows some conversion of the A_0 mode to S_0. The S_0 modes can then couple with the flexural resonances. It was inferred from the results presented in this section that vertical resonators and propagating waves are coupled at the laboratory scale. An experiment was next implemented in the field, to determine whether similar behavior was observed with tress as the vertical resonators in the medium.

4.5.2 Small Scale Seismic Experiment

The hypothesis that trees act as resonators where their resonating nature affects the propagation of Rayleigh surface waves through coupling was the focus of a study by [103]. This study was supported by numerical simulations, and it is considered as a preliminary study to implement the concept of locally resonant metamaterials for seismic purposes. The experiment in this study was conducted in a pine tree forest within the campus of the University of Grenoble Alpes. The ambient noise was recorded continuously over 1 h with two three-component seismometers (S_1 and S_2), inside and outside the forest, as shown in Fig. 4.10. Fig. 4.11 (blue curve) shows the averaged spectral ratio over windows of 10 min between the two seismometers and for the horizontal component. We observe two frequency bands that have a striking decrease in the spectral ratio. The first one is between 30 Hz and 45 Hz, and the second one between 90 Hz and 110 Hz. In other words, the energy penetrating into the forest gets attenuated at these frequency intervals. This observation is interpreted by the coupling between the trees that act as local resonators and the propagation of Rayleigh waves at the subsurface. The geophysical surveys in this region imply a surface velocity of between 300 m/s and 500 m/s. The heights of the trees in this forest varied between 10 m and 20 m. Spacing between the trees is variable between 2 m and 4 m. The effects of the roots were neglected because their

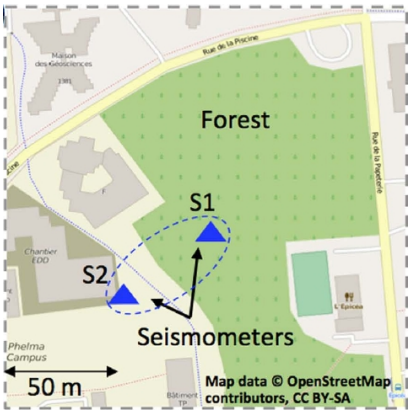

Figure 4.10: Forest location where the experiment was conducted. S_1 and S_2 are the two seismometers located inside and outside the forest, respectively (Figure from [103]).

scattering effect is of lower order compared to the resonance effect of the trees.

While using ambient noise data, we should keep in mind that most of the energy of the ambient vibrations propagate as surface waves (i.e., Rayleigh and Love waves), although here we are mostly interested in Rayleigh waves.

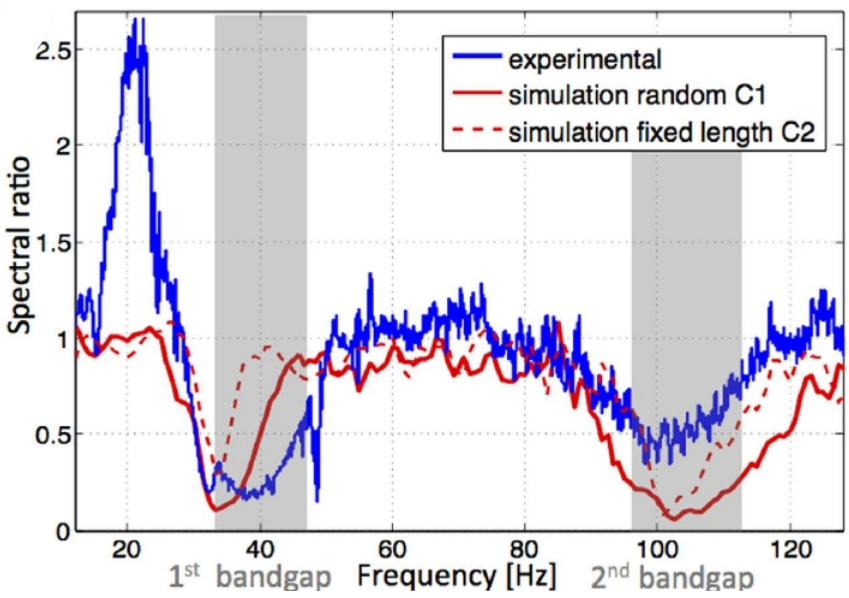

Figure 4.11: Experimentally measured (blue curve) and numerically simulated (red curves) spectral ratios. Solid and dashed red lines correspond to the configurations C_1 and C_2 (Figure from [103]).

In parallel to this experiment, 2D simulations were performed to model the propagation of Rayleigh waves in a halfspace. The medium was considered to be a linear, isotropic, and homogeneous elastic medium, and a linear array of 30 trees was added to the surface. The average height of the trees was set to 14 m ± 2.5 m. Trees are considered to be equivalent to vertical resonators. The numerical set-up is shown in Fig. 4.12. The source is a vertical force where the source time function is a

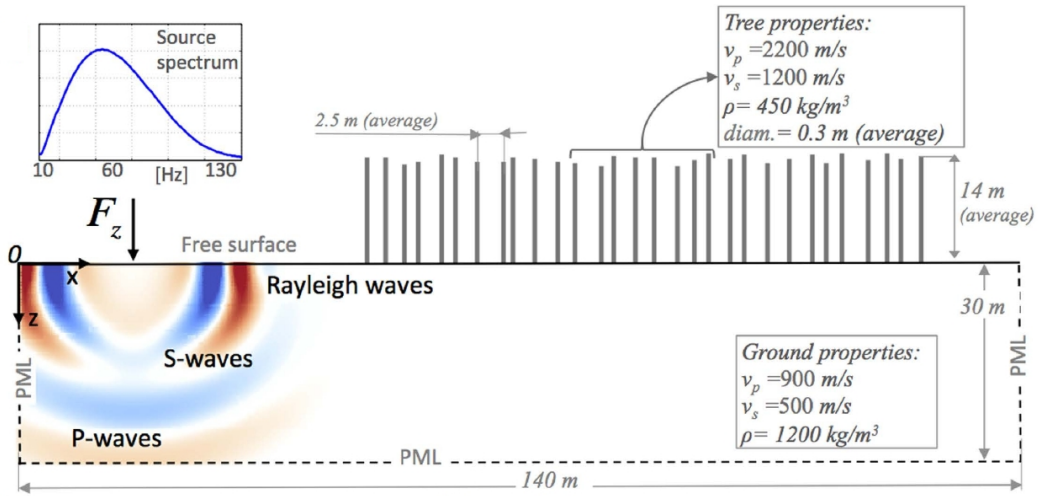

Figure 4.12: Two-dimensional numerical set-up. The elastic parameters of the ground and forest are also indicated. The red-blue color scale shows the vertical displacement u_z (Figure from [103]).

Ricker with a peak frequency at 60 Hz. Considering a shear-wave speed of 500 m/s, the wavelength of the surface waves varied between 4 m and 40 m for the frequency range of 10 Hz to 130 Hz. The spectral ratios for the horizontal displacement component is plotted in red (solid, dashed lines) for two different configurations. C_1 is configuration 1, where the height, thickness, and spacing of the trees were set to 12 m to 16 m, 0.2 m to 0.4 m and 1.5 m to 4 m, respectively. C_2 is configuration 2 where these parameters were set to 14 m, 0.2 m to 0.4 m, and 1.5 m to 4.0 m. In other words, C_1 focuses on the random sizes of the trees and the spacing between them, while C_2 corresponds to the case where the height of the trees is fixed. Fig. 4.11 shows that the bandgaps found by numerical experiments match those retrieved experimentally. The C_1 configuration explains better the experimental results (solid red curve). We note that this configuration corresponds to the case of trees with variable height (this case is more likely to be found in a natural forest than fixed-

height trees). Also, we observe that this configuration gives rise to a wider frequency bandgap compared to the C_2 configuration. This can be resolved by the physical explanation for such phenomena based on the coupling between the longitudinal resonance of the trees with the vertical component of the propagating Rayleigh waves. The compressional resonance frequency of the vertical structures is inversely proportional to the length of the resonator. So, the taller the tree (resonator), the lower its compressional resonance frequency. Trees with different heights will have different resonance frequencies, and the bandgap that corresponds to each of the trees will overlap and result in a wider bandgap.

To clarify the nature of Rayleigh wave propagation in the ground, the simulation results for the frequencies that lie within the first bandgap are compared for two different cases: first, in the absence, and second, in the presence, of trees on the ground. The results are shown in Fig. 4.13 over time. From Fig. 4.13b, we see that no Rayleigh waves propagate in the ground where the trees are. In this case, shear

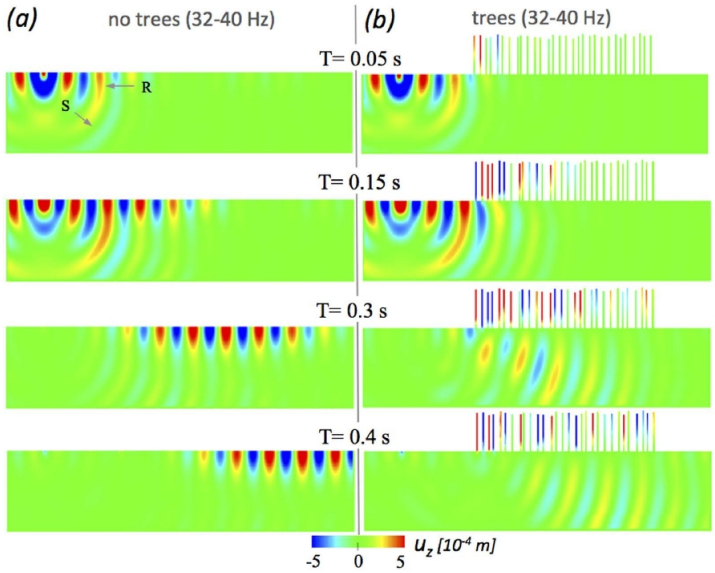

Figure 4.13: Results of the numerical simulations for the u_z component of the recordings at different times, and for two different set-ups: (a) half space without trees; (b) half space with trees. The recordings are filtered in the first bandgap. R and S indicate Rayleigh and S waves (Figure from [103]).

waves that are generated by the conversion of the Rayleigh waves into S waves,

occasionally propagate beneath the trees. As the polarization of these waves is horizontal, they do not interact with the compressional resonance of the trees, and hence they can propagate. This study confirms that trees in a forest form a locally resonant metamaterial that can interact with seismic surface waves. These results led to an experiment that was performed at the seismic scale, and is described in more detail in the following.

4.5.3 The METAFORET Experiment

The experiment conducted in the field is known as the 'METAFORET' experiment[1]. This unique experiment was aimed at investigating the potential efficiency of trees that are organized in a sub-wavelength configuration, in coupling with surface Rayleigh waves. This study is a pioneering one that might open up applications to seismic hazard. The resonance of the trees and their coupling with the surface waves can then be generalized to buildings and tall structures from the point of view of earthquake engineering and urban design.

The METAFORET experiment was implemented in October 2016 over 2 weeks in southwest France, in the Landes forest. It covers a surface of 120 m by 120 m, from which 90 m is a state-managed pine forest, and 30 m is an agricultural canola field (see Fig. 4.14).

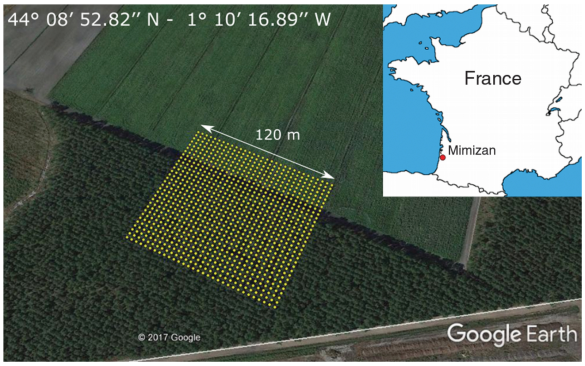

Figure 4.14: Aerial view of the METAFORET experiment with the forest and field. Yellow dots indicate the positions of the geophones deployed. Red circle in the inset marks the location of the experiment (Figure from [104]).

[1] A detailed description of the METAFORET project can be found at https://metaforet.osug.fr/.

The 2D Cartesian system is defined so that the x direction is parallel to the border between the field and the forest, and the y direction is perpendicular to this. The average distance between the trees is $\sim$ 2.5 m in the x direction, and 4 m in the y direction (see Fig. 4.15). Seismic receivers are geophones that were deployed on

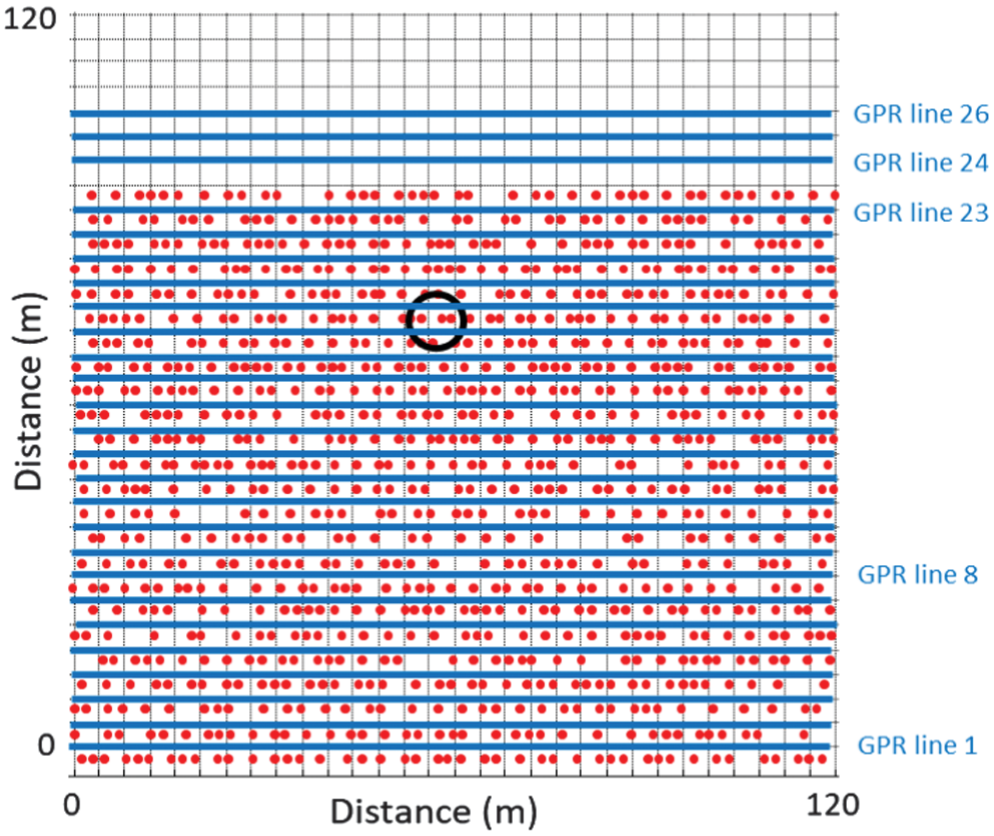

Figure 4.15: Distribution of trees (red dots) in the forest and lines of the GPR array (blue lines). The black circle marks the trees used to install the 3-component velocimeters. Nodes of the black background grid indicate the positions of seismic arrays deployed within the field and forest (Figure from [104]).

the nodes of the grid shown in Fig. 4.15. The inter-station distance was 4 m, which indicates deployment of 961 geophones within the area. The experiment includes both active and passive measurements. In the passive experiments, the geophones recorded the ambient noise over 2 weeks. In the active experiment, a shaker was used as an active source, and the responses were recorded at all 961 geophones. In the active experiments, two geophones were installed in two nodes close to the shaker, to record the emitted signal for further signal processing. The geophones

have a sampling frequency of 400 Hz and a lower corner frequency of 5 Hz. Apart from these one-component (vertical) geophones (Z-land instruments), there were also 100 3-component geophones (GIPP instruments) implemented in two different configurations: an array of 10 × 10 that was installed between the other geophone array, with an inter station distance of 4 m and the other one along a vertical line crossing the edge between the forest and the field, with 1-m inter-station distance. The source in the active experiments was a shaker of 70 kg that emitted a frequency-modulated sweep, where the frequency varied from 10 Hz to 100 Hz over 1 min. Each geophone recorded the waves excited by the emission of the source signal. The two geophones deployed in the vicinity of the shaker are of use here. The signals recorded by these geophones were considered as the emitted signal. The recordings at each sensor were cross-correlated with this emitted signal. The active source experiment

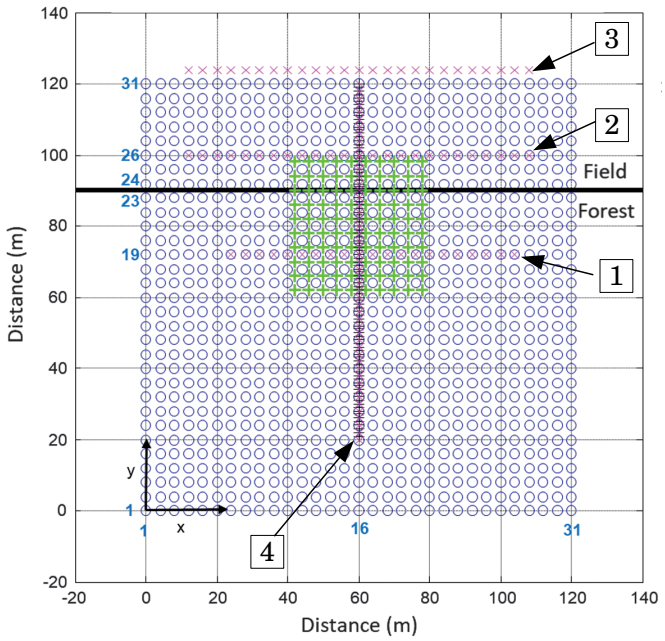

Figure 4.16: Distribution of the sensors and active shots in the METAFORET experiment. Circles mark the positions of vertical-component geophones. Pink crosses show the four active shots arrays. The '+' symbols (either black or green) mark the position of two configurations of 3-component geophones. The active shot arrays are numbered for further references (Figure modified after [104]).

was conducted along four lines, which are indicated as 1 to 4 in Fig. 4.16. Three

of these were located parallel to the boundary between the field and the forest, and the distance between the shots was 4 m. Each line of sources included 21 to 25 sources. The fourth configuration was arranged perpendicular to the boundary between the field and the forest, with 51 sources and 2 m distance between the shots. This configuration consists of sources both in the forest and the field. This line is the same line where the 3-component geophones were deployed. This configuration achieves an equivalent survey to the conventional ones in seismic surveys. As along this line the distance between the sensors was 1 m and the sources and receivers covered a straight line from the field to the forest, we can follow the propagation of waves traveling into the forest from the field (see Fig. 4.17).

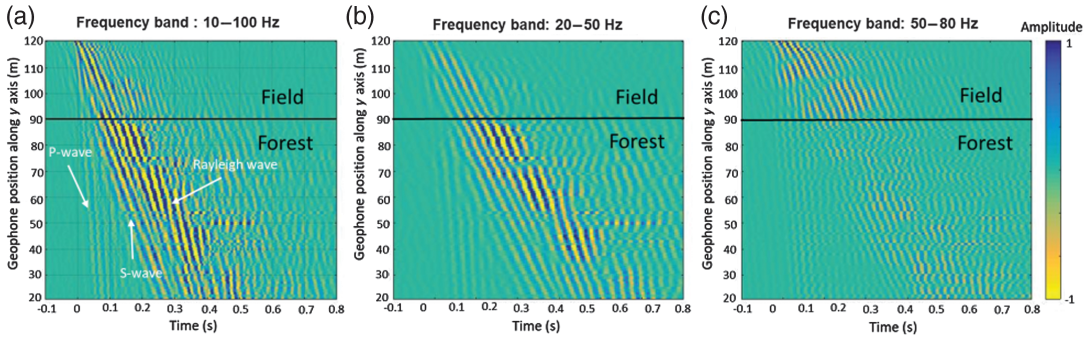

Figure 4.17: Time-space representation of the seismic field that was recorded along the dense array of three-component receivers implemented along a vertical line crossing the field-forest boundary. The source was a shaker located at x = 60 m and y = 120 m. The receivers extend from x = 60 m, y = 120 m to x = 60 m, y = 20 m. Different panels demonstrated this wave-field in terms of (a) raw data, (b) data filtered between 20 Hz and 50 Hz, and (c) data filtered between 50 Hz and 80 Hz (Figure from [104]).

From Fig. 4.17a, we can observe the emergence of three main wavefronts. The first is the P waves that have low amplitude and travel with a speed of $\sim$ 1000 m/s. Then the S waves arrive with slightly higher amplitudes, traveling with a speed of $\sim$ 400 m/s and finally Rayleigh waves arrive with a speed of about 350 m/s. The dispersive nature of these waves is observed. If we filter this raw data in two frequency bands, as below and above 50 Hz, we observe that waves with frequencies lower than 50 Hz penetrate into the forest, while at frequencies above 50 Hz, most

of the propagating Rayleigh waves are reflected at the boundary between the field and forest.

Fig. 4.18 is another representation of this observation, where the vertical wave-fields filtered below and above 50 Hz are shown at different times. The active source emits from inside the forest, and different snapshots show the propagation of the wave-field recorded by Z-land sensors.

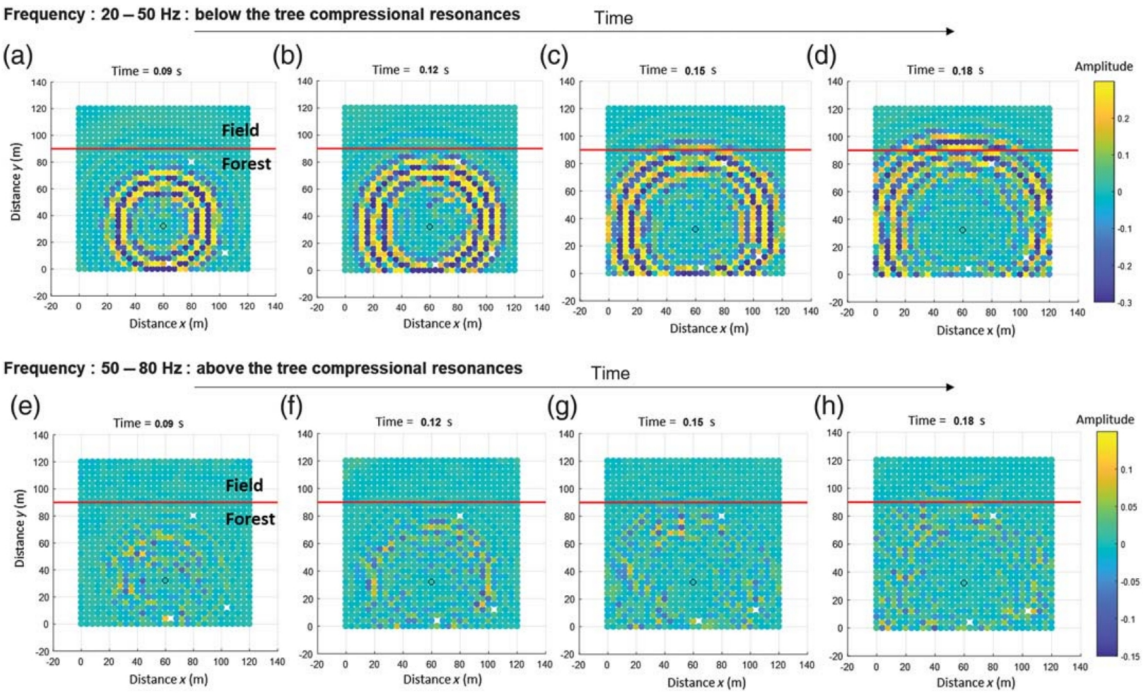

Figure 4.18: Measured seismic wave-field inside the forest on a 2D array of one-component Z-land receivers, with the excitation source at $x = 60$ m and $y = 30$ m (i.e., inside the forest). The temporal evolution of the wave-field filtered between 20 Hz and 50 Hz (a-d) and between 50 Hz and 80 Hz (e-h) are shown. The horizontal red line indicates the field-forest boundary (Figure from [104]).

Considering the trees as resonators that are distributed at sub-wavelength distances, and taking into account the possible metamaterial behavior of the forest, the coupling between the propagating waves and the resonances of the trees is the first scenario that comes to mind to explain the observed wave propagation. This is where the velocimeters came into play. In the METAFORET experiment, a series of three-component velocimeters were attached to the trunks of a few trees to investigate the interactions of the seismic wave-field with the trees. Velocimeters can provide

recordings below ∼5 Hz, which is the cut off frequency of one-component (Z-land) and three-component (GIPP) geophones. The measurements were done using both the ambient vibrations and the active sources. Two temporary experiments were performed: (1) A series of six velocimeters were installed in a tree located at the center of the METAFORET structure (Fig. 4.19). (2) A velocimeter was attached to six neighboring trees at 2.5 m above the ground (Fig. 4.15). These velocimeters recorded continuous 1-h data during experiments with the active source as well as during night time. Fig. 4.20a-c shows the normalized average frequency spectrum over a period of 12 h at night-time for two horizontal components (H_1 and H_2), which correspond to north and east directions, as well as the vertical component.

Figure 4.19: A tree with six three-component velocimeters attached to its trunk at different heights (Figure from [104]).

Gray curves are the result of averaging of Fourier spectrum over 12 hours of recording and the red curves correspond to averaging on trees. As we see from

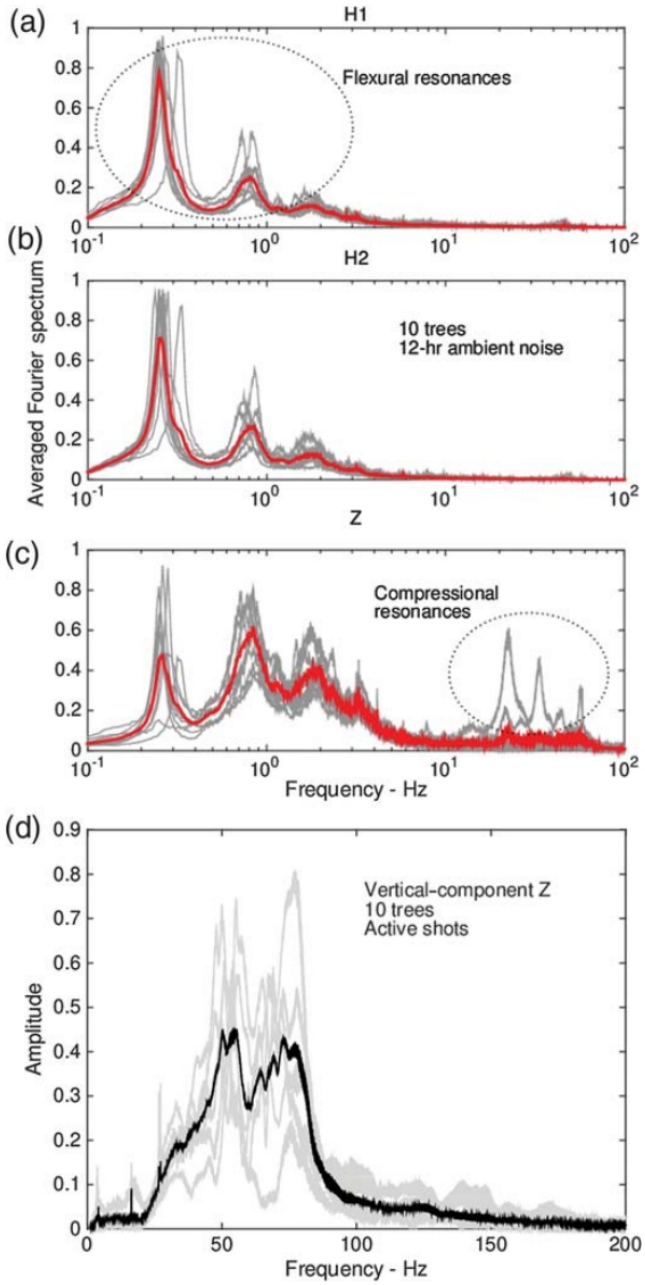

Figure 4.20: (a-c) Normalized Fourier spectra of the ambient recordings during a night with the instruments on the trees. H_1 and H_2 correspond to the radial and tangential directions with respect to the trunks of the trees; i.e., horizontal directions as well as vertical direction. Each gray curve is the result of averaging over 12 h of recordings, and the red curve is the average of the responses over the trees. (d) Vertical impulse response of 10 instrumented trees (in gray) during active shots, and the average of the responses over the trees (in black) (Figure from [104]).

Fig. 4.20a-b, three flexural resonances at frequencies of about 0.3, 0.9 and 2.0 Hz occur. Fig. 4.20c shows non-zero values for the Z component at frequencies that correspond to flexural modes. These are the modes that are present due to coupling with horizontal modes. At frequencies > 10 Hz, the dominating contribution in the spectra is the vertical motion. To zoom more on this behavior, we consider the vertical component of trees responses during an active source acquisition. This vertical response was obtained by deconvolving the responses recorded by the velocimeter according to the response recorded by a Z-land geophone deployed at the bottom of the tree. Ten responses and their averages are depicted in Fig. 4.20d. We observe that the frequency responses of the trees are between 40 Hz and 80 Hz, with a maximum at 50 Hz. So, the observed behavior above 50 Hz in Figs. 4.17 and 4.18 can be explained as: around 50 Hz, the trees compressional resonances couple with the vertical component of the Rayleigh surface waves, to result in a frequency band where the energy cannot propagate.

So far, we have seen the striking behaviors due to hybridization in a metamaterial that consisted of locally resonant elements at various scales and different set-ups. We saw the emergence of bandgaps, which can be explained through the coupling between the resonators and the corresponding component of the surface waves. In the following section, we describe the present study, which is closely related to what has been discussed so far in this chapter, and which will refer to or confirm some of these results through a different approach.

4.6 Cross-Correlation in a Metamaterial

In this section, we describe the present study. The objective was to determine the behavior of the cross-correlations in a medium of resonators. We also examined the potential of the cross-correlation process in the extraction of information related to the presence of a metamaterial in the medium. To do so, we used both laboratory and seismic data. The processing steps and the results are shown in the following.

4.6.1 Laboratory Experiment

We conducted an experiment on a thin plate in the ISTerre Laboratory in Grenoble. The experimental set-up (as shown in Fig. 4.21), was similar to that of [100]. This

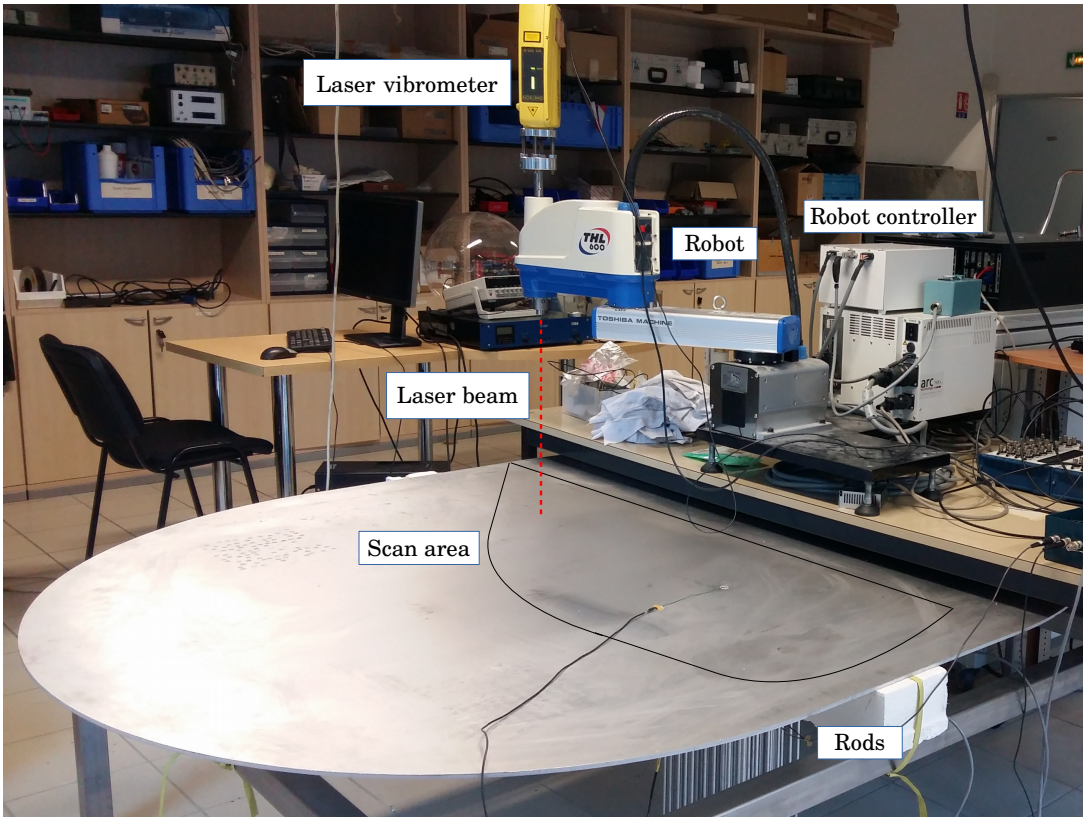

Figure 4.21: The experimental set-up, which consisted of an aluminum plate with 100 rods attached to its surface. There were five piezoelectric transducers glued to the surface of the plate. The field was scanned by a laser vibrometer.

set-up was based on an aluminum plate with the shape of Bunimovich stadium. The

dimensions of the 6-mm-thick plate were 2.0 m by 1.5 m. The plate was positioned horizontally, and five piezoelectric transducers were attached to its surface. These transducers acted as sources in these experiments and excited mostly the fundamental antisymmetric mode of Lamb waves (A_0) in the plate. The metamaterial region was built using 100 aluminum rods of 61 cm in length and 6.35 mm in diameter that were glued to the lower side of the plate, where the transducers were attached. The rods were attached so that they formed an ordered periodic structure. They covered a surface of approximately 324 cm^2 (square: 18 cm by 18 cm). The distance between the resonators was about 1.8 cm. The A_0 mode of Lamb waves has a typical speed of about 340 m/s at 2 kHz, which corresponds to a wavelength of 17.5 cm. Accordingly, the distance between the rods was $\sim \lambda/12$ and $\sim \lambda/4$ for A_0 mode at frequencies of 1 kHz and 9 kHz, respectively, which implies that this arrangement forms a structure of sub-wavelength order. As shown by [100] and explained in the previous section, this structure behaves as a locally resonant metamaterial.

Each transducer emits a linear chirp in the frequency band of 1000 Hz to 9000 Hz. The wave-field is scanned using a laser Doppler vibrometer positioned on the upper side of the plate, inside the area marked in Fig. 4.21. The scanning was performed on this area over a grid with 8 mm between consecutive scanned points in the x and y directions, leading to the total of 5888 scanned points. This scanned area was defined by taking into account the experimental limitations imposed by the robot that controlled the displacement of the laser vibrometer. The map of the scanned points and transducer positions are shown in Fig. 4.22.

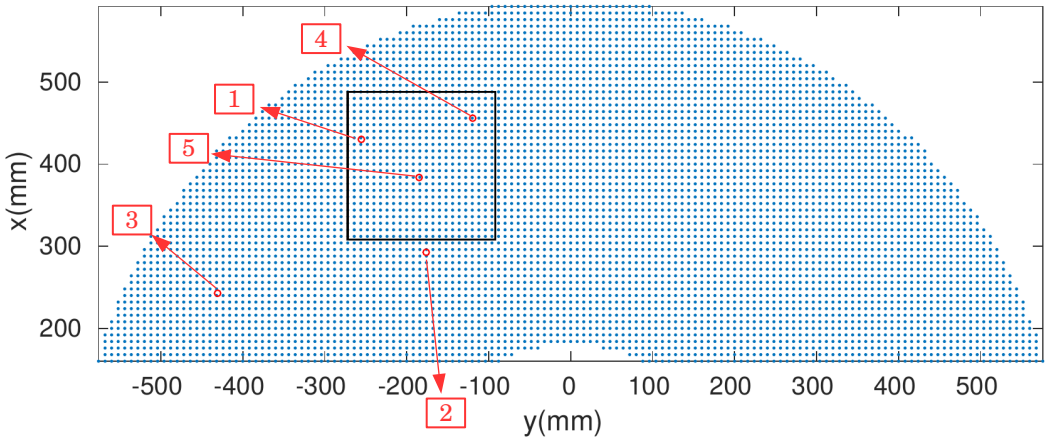

Figure 4.22: Map of the scanned points on the plate (blue dots) and the positions of five transducers (red circles), numbered from 1 to 5. Note that the plate itself is not shown here and the rectangle frame is plotted to give the coordinate of the points. The x and y directions are defined according to the movement of the robot for the scan. The black square marks the area where the locally resonant metamaterial is located.

4.6.1.1 Amplitude Spectrum of the Cross-Correlations of the Recordings

Our objective here is to study the behavior of the cross-correlations of the recordings at different frequency bands. In the following, we use the source-receiver reciprocity theorem (derived in chapter 2, section 2.2.1). In carrying out cross-correlations based on the source-receiver reciprocity, the transducers are considered as virtual receivers, and the scanned points as virtual sources. Thus, including five transducers in the set-up allows us to study the dependence of the results on the position of the virtual receivers with respect to the metamaterial region. We cross-correlate the recordings at a given pair of transducers (virtual receivers) and average the resulting cross-correlations over all possible virtual point sources. Examples of the amplitude spectra of the averaged cross-correlation ($C(t)$) obtained between the virtual receivers located in different positions with respect to the metamaterial region are shown in Fig. 4.23. Globally, we observe two drops in these spectra that correspond to two separate bandgaps, one between 2000 Hz and 3500 Hz, and the other between

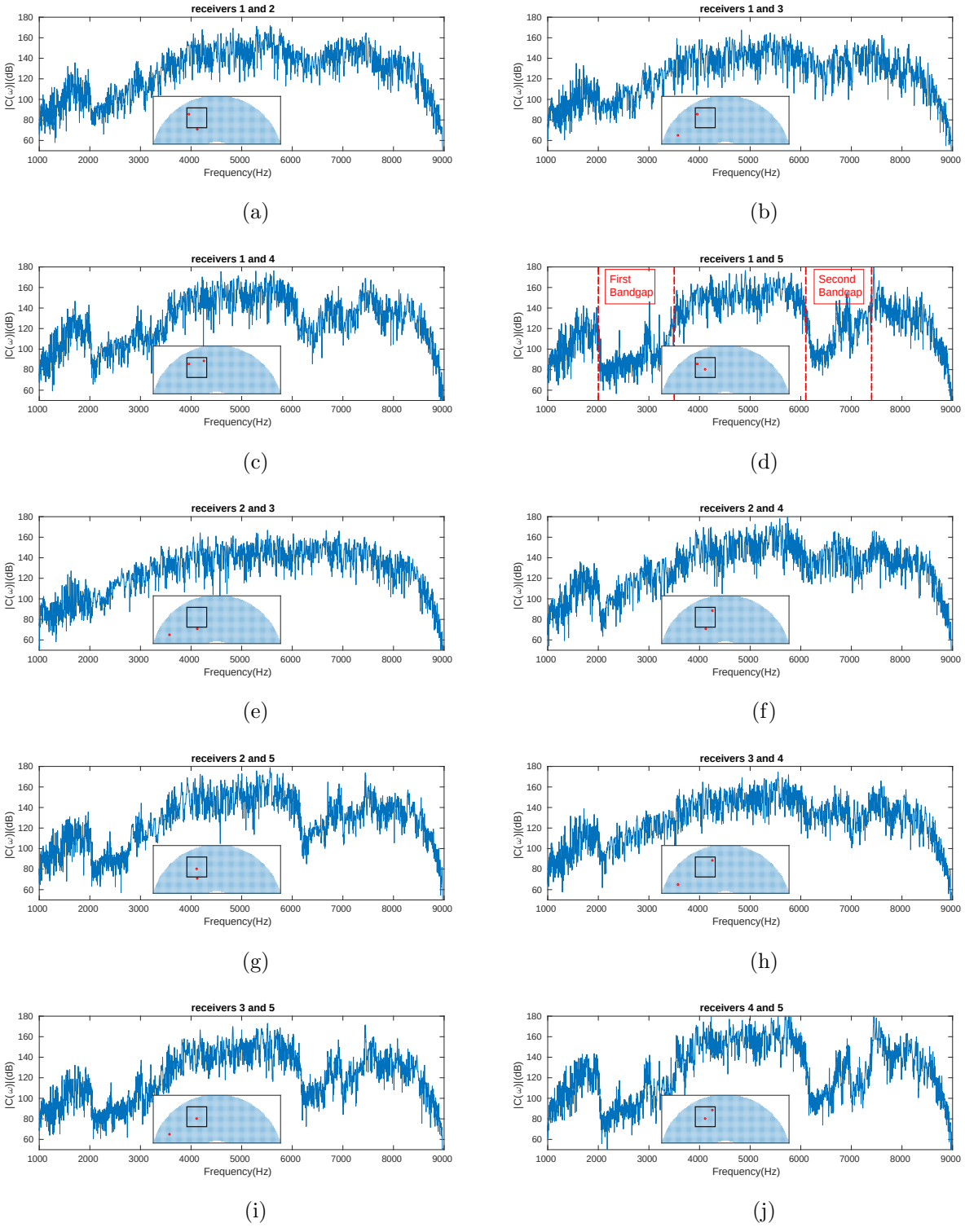

Figure 4.23: Amplitude spectra of the averaged cross-correlation (dB) over all of the possible virtual sources. Different panels correspond to different pairs of virtual receivers. Red circles mark the position of these virtual receivers.

6100 Hz and 7400 Hz (Fig. 4.23d, vertical dashed lines). These frequency bands match the frequencies of compressional resonances of an individual rod (Fig. 4.8c). As we saw in the previous section, the bandgaps in [100] were found by analyzing the field inside the metamaterial when the source was located outside. Since the analysis here is based on the amplitude spectrum of the averaged cross-correlations over all of virtual point sources and not on the individual recorded signals, we observe slightly different behaviors for the virtual receivers located in different positions with respect to the metamaterial. For example, once one of the virtual receivers is located inside the metamaterial region, the bandgaps at the above-mentioned frequency bands are more obvious (e.g., Fig. 4.23i). However, when both virtual receivers are located outside the metamaterial region, the bandgaps are not clear (e.g., Fig. 4.23e). The best configuration for recovering the bandgap is the one where the two transducers are located inside the metamaterial, as can be seen, for instance, in Fig. 4.23j. In general, we can see from all of the panels in Fig. 4.23 that the second bandgap is weaker than the first one, and hence it is less obvious to see in cases such as Fig. 4.23e. Adopting the cross-correlation technique, which involves an averaging over all of virtual point sources, motivated us to investigate the contributions of each virtual point source (both inside and outside the metamaterial region) in the cross-correlation within different frequency bands.

4.6.1.2 Spatial Map of the Virtual Source Contributions Based on Cross-Correlations

For a given pair of virtual receivers, we cross-correlate the recordings at these two receivers from each individual virtual point source, and normalize the cross-correlation function according to the energy of the individual signals involved in the cross-correlation, as for Eq. 2.29 in chapter 2. We keep the maximum value of this normalized cross-correlation and map it as a function of the virtual source position. This gives a measure of the contribution of each virtual source located at different positions with respect to the metamaterial in the final averaged cross-correlations. We start by considering the spatial map of the maximum of the normalized cross-correlation for the case where the two transducers are outside the metamaterial region. We filter the data before the cross-correlation in the frequency band of 6100 Hz to 6500 Hz, which is within the second bandgap (see Fig. 4.24).

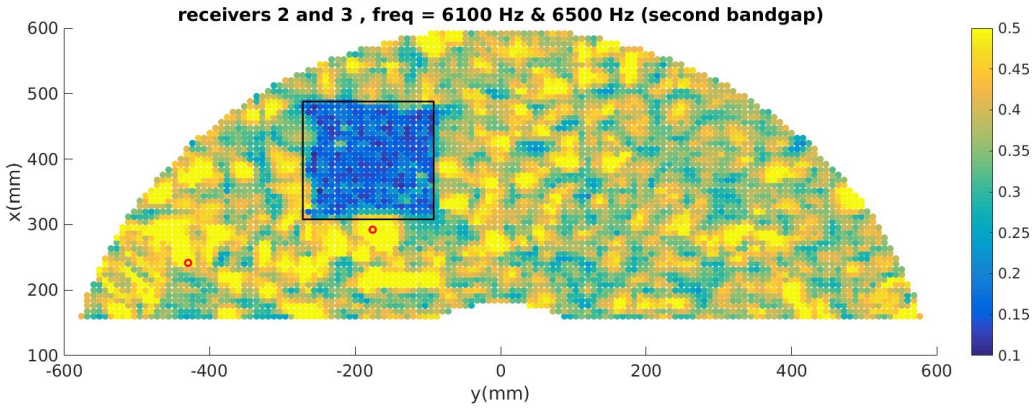

Figure 4.24: Spatial distribution of the maximum of the normalized cross-correlation of recordings at two virtual receivers (marked by red circles) from each virtual point source for data filtered within the second bandgap (between 6100 Hz and 6500 Hz) prior to cross-correlation. The black square marks the metamaterial region. Both of the virtual receivers are located outside the metamaterial.

We observe from Fig. 4.24 that the virtual point sources that contribute to the reconstruction of the Green's function in the bandgap between the two virtual receivers located outside the metamaterial are not the ones located inside the metamaterial region, while if we consider the same map for the frequencies corre-

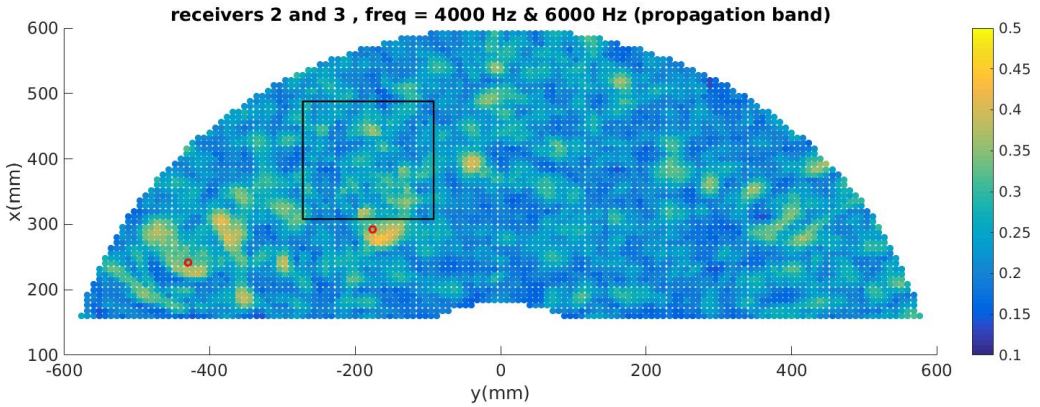

Figure 4.25: Similar to Fig. 4.24 for the frequencies within the propagation band (between 4000 Hz and 6000 Hz).

sponding to the propagation band, the contributions of the virtual point sources in the cross-correlations are approximately homogeneous throughout the plate, with the maximum contribution from the virtual sources that are close to the virtual receivers (see Fig. 4.25). We see that in the propagation band , it is not possible to distinguish any signs of the metamaterial. In other words, once the waves in the frequency band of 6100 Hz to 6500 Hz are excited inside the metamaterial region, they cannot propagate outside this region, and consequently their contribution in the reconstruction of the Green's function is almost null. However, the virtual sources outside this region contribute well to the retrieval of the Green's function. To validate this interpretation, we next move to the case where one of the virtual receivers is inside the metamaterial, and we repeat the analysis. The source contribution in the cross-correlation of the recordings is shown for different frequency bands (including first and second bandgaps, as well as the propagation band) in Fig. 4.26a-c for the case where one of the virtual receivers is inside the metamaterial area. Interestingly, we observe that for both bandgaps, most of the contribution is from the virtual sources that are close to the virtual receiver inside the metamaterial, and as we approach the borders of the metamaterial, the contribution of the virtual point sources decreases. Again, this means that at these frequency bands, if waves are excited outside the metamaterial, they cannot propagate inside the metamaterial region, and if they are excited inside this region, they are only received by very close

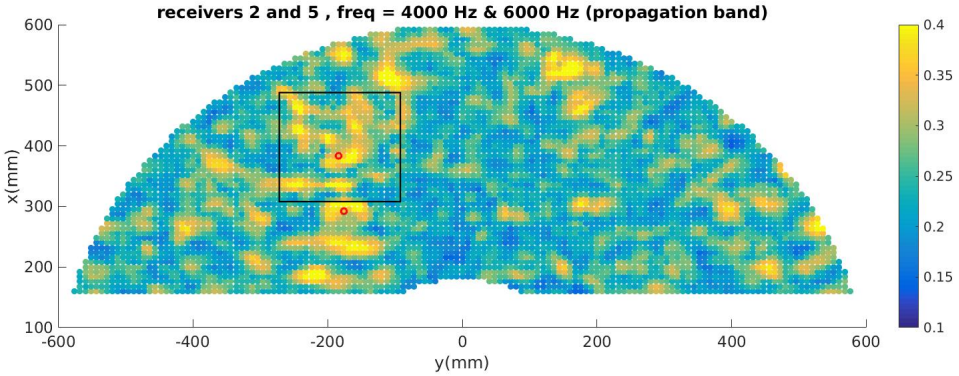

(a)

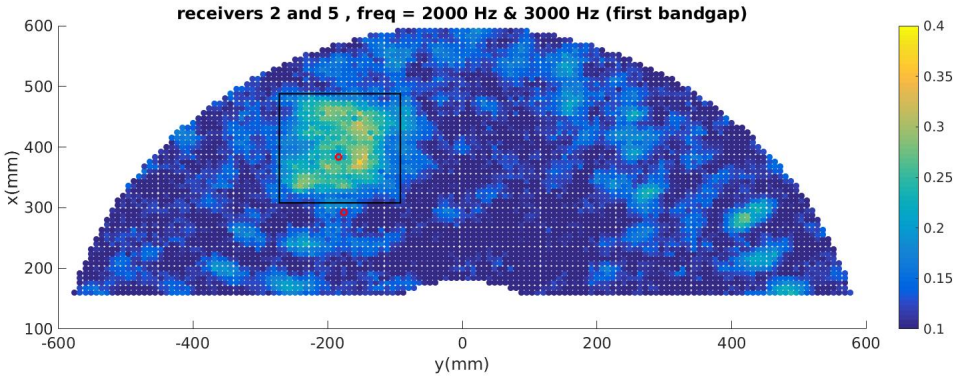

(b)

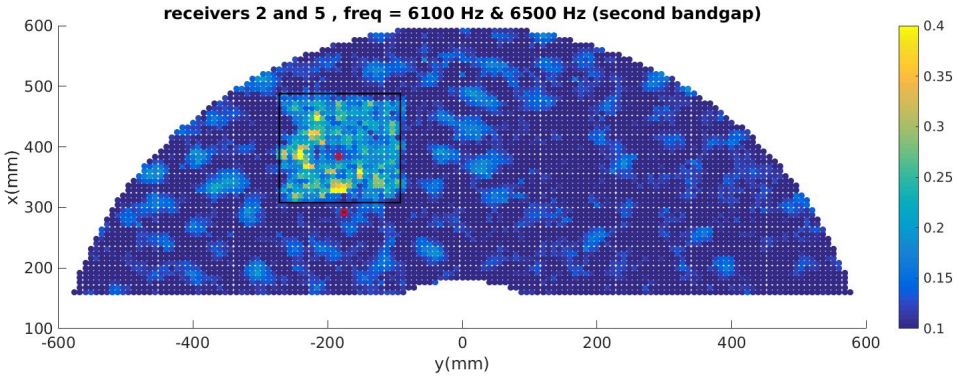

(c)

Figure 4.26: Spatial distribution of the maximum of the normalized cross-correlation of the recordings at two virtual receivers (marked by red circles) from each point source. The black square marks the metamaterial region. One of the virtual receivers is located inside the metamaterial, and the other one outside. (a) Propagation band. (b), (c) Within the first and second bandgaps, respectively.

receivers. As shown by [100], the wave-field measured within bandgaps received by receivers inside the metamaterial is not propagating waves, but evanescent waves. These waves have a non-negligible imaginary wavenumber, and their amplitude decays with distance. We checked this for another configuration of virtual receivers where one is inside and the other is outside the metamaterial region (see Fig. 4.27).

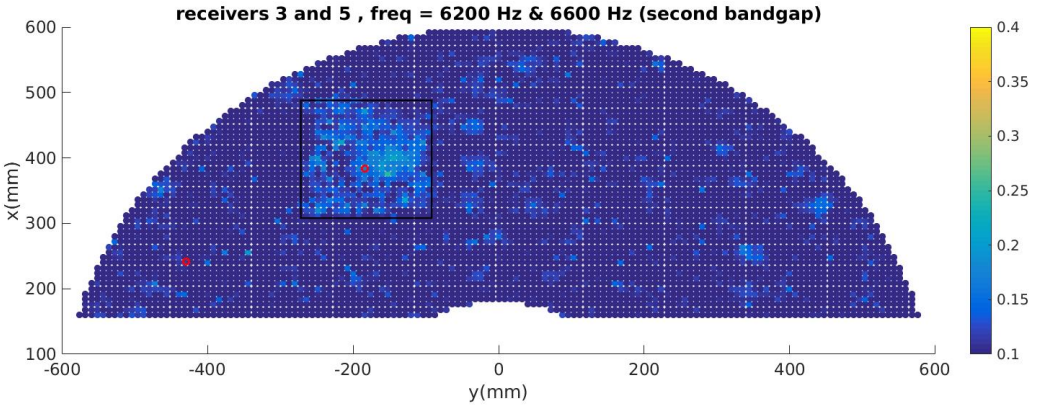

Figure 4.27: Similar to Fig. 4.24, but for a different pair of virtual receivers.

From Figs. 4.26b-c and 4.27, we see that once one of the virtual receivers is inside the metamaterial region, the spatial map of the highest contribution in the cross-correlation inside the bandgap has a more or less uniform pattern around the virtual receiver that is located inside the metamaterial, which is not the case as for the other virtual receiver that is outside the metamaterial region. We interpret this observation as evidence of the presence of evanescent waves. A detailed description of our interpretation based on the presence of the evanescent waves is given in Appendix A.

It is also helpful to look at the cross-correlation averaged over all of the possible virtual sources in each of the frequency bands and for each pair of virtual receivers. In the following, we show examples of the cross-correlations for the same pair of virtual receivers and at similar frequency bands to those shown in Figs. 4.24, 4.25, and 4.26.

The normalization of the cross-correlations is performed with respect to the maximum energy of each signal in the propagation band. This provides a better

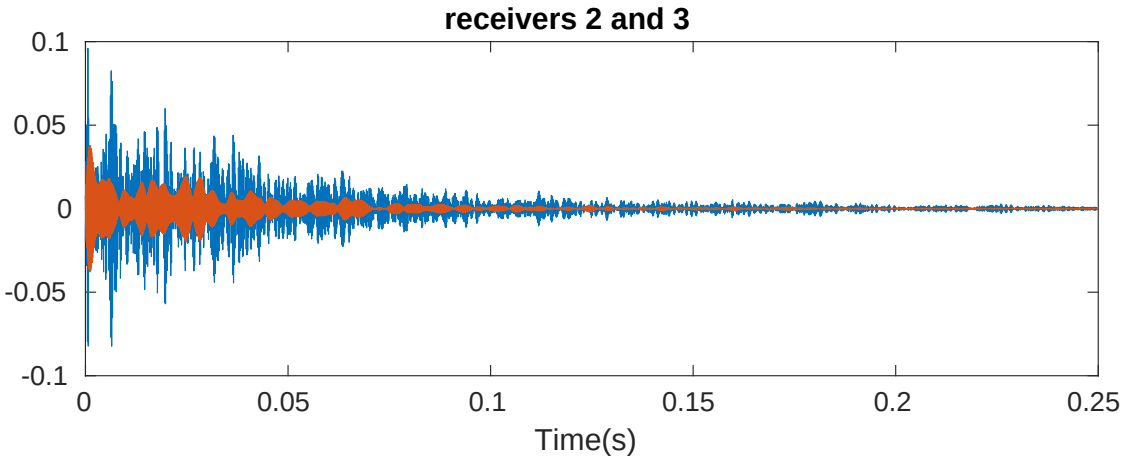

Figure 4.28: Cross-correlations of the data filtered between 4000 Hz and 6000 Hz in the propagation band (blue), and between 6100 Hz and 6500 Hz in the bandgap (orange), and averaged over all of the possible virtual point sources. Note that both transducers are outside the metamaterial region.

comparison of the respective amplitudes of the averaged cross-correlations for different frequency bands. From Fig. 4.28, we see the emergence of waves in both the propagation band and the bandgap. If we look at the same plot for the case where one of the virtual receivers is inside the metamaterial (same pair as Fig. 4.26), in the frequency bands that match Figs. 4.26a and 4.26c, we observe that in the bandgap the amplitude of the resulting averaged cross-correlation is very small compared to that obtained in the propagation band (see Fig. 4.29). Also, similar to the study of [100], we observe that the null amplitude of the signals in the bandgap is not only true for the direct arrivals, but is also true for the multiply reverberated part of the wave-field, known as the coda.

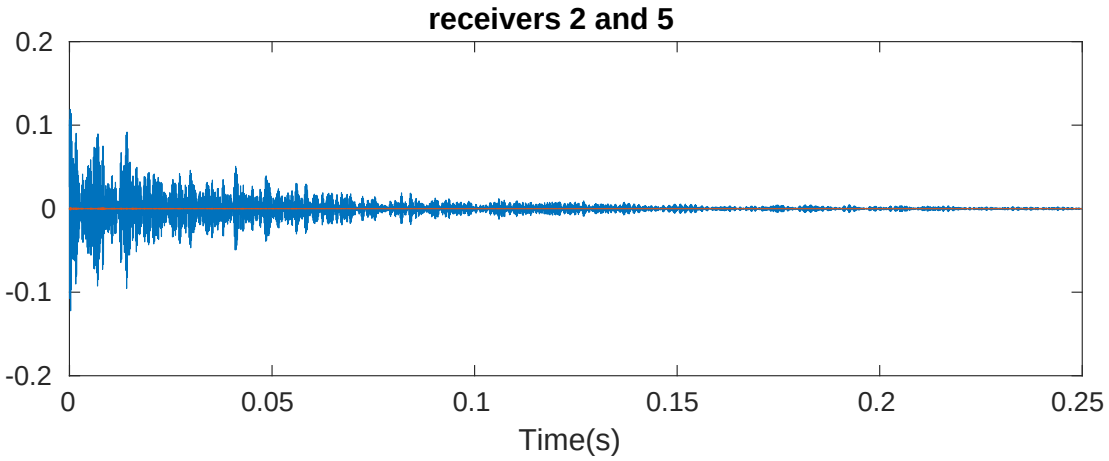

Figure 4.29: Cross-correlation of the data filtered between 4000 Hz and 6000 Hz in the propagation band (blue), and between 6100 Hz and 6500 Hz in the bandgap (orange), and averaged over all of the possible virtual point sources. Note that one virtual receiver is inside the metamaterial region, while the other is outside it.

4.6.1.3 Spatial Map of the Energy Distribution Based on Auto-Correlation (Virtual Receiver Inside the Metamaterial)

In this section, we base our analysis on the auto-correlation of the recordings. Similar to the previous section, we use the source-receiver reciprocity theorem, which means that we consider the transducers as virtual receivers and the scanned points as virtual sources. Applying the auto-correlation of the recordings corresponding to each virtual point source is a useful measure of the energy of the signals. We pick the transducer (virtual receiver) that is located inside the metamaterial, and auto-correlate the recordings from each virtual point source. We then keep the maximum value of the auto-correlation. This maximum is representative of the energy of the signal received at the virtual receiver location from each virtual source. We then map this value as a function of the position of the virtual source. In the following, we show these maps at different frequency bands for a virtual receiver that is inside the metamaterial area, and refer to this as the spatial energy distribution map (see Fig. 4.30). The frequency band of the filter is 200 Hz, and the consecutive panels in Fig. 4.30 show the transition in the received energy, starting from the propagation band, then entering the bandgap, and then entering the propagation band again. The data used in this analysis are obtained by scanning the surface of the plate over a smaller

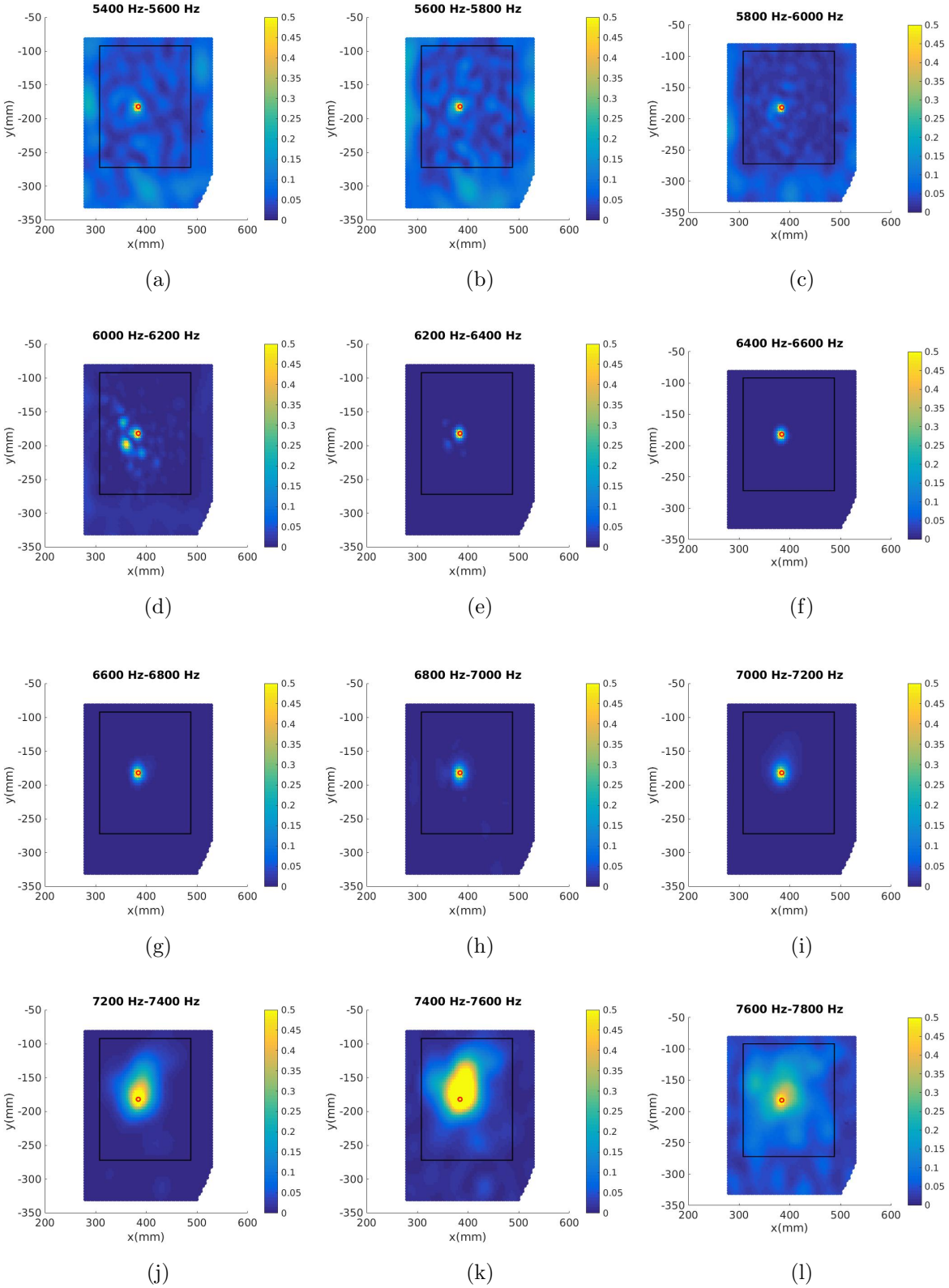

Figure 4.30: Spatial map of energy distribution at different frequency intervals, including the propagation band and the bandgap, for a virtual receiver located inside the metamaterial region.

area, but with a finer mesh grid (i.e., 4 mm in the x and y directions). That is why we only see part of the plate surface in Fig. 4.30, and not a large area as in Figs. 4.24 to 4.27. We observe from Fig. 4.30a-c that as we are in the propagation band, the maximum energy arrives from the neighboring points, although there is always some energy contribution from the points located outside the metamaterial. As we start to enter the bandgap at a frequency of about 6000 Hz (Fig. 4.30d), the contribution of the virtual sources located outside the metamaterial decreases drastically, until we enter the bandgap. Between 6200 Hz and 7400 Hz, no energy can be received from the virtual sources outside the metamaterial at this virtual receiver anymore, and only the surrounding points inside the metamaterial have a role (Fig. 4.30e-j). Once we enter the propagation band again, more points contribute to the energy distribution (Fig. 4.30k-l). At frequencies below the bandgap, the radius of this maximum energy region is much smaller compared to the radius in the frequencies above the bandgap. We interpret this observation as the sub-wavelength and supra-wavelength modes that can propagate due to the locally resonant metamaterial. In other words, these different patterns of the energy spots that are closely related to the wavelengths of the waves can be explained by hybridization effects. For the frequency band of 7200 Hz to 7400 Hz, we are approximately at the edge of the bandgap that corresponds to a smaller wavenumber compared to a free plate (i.e., the plate without rods). Consequently, a larger wavelength is observed. Another edge of the bandgap that corresponds to waves with larger wavenumber and hence smaller wavelength occurs at frequencies around 6000 Hz. This explains why the radius of the spot around the virtual receiver is smaller at frequencies below $\sim$ 6000 Hz, compared to those above $\sim$ 7200 Hz. The amplitude spectrum for the averaged auto-correlation over all of the virtual sources ($A(t)$) is shown in Fig. 4.31 for determining the bandgap and the propagation band. This is in agreement with what was demonstrated in the study of [100], which is shown here in Figs. 4.6a and 4.8a.

The propagation band and the bandgap are clearly observed here. If we focus on the frequency intervals corresponding to the bandgaps, we see that at certain frequencies within the first bandgap (around 2400 Hz, and close to 3000 Hz), there is transmission even though we are in the bandgap. Similar behavior is observed

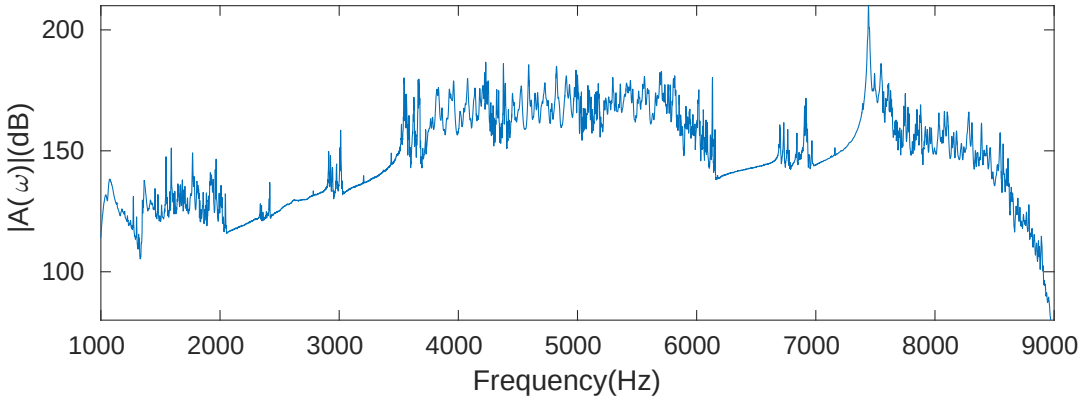

Figure 4.31: Amplitude spectrum of the averaged auto-correlations (dB) over all of the virtual point sources for a virtual receiver located inside the metamaterial region.

in the second bandgap around the frequency of 6800 Hz. We can also see this behavior in Fig. 4.23 although less clearly. This observation can be explained using Fig. 4.8c. We see that frequencies of 2400 Hz, 3000 Hz, and 6800 Hz match the flexural resonance frequency of the rods. We postulate that due to asymmetry in the geometry (i.e., the rods are attached to only one side of the plate), A_0 modes of the plate waves also contain a flexural component that couples with these flexural resonances, and hence leads to the transmission of these waves at these frequencies. In the following section, we extract more information on the metamaterial, still based on the spatial energy distribution.

4.6.1.4 Spatial Map of the Energy Distribution Based on Auto-Correlation (Virtual Receiver Outside the Metamaterial)

Similar to the previous section, here we are still interested in the energy of the signals extracted from the auto-correlation of the recordings. In contrast to the previous section, here we focus on a virtual source located outside the metamaterial region. To do so, we choose a transducer outside the metamaterial region, and plot the map of the energy distribution based on the maximum of the auto-correlation of the recordings filtered in consecutive frequency intervals of bandwidths of 200 Hz, starting at 5400 Hz, and ending at 7600 Hz. As we observe in Fig. 4.32, starting from the propagation band, the map is approximately homogeneous (Fig. 4.32a-

c). Once the bandgap starts, the contribution of energy from virtual point sources located inside the metamaterial region becomes almost zero (Fig. 4.32d-j). The region that corresponds to the minimum of energy matches the area covered by the rods very well. When the bandgap finishes and the propagation band starts again, some energy is received from all of the virtual sources on the plate (Fig. 4.32k-l).

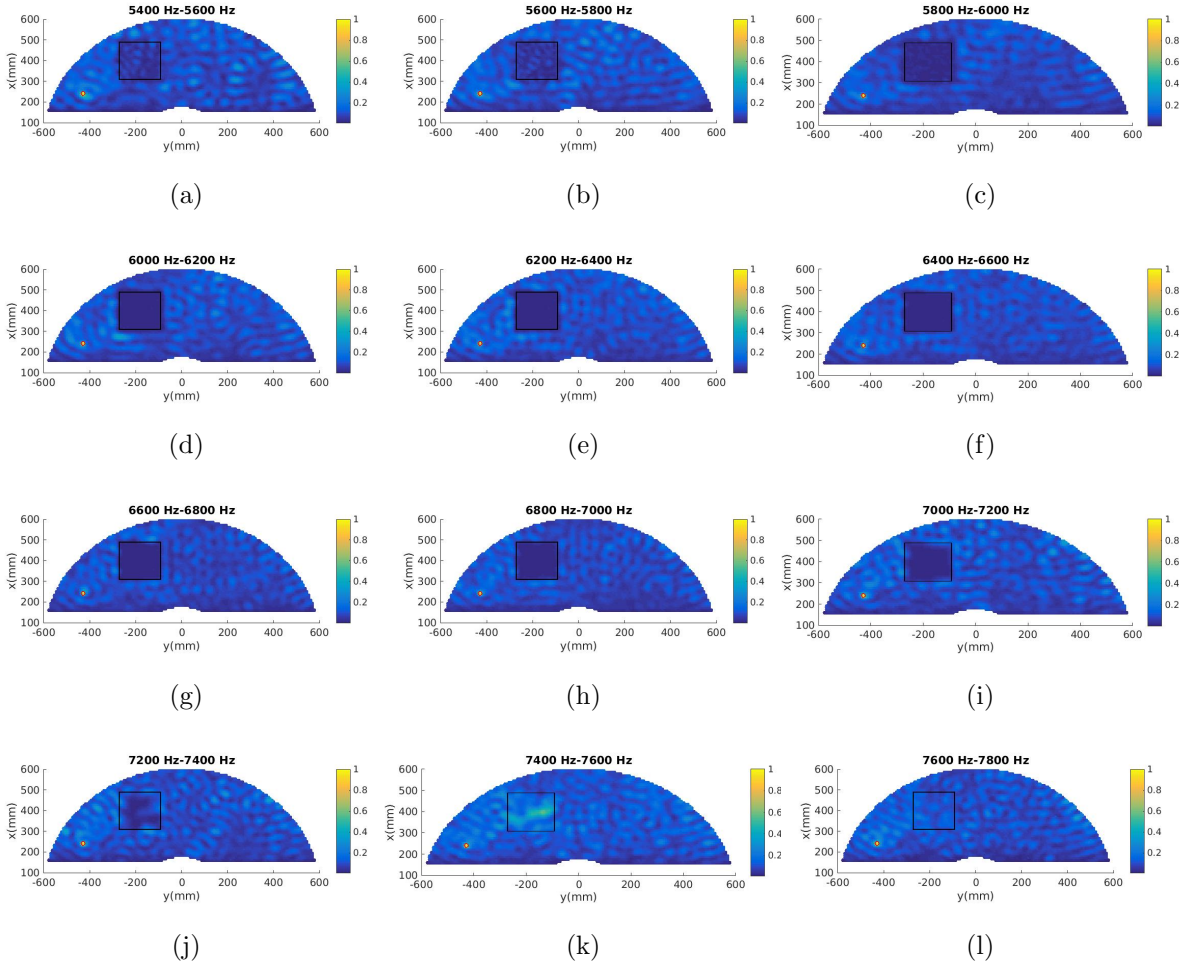

Figure 4.32: Spatial map of the energy distribution at different frequency intervals, including the propagation band and the bandgap, for a virtual receiver outside the metamaterial region. The black square marks the region of the metamaterial.

We conclude that by mapping the spatial energy distribution for a receiver that is outside the metamaterial, the bandgap and the metamaterial position on the plate can be retrieved. In the following, we apply a similar approach to the data collected from the METAFORET experiment.

4.6.2 METAFORET Experiment

In this section, we show the results obtained by processing data collected during the experiment explained in detail in section 4.5.3, known as the METAFORET experiment. We adopt an approach similar to that of the plate, where we provide the spatial map of the maximum of the normalized cross-correlations, referred to as the 'coherence'. We compute the coherence ($C_{xy}(t)$) between two given time signals $x(t)$ and $y(t)$ with energy $E(x(t))$ and $E(y(t))$ as:

$$C_{xy}(t) = \frac{x(t) \star y(t)}{\sqrt{E(x(t))E(y(t))}} \tag{4.22}$$

where $\star$ denotes the cross-correlation operator. In other words, we look for the cross-correlation of the signals normalized by the energy of each of the signals considered in the cross-correlation. We remind that the energy is obtained through time integral of the squared signal. Applying this normalization, we remove the biasing effects that can arise from the coupling between the shaker and the ground during the seismic experiment. Hence, we lose the information related to the amplitude, but we show that coherency provides useful information on the time dispersion of the signals. We use the source-receiver reciprocity (explained in detail in chapter two, section 2.2.1). We note that according to this theorem, the sources and receivers can be interchanged. Implementing this theorem, the points along the shot lines at this experiment are considered as virtual receivers, and the geophones as virtual sources. As shown in Fig. 4.16, there are four lines (1 to 4) along which the active shots were implemented. The distance between the geophones was 4 m in both the x and y directions. The distance between the sources was 4 m and 2 m along the horizontal and vertical lines of the active shots, respectively.

The difference between the METAFORET configuration and that of the laboratory plate is that we benefit from several 'receiver' pairs along each active shot line. This provides the opportunity to consider the averaged behavior of the coherency, where the averaging is applied over various pairs of virtual receivers.

4.6.2.1 Preliminary Results

For a given distance between a pair of virtual receivers along a given shot line, we compute the maximum of the coherence corresponding to each of the virtual

sources according to Eq. 4.22. We repeat this for the consecutive pair of virtual receivers that are separated by the same distance along the active shot line. In doing so, we finally take the average of all of the coherence values and plot the averaged maximum coherence values as a function of the virtual source position. We carry out this procedure for different frequency bands within the propagation band and the bandgap. The filter applied to the data is a bandpass 4th-order, of the Butterworth type with the bandwidth of 10 Hz. As the shot lines are located at different positions with respect to the area of study (i.e., inside the forest, along horizontal and vertical lines, and also outside the forest), we have the possibility to study various configurations depending on where the active shot line is located. In the following, we show some of the coherency maps along different lines and in different frequency bands. We start with shot line # 1 in Fig. 4.16, which includes 21 virtual receivers. In these maps, the positions of the virtual receivers are marked by red circles, and the red horizontal line highlights the end of the forest area. Each colored point on the coherency maps shows the average of the maximum value of the normalized correlation coefficient from a virtual source located at that point and averaged over all of the available virtual receivers separated by 20 m.

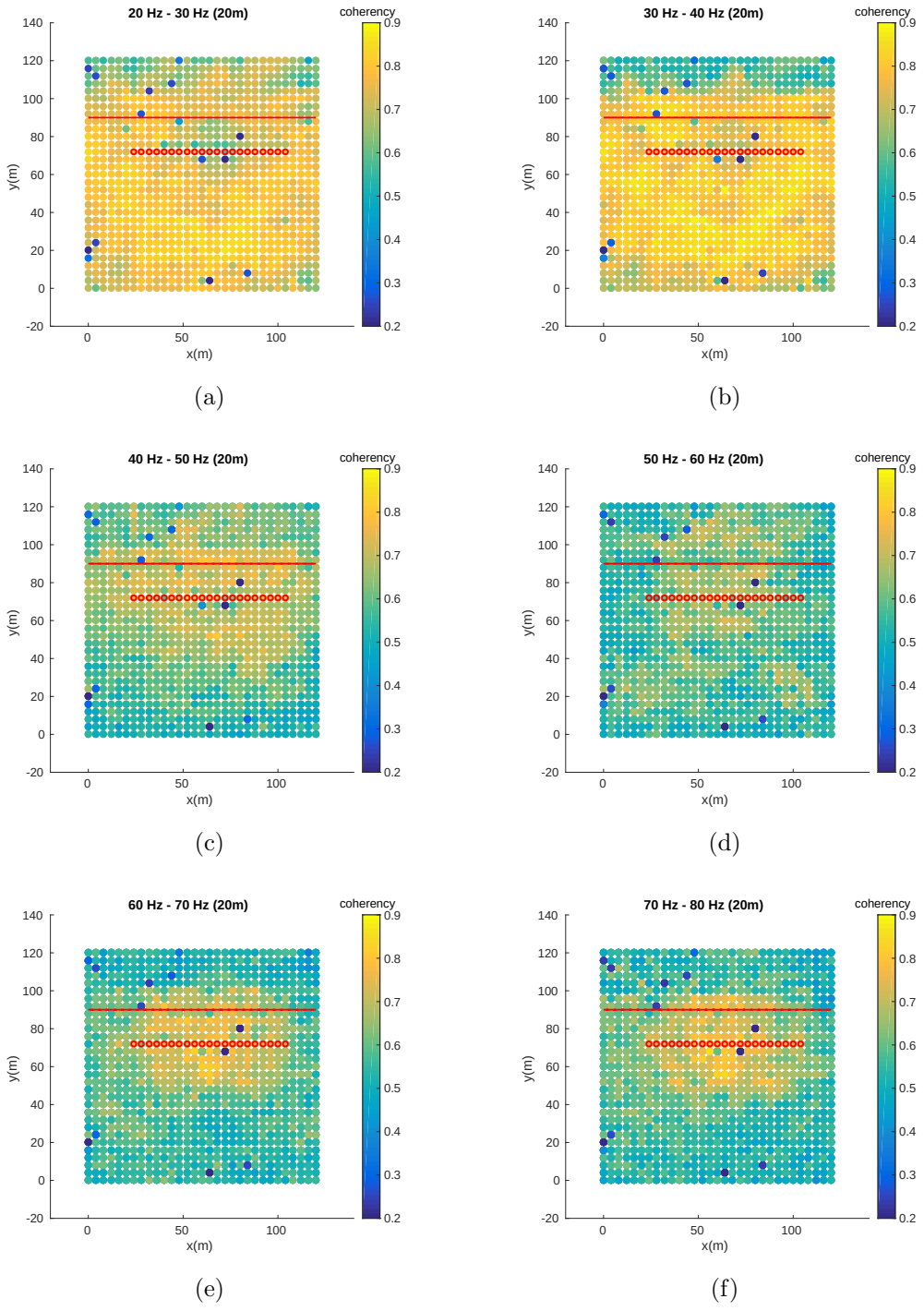

Figure 4.33: Spatial map of the average of the maximum of coherency received along a line of virtual receivers located horizontally inside the forest from the virtual sources distributed homogeneously in the field and the forest. The averaging over the maximum of coherency is performed for all of the possible virtual receiver pairs separated by 20 m. Panels (a) to (f) show these maps for the different frequency bands.

Fig. 4.33 shows the spatial distribution of the maximum of the coherence for the signals received from each virtual point source at two virtual receivers along the line shown by the red circles. The distance between two virtual receivers is kept fixed at 20 m, and these plots show the averaged value of the maximum coherency over all of the possible virtual receiver pairs at 20 m distance along the shot line at each frequency band.

We observe that the coherency of the received signals from a given virtual source is spatially homogeneous between 20 Hz and 30 Hz, with a high value of coherency. At 30 Hz to 40 Hz, the coherency is still high, with smaller values from the virtual sources located in the field. Between 40 Hz and 50 Hz, there is a remarkable drop in the coherency. We can note from Fig. 4.20 that this frequency band is very close to the band where there is a peak in the compressional resonance of the trees. So, this band can be considered as the edge of the bandgap where velocity varies rapidly according to the dispersion curve, which results in a decrease in the coherency of the waves. This decrease becomes even sharper between 50 Hz and 60 Hz. Between 60 Hz and 80 Hz, the maximum coherence increases again and the maximum of the coherency comes from the virtual sources that are near the virtual receivers. This can be interpreted as the presence of evanescent waves, which die rapidly due to their exponential decay, and can hence be captured only by the virtual receivers close to the virtual sources. Following the interpretation presented for these spatial maps of the maximum coherence, we can consider them as indirect measurements of the spreading of the signals. In the frequency bands where the scattering effects of the trees is significant, a longer and more dispersed signal is expected, compared to the frequency bands where there is no strong scattering. The stronger the scattering, the longer the waveforms. As we compute the coherency of the signals in a limited frequency band, there might be a less-scattered or more-scattered (and hence shorter or longer, respectively) signal compared to the inverse of the bandwidth of the applied filter. In other words, if the inverse of the bandwidth of the filter is larger than the dispersion of the signals (which itself is an indicator of the scattering in the medium), the resulting coherency is high. Since we keep the bandwidth fixed, the maps of the maximum coherency provide insight into the amount of dispersion of the signals, which is referred to as τ hereafter. To confirm this concept, we compute

the standard deviation of the signals based on their intensity in each frequency band averaged over all of the possible sources according to:

$$\tau^2 = \frac{\int I(t)t^2dt}{\int I(t)dt} - \left(\frac{\int I(t)tdt}{\int I(t)dt}\right)^2 \tag{4.23}$$

where I is the intensity of the signal. τ is a measure of the spreading of the signal intensity. In the following, we show the spatial maps of τ for different frequency bands averaged over all of the possible virtual receivers along the shot line.

Comparing the corresponding panels between Fig. 4.34 and Fig. 4.33, we observe that for a given frequency band, the virtual sources for which the maximum coherency is large match those for which the spreading time of the signals is smaller than the inverse of the bandwidth applied to the data (i.e., 0.1 s). For example, for the frequency interval between 50 Hz and 60 Hz, where the trees act as strong scatterers, more spread signals are expected due to the scattering. Virtual sources with a resulting $\tau < 0.1$ s (which is the width of the frequency filter in the time domain) are marked as dark blue to dark green. These points match the points of higher maximum coherency, which indicates that these points are less scattered than the points marked from dark green to yellow in Fig. 4.34. The yellow points in this map show a spreading time of around 0.2 s, which is interpreted to occur as a result of the scattering effects of the trees for the frequency band between 50 Hz and 60 Hz, for example. This longer spreading time is obviously observed more at points that are further from the virtual receivers, as they propagate for longer in the medium.

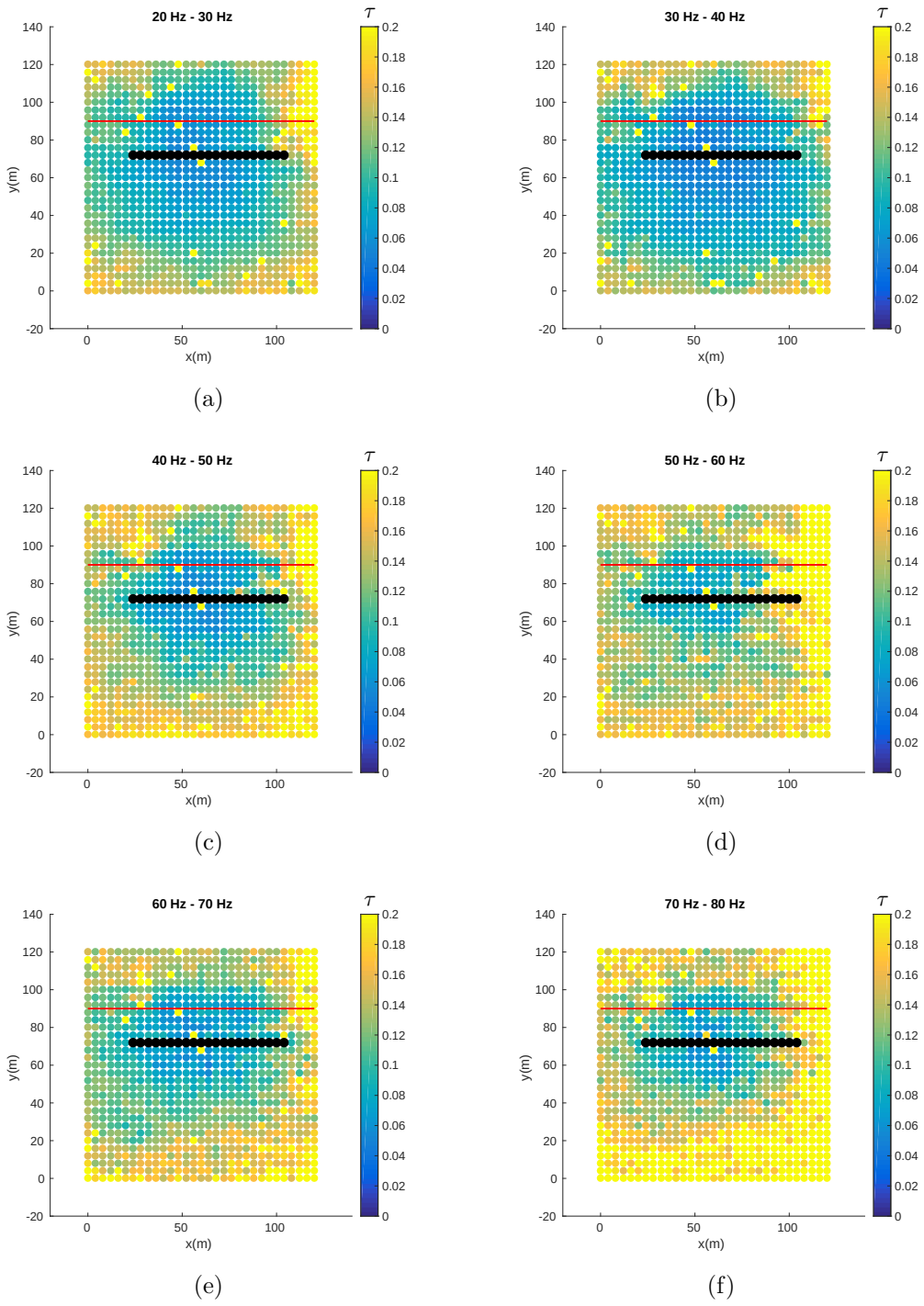

Figure 4.34: Spatial map of the spreading time of the signals (τ; in seconds) computed according to Eq. 4.23 along a horizontal line of virtual receivers inside the forest and from virtual sources that are arranged with regular spacing in the field and the forest and in different frequency bands. τ is averaged over all of the possible virtual receivers. Black circles mark the positions of the virtual receivers.

These observations are consistent, but we should also take into account the quality of the data, to determine whether a low coherence is due to a weak signal. To do so, we compute the signal-to-noise ratios (SNRs) of the signals for the different frequency bands, and average these over all of the virtual receivers. We observe that for all frequency bands, the SNR is above 30 dB even for the points that showed low coherence. This last confirms our interpretation of the observed coherency based on the spreading of the signal intensity. The spatial map of the SNR is shown in Appendix B.

We infer from the maps of maximum coherency that we can disentangle the propagation band and the bandgap based on the information provided by these maps. We clearly observed the effects of the trees and their scattering role for the case where the virtual receivers are inside the metamaterial region. As we have another line of virtual receivers in the forest (Fig. 4.16, shot line # 4), we repeat the measurements of the maximum of the coherency along this vertical line, to check whether the observations along line # 1 are confirmed. The spatial maps of coherency and time dispersion of the signals are shown in Appendix C.

Along the vertical line of virtual receivers in the forest, we observe a very similar pattern for the maximum of the coherency to that observed along the horizontal line in the forest, shown in Fig. 4.33. A spatially homogeneous maximum of coherency at frequencies between 20 Hz and 40 Hz that is followed by a drop in the coherency that marks the beginning of the bandgap and the low coherency remains with an inhomogeneous pattern at frequencies between 50 Hz and 60 Hz, which is an indicator of the bandgap. At higher frequencies (i.e., between 60 Hz and 80 Hz), we see high coherency coming from the virtual sources near the virtual receivers, which we interpret as the presence of evanescent waves.

The interpretations of the results obtained from the horizontal and vertical lines of the virtual receivers inside the forest are very similar to one another. We relate the observed drop in the coherency as a sign of the start of the bandgap, which is the result of the strong scattering effects of the trees. The trees in this experiment behave in a similar manner to the rods attached to the plate. In parallel, we relate these coherency values to the spreading of the signals, which is again an indicator of the scattering effect in the medium.

Our observations are confirmed by considering the map of maximum coherency along the active shot line that is in the canola field and outside the forest (Fig. 4.16, shot line # 3). The maps are shown in Appendix D.

As we are outside the forest, we do not expect to see the effects of the trees as clearly as in the case where the virtual receivers were inside the forest. We still observe high coherency coming from the forest at frequencies between 20 Hz and 30 Hz. The virtual sources that are in the forest and far from the virtual receivers give low coherence, which is due to a lower SNR. The maximum coherency then decreases, with lower coherence from the forest as we enter the bandgap around 50 Hz. Between 60 Hz and 80 Hz, the maximum coherency for this frequency range is lower than where the virtual receivers are inside the forest.

In summary, we have shown that cross-correlation and auto-correlation of the recordings are potentially useful to extract information for wave propagation in a metamaterial. We have applied this approach to data from laboratory experiments and to field data, with results that are consistent across both cases.

4.7 Conclusion

In this chapter, we addressed the problem of wave propagation inside a medium that includes locally resonant elements arranged at a sub-wavelength scale. The resulting structure, known as a metamaterial, shows particular features for the propagation of waves, which makes these structures potentially useful for different applications, including seismic hazard studies and earthquake engineering. The most highlighted feature related to the propagation of waves in such media occurs near the resonance frequency of the individual scattering elements, which can interact with one another and result in a frequency band where there is no propagation inside the region covered by these elements. These prohibited frequency bands of propagation are known as bandgaps, and they provide the opportunity to manipulate the wave propagation for different purposes. The sub-wavelength arrangement in such structures makes them more applicable at different scales compared to the bandgaps that occur due to Bragg scattering in ordered structures. We carried out various experiments similar to those previously implemented to better understand the behavior of such materials

and the coupling effects between the acoustic/seismic waves and the resonators.

For the present study, we conducted an experiment on a plate with a set of vertical rods that mimics a forest of resonators inside the medium. We adopted an approach based on the analysis of the cross-correlations of the recordings, to analyze the propagation of the waves. We also mapped the spatial distributions of the energy based on the auto-correlations of the recordings. The maps obtained based on both of these approaches were useful for localizing the metamaterial region as well as for defining the propagation bands and bandgaps. As for the seismic data, we used the data from the experiment conducted in 2016 in a region that consisted of a forest and a field (i.e., the METAFORET experiment). As our approach worked well for the laboratory data, we next applied it to the seismic data. We visualized the maximum values of the normalized cross-correlations (called the 'coherency') for the signals received at shot lines inside and outside the forest, and we averaged these over virtual receiver pairs separated by a given distance. We found a match between the behavior of these maps in the different frequency bands and the resonance frequency of the trees. We interpret our findings based on the scattering role of the trees and the spreading of the time signals, which is a mark of the presence of strong scattering in the medium. Our approach demonstrates the potential of trees for coupling with propagating waves, which can be used for manipulation of seismic wave propagation.

As one would expect, the results we obtain from the seismic data are not as clean as those obtained with the laboratory experiments. Processing the data of the METAFORET experiment is still an ongoing project, and it requires further studies, as there are still features and details that need to be more deeply understood.

Conclusion

Here, we recap the findings achieved in this dissertation and discuss the possible applications in seismology. In our work, the focus was on the problems linked to the retrieval of the transient response of the medium by cross-correlating the ambient recordings, a technique known as ambient-noise interferometry.

In the first part of our study (discussed in chapter 2), through conducting experiments on thin duralumin plates we showed that in reverberating media, the cross-correlation of recordings from spatially homogeneous and circular source distributions result in a very close convergence toward the transient response (also called the Green's function). This finding highlights the dominant role of reverberation in making the propagating wave-field diffuse so that the strong requirement of homogeneous source distribution can be relaxed. Focusing on the coda of the multiply-reverberated signals, first, we cross-correlated only the coda and quantified the similarity between the outcome of this cross-correlation and the Green's function. We found a very high similarity between the two. We observed that both the direct and coda parts of the Green's function can be retrieved by cross-correlating only the coda of the recordings. Second, zooming more on the coda, we cross-correlated a window in the coda and quantified the similarity between the resulting cross-correlation and the Green's function. We related the similarity to the statistical properties of the plate and the number of noise sources as well as the window length. On one side, when we cross-correlate a large window in the coda, similarity reaches to about $1/\sqrt{3}$ with a single source. On the other side, a perfect reconstruction can be obtained with a very small window but a uniform distribution of sources. Also, based on the modal decomposition, we showed the effect of a

non-deterministic noise (e.g., electronic noise) in the reconstruction of the Green's function.

In seismology, taking advantage of the diffusive character of coda of earthquakes, the cross-correlation has been applied to these multiply-reverberated waves. Scatterers in a multiple-scattering medium like the Earth, can be considered as secondary sources. These secondary sources result in the diffusivity of the wave-field and make the coda of earthquakes eligible to be cross-correlated in order to retrieve the Green's function. This part of our study is useful in such cases, as we evaluated the respective contribution of the direct arrivals and the coda in reconstruction of the Green's function.

In the second part of our study (described in chapter 3), we focused on a reverberating medium that includes scatterers. Our objective was to estimate the strength of the scatterer taking advantage of the high sensitivity of the coda to the variations in the medium. We focused on the coda of the Green's function that is retrieved passively, i.e., through cross-correlation of ambient recordings. The variations in the coda of the Green's function before and after the appearance of a scatterer and also before and after the displacement of the scatterer are tracked in time. We proposed a formalism to find the strength of the scatterer by fitting to this temporal variation which shows an exponential decay. Tracking temporal variations in the coda of the recordings or Green's function and extracting information taking advantage of the sensitivity of the coda to small changes in the medium, is what is done for monitoring purposes in seismology in volcanically and/or tectonically active regions. In this approach which is known as Coda Wave Interferometry (CWI), travel time variations are known to be the reason for changes in the coda. Our method which aims to find the scattering strength of the scatterer embedded in a reverberating medium is an intermediate step between CWI where dynamics of the medium is of interest and LOCADIFF where information on the scatterer itself is probed in a multiple scattering medium. Coda in a reverberant medium has already been used in Diffuse Reverberant Acoustic-Wave Spectroscopy (DRAWS) to find the properties of the moving scatterers. Here, for the first time we used DRAWS for dispersive

waves and followed the variations in the coda of the Green's function due to the appearance of the scatterer in the medium and not only due to its displacement. Our results suggest the applicability of passive Diffusive Wave Spectroscopy in the Earth sciences.

In the last part of this dissertation (discussed in chapter 4), we extended the case of the medium with scatterers to the case where there are several resonating scatterers introduced in the medium and organized at a sub-wavelength order. We studied for the first time the behavior of the cross-correlation of the recordings in different frequency bands in such materials. We started with a small-scale laboratory experiment. The configuration built in the laboratory consisted of a set of vertical steel rods attached to a thin plate with sub-wavelength distance between them. We analyzed the cross-correlation and auto-correlation of the recordings in different frequency bands and caught some behaviors that are well explained based on the regimes corresponding to propagation band and forbidden band. We also processed seismic data adopting the same approach (i.e., cross-correlation of the signals). In the experiment known as 'METAFORET', the influence of the resonance of trees on propagation of Rayleigh waves is studied. This experiment paves the way for better understanding of metamaterials behavior for their further application in seismic hazard domain. We found out that both laboratory and METAFORET experiments showed typical behaviors of bandgap metamaterials where some frequencies corresponding to the compressional resonance of trees/rods are attenuated and cannot propagate in the area covered by resonators. The observed behavior of spatial maps of energy (based on auto-correlation of signals) and maximum of coherence (based on cross-correlation of the signals) provided information on the propagation of waves in these media at different frequency bands. Our results were consistent with the ones obtained through different approaches in previous studies. This proves the reliability of cross-correlation of recordings in carrying information that can be used for locating the region within the medium that is consisted of locally resonant scatterers as well as identifying different regimes of propagation. Determining the position of metamaterial region and frequency intervals corresponding to bandgap are essential

for further manipulation of the waves depending on the application. Processing the METAFORET data is still ongoing and deeper understanding of the structure of the area and velocity profiles of the region have to be taken into account in order to interpret some of the observations.

Supplemental Material

Abstract

This manuscript contains the calculations of the similarity coefficients for the two cases discussed in chapter 2. The detailed derivation of the similarity to the best-obtained cross-correlation is provided for two different cases: first, when one signal is cut in time prior to the cross-correlation; and secondly, when the effect of instrumental noise is considered in the cross-correlation. We also compute in details the spatial correlation of the squared eigenmodes for two different geometries which appear in the first two sections. Next, we added a table to show the position of the transducers on the plate used for conducting the experiments described in chapter 2. The last part of this material demonstrates the computation of the maximum time that needs to be considered when fitting to the decay of the similarity coefficient curves in time. This fitting step is a necessary step in finding the scattering cross section of a scatterer.

I Time-Limited Cross-Correlation and Convergence toward the Best Cross-Correlation

I.I Relationship between Similarity Coefficient and Variance

We look for the similarity coefficient between the cross-correlation that is obtained by cross-correlation of the two full-time signals averaged over all of the possible point sources ($C_\infty(\mathbf{r}_l^R, \mathbf{r}_{l'}^R, t)$), and the one that is obtained by cross-correlation of a full signal with a windowed one and averaged over a subset of sources ($C_N^{dT}(\mathbf{r}_l^R, \mathbf{r}_{l'}^R, t)$). Here, the subscript and superscript denote the number of sources and the length of

the window considered in the cross-correlation, respectively. We write the similarity coefficient between $C_\infty(\mathbf{r}_l^R, \mathbf{r}_{l'}^R, t)$ and $C_N^{dT}(\mathbf{r}_l^R, \mathbf{r}_{l'}^R, t)$ according to the definition of the Pearson correlation coefficient,

$$S(C_\infty, C_N^{dT}) = \frac{\int \left\langle C_N^{dT}(\mathbf{r}_l^R, \mathbf{r}_{l'}^R, t) C_\infty(\mathbf{r}_l^R, \mathbf{r}_{l'}^R, t) \right\rangle dt}{\sqrt{\int \left\langle (C_N^{dT}(\mathbf{r}_l^R, \mathbf{r}_{l'}^R, t))^2 \right\rangle dt} \sqrt{\int \left\langle (C_\infty(\mathbf{r}_l^R, \mathbf{r}_{l'}^R, t))^2 \right\rangle dt}}. \tag{I.1}$$

We measure $S(C_\infty, C_N^{dT})$. However, on the other hand, as an intermediate step, to analytically estimate $S(C_\infty, C_N^{dT})$, we introduce the fluctuation of C_N^{dT} as

$$C_N^{dT}(\mathbf{r}_l^R, \mathbf{r}_{l'}^R, t) \triangleq \mathscr{C}(\mathbf{r}_l^R, \mathbf{r}_{l'}^R, t) + \delta C_N^{dT}(\mathbf{r}_l^R, \mathbf{r}_{l'}^R, t) \tag{I.2}$$

where $\mathscr{C}(\mathbf{r}_l^R, \mathbf{r}_{l'}^R, t)$ is the cross-correlation obtained by windowing one signal and averaging over a large number of sources and δC_N^{dT} is the fluctuation around this value. As both $\mathscr{C}(\mathbf{r}_l^R, \mathbf{r}_{l'}^R, t)$ and $C_\infty(\mathbf{r}_l^R, \mathbf{r}_{l'}^R, t)$ are proportional to the same function $ImG(\mathbf{r}_l^R, \mathbf{r}_{l'}^R, t)$, it is straightforward to show that

$$S(C_\infty, C_N^{dT}) = S(\mathscr{C}, C_N^{dT}) \tag{I.3}$$

Substituting Eq. I.2 into Eq. I.1, the similarity coefficient $S(\mathscr{C}, C_N^{dT})$ can be expressed as:

$$S(\mathscr{C}, C_N^{dT}) = \frac{1}{\sqrt{1 + \frac{\int <\delta C_N^{dT}(\mathbf{r}_l^R, \mathbf{r}_{l'}^R, t)^2> dt}{\int <\mathscr{C}(\mathbf{r}_l^R, \mathbf{r}_{l'}^R, t)^2> dt}}} = \frac{1}{\sqrt{1+Y}} \tag{I.4}$$

where Y is $\frac{\int <\delta C_N^{dT}(\mathbf{r}_l^R, \mathbf{r}_{l'}^R, t)^2> dt}{\int <\mathscr{C}(\mathbf{r}_l^R, \mathbf{r}_{l'}^R, t)^2> dt}$. As a consequence, the estimation of $\mathscr{C}(\mathbf{r}_l^R, \mathbf{r}_{l'}^R, t)$ and $\delta C_N^{dT}(\mathbf{r}_l^R, \mathbf{r}_{l'}^R, t)$ leads to $S(C_\infty, C_N^{dT})$.

I.II Modal Expression of the Correlation Function

The Green's function ($G(\mathbf{r}_l^R, \mathbf{r}_k^S, t)$) expanded in terms of eigen modes ($\phi_n(\mathbf{r})$) and eigen frequencies (ω_n) is written as follows in the frequency domain:

$$G(\mathbf{r}_l^R, \mathbf{r}_k^S, \omega) = \frac{1}{\rho_s} \sum_n \frac{\phi_n(\mathbf{r}_k^S)\phi_n(\mathbf{r}_l^R)}{(\omega^2 - \omega_n^2) - 2j\omega\alpha_n}. \tag{I.5}$$

where α_n is half of the inverse of the decay time of each mode, ρ_s is the surface density, and $\mathbf{r}_k^S$ and $\mathbf{r}_l^R$ are the kth source position and the lth receiver position, respectively.

This modal representation in the time domain is expressed as

$$G(\mathbf{r}_l^R, \mathbf{r}_k^S, t) = \frac{1}{\rho_s} \sum_n \frac{\phi_n(\mathbf{r}_k^S)\phi_n(\mathbf{r}_l^R)}{\omega_n} \exp(-t\alpha_n) \sin(\omega_n t). \tag{I.6}$$

What we use as data for the cross-correlation associated to a specific receiver $\mathbf{r}_l^R$ is

$$d(\mathbf{r}_l^R, \mathbf{r}_k^S, t) = G(\mathbf{r}_l^R, \mathbf{r}_k^S, t) \otimes f(t) \tag{I.7}$$

where $f(t)$ is the convolution of the source signal ($f_c(t)$) with its time reversed: $f(t) = f_c(t) \otimes f_c(-t)$. We will have similar data for the second receiver $\mathbf{r}_{l'}^R$, but what we use as the input for computation of the cross-correlation associated to this receiver is this data cut in time, i.e.,

$$d(\mathbf{r}_{l'}^R, \mathbf{r}_k^S, t) = \left[G(r_{l'}^R, \mathbf{r}_k^S, t) \otimes f(t)\right] W(t) \tag{I.8}$$

where $W(t)$ is the window function. The cross-correlation of these two reads as:

$$C(\mathbf{r}_l^R, \mathbf{r}_{l'}^R, t) = \sum_{k=1}^{N} G(r_l^R, \mathbf{r}_k^S, -t) \otimes f(-t) \otimes d(r_{l'}^R, \mathbf{r}_k^S, t) \tag{I.9}$$

where $\otimes$ is the convolution operator.
Substituting $d(\mathbf{r}_{l'}^R, \mathbf{r}_k^S, t)$ gives

$$C(\mathbf{r}_l^R, \mathbf{r}_{l'}^R, t) = \sum_{k=1}^{N} G(\mathbf{r}_l^R, \mathbf{r}_k^S, -t) \otimes f(-t) \otimes \left(\left[G(\mathbf{r}_{l'}^R, \mathbf{r}_k^S, t) \otimes f(t)\right] W(t)\right) \tag{I.10}$$

When the duration of $f(t)$ is much smaller than the length of the window, it is possible to commute $f(t)$ and $W(t)$.

$$C(\mathbf{r}_l^R, \mathbf{r}_{l'}^R, t) \approx \sum_{k=1}^{N} G(\mathbf{r}_l^R, \mathbf{r}_k^S, -t) \otimes f(-t) \otimes \left(G(\mathbf{r}_{l'}^R, \mathbf{r}_k^S, t) W(t)\right) \otimes f(t) \tag{I.11}$$

We denote $f(-t) \otimes f(t)$ as $f'(t)$. Using the definition of convolution

$$C(\mathbf{r}_l^R, \mathbf{r}_{l'}^R, t) \approx \left[\sum_{k=1}^{N} \int G(\mathbf{r}_l^R, \mathbf{r}_k^S, \tau - t) G(\mathbf{r}_{l'}^R, \mathbf{r}_k^S, \tau) W(\tau) d\tau\right] \otimes f'(t) \tag{I.12}$$

From now on, we concentrate on what we have between the brackets, and we represent this as $C_N^{dT}(\mathbf{r}_l^R, \mathbf{r}_{l'}^R, t)$.

$$C_N^{dT}(\mathbf{r}_l^R, \mathbf{r}_{l'}^R, t) = \sum_{k=1}^{N} \int G(\mathbf{r}_l^R, \mathbf{r}_k^S, \tau - t) G(\mathbf{r}_{l'}^R, \mathbf{r}_k^S, \tau) W(\tau) d\tau \tag{I.13}$$

By substituting G from Eq. I.6

$$C_N^{dT}(\mathbf{r}_l^R, \mathbf{r}_{l'}^R, t) = \frac{1}{\rho^2} \sum_{k,n,n'} e^{t\alpha_{n'}} \int \frac{\phi_{n'}(\mathbf{r}_k^S)\phi_{n'}(\mathbf{r}_l^R)}{\omega_{n'}} \frac{\phi_n(\mathbf{r}_k^S)\phi_n(\mathbf{r}_{l'}^R)}{\omega_n} \cdot e^{-\tau(\alpha_n+\alpha_{n'})} \sin(\omega_n\tau) W(\tau) \sin(\omega_{n'}[\tau - t]) H(\tau - t) d\tau \tag{I.14}$$

Then we use a trigonometry identity. Hence, Eq. I.14 becomes

$$C_N^{dT}(\mathbf{r}_l^R, \mathbf{r}_{l'}^R, t) = \frac{1}{2\rho^2} \sum_{k,n,n'} e^{t\alpha_{n'}} \int \frac{\phi_{n'}(\mathbf{r}_k^S)\phi_{n'}(\mathbf{r}_l^R)}{\omega_{n'}} \frac{\phi_n(\mathbf{r}_k^S)\phi_n(\mathbf{r}_{l'}^R)}{\omega_n} e^{-\tau(\alpha_n+\alpha_{n'})} \cdot W(\tau) H(\tau - t) \left[\cos(\omega_{n'}t + (\omega_n - \omega_{n'})\tau) - \cos((\omega_n + \omega_{n'})\tau - \omega_{n'}t)\right] d\tau \tag{I.15}$$

We now divide this Equation into the separate summations, where $n = n'$ and $n \neq n'$.

$$\begin{aligned} C_N^{dT}(\mathbf{r}_l^R, \mathbf{r}_{l'}^R, t) &= \frac{1}{2\rho^2} e^{t\alpha_n} \int W(\tau) H(\tau - t) e^{-2\tau\alpha_n} d\tau \sum_{k,n} \cos(\omega_n t) \frac{\phi_n^2(\mathbf{r}_k^S)\phi_n(\mathbf{r}_l^R)\phi_n(\mathbf{r}_{l'}^R)}{\omega_n^2} \\ &- \frac{1}{2\rho^2} e^{t\alpha_n} \sum_{k,n} \int W(\tau) H(\tau - t) e^{-2\tau\alpha_n} \frac{\phi_n^2(\mathbf{r}_k^S)\phi_n(\mathbf{r}_l^R)\phi_n(\mathbf{r}_{l'}^R)}{\omega_n^2} \cos(2\omega_n\tau - \omega_n t) d\tau \\ &+ \frac{1}{2\rho^2} \sum_{k,n\neq n'} e^{t\alpha_{n'}} \int W(\tau) H(\tau - t) \frac{\phi_{n'}(\mathbf{r}_k^S)\phi_{n'}(\mathbf{r}_l^R)}{\omega_{n'}} \frac{\phi_n(\mathbf{r}_k^S)\phi_n(\mathbf{r}_{l'}^R)}{\omega_n} e^{-\tau(\alpha_n+\alpha_{n'})} \\ &\cdot \left[\cos(\omega_{n'}t + (\omega_n - \omega_{n'})\tau) - \cos((\omega_n + \omega_{n'})\tau - \omega_{n'}t)\right] d\tau \end{aligned} \tag{I.16}$$

If we assume that the integration time window is long compared to the minimum period, then we can neglect the second term on the right-hand side, and also the term including $\cos((\omega_n + \omega_{n'})\tau - \omega_{n'}t)$ in the last term, due to the rapid oscillation with respect to the other terms. We also assume that the attenuation time is not dependent on n. So, Eq. I.16 simplifies to

$$\begin{aligned} C_N^{dT}(\mathbf{r}_l^R, \mathbf{r}_{l'}^R, t) &= \frac{1}{2\rho^2} e^{t\alpha_n} \int W(\tau) H(\tau - t) e^{-2\tau\alpha_n} d\tau \sum_{k,n} \cos(\omega_n t) \frac{\phi_n^2(\mathbf{r}_k^S)\phi_n(\mathbf{r}_l^R)\phi_n(\mathbf{r}_{l'}^R)}{\omega_n^2} \\ &+ \frac{1}{2\rho^2} \sum_{k,n\neq n'} e^{t\alpha_{n'}} \int \frac{\phi_{n'}(\mathbf{r}_k^S)\phi_{n'}(\mathbf{r}_l^R)}{\omega_{n'}} \frac{\phi_n(\mathbf{r}_k^S)\phi_n(\mathbf{r}_{l'}^R)}{\omega_n} W(\tau) H(\tau - t) e^{-\tau(\alpha_n+\alpha_{n'})} \\ &\cdot \cos(\omega_{n'}t + (\omega_n - \omega_{n'})\tau) d\tau \end{aligned} \tag{I.17}$$

Next, we define $\mathscr{C}(\mathbf{r}_l^R, \mathbf{r}_{l'}^R, t)$. This cross-correlation is obtained when there are enough noise sources for $C_N^{dT}(\mathbf{r}_l^R, \mathbf{r}_{l'}^R, t)$; i.e., $\sum_k \phi_n(\mathbf{r}_k^S)\phi_{n'}(\mathbf{r}_k^S) = \delta_{n,n'} N < \phi^2 >^2$.

$$\mathscr{C}(\mathbf{r}_l^R, \mathbf{r}_{l'}^R, t) = \frac{N < \phi^2 >}{2\rho^2} e^{t\alpha_n} \left(\int W(\tau) H(\tau - t) e^{-2\tau\alpha_n} d\tau \right) \sum_n \cos(\omega_n t) \frac{\phi_n(\mathbf{r}_l^R)\phi_n(\mathbf{r}_{l'}^R)}{\omega_n^2} \tag{I.18}$$

[2]Note that as a consequence of the orthogonality of modes: $\int < \phi^2 > dS = 1$, $< \phi^2 >= 1/S$.

I.III Estimation of $\delta C_N^{dT}(\mathbf{r}_l^R, \mathbf{r}_{l'}^R, t)$

We define the variance in $C_N^{dT}(\mathbf{r}_l^R, \mathbf{r}_{l'}^R, t)$ due to the limited number of sources as:

$$\delta C_N^{dT}(\mathbf{r}_l^R, \mathbf{r}_{l'}^R, t) = C_N^{dT}(\mathbf{r}_l^R, \mathbf{r}_{l'}^R, t) - \mathscr{C}(\mathbf{r}_l^R, \mathbf{r}_{l'}^R, t) \tag{I.19}$$

Substituting Eq. (I.17) and Eq. (I.18) in Eq. (I.19)

$$\begin{aligned}
&\delta C_N^{dT}(\mathbf{r}_l^R, \mathbf{r}_{l'}^R, t) = \\
&\frac{1}{2\rho^2} e^{t\alpha_n} \int W(\tau) H(\tau - t) e^{-2\tau\alpha_n} d\tau \sum_{k,n} \cos(\omega_n t) \frac{\left(\phi_n^2(\mathbf{r}_k^S) - \langle \phi^2 \rangle\right) \phi_n(\mathbf{r}_l^R) \phi_n(\mathbf{r}_{l'}^R)}{\omega_n^2} \\
&+ \frac{1}{2\rho^2} \sum_{k,n \neq n'} e^{t\alpha_{n'}} \int \frac{\phi_{n'}(\mathbf{r}_k^S) \phi_{n'}(\mathbf{r}_l^R)}{\omega_{n'}} \frac{\phi_n(\mathbf{r}_k^S) \phi_n(\mathbf{r}_{l'}^R)}{\omega_n} W(\tau) H(\tau - t) e^{-\tau(\alpha_n + \alpha_{n'})} \\
&\cdot \cos(\omega_{n'} t + (\omega_n - \omega_{n'})\tau) d\tau
\end{aligned} \tag{I.20}$$

We define $\widetilde{M}(\omega_{n'} - \omega_n)$ as the Fourier transform of $W(\tau)H(\tau - t)e^{-\tau(\alpha_n + \alpha_{n'})}$. So, Eq. (I.20) reads

$$\begin{aligned}
\delta C_N^{dT}(\mathbf{r}_l^R, \mathbf{r}_{l'}^R, t) = &\frac{1}{2\rho^2} e^{t\alpha_n} \widetilde{M}(0) \sum_{k,n} Re e^{j\omega_n t} \frac{\left(\phi_n^2(\mathbf{r}_k^S) - \langle \phi^2 \rangle\right) \phi_n(\mathbf{r}_l^R) \phi_n(\mathbf{r}_{l'}^R)}{\omega_n^2} \\
&+ \frac{1}{2\rho^2} \sum_{k,n \neq n'} e^{t\alpha_{n'}} \frac{\phi_{n'}(\mathbf{r}_k^S) \phi_{n'}(\mathbf{r}_l^R)}{\omega_{n'}} \frac{\phi_n(\mathbf{r}_k^S) \phi_n(\mathbf{r}_{l'}^R)}{\omega_n} Re[\widetilde{M}(\omega_{n'} - \omega_n) e^{j\omega_{n'} t}]
\end{aligned} \tag{I.21}$$

where we assumed that α_n is frequency independent.

Next, we consider the average value of $\delta C_N^{dT}(\mathbf{r}_l^R, \mathbf{r}_{l'}^R, t)^2$.

$$\begin{aligned}
\left\langle \delta C_N^{dT}(\mathbf{r}_l^R, \mathbf{r}_{l'}^R, t)^2 \right\rangle = &\frac{1}{4\rho^4} e^{2t\alpha_n} \left| \widetilde{M}(0) \right|^2 \left[\sum_n \left\langle \left((\sum_k \phi_n^2(\mathbf{r}_k^S)) - N \left\langle \phi^2 \right\rangle \right)^2 \right\rangle \right. \\
&\left. \cdot \frac{< \phi_n^2(\mathbf{r}_l^R) \phi_n^2(\mathbf{r}_{l'}^R) >}{2\omega_n^4} \right] + \frac{1}{8\rho^4} e^{2t\alpha_{n'}} \sum_{n \neq n'} \frac{\left| \widetilde{M}(\omega_{n'} - \omega_n) \right|^2}{\omega_n^2 \omega_{n'}^2} \left\langle \left(\sum_k \phi_n(\mathbf{r}_k^S) \phi_{n'}(\mathbf{r}_k^S) \right) \right. \\
&\left. \cdot \left(\sum_{k'} \phi_n(\mathbf{r}_{k'}^S) \phi_{n'}(\mathbf{r}_{k'}^S) \right) \right\rangle \left\langle \phi_n^2(\mathbf{r}_{l'}^R) \right\rangle \left\langle \phi_{n'}^2(\mathbf{r}_l^R) \right\rangle
\end{aligned} \tag{I.22}$$

where we neglected the cross term, as the average of the product of the two modes at different locations goes to zero. Let us first look at the first term on the right-hand

side of Eq. I.22 and rewrite this as:

$$\frac{1}{4\rho^4}e^{2t\alpha_n}\left|\widetilde{M}(0)\right|^2\left[\sum_n\left\langle\left((\sum_k\phi_n^2(\mathbf{r}_k^S))-N\left\langle\phi^2\right\rangle\right)^2\right\rangle\frac{<\phi_n^2(\mathbf{r}_l^R)\phi_n^2(\mathbf{r}_{l'}^R)>}{2\omega_n^4}\right]=$$
$$\frac{1}{4\rho^4}e^{2t\alpha_n}\left|\widetilde{M}(0)\right|^2N^2<\phi^2>^2\left[\sum_n\left\langle\left((\sum_k\phi_n^2(\mathbf{r}_k^S))/N<\phi^2>-1\right)^2\right\rangle\right]$$
$$\cdot\frac{1}{2}\int\frac{\sum_n\delta(\omega-\omega_n)<\phi_n^2(\mathbf{r}_l^R)\phi_n^2(\mathbf{r}_{l'}^R)>}{\omega^4}d\omega \tag{I.23}$$

where we used the property of the dirac delta function to replace the sum over n with an integral over a sum of dirac functions.

We next use the definition of modal density (n_0) as $n_0(\omega)=\sum_{n=0}^{\infty}\delta(\omega-\omega_n)$. Taking all of this into account, Eq. I.23 reads

$$\frac{1}{4\rho^4}e^{2t\alpha_n}\left|\widetilde{M}(0)\right|^2\left[\sum_n\left\langle\left((\sum_k\phi_n^2(\mathbf{r}_k^S))-N\left\langle\phi^2\right\rangle\right)^2\right\rangle\frac{<\phi_n^2(\mathbf{r}_l^R)\phi_n^2(\mathbf{r}_{l'}^R)>}{2\omega_n^4}\right]=$$
$$\frac{1}{4\rho^4}e^{2t\alpha_n}\left|\widetilde{M}(0)\right|^2N^2<\phi^2>^2\left[\sum_n\left\langle\left((\sum_k\phi_n^2(\mathbf{r}_k^S))/N<\phi^2>-1\right)^2\right\rangle\right]$$
$$\cdot\frac{1}{2}\int\frac{n_0(\omega)}{\omega^4}d\omega[<\phi_n^2(\mathbf{r}_l^R)\phi_n^2(\mathbf{r}_{l'}^R)>] \tag{I.24}$$

We next evaluate $<\phi_n^2(\mathbf{r}_l^R)\phi_n^2(\mathbf{r}_{l'}^R)>$. Assuming $\phi_n(\mathbf{r}_l^R)$ and $\phi_n(\mathbf{r}_{l'}^R)$ as Gaussian random variables, we can write

$$\begin{aligned}&<\phi_n^2(\mathbf{r}_l^R)\phi_n^2(\mathbf{r}_{l'}^R)>=<\phi_n(\mathbf{r}_l^R)\phi_n(\mathbf{r}_l^R)><\phi_n(\mathbf{r}_{l'}^R)\phi_n(\mathbf{r}_{l'}^R)>\\&+<\phi_n(\mathbf{r}_l^R)\phi_n(\mathbf{r}_{l'}^R)><\phi_n(\mathbf{r}_l^R)\phi_n(\mathbf{r}_{l'}^R)>\\&+<\phi_n(\mathbf{r}_l^R)\phi_n(\mathbf{r}_{l'}^R)><\phi_n(\mathbf{r}_l^R)\phi_n(\mathbf{r}_{l'}^R)>=\\&<\phi^2>^2\left(1+\frac{2<\phi_n(\mathbf{r}_l^R)\phi_n(\mathbf{r}_{l'}^R)>^2}{<\phi^2>^2}\right)=<\phi^2>^2(1+F(\delta r)).\end{aligned} \tag{I.25}$$

Finally, the first term on the right-hand side of Eq. I.22 becomes

$$\frac{1}{4\rho^4}e^{2t\alpha_n}\left|\widetilde{M}(0)\right|^2\left[\sum_n\left\langle\left(\sum_k\phi_n^2(\mathbf{r}_k^S)-N\left\langle\phi^2\right\rangle\right)^2\right\rangle\frac{\left\langle\phi_n^2(\mathbf{r}_l^R)\phi_n^2(\mathbf{r}_{l'}^R)\right\rangle}{2\omega_n^4}\right]=$$
$$\frac{1}{8\rho^4}e^{2t\alpha_n}\left|\widetilde{M}(0)\right|^2\left\langle\phi^2\right\rangle^4\left(\int\frac{n_0(\omega)}{\omega^4}d\omega\right)N^2\left\langle\left(\frac{\sum_k\phi_n^2(\mathbf{r}_k^S)}{N\left\langle\phi^2\right\rangle}-1\right)^2\right\rangle[1+F(\delta r)]$$
$$=\frac{C_0^2}{\int n_0(\omega)d\omega}\left\langle\left(\frac{\sum_k\phi_n^2(\mathbf{r}_k^S)}{N\left\langle\phi^2\right\rangle}-1\right)^2\right\rangle[1+F(\delta r)] \tag{I.26}$$

where $C_0^2 = \frac{1}{8\rho^4} e^{2t\alpha_n} \left|\widetilde{M}(0)\right|^2 N^2 < \phi^2 >^4 \frac{1}{\omega^4} (\int n_0(\omega) d\omega)^2$. We assumed that the bandwidth is small enough to take $\frac{1}{\omega^4}$ out of the integral.

We next consider the second term on the right-hand side of Eq. I.22. Let us first simplify $\sum_{n \neq n'} \left|\widetilde{M}(\omega_{n'} - \omega_n)\right|^2$, and write it as

$$\sum_{n \neq n'} \left|\widetilde{M}(\omega_{n'} - \omega_n)\right|^2 = \int_\omega \int_{\omega'} \sum_{n \neq n'} \left|\widetilde{M}(\omega' - \omega)\right|^2 \sum_{n'=0}^{\infty} \delta(\omega' - \omega_{n'}) \sum_{n=0}^{\infty} \delta(\omega - \omega_n) d\omega' d\omega \tag{I.27}$$

We see that the definition of modal density appears. We now define $\kappa(\delta\omega, \omega) = \frac{<n_0(\omega) n_0(\omega + \delta\omega)>}{n_0(\omega)}$

$$\sum_{n \neq n'} \left|\widetilde{M}(\omega_{n'} - \omega_n)\right|^2 = \int \int n_0(\omega) \kappa(\delta\omega, \omega)) \left|\widetilde{M}(\delta\omega)\right|^2 d\delta\omega d\omega \tag{I.28}$$

And hence the second term on the right-hand side of Eq. I.22 reads

$$\begin{aligned}
&\frac{1}{8\rho^4} e^{2t\alpha_{n'}} \sum_{n \neq n'} \frac{\left|\widetilde{M}(\omega_{n'} - \omega_n)\right|^2}{\omega_n^2 \omega_{n'}^2} \left\langle \left(\sum_k \phi_n(\mathbf{r}_k^S) \phi_{n'}(\mathbf{r}_k^S) \right) \left(\sum_{k'} \phi_n(\mathbf{r}_{k'}^S) \phi_{n'}(\mathbf{r}_{k'}^S) \right) \right\rangle \\
&\cdot \left\langle \phi_n^2(\mathbf{r}_l^R) \right\rangle \left\langle \phi_{n'}^2(\mathbf{r}_{l'}^R) \right\rangle = \frac{1}{8\rho^4} e^{2t\alpha_{n'}} \left|\widetilde{M}(0)\right|^2 N^2 \int \frac{n_0(\omega)}{\omega^4} d\omega \left\langle \phi^2 \right\rangle^4 \\
&\cdot \left(\int \kappa(\delta\omega, \omega) \frac{\left|\widetilde{M}(\delta\omega)\right|^2}{\left|\widetilde{M}(0)\right|^2} d\delta\omega \right) \frac{\left\langle \left(\sum_k \phi_n(\mathbf{r}_k^S) \phi_{n'}(\mathbf{r}_k^S) \right)^2 \right\rangle}{N^2 \left\langle \phi^2 \right\rangle^2} = \\
&\frac{C_0^2}{\int n_0(\omega) d\omega} \left(\int \kappa(\delta\omega, \omega) \frac{\left|\widetilde{M}(\delta\omega)\right|^2}{\left|\widetilde{M}(0)\right|^2} d\delta\omega \right) \frac{\left\langle \left(\sum_k \phi_n(\mathbf{r}_k^S) \phi_{n'}(\mathbf{r}_k^S) \right)^2 \right\rangle}{N^2 \left\langle \phi^2 \right\rangle^2}
\end{aligned} \tag{I.29}$$

So, finally, Eq. I.22 becomes

$$\begin{aligned}
\left\langle \delta C_N^{dT}(\mathbf{r}_l^R, \mathbf{r}_{l'}^R, t)^2 \right\rangle &= \frac{C_0^2}{\int n_0(\omega) d\omega} \left[\left\langle \left(\sum \phi_n^2(\mathbf{r}_k^S) / N \left\langle \phi^2 \right\rangle - 1 \right)^2 \right\rangle \right. \\
&\cdot [1 + F(\delta r)] + \left(\int \kappa(\delta\omega, \omega) \frac{\left|\widetilde{M}(\delta\omega)\right|^2}{\left|\widetilde{M}(0)\right|^2} d\ \delta\omega \right) \\
&\left. \cdot \frac{\left\langle \left(\sum_k \phi_n(\mathbf{r}_k^S) \phi_{n'}(\mathbf{r}_k^S) \right)^2 \right\rangle}{N^2 \left\langle \phi^2 \right\rangle^2} \right]
\end{aligned} \tag{I.30}$$

I.IV Estimation of $\left\langle \mathscr{C}(\mathbf{r}_l^R, \mathbf{r}_{l'}^R, t)^2 \right\rangle$

From Eq. (I.18),

$$\left\langle \mathscr{C}(\mathbf{r}_l^R, \mathbf{r}_{l'}^R, t)^2 \right\rangle = \frac{N^2 < \phi^2 >^2}{4\rho^4} e^{2t\alpha_n} \left(\int W(\tau) H(\tau - t) e^{-2\tau\alpha_n} d\tau \right)^2 \left(\sum_n \cos^2(\omega_n t) \frac{\left\langle \phi_n^2(\mathbf{r}_l^R) \phi_n^2(\mathbf{r}_{l'}^R) \right\rangle}{\omega_n^4} + \sum_{n \neq n'} \cos(\omega_n t) \cos(\omega_{n'} t) \frac{\left\langle \phi_n(\mathbf{r}_l^R) \phi_{n'}(\mathbf{r}_{l'}^R) \right\rangle^2}{\omega_n^2 \omega_{n'}^2} \right). \tag{I.31}$$

Taking the integral and neglecting the rapidly oscillating terms,

$$\left\langle \int \mathscr{C}(\mathbf{r}_l^R, \mathbf{r}_{l'}^R, t)^2 dt \right\rangle = \frac{N^2 < \phi^2 >^2}{4\rho^4} \int (e^{2t\alpha_n} \left(\int W(\tau) H(\tau - t) e^{-2\tau\alpha_n} d\tau \right)^2 \sum_n \frac{\left\langle \phi_n^2(\mathbf{r}_l^R) \phi_n^2(\mathbf{r}_{l'}^R) \right\rangle}{2\omega_n^4} + \sum_{n \neq n'} \cos((\omega_n - \omega_{n'})\, t) \frac{\left\langle \phi_n(\mathbf{r}_l^R) \phi_{n'}(\mathbf{r}_{l'}^R) \right\rangle^2}{2\omega_n^4}) dt \tag{I.32}$$

As for the previous section, the introduction of the modal density and the modal density correlation function leads to

$$\left\langle \int \mathscr{C}(\mathbf{r}_l^R, \mathbf{r}_{l'}^R, t)^2 dt \right\rangle = \frac{N^2 < \phi^2 >^2}{8\rho^4} \int \frac{n_0(\omega) d\omega}{\omega^4} \int (e^{2t\alpha_n} \left(\int W(\tau) H(\tau - t) e^{-2\tau\alpha_n} d\tau \right)^2 \left(\left\langle \phi_n^2(\mathbf{r}_l^R) \phi_n^2(\mathbf{r}_{l'}^R) \right\rangle + \kappa(t) \left\langle \phi_n(\mathbf{r}_l^R) \phi_n(\mathbf{r}_{l'}^R) \right\rangle^2 \right)) dt \tag{I.33}$$

where $\kappa(t)$ is the inverse Fourier transform of $\kappa(\delta\omega)$. As $\kappa(\delta\omega) = n_0$ for a regular cavity, $\kappa(t) = n_0 \delta(t)$. The second term can thus be neglected because it is only significant when t=0 and $\mathbf{r}_l^R = \mathbf{r}_{l'}^R$. Then,

$$\left\langle \int \mathscr{C}(\mathbf{r}_l^R, \mathbf{r}_{l'}^R, t)^2 dt \right\rangle \approx \frac{(1 + F(\delta r))}{\int n_0(\omega) d\omega} \int C_0^2 dt. \tag{I.34}$$

I.V Estimation of the Similarity Coefficient $S(C_\infty, C_N^{dT})$

Substituting Eq. I.30 and Eq. I.34, Y reads

$$Y = \left\langle \left(\sum_k \phi_n^2(\mathbf{r}_k^S)/N \left\langle \phi^2 \right\rangle - 1 \right)^2 \right\rangle + \frac{\left(\int \kappa(\delta\omega, \omega) \frac{\left| \widetilde{M}(\delta\omega) \right|^2}{\left| \widetilde{M}(0) \right|^2} d\delta\omega \right) \frac{\left\langle \left(\sum_k \phi_n(\mathbf{r}_k^S) \phi_{n'}(\mathbf{r}_k^S) \right)^2 \right\rangle}{N^2 \left\langle \phi^2 \right\rangle^2}}{1 + F(\delta r)} \tag{I.35}$$

Before going further, we simplify this Equation.

First, we consider $\left\langle \left(\sum_k \phi_n^2(\mathbf{r}_k^S)/N \left\langle \phi^2 \right\rangle - 1 \right)^2 \right\rangle$ and rewrite it as

$\left\langle \left(\frac{1}{N}\sum_k a_k^2 - 1\right)^2 \right\rangle$, where $a_k^2 = \frac{\phi_n^2(\mathbf{r}_k^S)}{\langle \phi^2 \rangle}$.

$$\left\langle \left(\frac{1}{N}\sum_k a_k^2 - 1\right)^2 \right\rangle = \frac{1}{N^2}\sum_{k,k'=1}^{N} \langle a_k^2 a_{k'}^2 \rangle + 1 - \frac{2}{N}\left\langle \sum_{k=1}^{N} a_k^2 \right\rangle = \frac{1}{N^2}\left[3N\langle a_k^2\rangle^2 + N(N-1)\langle a_k^2\rangle^2\right] - 1 = \frac{2}{N}\langle a_k^2\rangle^2 + \langle a_k^2\rangle^2 - 1 = \frac{2}{N} \tag{I.36}$$

Next, we consider $\left\langle \left(\sum_k \phi_n(\mathbf{r}_k^S)\phi_{n'}(\mathbf{r}_k^S)\right)^2 \right\rangle$.

$$\left\langle \left(\sum_k \phi_n(\mathbf{r}_k^S)\phi_{n'}(\mathbf{r}_k^S)\right)^2 \right\rangle = \sum_{k,k'=1}^{N} \left\langle \phi_n(\mathbf{r}_k^S)\phi_n(\mathbf{r}_{k'}^S)\phi_{n'}(\mathbf{r}_k^S)\phi_{n'}(\mathbf{r}_{k'}^S)\right\rangle = \sum_{k,k'=1}^{N} \left\langle \phi_n(\mathbf{r}_k^S)\phi_n(\mathbf{r}_{k'}^S)\right\rangle \left\langle \phi_{n'}(\mathbf{r}_k^S)\phi_{n'}(\mathbf{r}_{k'}^S)\right\rangle = N\left\langle \phi^2 \right\rangle^2 \tag{I.37}$$

Using Eq. I.36 and Eq. I.37, Y simplifies to

$$Y = \frac{\frac{2}{N}\left[1 + F(\delta r)\right] + \left(\int \kappa(\delta\omega,\omega)) \frac{\left|\widetilde{M}(\delta\omega)\right|^2}{\left|\widetilde{M}(0)\right|^2} d\delta\omega\right)\frac{1}{N}}{1 + F(\delta r)} \tag{I.38}$$

Substituting Eq. I.38 in Eq. I.4, the similarity coefficient $S(C_\infty, C_N^{dT})$ reads

$$S(C_\infty, C_N^{dT}) = \frac{1}{\sqrt{1 + \frac{\frac{2}{N}[1+F(\delta r)] + \left(\int \kappa(\delta\omega,\omega)) \frac{\left|\widetilde{M}(\delta\omega)\right|^2}{\left|\widetilde{M}(0)\right|^2} d\delta\omega\right)\frac{1}{N}}{1+F(\delta r)}}} \tag{I.39}$$

We assume that $\kappa(\delta\omega, \omega)$ is equal to the average value of the modal density. We next simplify $\int \frac{\left|\widetilde{M}(\delta\omega)\right|^2}{\left|\widetilde{M}(0)\right|^2} d\delta\omega$. If we replace $\omega' - \omega = \omega$ and $\alpha_n = \alpha_{n'}$, then according to the definition of the Fourier transform

$$\widetilde{M}(\omega) = \int_{T_{min}}^{T_{max}} e^{-2\alpha\tau} e^{-j\omega\tau} d\tau = \frac{e^{-i\omega T_{min} - 2\alpha T_{min}}}{i\omega + 2\alpha} - \frac{e^{-i\omega T_{max} - 2\alpha T_{max}}}{i\omega + 2\alpha}, \tag{I.40}$$

and

$$\widetilde{M}(0) = \int_{T_{min}}^{T_{max}} e^{-2\alpha\tau} d\tau = \frac{e^{-2\alpha T_{min}}}{2\alpha} - \frac{e^{-2\alpha T_{max}}}{2\alpha}. \tag{I.41}$$

Using Eq. (I.40) and Eq. (I.41),

$$\int \frac{\left|\widetilde{M}(\omega)\right|^2}{\left|\widetilde{M}(0)\right|^2} d\omega = \frac{2\pi\alpha(e^{2\alpha T_{max}} + e^{2\alpha T_{min}})}{(e^{\alpha T_{max}} - e^{\alpha T_{min}})(e^{\alpha T_{max}} + e^{\alpha T_{min}})} = 2\pi\alpha \coth(\alpha(T_{max} - T_{min})). \tag{I.42}$$

And finally $S(C_\infty, C_N^{dT})$ reads

$$S(C_\infty, C_N^{dT}) = \frac{1}{\sqrt{1 + \frac{\frac{2}{N}[1+F(\delta r)] + (n_0(\omega) 2\pi\alpha \coth(\alpha(T_{max} - T_{min})))\frac{1}{N}}{1+F(\delta r)}}}. \tag{I.43}$$

II Instrumental-Noise Affected Recordings and Convergence toward the Best Cross-Correlation

In this part, we quantify the contribution of the noise. In other words, we only consider the effects of variations in the cross-correlation induced by noise and not by the insufficient number of sources (the latter case is studied in part I in detail). To this end, we cross-correlate two time-windowed signals in the coda part of the recordings. The reason why we do not cross-correlate a windowed signal with the full-time signal is that in this case the effects of the noise will not be finite. Here, we look for the similarity coefficient between the cross-correlation obtained between the two windowed signals considering all of the available sources (C_∞^{dT}) and the reference source (C_∞). We write the similarity coefficient $S(C_\infty, C_\infty^{dT})$ as:

$$S(C_\infty, C_\infty^{dT}) = \frac{\int \left\langle C_\infty^{dT}(\mathbf{r}_l^R, \mathbf{r}_{l'}^R, t) C_\infty(\mathbf{r}_l^R, \mathbf{r}_{l'}^R, t) \right\rangle dt}{\sqrt{\int \langle (C_\infty^{dT}(\mathbf{r}_l^R, \mathbf{r}_{l'}^R, t))^2 \rangle \, dt} \sqrt{\int \langle (C_\infty(\mathbf{r}_l^R, \mathbf{r}_{l'}^R, t))^2 \rangle \, dt}} \tag{II.1}$$

Similar to the previous section, we introduce the fluctuation of C_∞^{dT} as:

$$C_\infty^{dT}(\mathbf{r}_l^R, \mathbf{r}_{l'}^R, t) \triangleq \mathscr{C}'(\mathbf{r}_l^R, \mathbf{r}_{l'}^R, t) + \delta n(t) \tag{II.2}$$

where $\delta n(t)$ is the variance in the obtained cross-correlation due to the instrumental noise, and $\mathscr{C}'(\mathbf{r}_l^R, \mathbf{r}_{l'}^R, t)$ is the ideal cross-correlation obtained by cross-correlation of two time-limited windows when there are sufficient noise sources.

Substituting Eq. II.2 into Eq. II.1, the simplified $S(C_\infty, C_\infty^{dT})$ is written as:

$$S(C_\infty, C_\infty^{dT}) = \frac{1}{\sqrt{1 + \frac{\int <\delta n(\mathbf{r}_l^R, \mathbf{r}_{l'}^R, t)^2> dt}{\int <C_\infty(\mathbf{r}_l^R, \mathbf{r}_{l'}^R, t)^2> dt}}} = \frac{1}{\sqrt{1+Z}} \tag{II.3}$$

where Z is $\frac{\int <\delta n(\mathbf{r}_l^R, \mathbf{r}_{l'}^R, t)^2> dt}{\int <C_\infty(\mathbf{r}_l^R, \mathbf{r}_{l'}^R, t)^2> dt}$. Similar to the previous section, and because $\mathscr{C}'(\mathbf{r}_l^R, \mathbf{r}_{l'}^R, t)$ and $C_\infty(\mathbf{r}_l^R, \mathbf{r}_{l'}^R, t)$ are proportional to $ImG(\mathbf{r}_l^R, \mathbf{r}_{l'}^R, t)$,

$$S(C_\infty, C_\infty^{dT}) = S(\mathscr{C}', C_\infty^{dT}) \tag{II.4}$$

and hence Z can be rewritten as $\frac{\int <\delta n(\mathbf{r}_l^R, \mathbf{r}_{l'}^R, t)^2> dt}{\int <\mathscr{C}'(\mathbf{r}_l^R, \mathbf{r}_{l'}^R, t)^2> dt}$.

The goal here is to consider the effects of electronic noise on the cross-correlations, and hence on the similarity coefficient.

We assume that the estimated Green's function ($G_m(\mathbf{r}_l^R, \mathbf{r}_k^S, t)$) coincides with the sum of the exact Green's function $G(\mathbf{r}_l^R, \mathbf{r}_k^S, t)$, and the instrument-related error n

$$G_m(\mathbf{r}_l^R, \mathbf{r}_k^S, t) = G(\mathbf{r}_l^R, \mathbf{r}_k^S, t) + n(t) \tag{II.5}$$

In the experimental case, we cross-correlate the two windowed recordings and call this $C_\infty^{dT}(\mathbf{r}_l^R, \mathbf{r}_k^S, t)$. Here, we temporarily, and from a theoretical point of view, call $C_\infty^{dT}(\mathbf{r}_l^R, \mathbf{r}_k^S, t)$ as $C_{N,n}^{dT}(\mathbf{r}_l^R, \mathbf{r}_k^S, t)$ to emphasize that the cross-correlations are affected by the noise (n). Applying the definition of cross-correlation, $C_{N,n}^{dT}(\mathbf{r}_l^R, \mathbf{r}_k^S, t)$ reads

$$C_{N,n}^{dT}(\mathbf{r}_l^R, \mathbf{r}_{l'}^R, t) = \sum_k \int \left[G(\mathbf{r}_k^S, \mathbf{r}_l^R, \tau - t) + n_{l,k}(\tau - t)\right] W(\tau - t) \left[G(\mathbf{r}_k^S, \mathbf{r}_{l'}^R, \tau) + n_{l',k}(\tau)\right] W(\tau) d\tau \tag{II.6}$$

The cross-correlations are summed over all of the available sources located at r_k^S.

To get Z, we first calculate

$$\begin{aligned}\left\langle C_{N,n}^{dT}(\mathbf{r}_l^R, \mathbf{r}_{l'}^R, t)^2 \right\rangle = \\ \left\langle \mathscr{C}_0'^2(\mathbf{r}_l^R, \mathbf{r}_{l'}^R, t) \right\rangle + \int \left\langle G^2(\mathbf{r}_k^S, \mathbf{r}_l^R, \tau - t) \right\rangle H(\tau - t) W(\tau) d\tau \int n_{l',k}^2(\tau) W(\tau') d\tau' + \\ \int \left\langle G^2(\mathbf{r}_k^S, \mathbf{r}_l^R, \tau) \right\rangle W(\tau) d\tau \int n_{l',k}^2(\tau') W(\tau' - t) d\tau' + \left(\int n_{l',k}^2 W(\tau' - t) d\tau' \right)^2\end{aligned} \tag{II.7}$$

where $\mathscr{C}_0'(\mathbf{r}_l^R, \mathbf{r}_{l'}^R, t)$ is the product of the Gs that are not disturbed by the noise (indicated by subscript 0).

We first compute $\left\langle G^2(\mathbf{r}_k^S, \mathbf{r}_l^R, \tau) \right\rangle$. Using the modal expansion of the Green's function,

$$G(\mathbf{r}_k^S, \mathbf{r}_l^R, t) = \frac{1}{\rho_s} \sum_n \frac{\phi_n(\mathbf{r}_k^S) \phi_n(\mathbf{r}_l^R)}{\omega_n} \exp(-t\alpha_n) \sin(\omega_n t). \tag{II.8}$$

$G^2(\mathbf{r}_k^S, \mathbf{r}_l^R, \tau)$ reads

$$G^2(\mathbf{r}_k^S,\mathbf{r}_l^R,\tau) = \frac{1}{2\rho_s^2}\sum_{n,n'}\frac{\phi_n(\mathbf{r}_k^S)\phi_n(\mathbf{r}_l^R)\phi_{n'}(\mathbf{r}_k^S)\phi_{n'}(\mathbf{r}_l^R)}{\omega_n\omega_{n'}}\exp(-t(\alpha_n+\alpha_{n'}))\left[\cos(\omega_n-\omega_{n'})t-\cos(\omega_n+\omega_{n'})t\right] \tag{II.9}$$

where we used the trigonometry identity.

Neglecting the rapidly oscillating terms and rewriting $G^2(\mathbf{r}_k^S,\mathbf{r}_l^R,\tau)$ as the sum of two terms for $n \neq n'$ and $n = n'$, gives

$$G^2(\mathbf{r}_k^S,\mathbf{r}_l^R,\tau) = \frac{1}{2\rho_s^2}\sum_{n\neq n'}\frac{\exp(-t(\alpha_n+\alpha_{n'}))\phi_n(\mathbf{r}_k^S)\phi_n(\mathbf{r}_l^R)\phi_{n'}(\mathbf{r}_k^S)\phi_{n'}(\mathbf{r}_l^R)}{\omega_n\omega_{n'}}(\cos(\omega_n-\omega_{n'})t) + \frac{1}{2\rho_s^2}\sum_n\frac{\exp(-2t\alpha_n)\phi_n^2(\mathbf{r}_k^S)\phi_n^2(\mathbf{r}_l^R)}{\omega_n^2} \tag{II.10}$$

Using Eq. I.25 and considering $<\phi_n(\mathbf{r}_k^S)\phi_n(\mathbf{r}_l^R)>=0$, $\left\langle G^2(\mathbf{r}_k^S,\mathbf{r}_l^R,\tau)\right\rangle$ becomes

$$\left\langle G^2(\mathbf{r}_k^S,\mathbf{r}_l^R,\tau)\right\rangle = \frac{e^{-2\tau\alpha_n}}{2{\rho_s}^2}\sum\frac{\left\langle\phi^2\right\rangle^2(1+F(\delta r))}{\omega_n^2} = \frac{\left\langle\phi^2\right\rangle^2 e^{-2\tau\alpha_n}(1+F(\delta r))}{2\rho_s^2}\int\frac{n_0(\omega)}{\omega^2}d\omega \tag{II.11}$$

and subsequently

$$\int\left\langle G^2(\mathbf{r}_k^S,\mathbf{r}_l^R,\tau-t)\right\rangle H(\tau-t)W(\tau)d\tau = \frac{\left\langle\phi^2\right\rangle^2(1+F(\delta r))\int e^{-2(\tau-t)\alpha_n}H(\tau-t)W(\tau)d\tau}{2{\rho_s}^2}\int\frac{n_0(\omega)}{\omega^2}d\omega \tag{II.12}$$

Assuming n to be white noise, n^2 is equal to $\Pi_n B$, where Π_n and B are the noise level and the bandwidth, respectively. Hence, Eq. II.7 becomes

$$\left\langle C_{N,n}^{dT}(\mathbf{r}_l^R,\mathbf{r}_{l'}^R,t)^2\right\rangle = \left\langle\mathscr{C}_0'(\mathbf{r}_l^R,\mathbf{r}_{l'}^R,t)^2\right\rangle + \frac{\mathscr{C}'(\mathbf{r}_l^R,\mathbf{r}_{l'}^R,t=0)\left[1+F(\delta r)\right]}{N}\left[\frac{\int e^{-2(t-\tau)\alpha_n}H(\tau-t)W(\tau)d\tau}{\int e^{-2\tau\alpha_n}W(\tau)d\tau}+1\right]\Pi_n B[T_{max}-T_{min}] + \left(\Pi_n B[T_{max}-T_{min}]\right)^2 \tag{II.13}$$

$\mathscr{C}'(\mathbf{r}_l^R,\mathbf{r}_{l'}^R,t)$ is obtained by cross-correlation of two time-limited windows when there are enough noise sources. On the other hand, using Eq. I.18, we can write $\mathscr{C}'(\mathbf{r}_l^R,\mathbf{r}_{l'}^R,t)$ as

$$\mathscr{C}'(\mathbf{r}_l^R, \mathbf{r}_{l'}^R, t) = \frac{N < \phi^2 >}{2\rho_s^2} e^{t\alpha_n} \left(\int W(\tau) W(\tau - t) e^{-2\tau\alpha} d\tau \right) \sum_n \cos(\omega_n t) \frac{\phi_n(\mathbf{r}_l^R) \phi_n(\mathbf{r}_{l'}^R)}{\omega_n^2} \tag{II.14}$$

So,

$$\mathscr{C}'(\mathbf{r}_l^R, \mathbf{r}_{l'}^R, t = 0) = \frac{N < \phi^2 >}{2\rho_s^2} \left(\int_{T_{min}}^{T_{max}} W(\tau) e^{-2\tau\alpha} d\tau \right) \int \frac{n_0(\omega)}{\omega^2} d\omega \tag{II.15}$$

and

$$\mathscr{C}'(\mathbf{r}_l^R, \mathbf{r}_{l'}^R, t = 0) = \frac{N < \phi^2 >}{4\alpha\rho_s^2} (\int \frac{n_0(\omega)}{\omega^2} d\omega)(e^{-2\alpha T_{min}} - e^{-2\alpha T_{max}}) \tag{II.16}$$

And we can write

$$< (\mathscr{C}'(\mathbf{r}_l^R, \mathbf{r}_{l'}^R, t))^2 >= \mathscr{C}'(\mathbf{r}_l^R, \mathbf{r}_{l'}^R, t = 0)^2 \left[\frac{e^{-2\alpha T_{min}} - e^{-2\alpha(T_{max} - t)}}{e^{-2\alpha T_{min}} - e^{-2\alpha T_{max}}} \right]^2 \frac{(1 + F(\delta r))}{2 \int n_0(\omega) d\omega} \tag{II.17}$$

and the variations in the cross-correlation due to the noise are

$$\left\langle C_{N,n}^{dT}(\mathbf{r}_l^R, \mathbf{r}_{l'}^R, t)^2 \right\rangle - \left\langle \mathscr{C}'(\mathbf{r}_l^R, \mathbf{r}_{l'}^R, t)^2 \right\rangle =$$
$$\frac{\mathscr{C}'(\mathbf{r}_l^R, \mathbf{r}_{l'}^R, t = 0) \left[1 + F(\delta r)\right]}{N} \left[\frac{\int e^{-2(t-\tau)\alpha_n} H(\tau - t) W(\tau) d\tau}{\int e^{-2\tau\alpha_n} W(\tau) d\tau} + 1 \right] \Pi_n B[T_{max} - T_{min}]$$
$$+ \left(\Pi_n B[T_{max} - T_{min}]\right)^2 \tag{II.18}$$

Substituting for Z, gives,

$$1 + Z =$$
$$1 + \frac{\int \mathscr{C}'(\mathbf{r}_l^R, \mathbf{r}_{l'}^R, t = 0) \left[1 + F(\delta r)\right] dt}{N \int < (\mathscr{C}'(\mathbf{r}_l^R, \mathbf{r}_{l'}^R, t))^2 > dt} \left[\int (\frac{\int e^{-2(t-\tau)\alpha_n} H(\tau - t) W(\tau) d\tau}{\int e^{-2\tau\alpha_n} W(\tau) d\tau} + 1) dt \right] \Pi_n B[T_{max} - T_{min}]$$
$$+ \frac{\int \left(\Pi_n B[T_{max} - T_{min}]\right)^2 dt}{\int < (\mathscr{C}'(\mathbf{r}_l^R, \mathbf{r}_{l'}^R, t))^2 > dt} \tag{II.19}$$

or,

$$1+Z=$$

$$1+\frac{\int n_0(\omega)d\omega}{N\mathscr{C}'(\mathbf{r}_l^R,\mathbf{r}_{l'}^R,t=0)}\left[\frac{\int(\frac{\int e^{-2(t-\tau)\alpha_n}H(\tau-t)W(\tau)d\tau}{\int e^{-2\tau\alpha_n}W(\tau)d\tau}+1)dt}{\int\left[\frac{e^{-2\alpha T_{min}}-e^{-2\alpha(T_{max}-t)}}{e^{-2\alpha T_{min}}-e^{-2\alpha T_{max}}}\right]^2 dt}\right]\frac{\Pi_n B[T_{max}-T_{min}]}{\alpha_n\int W(\tau)e^{-2\tau\alpha_n}d\tau(1+F(\delta r))}$$

$$+\frac{\int\left(\Pi_n B[T_{max}-T_{min}]\right)^2 dt}{\int<(\mathscr{C}'(\mathbf{r}_l^R,\mathbf{r}_{l'}^R,t))^2>dt}$$

We next apply a simplification and neglect the last term, as it is of the second order.

Assuming a small t ($t\approx 0$), the term in the brackets simplifies to 2, and the similarity coefficient can be finally expressed as:

$$S(C_\infty,C_\infty^{dT})\approx\left(1+\frac{\beta B[T_{max}-T_{min}]}{N(e^{-T_{min}/\tau_a}-e^{-T_{max}/\tau_a})}\right)^{-0.5} \tag{II.20}$$

where

$$\beta=\frac{2\Pi_n}{\mathscr{C}'(\mathbf{r}_l^R,\mathbf{r}_{l'}^R,t=0)(1+F(\delta r))}. \tag{II.21}$$

The dimensionless value β indicates the noise-to-signal ratio.

III Spatial Correlation of the Squared Eigen-Modes

In the last section of this material, we derive the expression for the spatial correlation of the squared eigen modes $<\phi_n^2(\mathbf{r})\phi_n^2(\mathbf{r}')>$ and the expression of F (that appeared in the calculus of the similarity coefficient in both previous sections) for two different cases: Chaotic geometry and integrable cavity. Here, $\mathbf{r}$ and $\mathbf{r}'$ can be considered as the generalized form for $(\mathbf{r}_l^R)$ and $(\mathbf{r}_{l'}^R)$.

- **Chaotic geometry**

In case of a chaotic geometry, Berry stated that the eigenmodes behave as Gaussian variables with a spatial correlation given by

$$\langle\phi_n(\mathbf{r})\phi_n(\mathbf{r}')\rangle=\langle\phi\rangle^2 J_0(k\delta r). \tag{III.1}$$

The relationship between the fourth order moment of a Gaussian variable in terms of second order moments (similar to Eq. (I.25)) yields

$$\left\langle \phi_n^2(\mathbf{r})\phi_n^2(\mathbf{r}')\right\rangle = \left\langle \phi_n^2(\mathbf{r})\right\rangle \left\langle \phi_n^2(\mathbf{r}')\right\rangle + 2\left\langle \phi_n(\mathbf{r})\phi_n(\mathbf{r}')\right\rangle^2. \tag{III.2}$$

Using Eq. (III.1), it comes

$$\left\langle \phi_n^2(\mathbf{r})\phi_n^2(\mathbf{r}')\right\rangle = \left\langle \phi^2\right\rangle^2 \left[1 + 2J_0(k\delta r)^2\right], \tag{III.3}$$

and therefore

$$F(\delta r) = 2J_0(k\delta r)^2 \tag{III.4}$$

- **Integrable cavity**

For a clamped rectangular plate, the expression of the eigenmode separated in two dimensions (x and y) is given by

$$\phi(x,y) = \frac{2\sin(k_x x)\sin(k_y y)}{\sqrt{A}}, \tag{III.5}$$

where A is the plate area (e.g.[55]). For simplicity in this section, we drop n (which normally appears as the subscript for ϕ and the coefficient for k in the argument of sin).

We compute $\langle\phi^2(x,y)\phi^2(x',y')\rangle$ in a similar manner to the one used in [55] to estimate the spatial correlation of the eigenmodes. Strictly speaking, the averaging has to be performed by integrating over a quarter of a ring of radius k and thickness dk (positive k_x and k_y). However here, to facilitate the calculus and without amending the result, the integration is done over the full ring,

$$\left\langle \phi^2(x,y)\phi^2(x',y')\right\rangle = \frac{16}{A^2 2\pi k\delta k}\int_0^{2\pi}\int_k^{k+\delta k}\left\langle \sin^2(k_x x)\sin^2(k_y y)\sin^2(k_x x')\sin^2(k_y y')\right\rangle k dk d\theta, \tag{III.6}$$

with $k_x = k\cos\theta$ and $k_y = k\sin\theta$.

This integral can be estimated using the following trigonometric identity

$$\sin^2(k_x x)\sin^2(k_x x') = \frac{(1-\cos(2k_x x)-\cos(2k_x x'))}{4} + \frac{\cos(2k_x[x-x']) + \cos(2k_x[x+x'])}{8}. \tag{III.7}$$

Similar to [55], an expression that is valid for all x and x' can be worked out. However, for the sake of simplicity, we assume here that the position coordinates x and x' are sufficiently far (farther than a couple of wavelengths) from the plate borders. In such a case, only the terms $1/4$ and $\cos(2k_x[x-x'])$ significantly contribute to the integral because the other terms oscillate much faster with respect to k_x. The same goes for k_y terms in Eq. (III.6).

Finally, it comes

$$\left\langle \phi^2(x,y)\phi^2(x',y') \right\rangle = \frac{1}{A^2 2\pi}\int_0^{2\pi}\left[1+\frac{\cos(2k_x[x-x'])+\cos(2k_y[y-y'])}{2}+\frac{\cos(2k_x[x-x'])\cos(2k_y[y-y'])}{4}\right]d\theta. \tag{III.8}$$

The 2 next integral identities,

$$\int_0^{2\pi}\cos(A\cos\theta)d\theta=\int_0^{2\pi}\cos(A\sin\theta)d\theta=2\pi J_0(A) \tag{III.9}$$

and

$$\int_0^{2\pi}\cos(A\cos\theta)\cos(A\sin\theta)d\theta=2\pi J_0(\sqrt{A^2+B^2}), \tag{III.10}$$

yield an analytical expression in terms of 0-th order first kind Bessel functions

$$\left\langle \phi^2(x,y)\phi^2(x',y') \right\rangle \propto \frac{1}{A^2}\left[1+\frac{J_0(2k\,|\delta x|)+J_0(2k\,|\delta y|)}{2}+\frac{J_0(2k\delta r)}{4}\right], \tag{III.11}$$

where $\delta x = x'-x$, $\delta y = y'-y$ and $\delta r = r'-r$. Using the same procedure, it can be easily deduced that

$$\left\langle \phi^2(x,y) \right\rangle = \frac{1}{A} \tag{III.12}$$

So, finally we obtain the expression of the spatial correlation of the squared eigen modes as

$$\left\langle \phi^2(x,y)\phi^2(x',y') \right\rangle = \left\langle \phi^2 \right\rangle^2\left[1+\frac{J_0(2k\,|\delta x|)+J_0(2k\,|\delta y|)}{2}+\frac{J_0(2k\delta r)}{4}\right]. \tag{III.13}$$

When $x = x'$ and $y = y'$, we find the already known relationship between the fourth order moment and the second order moment of the eigenmodes in a rectangular plate ([105], P.101)

$$\left\langle \phi^4 \right\rangle = \left\langle \phi^2 \right\rangle^2 \left(\frac{3}{2}\right)^2. \tag{III.14}$$

From Eq. (III.13), we easily deduce that in case of a rectangular plate,

$$F(\delta x, \delta y) = \frac{J_0(2k\,|\delta x|) + J_0(2k\,|\delta y|)}{2} + \frac{J_0(2k\delta r)}{4}. \tag{III.15}$$

IV Horizontal Coordinates of the Transducers on the Plate

In this section, the coordinates of the transducers are displayed. The origin is the left lower corner of the plate on the same side where the transducers are attached.

Table 4.1: Coordinates of the transducers

Transducer	x(cm)	y(cm)
1	20.5	39
2	17.5	25.5
3	30.5	34.5
4	29	23
5	23	18

V Derivation of the Condition on the Maximum Time Considered in the Fitting to the Similarity Coefficient Decay

We showed that the similarity coefficient in both cases I and II decays exponentially in time as proportional to $\exp(-t/\tau)$. In terms of mean free path, we rewrite the exponential term as

$$e^{-L/l_s} = e^{-V_g T/l_s} \tag{V.1}$$

where l_s is the scattering mean free path, V_g is the group velocity. For a broadband signal, the similarity coefficient $S(t)$ can be written as

$$S(t) \propto \frac{1}{\Delta B} \int_{\Delta B} e^{-V_g(\omega)T/l_s} d\omega \tag{V.2}$$

where $V_g(\omega)$ reminds the dispersion of waves in plates i.e., the wave speed depends on the frequency. We perform Taylor expansion of $V_g(\omega)$ around a fixed frequency ω_0:

$$V_g(\omega) = V_g(\omega_0) + \frac{\partial V_g}{\partial \omega}(\omega - \omega_0) \tag{V.3}$$

We remind that at low frequency regime, group velocity (V_g) of A_0 mode of Lamb waves is given by

$$V_g(\omega) = 2\sqrt{\omega} \left(\frac{D}{\rho e}\right)^{\frac{1}{4}} \tag{V.4}$$

which is twice the phase speed at this regime. Deriving Eq. V.4 with respect to ω gives

$$\frac{\partial V_g}{\partial \omega} = \left(\frac{D}{\rho e}\right)^{\frac{1}{4}} \frac{1}{\sqrt{\omega}} = \frac{V_g}{2\omega} \tag{V.5}$$

Substituting Eq. V.5 in Eq. V.3 and multiplying both sides by T/l gives

$$\frac{V_g(\omega)T}{l_s} = V_g(\omega_0)\frac{T}{l_s} + \frac{V_g(\omega_0)}{2\omega_0}\frac{\Delta\omega T}{l_s} \tag{V.6}$$

In our fitting process based on the formulae that we provided in the manuscript, we substitute the group velocity in a given frequency band by the group velocity of the central frequency. Adopting this approximation implies that the second term on the RHS of Eq. V.6 should be much smaller than one in order to be neglected. So, the condition is: $\frac{V_g(\omega_0)}{2\omega_0}\frac{\Delta\omega T}{l_s} << 1$. This means that the condition we have on T is given by

$$T << \frac{2\omega_0\tau}{\Delta\omega} \tag{V.7}$$

where $\tau = l_s/V_g$.

Appendix A

In this Appendix, we explain the approximately uniform pattern that is observed for the contribution of each virtual source in the cross-correlation in the bandgap when one of the virtual receivers is located inside the metamaterial region.

We define this explanation following a simple schema. Assuming that for frequency bands that lie within the bandgaps, there are evanescent waves, we describe these as $\exp(-\alpha d)$, where d is the distance and α is the decaying length of the evanescent waves. Let us assume two separate cases: (1) The two virtual receivers are separated by a distance L and a virtual source is between these two. This case is schematically shown in Fig. A.1. We define the corresponding

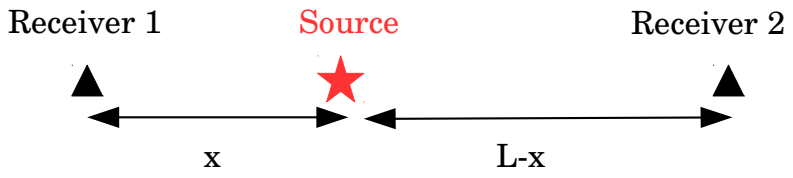

Figure A.1: Schematic illustration of a source located between two receivers.

amplitude of the cross-correlation of the recordings as proportional to the product of the two evanescent waves that decay exponentially according to the distance between the source and the receiver. So, in this case, they will decay as $\exp(-x\alpha).\exp(-(L-x)\alpha) = \exp(-L\alpha)$. This relation indicates that while in the bandgap, where a source is between the two receivers, the amplitude of the cross-correlations will decay by a constant that does not depend on the distance between the source and the receiver. This explains the approximately homogeneous pattern observed around the virtual receiver located inside the metamaterial in the maps of the contribution of virtual point sources in the cross-correlation. (2) This case

explains the configuration where the source is not between the two virtual receivers (see Fig. A.2). In this case, the amplitude of the cross-correlation will decay as

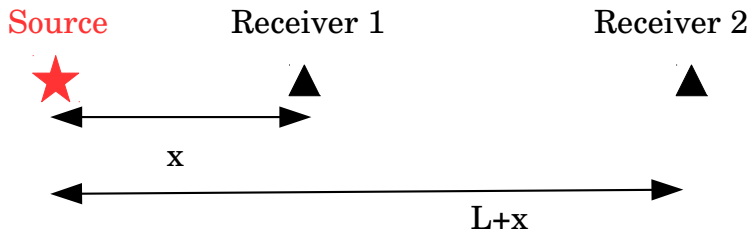

Figure A.2: Schematic illustration of a source not located between two receivers.

$\exp(-x\alpha).\exp(-(L+x)\alpha) = \exp(-(2x+L)\alpha)$. Consequently, the maximum of the cross-correlation will depend on the distance between the virtual source and each virtual receiver.

Appendix B

In this Appendix, we show spatial maps of signal-to-noise ratio (in dB) at different frequency bands for the signals received by virtual receivers located inside the forest and averaged over all these receivers. Black circles mark the virtual receivers position.

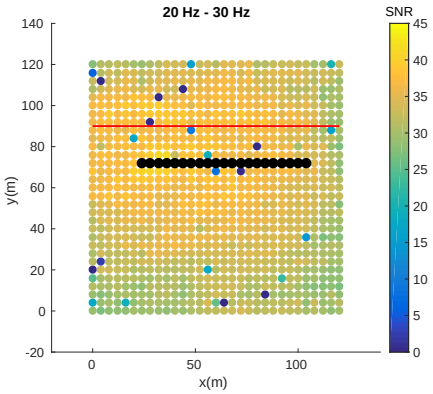
20 Hz - 30 Hz
SNR
y(m)
x(m)

(a)

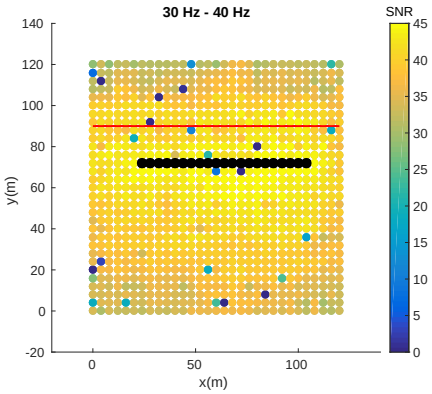
30 Hz - 40 Hz
SNR
y(m)
x(m)

(b)

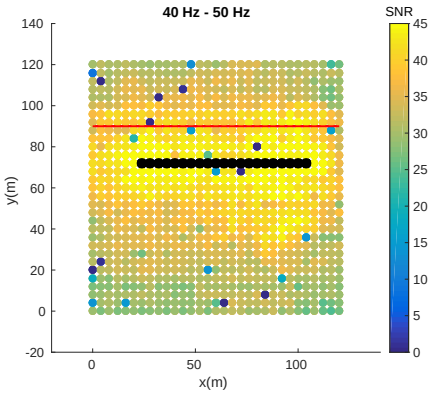
40 Hz - 50 Hz
SNR
y(m)
x(m)

(c)

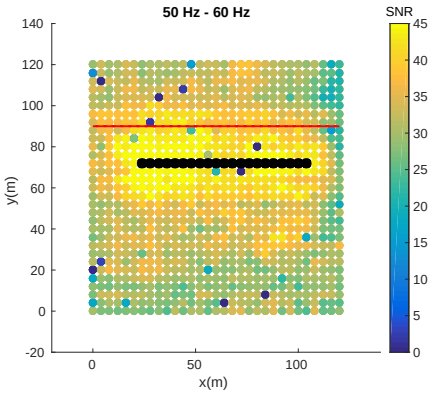
50 Hz - 60 Hz
SNR
y(m)
x(m)

(d)

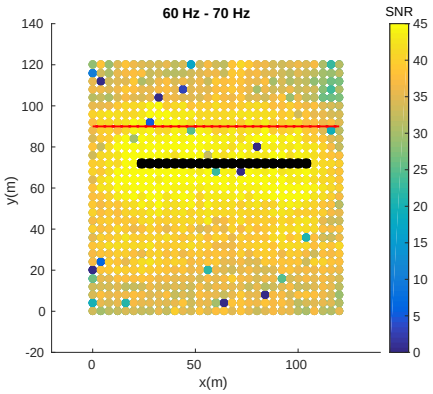
60 Hz - 70 Hz
SNR
y(m)
x(m)

(e)

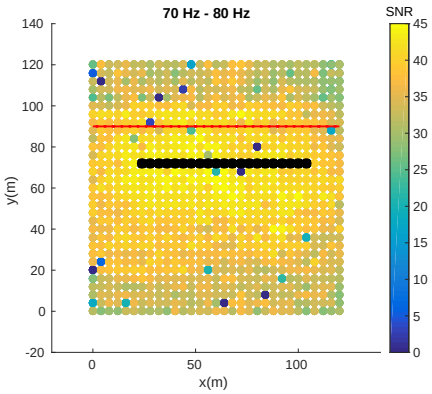
70 Hz - 80 Hz
SNR
y(m)
x(m)

(f)

Appendix C

In this Appendix, we show spatial map of average of maximum of coherency received along a line of virtual receivers inside the forest arranged vertically with respect to the border between the field and the forest from virtual sources distributed homogeneously in the field and the forest. The distance between the virtual receivers along this line is 2 m. The averaging over maximum of coherency is performed over all possible virtual receiver pairs separated by 20 m. Panels (a) to (f) show these maps in different frequency bands. We also show the averaged value of time dispersion of signals at different frequency bands averaged over all virtual receivers along the line.

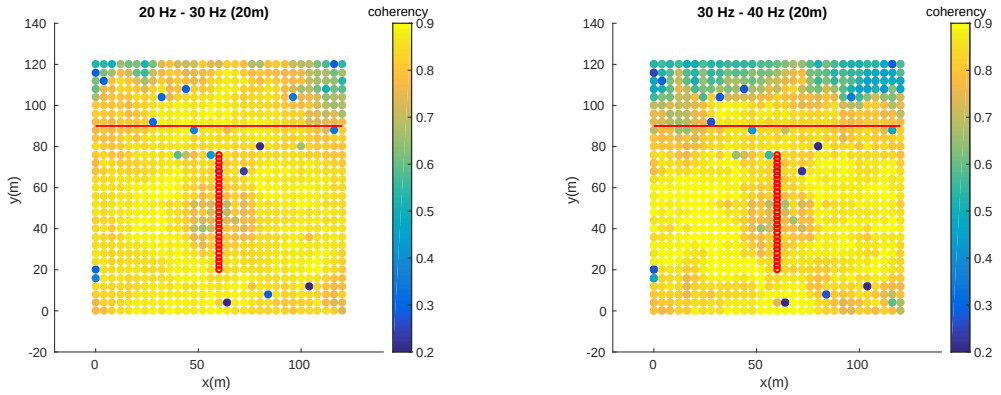

(a)

(b)

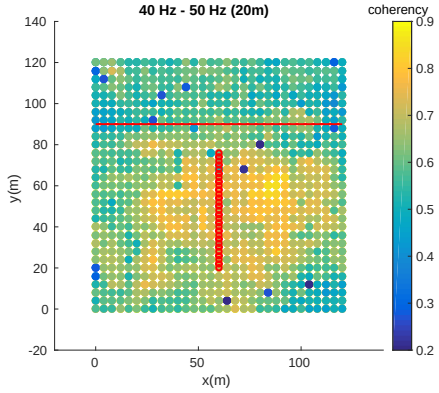

(c)

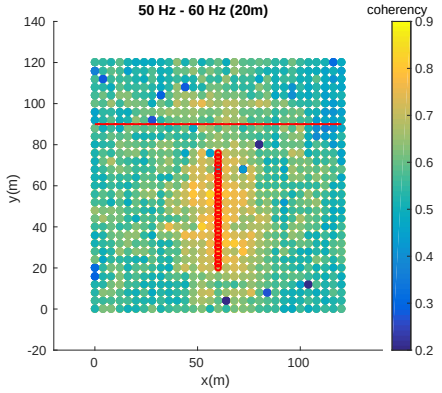

(d)

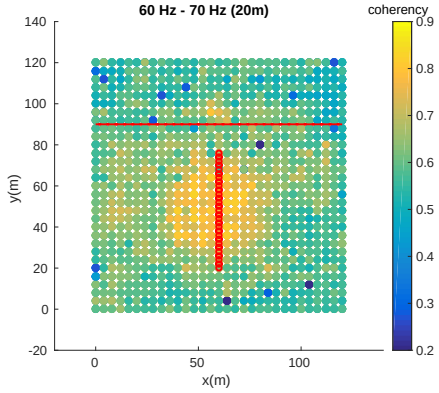

(e)

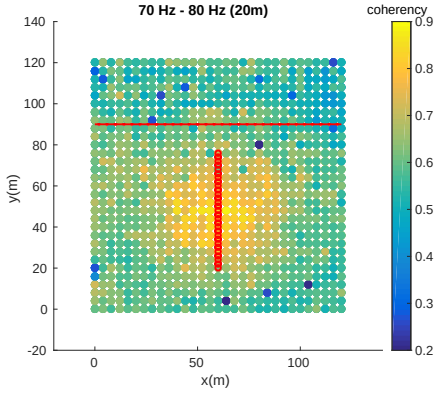

(f)

Figure C.1: Spatial map of average of maximum of coherency received along a line of virtual receivers.

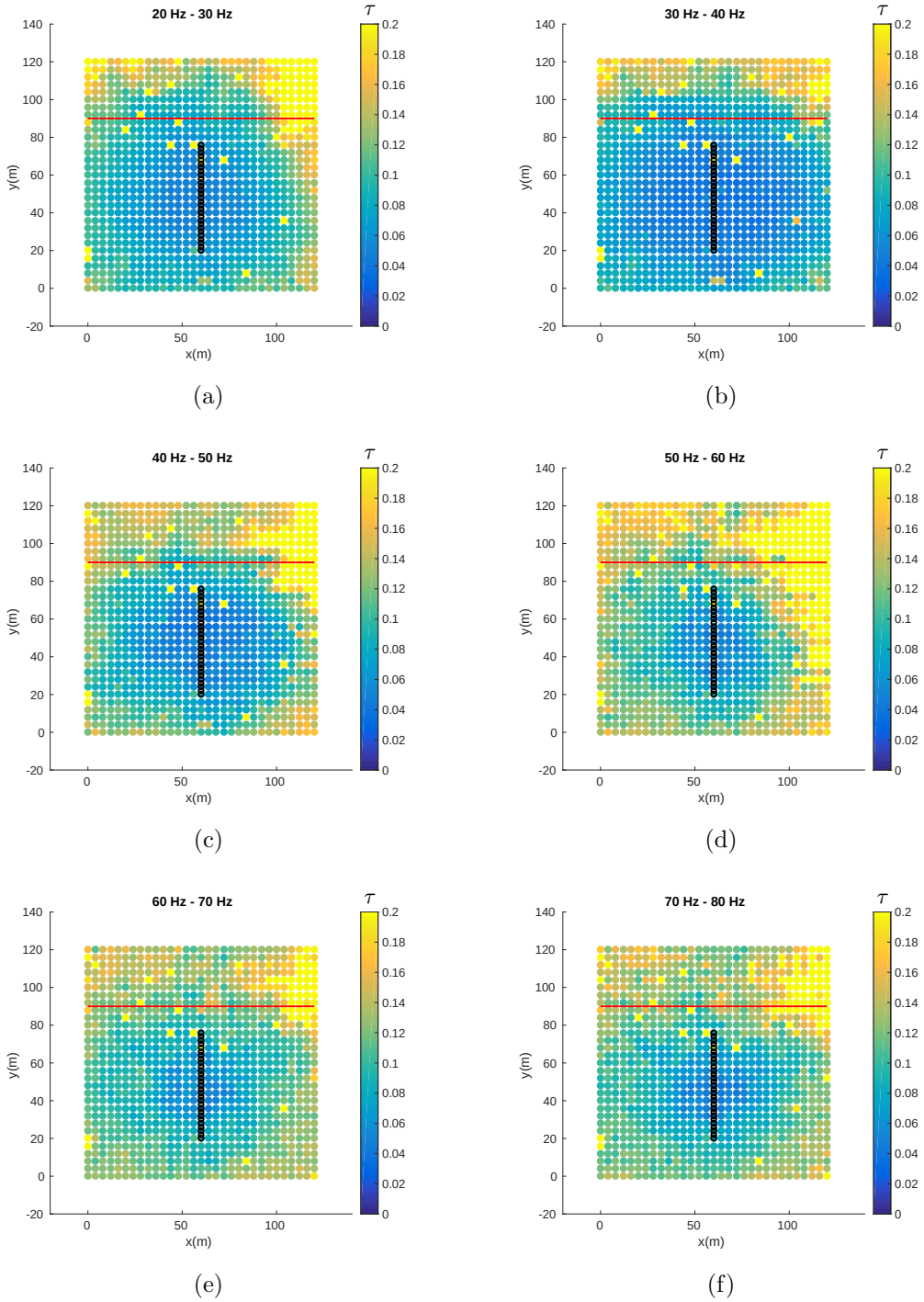

Figure C.2: Spatial map of spreading time of signals (τ) in seconds.

Appendix D

In this Appendix, we show spatial maps of average of maximum of coherency along a line of virtual receivers located along a horizontal line in the field and outside the forest from virtual sources distributed homogeneously in the field and the forest. The averaging over maximum of coherency is performed over all possible virtual receiver pairs separated by 20 m.

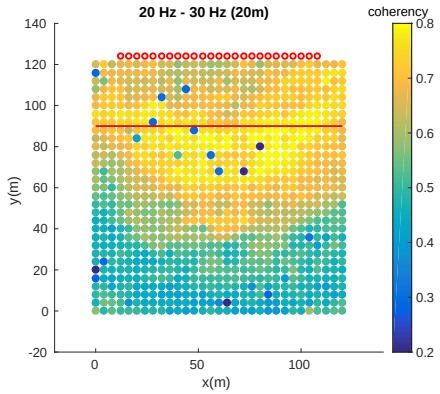
20 Hz - 30 Hz (20m)
coherency
y(m)
x(m)

(a)

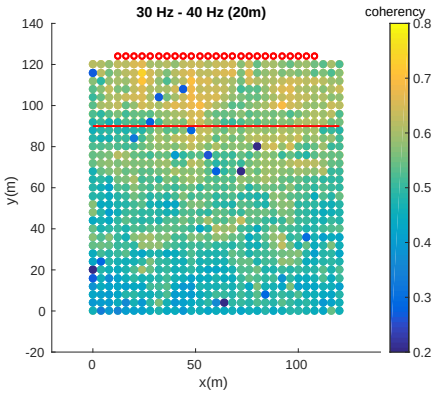
30 Hz - 40 Hz (20m)
coherency
y(m)
x(m)

(b)

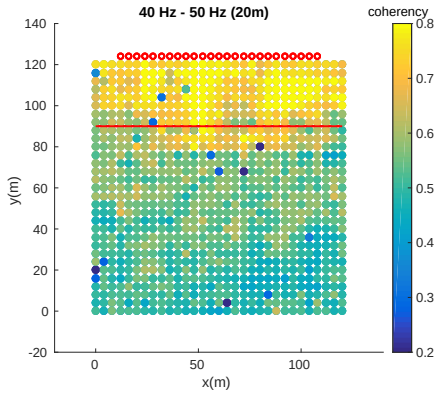
40 Hz - 50 Hz (20m)
coherency
y(m)
x(m)

(c)

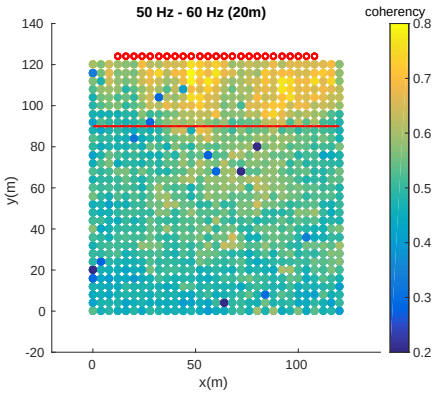
50 Hz - 60 Hz (20m)
coherency
y(m)
x(m)

(d)

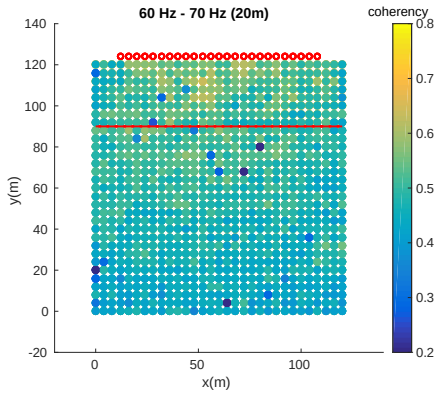
60 Hz - 70 Hz (20m)
coherency
y(m)
x(m)

(e)

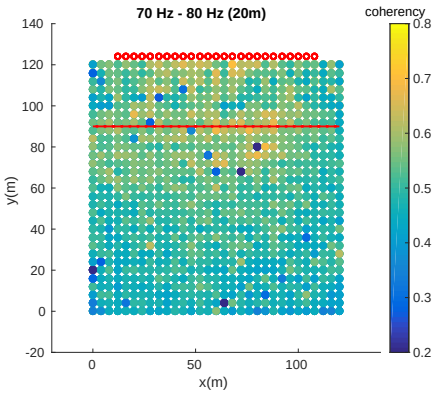
70 Hz - 80 Hz (20m)
coherency
y(m)
x(m)

(f)

Bibliography

[1] L. Chehami, E. Moulin, J. de Rosny, C. Prada, O. Bou Matar, F. Benmeddour, and J. Assaad. Detection and localization of a defect in a reverberant plate using acoustic field correlation. *Journal of Applied Physics*, 115(10):104901, 2014. 1.1, 2.3, 2.3, 3.1

[2] H. Lamb. On waves in an elastic plate. In *Proceedings of the Royal Society of London A: Mathematical, Physical and Engineering Sciences*, volume 93. The Royal Society, 1917. 1.2

[3] D. Royer and E. Dieulesaint. *Elastic waves in solids I.* Springer-Verlag Berlin, Heidelberg, 2000. 1.2, 1.3, 3.3, 4.1, 4.2

[4] O. Xéridat. Ondes de lamb en milieux complexes : propagation, diffusion, localisation. *Ph.D thesis, University of Nice Sophia Antipolis (UNS)*, 2011. 1.4, 1.5

[5] E. Ventsel and T. Krauthammer. *Thin plates and shells: theory, analysis and application.* Marcel Dekker, Inc., 2001. 1.3, 1.3.1

[6] R.D. Mindlin. Influence of rotary inertia and shear on flexural motions of isotropic, elastic plates. *Journal of Applied Mechanics*, 18, 1951. 1.3, 1.3.2

[7] R.D. Mindlin. Thickness-shear and flexural vibrations of crystal plates. *Journal of Applied Physics*, 22(316), 1951. 1.3, 1.3.2

[8] S. Timoshenko and S. Woinowsky-Krieger. *Theory of plates and shells.* New York : McGraw-Hill, 2nd ed edition, 1959. 1.3.1

[9] C. Vemula and N. Norris. Flexural wave propagation and scattering on thin plates using mindlin theory. *Wave Motion*, 26, 1997. 1.3.2

[10] J.D. Achenbach. *Wave propagation in elastic solids.* North-holland., 1973. 1.3.2

[11] A.W. Leissa. *Vibration of plates.* NASA SP-160, 1969. 1.4

[12] D.K. Miller and D.H. Franklin. *Modal density of thin circular cylinders.* NASA CR-897, 1967. 1.4.1

[13] F.D. Hart and K.C. Shah. *Compendium of modal densities for structures.* NASA CR-1773, 1971. 1.4.1

[14] H. Weyl. Das asymptotische verteilungsgesetz der eigenwerte linearer partieller differentialgleichungen (mit einer anwendung auf die theorie der hohlraumstrahlung). *Math. Ann.*, 71:441–479, 1912. 1.4.1

[15] K. Aki. Space and time spectra of stationary stochastic waves, with special reference to microtremors. *Bull. Earth. Res. Inst.*, 35:415–456, 1957. 2.1, 2.2

[16] L. Boschi and C. Weemstra. Stationary-phase integrals in the cross correlation of ambient noise. *Reviews of Geophysics*, 53, 2015. 2.1, 2.2.1, 3.1, 3.4

[17] M. Campillo and A. Paul. Long-range correlations in the diffuse seismic coda. *Science*, 299(5606):547–549, 2003. 2.1

[18] F. Brenguier, N.M. Shapiro, M. Campillo, V. Ferrazzini, Z. Duputel, O. Coutant, and A. Nercessian. Towards forecasting volcanic eruptions using seismic noise. *Nature Geoscience*, 1, 2008. 2.1, 3.1

[19] Jon F. Claerbout. Synthesis of a layered medium from its acoustic transmission response. *Geophysics*, 33(2):264–269, 1968. 2.2

[20] R. L. Weaver and O. I. Lobkis. Ultrasonics without a source: Thermal fluctuation correlations at mhz frequencies. *Physical Review Letters*, 87(13), 2001. 2.2, 3.1

[21] O. I. Lobkis and R. L. Weaver. On the emergence of the Green's function in the correlations of a diffuse field. *Journal of the Acoustical Society of America*, 110(6):3011–3017, December 2001. 2.2

[22] T. L. Duvall Jr, S. M. Jeffferies, J. W. Harvey, and M. A. Pomerantz. Time-distance helioseismology. *Nature*, 362:430–432, 1993. 2.2

[23] R. Snieder. Extracting the Green's function from the correlation of coda waves: A derivation based on stationary phase. *Phys. Rev. E*, 69:046610, Apr 2004. 2.2, 2.2.2

[24] P. Roux, K. Sabra, W. A. Kuperman, and A. Roux. Ambient noise cross correlation in free space: Theoretical approach. *J. Acoust. Soc. Am.*, 117(1):79–84, 2005. 2.2, 2.3, 2.6

[25] K. Wapenaar and J. Fokkema. Green's function representations for seismic interferometry. *Geophysics*, 71(4):SI33–SI46, 2006. 2.2.1, 2.2.1, 2.5

[26] H. Douma. Generalized representation theorems for acoustic wavefields in perturbed media. *Geophys, J. Int*, 179:319–332, 2009. 2.2.1

[27] A. T. de hoop. Time-domain reciprocity theorems for acoustic wave fields in fluids with relaxation. *The Journal of the Acoustical Society of America*, 84, 1988. 2.2.1, 2.2.1

[28] J. Lin, J. Li, X. Li, and N. Wang. A hierarchical generalization of the acoustic reciprocity theorem involving higher-order derivatives and interaction quantities. *JASA Express Letters*, 140(4), 2016. 2.2.1

[29] M. Fink. Time reversed acoustics. *Physics Today*, 50(3), 1997. 2.2.1

[30] L.E. Kinsler, A.R. Frey, A.B. Coppens, and J.V. Sanders. *Fundamentals of Acoustics*. Wiley, Hoboken, N.J., 1999. 2.2.2, 3.4

[31] L. Stehly, M. Campillo, and N. M. Shapiro. A study of the seismic noise from its long-range correlation properties. *Journal of Geophysical Research*, 111, 2006. 2.2

[32] K. Wapenaar, D. Draganov, R. Snieder, X. Campman, and A. Verdel. Tutorial on seismic interferometry: Part 1 — basic principles and applications. *Geophysics*, 75(5), 2010. 2.3, 2.2.2

[33] A. Hejazi Nooghabi, L. Boschi, P. Roux, and J. de Rosny. Coda reconstruction from cross-correlation of a diffuse field on thin elastic plates. *Phys. Rev. E*, 96, 2017. 2.2.2, 3.1, 3.4

[34] E. Larose, P. Roux, M. Campillo, and A. Derode. Fluctuations of correlations and Green's function reconstruction: Role of scattering. *Journal of Applied Physics*, 103(11), 2008. 2.3, 3.1

[35] B. A. van Tiggelen. Green function retrieval and time reversal in a disordered world. *Phys. Rev. Lett.*, 91(24):243904, DEC 12 2003. 2.3

[36] J. de Rosny and M. Davy. Green's function retrieval and fluctuations of cross density of states in multiple-scattering media. *EPL (Europhysics Letters)*, 106(5):54004, 2014. 2.3

[37] T. Nowakowski, L. Daudet, and J. de Rosny. Localization of acoustic sensors from passive Green's function estimation. *The Journal of the Acoustical Society of America*, 138(5):3010–3018, 2015. 2.3

[38] K.G. Sabra, A. Srivastava, F.L. di Scalea, I. Bartoli, P. Rizzo, and S. Conti. Structural health monitoring by extraction of coherent guided waves from diffuse fields. *The Journal of the Acoustical Society of America*, 123(1):EL8–EL13, 2008. 2.3

[39] L. Chehami, J. de Rosny, C. Prada, E. Moulin, and J. Assaad. Experimental study of passive defect localization in plates using ambient noise. *IEEE transactions on ultrasonics, ferroelectrics, and frequency control*, 62(8):1544–1553, 2015. 2.3

[40] E. Larose, P. Roux, and M. Campillo. Reconstruction of Rayleigh-Lamb dispersion spectrum based on noise obtained from an air-jet forcing. *The Journal of the Acoustical Society of America*, 122(6):3437–3444, 2007. 2.3

[41] A. Colombi, L. Boschi, P. Roux, and M. Campillo. Green's function retrieval through cross-correlations in a two-dimensional complex reverberating medium. *The Journal of the Acoustical Society of America*, 135(3):1034–1043, 2014. 2.3

[42] A. Duroux, K.G. Sabra, J. Ayers, and M. Ruzzene. Extracting guided waves from cross-correlations of elastic diffuse fields: Applications to remote structural health monitoring. *The Journal of the Acoustical Society of America*, 127(1):204–215, 2010. 2.3

[43] F. Fahy and P. Gardonio. *Sound and structural vibration, radiation, transmission and response*. Academic Press, 2007. 2.3, 2.6

[44] J. Proakis and D. Manolakis. *Digital signal processing principles, algorithms, and applications*. Prentice Hall, 1996. 2.5.1

[45] T. D. Mikesell, K. van Wijk, T. E. Blum, R. Snieder, and H. Sato. Analyzing the coda from correlating scattered surface waves. *J. Acoust. Soc. Am.*, 131, 2012. 2.5.1

[46] E. Moulin, F. Benmeddour, H. Achdijan, L. Chehami, J. Assaad, J. de Rosny, and C. Prada. Exploitation of the reverberant propagation of elastic waves in structures: towards a concept of low-resource shm sensor network. *Physics Procedia*, 2015. 2.6

[47] L. Chehami. Surveillance passive des milieux reverberants par correlation de bruit ambiant: appliacation a la localisation de defauts. *Ph.D thesis, University of Valenciennes*, 2015. 2.6

[48] W. H. Press, S. A. Teukolsky, W. T. Vetterling, and B. P. Flannery. *Numerical recipes in c, the art of scientific computing*. Cambridge University Press, 1992. 2.7, 2.7

[49] M. Davy, J. de Rosny, and P. Besnier. Green's function retrieval with absorbing probes in reverberating cavities. *Physical Review Letters*, 116(21):213902, 2016. 2.7

[50] RH Lyon. Statistical analysis of power injection and response in structures and rooms. *The Journal of the Acoustical Society of America*, 45(3):545–565, 1969. 2.8

[51] M. L. Mehta. *Random matrices*, volume 142. Academic press, 2004. 2.8

[52] M. Wright and R. Weaver. *New directions in linear acoustics and vibration: quantum chaos, random matrix theory and complexity.* Cambridge University Press, 2010. 2.8

[53] KB Efetov. Supersymmetry and theory of disordered metals. *advances in Physics*, 32(1):53–127, 1983. 2.8

[54] M. Berry. Regular and irregular semiclassical wavefunctions. *Journal of Physics A: Mathematical and General*, 10(12):2083, 1977. 2.8

[55] MW. Bonilha and FJ. Fahy. On the vibration field correlation of randomly excited flat plate structures, i: Theory. *Journal of sound and vibration*, 214(3):443–467, 1998. 2.8, III, III

[56] A. Derode, E. Larose, M. Campillo, and M. Fink. How to estimate the Green's function of a heterogeneous medium between two passive sensors? application to acoustic waves. *Appl. Phys. Lett.*, 83, 2003. 2.10

[57] A. Derode, E. Larose, M. Tanter, J. de Rosny, A. Tourin, M. Campillo, and M. Fink. Recovering the Green's function from field-field correlations in an open scattering medium (l). *The Journal of the Acoustical Society of America*, 113(6):2973–2976, 2003. 2.10

[58] C. Draeger and M. Fink. One-channel time reversal of elastic waves in a chaotic 2d-silicon cavity. *Physical Review Letters*, 79(3):407, 1997. 2.10

[59] C. Draeger and M. Fink. One-channel time-reversal in chaotic cavities: Theoretical limits. *The Journal of the Acoustical Society of America*, 105(2):611–617, 1999. 2.10

[60] M. Fink and E. Fort. From the time-reversal mirror to the instantaneous time mirror. *The European Physical Journal Special Topics*, 226(7), 2017. 2.10

[61] J. Loschmidt. Uber den zustand des warmegleichgewichts eines systems von korpern mit rucksicht auf die schwerkraft. *Sitzungsberichte der Akademie der Wissenschaften*, 73:128–142, 1876. 2.10

[62] E. Akkermans and G. Montambaux. Mesoscopic physics of photons. *J. Opt. Soc. Am. B*, 21(1):101–112, Jan 2004. 3.1

[63] R. Snieder. The theory of coda wave interferometry. *Pure and Applied Geophysics*, 163, 2006. 3.1

[64] K. Aki and B. Chouet. Origin of coda waves: Source, attenuation, and scattering effects. *Journal of Geophysical Research*, 80(23):3322–3342, 1957. 3.1

[65] G. Poupinet, W. L. Ellsworth, and J. Frechet. Monitoring velocity variations in the crust using earthquake doublets: an application to the calaveras fault, california. *Journal of Geophysical Research*, 1984. 3.1

[66] A. Grêt, R. Snieder, and J. Scales. Time-lapse monitoring of rock properties with coda wave interferometry. *Journal of Geophysical Research*, 111, 03 2006. 3.1, 3.1

[67] V. Rossetto, L. Margerin, T. Planès, and E. Larose. Locating a weak change using diffuse waves: Theoretical approach and inversion procedure. *Journal of Applied Physics*, 109(3):034903, February 2011. 3.1

[68] P. Sheng. *Introduction to Wave Scattering, Localization, and Mesoscopic Phenomena*. Academic Press, San Diego, 1995. 3.1, 3.2.1, 3.2.2, 3.3

[69] D. J. Pine, D. A. Weitz, P. M. Chaikin, and E. Herbolzheimer. Diffusing wave spectroscopy. *Phys. Rev. Lett.*, 60:1134–1137, Mar 1988. 3.1

[70] M. L. Cowan, J. H. Page, and D. A. Weitz. Velocity fluctuations in fluidized suspensions probed by ultrasonic correlation spectroscopy. *Phys. Rev. Lett.*, 85:453–456, Jul 2000. 3.1

[71] M. L. Cowan, I. P. Jones, J. H. Page, and D. A. Weitz. Diffusing acoustic wave spectroscopy. *Phys. Rev. E*, 65:066605, Jun 2002. 3.1

[72] J. de Rosny and P. Roux. Multiple scattering in a refelcting cavity: Application to fish counting in a tank. *J. Acoust. Soc. Am.*, 2001. 3.1

[73] J. de Rosny, P. Roux, M. Fink, and J.H. Page. Field fluctuation spectroscopy in a reverberant cavity with moving scatterers. *Physical review letters*, 90 9:094302, 2003. 3.1, 3.3, 3.3

[74] S. G. Conti, J. de Rosny, P. Roux, and D. Demer. Characterization of scatterer motion in a reverberant medium. *Journal of the Acoustical Society of America*, 119:769–776, 02 2006. 3.1

[75] P. Roux, W. A. Kuperman, and NAPL Grp. Extracting coherent wave fronts from acoustic ambient noise in the ocean. *J. Acoust. Soc. Am.*, 116(4, Part 1):1995–2003, October 2004. 3.1

[76] M. Campillo, P. Roux, B. Romanowicz, and A. Dziewonski. Seismic imaging and monitoring with ambient noise correlations. *Treatise on Geophysics*, pages 256–271, 2014. 3.1, 3.4

[77] K. Sabra, S. Conti, P. Roux, and W. Kuperman. Passive in vivo elastography from skeletal muscle noise. *Appl. Phys. Lett.*, 90, 2007. 3.1

[78] J. de Rosny and M. Davy. Green's function retrieval and fluctuations of cross density of states in multiple-scattering media. *EPL*, 106(5):54004, 2014. 3.1

[79] F. Brenguier, M. Campillo, T. Takeda, Y. Aoki, N. M. Shapiro, X. Briand, K. Emoto, and H. Miyake. Mapping pressurized volcanic fluids from induced crustal seismic velocity drops. *Science*, 345(6192):80–82, 2014. 3.1

[80] A. N. Norris and C. Vemula. Scattering of flexural waves on thin plates. *Journal of Sound and Vibration*, 181, 1995. 3.2.2

[81] A. Derode, P. Roux, and M. Fink. Robust acoustic time reversal with high-order multiple scattering. *Physical Review Letters*, 75, 1995. 3.3

[82] Yakov G. Sinai. Dynamical systems with elastic reflections. *Russian Mathematical Surveys*, 25:137–189, 1970. 3.4

[83] F. Mortessagne, O. Legrand, and D. Sornette. Transient chaos in room acoustics. *Chaos: An Interdisciplinary Journal of Nonlinear Science*, 3(4):529–541, 1993. 3.4

[84] V. G. Veselago. The electrodynamics of substances with simultaneously negative values of ϵ and μ. *Sov. Phys. Usp.*, 10(4), 1968. 4.2

[85] J. B. Pendry, A. J. Holden, D. J. Robbins, and W. J. Stewart. Magnetism from conductors and enhanced nonlinear phenomena. *IEEE Transactions on Microwave Theory and Techniques*, 47(11), 1999. 4.2

[86] J. B. Pendry. Negative refraction makes a perfect lens. *Phys. Rev. Lett.*, 85, 2000. 4.2, 4.4

[87] H. Tao, N. I. Landy, C. M. Bingham, X. Zhang, R. D. Averitt, and W. J. Padilla. A metamaterial absorber for the terahertz regime: Design, fabrication and characterization. *Opt. Express*, 16(10), 2008. 4.2

[88] C. Kittel. *Introduction to Solid State Physics*. Wiley, New York, 1996. 4.3.1

[89] E. Yablonovitch. Inhibited spontaneous emission in solid-state physics and electronics. *Phys. Rev. Lett.*, 58:2059–2062, 1987. 4.3.1

[90] R. Martinez-Sala, J. Sancho, J. V. Sánchez, V. Gómez, J. Llinares, F. Meseguer, and F. Meseguer. Sound attenuation by sculpture. *Nature*, 378. 4.3.1

[91] P. Deymier. *Acoustic Metamaterials and Phononic Crystals*. Springer, Berlin, 2013. 4.3.2

[92] R. Abdeddaim, A. Ourir, and J. de Rosny. Realizing a negative index metamaterial by controlling hybridization of trapped modes. *Phys. Rev. B*, 83, 2011. 4.3.2

[93] J. Steele, N. Grady, P. Nordlander, and N. Halas. *Plasmon hybridization in complex nanostructures*, volume 131. Springer Netherlands, Dordrecht, 2007. 4.3.2

[94] X. Jing, P. Sheng, and M. Zhou. Acoustic and electromagnetic quasimodes in dispersed random media. *Physical review. A*, 46, 1992. 4.3.2

[95] I. E. Psarobas, A. Modinos, R. Sainidou, and N. Stefanou. Acoustic properties of colloidal crystals. *Phys. Rev. B*, 65, 2002. 4.3.2

[96] T. Still, W. Cheng, M. Retsch, R. Sainidou, J. Wang, U. Jonas, N. Stefanou, and G. Fytas. Simultaneous occurrence of structure-directed and particle-resonance-induced phononic gaps in colloidal films. *Phys. Rev. Lett.*, 100, 2008. 4.3.2

[97] A. Lagendijk. *Vibrational Relaxation Studied with Light*. Springer US, 1993. 4.3.2

[98] J. de Rosny, G. Lerosey, and M. Fink. Theory of electromagnetic time-reversal mirrors. *IEEE Transactions on Antennas and Propagation*, 58(10), 2010. 4.4

[99] J. Zhu, J. Christensen, J. Jung, L. Martin-Moreno, X. Yin, L. Fok, X. Zhang, and F. J. Garcia-Vidal. A holey-structured metamaterial for acoustic deep-subwavelength imaging. *Nature Physics*, 7, 2010. 4.4, 4.5.1

[100] M. Rupin, F. Lemoult, G. Lerosey, and P. Roux. Experimental demonstration of ordered and disordered multiresonant metamaterials for lamb waves. *Phys. Rev. Lett.*, 112, 2014. 4.5.1, 4.5, 4.6, 4.8, 4.9, 4.6.1, 4.6.1, 4.6.1.1, 4.6.1.2, 4.6.1.2, 4.6.1.3

[101] F. Lemoult, N. Kaina, M. Fink, and G. Lerosey. Wave propagation control at the deep subwavelength scale in metamaterials. *Nature Physics*, 9. 4.5.1

[102] R. Craster and S. Guenneau. *World Scientific Handbook of Metamaterials and Plasmonics*, volume 2. World Scientific, 2017. 4.7

[103] A. Colombi, P. Roux, S. Guenneau, P. Gueguen, and R. V. Craster. Forests as a natural seismic metamaterial: Rayleigh wave bandgaps induced by local resonances. *Scientific Reports*, 6, 2016. 4.5.2, 4.10, 4.11, 4.12, 4.13

[104] P. Roux, D. Bindi, T. Boxberger, A. Colombi, F. Cotton, I. Douste-Bacque, S. Garambois, P. Gueguen, G. Hillers, D. Hollis, T. Lecocq, and I. Pondaven. Toward seismic metamaterials: The metaforet project. *Seismological Research Letters*, 89(2A):582, 2018. 4.14, 4.15, 4.16, 4.17, 4.18, 4.19, 4.20

[105] R. H. Lyon and R. G. DeJong. *Theory and Application of Statistical Energy Analysis*, chapter 4, pages 81–107. Newnes, Boston, second edition edition, 1995. III